UNIVERSITY OF LEEDS

Generation and application of automatically determined depth phase picks (pmP, pP, sP, sS)

Alice Emily Blackwell

Submitted in accordance with the requirements for the degree of Doctor of Philosophy

The University of Leeds

Faculty of Environment

School of Earth and Environment

March 2025

Declaration

The candidate confirms that the work submitted is her own, except where work which has formed part of jointly authored publications has been included. The contribution of the candidate and the other authors to this work has been explicitly indicated below. The candidate confirms that appropriate credit has been given within the thesis where reference has been made to the work of others.

The work in Chapter 2 appears in the following publication:

Blackwell, A., Craig, T. and Rost, S., 2024. Automatic relocation of intermediate-depth earthquakes using adaptive teleseismic arrays. Geophysical Journal International, 239(2), pp.821-840.

AB acquired the data, developed the methodology, conducted the data analysis, created the figures, and wrote/edited the manuscript. TC and SR conceptualized the work, supervised and provided weekly suggestions, discussions and feedback on the methodology/results, and reviewed/edited the manuscript. The manuscript was additionally edited to reflect the comments from two anonymous reviewers.

Acknowledgements

I would like to express my deepest gratitude to both of my supervisors, Tim and Sebastian, for their unwavering support, guidance, and encouragement throughout the course of my Ph.D. Their expertise, constructive feedback, and constant mentorship have been invaluable in shaping my research and academic growth. I am truly grateful for their patience and belief in my abilities.

I would also like to acknowledge and thank my collaborators at the International Seismological Centre, whose warm welcome, insights, collaboration, and discussions greatly enriched my Ph.D experience, and the development of my work in Chapters 4 and 7. Their previous experience with machine learning also played a crucial role in expediting the research presented in Chapter 5, and I deeply appreciate their contributions to this project.

Finally, I would like to extend heartfelt thanks to my friends and family – with special mentions to Oliver, Clarrie, my Mum (Lucy), Emma, Hannah, Andrew, Eilish, and all those in 8.152 – for their continued support. Their camaraderie, understanding, and encouragement have been vital in helping me navigate the challenges of my Ph.D. I am lucky to have shared this experience with such wonderful people.

Thank you to everyone who has played a part in making this journey a memorable one.

Abstract

Depth phases (near-source surface reflections, e.g. *pP*) are crucial for accurate determination of intermediate-depth earthquake (occurring between 60–300 km depth) locations using global seismic data. However, detection of these phases suffers from poor signal-to-noise ratios in the direct wave coda. To address this limitation, I developed an automated approach to group globally-distributed stations at teleseismic distances into *ad-hoc* arrays with apertures of 2.5°, before optimising and applying phase-weighted beamforming techniques to each array. Resultant vespagrams allow automated picking algorithms to determine *P*, *pmP*, *pP*, *sP*, *S* and *sS* arrivals, which are subsequently used to determine high resolution event locations (using 1D and 3D approaches) and Moho depths. Improvements in event location and Moho depths, from incorporating *ad-hoc* array-determined phases, enhance our ability to establish subduction zone geometry, investigate the governing controls on intra-slab deformation, and analyse the rheology of the slab and mantle wedge.

I demonstrate my approach by relocating 1046 intermediate-depth events (based upon 68,075 depth phase detections) and generating Moho depth maps (using 2965 *pmP* detections) on a continental-scale for the South American Subduction Zone, with the Peruvian flat slab and northern Chile acting as validation regions. The final 3D event locations indicate a deeper subducting slab than previously suggested, highlighting limitations in current global slab models. In Peru, the relocated seismicity nucleates on the bounding bends of the flat slab, indicating the influence of flexural bending in the presence of dehydration embrittlement, and in-line with hydrated slab bathymetric features. In contrast, Chilean earthquakes occur continuously along the normally subducting slab and show signs of a double seismogenic zone, alongside other slab features. Amplitude analysis of *pmP* and *pP* arrivals also indicates a cold, dry, isolated mantle wedge overlying the Peruvian flat slab, which transitions into warmer, viscously coupled mantle beyond the distal bend

and into Chile.

Contents

List of Figures

Chapter 1

Introduction

This thesis focuses on leveraging the increasing volume of readily available teleseismic data, passively sourced from intermediate-depth earthquakes, to automatically generate: (1) phase catalogues (including depth phases) to integrate into global databases, (2) high resolution intermediate-depth earthquake catalogues, and (3) Moho depth maps, from P wave coda – and to a lesser extent, S wave coda – picks. These additional constraints can be used to infer geological and geophysical characteristics for a geodynamic setting, and interpret regional controls. I have concentrated on applying these approaches to subduction zones – specifically the South American Subduction Zone, with large regional test areas in Peru and northern Chile – to demonstrate their capability. Further explanation for the use of the South American Subduction Zone as a case study is provided in Section 1.3.4.

During this chapter, I will establish context, key concepts and motivation for the work discussed in the following chapters. These include an introduction to the challenges of earthquake relocation, and the application of seismology to overcome them, before discussing intermediate-depth earthquakes, their nucleation in subduction zones and why we need to accurately determine their hypocentral locations.

1.1 Earthquake location and current catalogues

Locating earthquakes using seismic data is an essential part of seismology (Geiger, 1910; Engdahl et al., 1998; Waldhauser & Ellsworth, 2000; Bondár & Storchak, 2011; Robinson et al., 2013; Tibuleac, 2014; Florez & Prieto, 2017; Sippl et al., 2018; Craig, 2019;

Münchmeyer et al., 2024) with a large number of proposed approaches to improve accuracy. The approaches break down into several categories of choice: local, teleseismic (30-90°) or global data; single station data, or multi-station arrays; phase arrival time based or waveform based; 1D or 3D location; absolute or relative location.

Well established earthquake catalogues, for example the ISC or ISC-EHB catalogues (Bondár & Storchak, 2011; Weston et al., 2018; Engdahl et al., 2020a), use local, teleseismic and globally determined phase arrivals from single station data to relocate their earthquakes to an absolute 3D location with a linearized inversion, using phases defined in Storchak et al. (2003). However, those who conduct smaller regional studies favour different approaches, tailored to their purpose and with the possibility of higher computational demands.

For example, Sippl et al. (2018) generate an automatic microseismicity catalogue for northern Chile using local, single station continuous data (largely from the IPOC network (GFZ & CNRS-INSU, 2006)) in conjunction with an automated iterative picking routine involving short-term average over long term average (STA/LTA) (Allen, 1982) event detection, traveltime based event association, and P (Di Stefano et al., 2006) and S (Diehl et al., 2009) phase pickers. The events are subsequently relocated using the phases and a 1D inversion (Kissling et al., 1994) to simultaneously solve for velocity and hypocentral depth, and finally relocated using the double difference approach (Waldhauser & Ellsworth, 2000). Applying the double difference approach updates the catalogue of events from absolute 3D locations to locations which consider the event population relative to one another.

Double difference relocations consider neighbouring event pairs, which are assumed to have similar ray paths, and the differences in their observed travel times relative to theoretical travel time, in order to iteratively determine the expected vector difference between their hypocentres, independently of velocity structure (Waldhauser & Ellsworth, 2000). Applying a double difference algorithm is helpful for identifying geometries and features defined by seismicity at depth. Other catalogues which use the double difference approach include Schaff and Waldhauser (2005), Rietbrock and Waldhauser (2004), Nippress and Rietbrock (2007), Pesicek et al. (2010) and Kumar et al. (2016).

To determine high resolution depth locations for earthquakes without local deployments or seismic stations, teleseismic (30-90°) phase arrivals (e.g. Murphy & Barker, 2006; Tibuleac, 2014; Florez & Prieto, 2017; Craig, 2019) or waveform inversions are favoured

(e.g. Craig et al., 2011; Devlin et al., 2012; Craig & Hull, 2024). The use of waveform inversions is computationally and analytically intensive, which limits studies to individual events, seismic sequences or small 3D regions. In contrast, teleseismic phase arrivals can be scaled up to form regional to global earthquake catalogues, using either a 1D (Craig, 2019) or 3D (Bondár & Storchak, 2011) relocation approach. Using teleseismic data has an advantage when it comes to determining more accurate event depths, as the epicentral distance bounds allow depth phases to be recorded. Depth phases (see Section 1.2.1) provide a crucial constraint on depth by reducing the effect of the origin time-event depth trade-off (e.g. Billings et al., 1994), yet unfortunately depth phases can often be obscured by the direct arrival coda and/or are small in amplitude, which renders them difficult to pick consistently. Here is where researchers have begun to expand upon array seismology, and apply array processing concepts to assist manual or semi-automatic depth phase identification – with global stacks (Woodgold, 1999; Murphy & Barker, 2006; Fang & van der Hilst, 2019) and statically assembled, 'medium'-aperture *ad-hoc* arrays (Tibuleac, 2014; Florez & Prieto, 2017).

Alternatively, Münchmeyer et al. (2024) have developed and trained two deep learning models to detect depth phases on single station teleseismic data, using the ISC-EHB phase catalogue (Engdahl et al., 2020b). The models are based upon the PhaseNet U-Net-type model (W. Zhu & Beroza, 2019), and consider either single station data, or a multi-station approach. The multi-station approach additionally analyses the move-out of the depth phases with respect to epicentral distance on single station seismograms, to determine phase coherence and traveltime probability. The multi-station model provides more consistent depth phase picks and, consequently, back-projected relocation results (Münchmeyer et al., 2024). Depth phases and array processing techniques will be discussed in greater detail in Sections 1.2.1 and 1.2.2.

Current earthquake relocation and catalogues are therefore hindered by several factors, as described above:

1. Near-to-source receivers are needed to provide depth resolution, and to reduce the effect of the origin time-depth trade-off, if depth phases are not incorporated.

2. Teleseismic traveltime based approaches using depth phases are limited by manual or semi-automatic phase picking and verification, and machine learning pickers require time- and data-intensive, computationally expensive training on both single station

and array data.

3. Current array processing approaches which determine depth phase arrival times – to provide depth resolution during relocation – give limited consideration for: the near-to-receiver velocity structure; maximising the available teleseismic station density per event; or generating location errors.

4. If computationally intensive waveform modelling is used to ascertain accurate source locations and characteristics, the study size needs to be small/sub-regional.

This thesis intends to address the limitations experienced by previous earthquake catalogues, using an approach presented in Chapters 2, 3, 4 and 7 – a summary workflow is available in Appendix A.15. The approach enables the dynamic creation of *ad-hoc* arrays from the available teleseismic stations per event, *ad-hoc* array tailored processing and automatic detection of depth phases to improve depth resolution during event relocation. High resolution results are achieved without near-to-source seismometers, expensive computational or analytical processes, or significant scaling limits.

1.2 Array processing

Array processing takes seismic data from a group of stations (an array), and allows the data to be considered as an ensemble. This provides the opportunity to improve the signal-to-noise ratio of any arrivals in seismic data, and extract local-to-receiver parameters such as horizontal slowness and backazimuth (Rost & Thomas, 2002).

The apertures of the arrays – used in this context – can be variable in size from small-aperture (typically $<0.4^\circ$ or 50 km (e.g. Heyburn & Bowers, 2008; Craig & Heyburn, 2015)), 'medium'-aperture (typically $<5^\circ$ or 556 km (Florez & Prieto, 2017)), and wide-aperture (typically these can be $>9^\circ$ or 1000 km) or global arrays (Woodgold, 1999; Murphy & Barker, 2006; Tibuleac, 2014; Craig, 2019; Fang & van der Hilst, 2019).

Intentionally designed small-aperture arrays tend to be globally sparse, whilst wide-aperture arrays suffer from loss of signal coherency across the entire aperture (Langston, 2014). With the increasing density of seismic data globally, *ad-hoc* medium-aperture arrays can now be built with relative ease from the available stations (Florez & Prieto, 2017), and used to assess recent earthquakes. Forming medium-aperture arrays from available stations circumvents a global deficit in designed small- or medium-aperture arrays, and opens

the door to applying array processing approaches to persistent seismic data issues, such as detecting low amplitude depth phases (Section 1.2.1).

1.2.1 Depth phases

Depth phases are near-source surface reflections, which offer an additional constraint on earthquake depth. They are a crucial observation to limit the origin time-event depth trade-off which occurs during event relocation, when local receivers are unavailable (Bondár & Storchak, 2011).

For the purpose of this thesis, I will be largely employing the use of the pP, sP and sS depth phases in Chapters 2, 3, 4, 5 and 7. The ray paths for each are as follows (Figure 1.1):

- pP – P wave with an upwards take-off angle, reflects off the free surface, and travels to the receiver as a P wave.
- sP – S wave with an upwards take-off angle, reflects off the free surface, converts, and travels to the receiver as a P wave.
- sS – S wave with an upwards take-off angle, reflects off the free surface, and travels to the receiver as a S wave.

Additionally, I also analyse at depth underside reflections in Chapters 6 and 7:

- pmP – P wave with an upwards take-off angle, reflects off the Moho, and travels to the receiver as a P wave.

Event depth can be determined from the relative delay time between the depth phase(s) and their associated direct phase (e.g. pP to P), assuming that the ray paths of the phases are similar after the depth phase surface reflection, and the near-source velocity structure is well constrained. Therefore, the relative time between the depth phases and the direct arrival is unaffected by the distal velocity structure, the resultant depth is independent of the location coordinates and absolute travel times of the phases are not required when applying this approach. The advantages of using depth phases to precisely determine earthquake depth are considerable, and enable a simpler path to improving event depth resolution – hence their popularity (Engdahl et al., 1998; Murphy & Barker, 2006; Letort et al., 2016; Florez & Prieto, 2017; Craig, 2019).

The weakness in using depth phases is that they are difficult to detect and identify, partic-

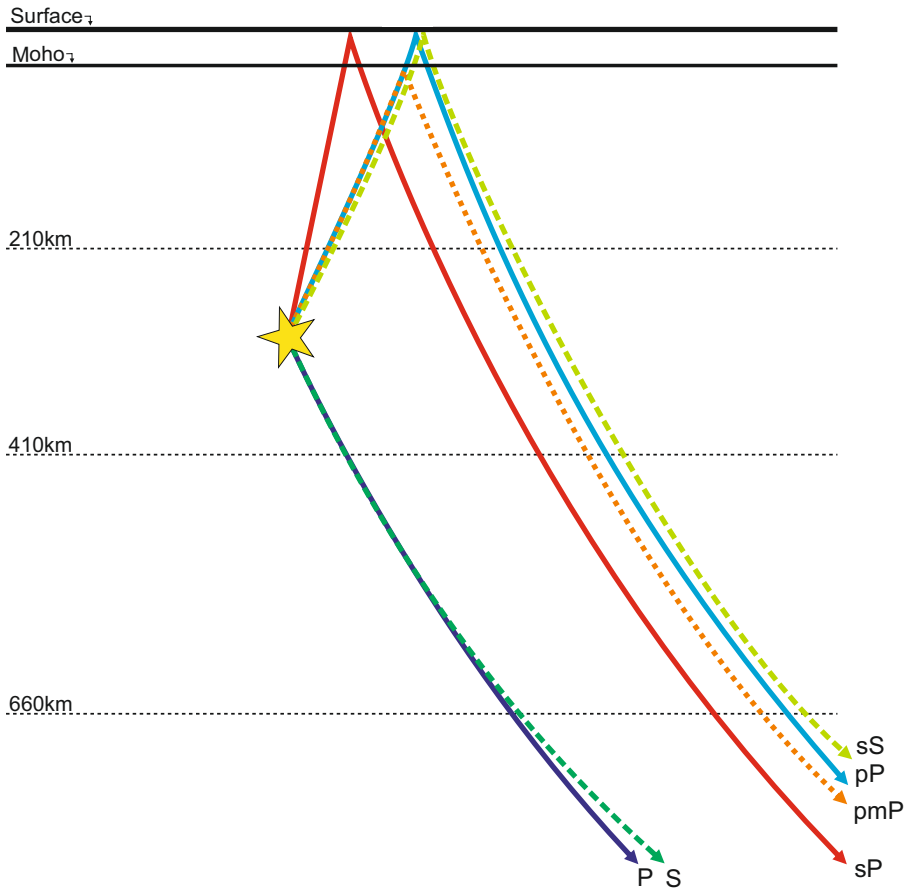

Figure 1.1: Theoretical ray paths for P, pmP, pP, sP, S and sS for a 300 km deep earthquake using the ak135 velocity model (Kennett et al., 1995).

ularly for smaller magnitude earthquakes ($M_w < 6$). The relatively low amplitude arrivals tend to be surrounded by increased 'noise' levels from the direct phase coda and, at distances less than 30° or depths of less than 40 km, are likely to overlap with the direct phase arrival. Factors which control the detectability of the depth phases include the complexity of the near-source velocity structure, the event magnitude and radiation pattern, and the ray path attenuation. Furthermore, there is a trade-off between the event magnitude and the depth of the event when it comes to depth phase detectability, since larger magnitude earthquakes will have longer, potentially more complex source-time functions, which in combination with a shallow event with shorter relative time delays between the depth phases and the direct arrival, will result in overlapping and interfering arrivals at the receiver. To succeed in identifying and picking depth phases universally, application of signal-to-noise enhancing methodologies is required.

1.2.2 Array processing techniques

This section will introduce basic array processing concepts used during Chapters 2, 3, 4, 6 and 7. Within these chapters there is also further discussion about the development of phase detection and identification routines, which builds upon the techniques outlined in this section.

A key array processing technique used is beamforming, where data are slowness corrected to a designated coordinate within the array aperture, stacked into a beam and normalised (Figure 1.2). Beamforming removes incoherent noise through destructive interference, whilst retaining coherent, constructive signal (i.e. phase arrivals, see Figure 1.3).

The linear beamforming process can be applied to an array of waveforms using:

$$b(t) = \frac{1}{M} \sum_{i=1}^{M} x_i(t - \mathbf{r}_i \cdot \mathbf{u}), \tag{1.1}$$

where M is the number of stations, x_i is the recorded trace at station i, $\mathbf{r}$ is a two component vector describing the location of station i relative to the reference station and $\mathbf{u}$ is a two component horizontal slowness vector. The dot product of $\mathbf{r}$ and $\mathbf{u}$ represents the timeshift a trace needs to undergo, for a specific slowness, in order to align its expected phase arrivals with those from the reference location, to stack coherently.

Beams are generated for a specific backazimuth and horizontal slowness, assuming that the

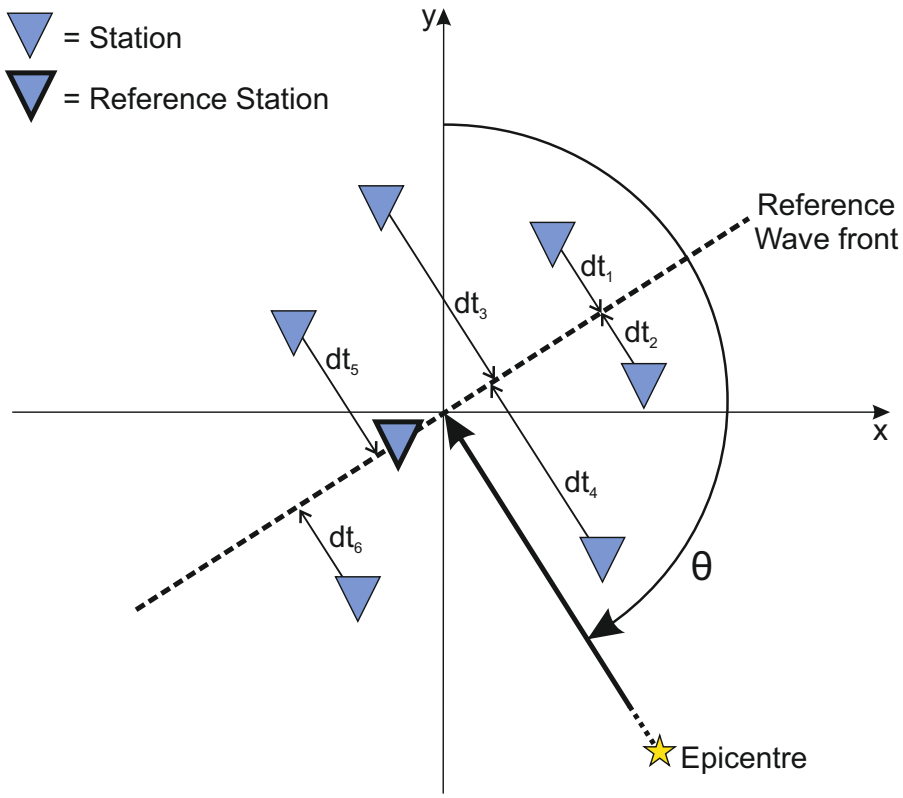

Figure 1.2: Cartoon of an array in the horizontal plane, showing how station data is corrected to the reference station during linear beamforming, with a time shift (dt_i) calculated using a specific horizontal slowness for the array. θ is the backazimuth – the bearing between north and the earthquake epicentre.

wavefront is planar and velocity variations are minimal across the aperture of the array, although it is also possible to beamform with a spherical wavefront assumption (Ward et al., 2020, 2021). The necessity of this depends on the array aperture versus the wavefront curvature. For wide aperture arrays where the phases are unlikely to be coherent across the aperture, time-compressional or distance-dependent waveform windowing are used for beamforming the array (Woodgold, 1999; Murphy & Barker, 2006; Craig, 2019).

The values for backazimuth and horizontal slowness can be calculated theoretically using ray tracing (Crotwell et al., 1999) between the source and reference location, in conjunction with a 1D velocity model. However, the best-fitting values can alternatively by found directly from the array data using F-K analysis or beampacking, which allows local-to-receiver calibration and acknowledgement of the velocity structure variations (Rost & Thomas, 2002). Beampacking is simply the application of beamforming for a specific phase arrival, in a grid search for backazimuth and slowness to find the values which provide the greatest beam amplitude. The impact of using the best-fitting slowness and backazimuth relative to the theoretically calculated values is demonstrated in Chapters 2, 3 and 7 (also see Appendix A.4).

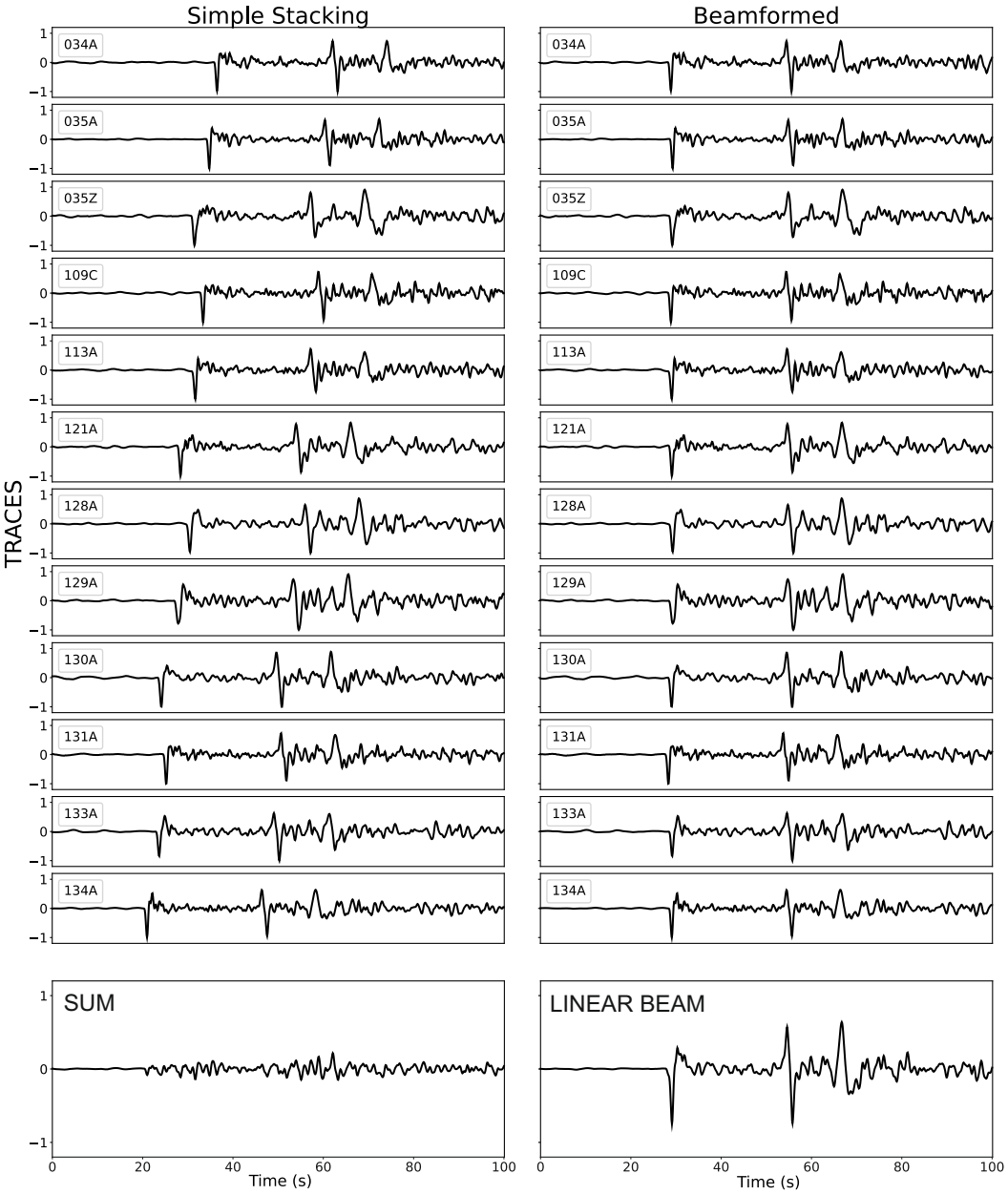

Figure 1.3: Comparison between simple stacking (left) and beamforming (right). Where the upper panels display the traces, already aligned in the beamforming case, and the lowest panel displays the stack. Normlalised velocity data from the m_b 6.2, 23rd May 2010 earthquake in Peru, for an array at a 50.7° epicentral distance from the hypocentre.

The beams created during linear beamforming can be weighted to improve the relative amplitude of coherent arrivals with low relative amplitudes (e.g. depth phases) using phase-weighted stacking (Schimmel & Paulssen, 1997). Phase-weighted stacking is a non-linear method, which weights the sample points in a beam according to an amplitude independent coherency measure – the instantaneous phase.

The instantaneous phase is a factor in the phase stack, which is calculated and applied to the linear beam as follows:

$$b_p(t) = b(t) \left| \frac{1}{M} \sum_{m=1}^{M} e^{i\phi_m(t)} \right|^v , \tag{1.2}$$

where b_p is the phase-weighted stack, b_t is the linear beam, M is the number of seismograms in the beam, ϕ_m is the mth instantaneous phase, and v is the weighting exponent. The phase stack consists of the term inside the modulus.

The phase stack weights perfectly coherent signals with 1, and down-weights less coherent signal towards zero for a given sample point of the linear beam. The phase stack is also given an exponent, this exponent controls the level of suppression for incoherent signal (larger exponents result in greater suppression). An example showing linear and phase-weighted beamforming is shown in Figure 1.4. The consequent phase-weighted waveforms are distorted by the application of a coherency weighting, and should not be used for waveform analysis. It is also worth noting that phases which are not consistently observed across an array will be down-weighted, due to a lack of array coherence. Similarly, if the slowness correction applied to the stations during beamforming to align the data to the same reference location is poor, the arrivals could be down-weighted due to lower coherency and reduce the visibility of the phase in the stack. The impact of applying the best-fitting slowness correction to a linear beam is demonstrated in Chapters 2, 3 and 7, without which key phases may not be detected.

The linear or phase-weighted beams can also be generated whilst varying only one parameter – either horizontal slowness or backazimuth – to create multiple beams for the same array. The multiple beams can subsequently be combined to construct a vespagram (Davies et al., 1971). Vespagrams indicate how amplitude behaves as a function of slowness or backazimuth, which may form a useful indicator of confidence in a phase arrival's coherency across an array (see Chapters 2, 3 and 7). An example phase-weighted

Figure 1.4: Normalised, slowness corrected traces beamformed into a linear beam and phase-weighted (PW) with an exponent for 4 to improve the signal-to-noise ratio of the S and sS arrivals. Data from m_b 6.2, 23rd May 2010 intermediate-depth event in Peru, from a group of stations (labelled) with a geometric centre 66.1° from the event.

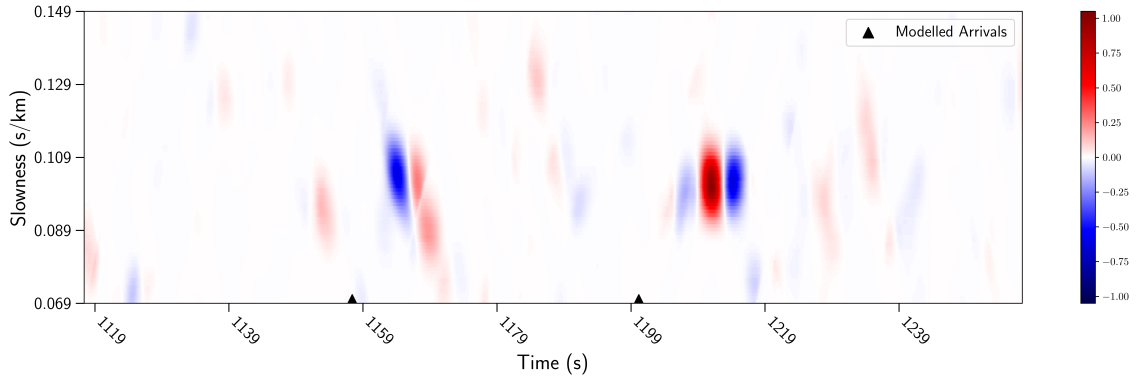

Figure 1.5: Normalised amplitude vespagram constructed with phase-weighted, transverse component beams. Data from m_b 6.2, 23rd May 2010 intermediate-depth event in Peru, from a group of stations (see Figure 1.4) with a geometric centre 66.1° from the event. Modelled arrival times for S and sS shown with black triangle markers. Colourbar shows normalised amplitude from –1 (blue) to 1 (red), with 0 indicated by white.

vespagram is shown in Figure 1.5, constructed using the traces beamformed in Figure 1.4.

1.3 Subduction zones

Subduction zones are a key setting for earthquakes, particularly for seismicity which occurs below the crust (i.e. more than approximately 40 km deep). This section introduces the geometry and forces involved at a subduction zone and their link to the three main categories of earthquakes for the setting – megathrust, intermediate-depth and deep. I then discuss in more detail the occurrence of intermediate-depth earthquakes, their possible nucleation mechanisms, and how improved hypocentral relocation could help to constrain hypothesises.

1.3.1 Subduction zone dynamics

Subduction zones occur where the convergence between two lithospheric plates (i.e. an oceanic and a continental plate, or two oceanic plates) is accommodated by one plate descending beneath the other. A combination of forces allows a dynamic equilibrium (Figure 1.6) to be established between the plates and the supporting mantle (Forsyth & Uyeda, 1975), whereby the sinking denser plate – also known as the slab – bends and unbends underneath the less dense plate (Sandiford et al., 2020). Several drivers for subduction and continued convergence have been investigated, of which slab pull – the negative buoyancy that a denser down-dip slab exerts on the remaining plate – is thought to be the dominant driver. Other geodynamic forces, including ridge push and viscous coupling between the lithosphere and the underlying asthenosphere, are considered second

order contributors (Forsyth & Uyeda, 1975).

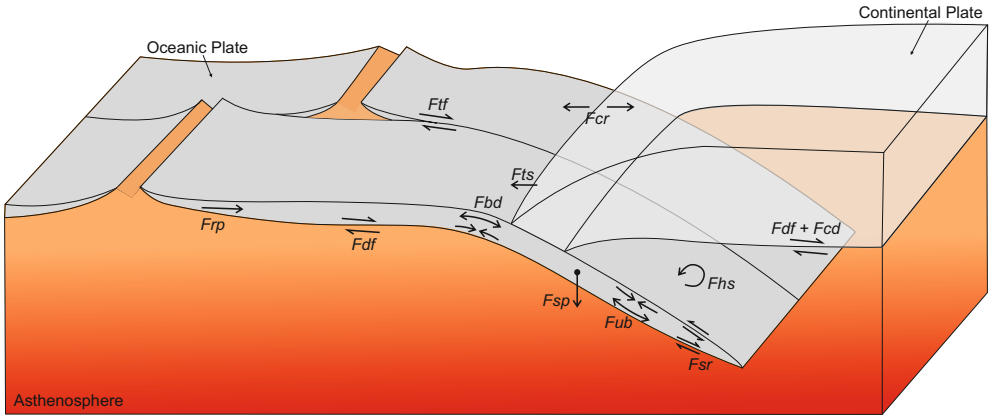

Figure 1.6: Schematic of the geodynamic forces influencing a subduction zone, adapted from Forsyth and Uyeda (1975). The forces are defined as: Fsp = Slab Pull, Frp = Ridge Push, Fsr = Slab Resistance, Fdf = Mantle Drag on the oceanic plate, Fdf + Fcd = Mantle Drag on the continental plate (allows for greater mantle viscosity underneath continental crust), Fhs = Hydrodynamic Suction, Fbd = Slab Bending, Fub = Slab Unbending, Fcr = Colliding Resistance, Fts = Trench Suction, and Ftf = Transform Fault Resistance.

The location and style of seismicity expressed at a subduction zone is directly related to the geodynamic system. It is therefore important to understand and investigate the regional and local forces present. Key force components for earthquake nucleation are: negative and positive buoyancy forces from metamorphic phase conversion; thermal contrasts and isostasy; slab flexure during bending and unbending; rheological resistance at the slab interface; mantle resistance towards slab penetration and hydrodynamic suction within the mantle wedge (van Hunen et al., 2004; Sandiford et al., 2020). The combination and influence of the respective forces present on a slab affects the angle of slab dip and the strain that the slab is internally accommodating. If the forces and thus the slab angle are dynamically altering, the adjustments will positively or negatively feed back to the individual force contributions, therefore allowing a shift in the dominating controls on earthquake nucleation, and the subsequent style of seismicity. As a result we can use earthquakes, their seismic expressions and locations, to study the geometry, deformation and rheology of subducting slabs.

1.3.1.1 Flat slab subduction

Flat slab subduction zones – where the down-going plate subducts at a sub-horizontal angle (less than 5°) over a sustained distance (greater than 100 km) (Taramõn et al., 2015) –

were originally identified using earthquake locations to infer slab geometry (e.g. in Peru, Barazangi & Isacks, 1976). However to this day, the origin and driving mechanisms behind the development of flat slabs remain poorly understood, largely due to the apparent lack of consistent global controls. Previous studies have suggested a range of factors which could initiate and sustain flat slab subduction, including the subduction of buoyant features (e.g., Pilger, 1981; Gutscher et al., 2000; van Hunen et al., 2002), forced trench retreat from an overthrusting continental plate (e.g., van Hunen et al., 2004; Schepers et al., 2017), and strong hydrodynamic suction in the mantle wedge (e.g., Tovish et al., 1978; Ma & Clayton, 2015) possibly enhanced by a thick/cratonic overriding plate (e.g., Taramõn et al., 2015). For margins in close proximity to oceanic hotspots, slab–plume interactions have also been suggested as a contributing factor (e.g., Betts et al., 2012).

The subduction of buoyant features on the down-going slab remains the longest-standing hypothesis for the development of flat slab subduction (Pilger, 1981). However, this idea is challenged by the absence of a consistent spatial correlation between buoyant features and flat slab segments. This is evidenced by a lack of modern flat slab segments on the western edge of the Pacific Plate despite the subduction of ridges (e.g. Kamchatka and the Emperor Ridge) (Schellart, 2020), and the presence of a well-developed flat slab beneath central Mexico, where the subducting Cocos Plate lacks an obvious buoyant feature (Manea et al., 2017).

Consequently, researchers now favour a combination of interplaying factors to explain flat slab subduction (Manea et al., 2012; Antonijevic et al., 2015). For example, the subduction of a buoyant feature may be reinforced by an enhanced mantle suction and forced trench retreat (van Hunen et al., 2004). Schellart (2020) propose that these combinations are more likely to occur at old, established and wide subduction zones – such as the South American Subduction Zone (SASZ), where both Peru and central Chile have flat subducting slab segments of the down-going Nazca Plate. The seismicity of the Peruvian flat slab segment of the Nazca Plate will be studied further in Chapters 2, 4, 6 and 7, with Chapter 7 also addressing the seismicity of the Pampean (northern Chile) flat slab segment further south.

1.3.1.2 Subduction zone earthquakes

Broadly there are three categories of earthquakes associated with the slab of a subduction zone. As subduction occurs, the down-going slab bends into the trench to cause extensional outer rise faulting, and is then subject to megathrust earthquakes between the

under-thrusting slab and the overriding plate edge, intermediate-depth earthquakes within the slab between 60-300 km deep into the mantle, and deep earthquakes at depths >300 km – although deep earthquakes are not ubiquitous (Frohlich, 2006). Megathrust events are strongly related to frictional forces between the two plates (Lay et al., 2012; Yang et al., 2012), whilst the controls on intermediate- depth and deep earthquake nucleation are still debated (Hacker et al., 2003; John et al., 2009; Ferrand et al., 2017; Sandiford et al., 2020). In addition to their tectonic significance, earthquakes at depth serve as valuable seismic sources. The ray paths generated by these events can be used to investigate surrounding velocity structures, such as the Mohorovičić (Moho) discontinuity (McGlashan et al., 2008; Phillips et al., 2012). As this thesis uses intermediate-depth events for insights into subduction zones, further discussion on the controls over intermediate-depth earthquake nucleation can be found in Section 1.3.2.

1.3.2 Intermediate-depth earthquakes

Intermediate-depth earthquakes are defined as occurring between 60-300 km deep (Frohlich, 2006), and include any events which do not nucleate using the same frictional mechanism as the seismogenic zone, megathrust earthquakes (Yang et al., 2012; Sippl et al., 2018). Geometrically, the lower extent of the megathrust seismogenic zone can be defined as where the slab interface exists below the Moho of the overriding plate, and is in direct contact with the mantle wedge. Before the depth limit of the megathrust events, intermediate-depth earthquakes begin to occur intra-slab, and deepen away from the slab top interface with respect to absolute depth/distance from the trench (Hayes et al., 2018). Meanwhile, the mantle couples to the slab interface and is viscously dragged and deformed – this viscously deformed mantle is termed the mantle wedge (van Keken, 2003). The down-dip intra-slab seismicity forms a plane, representative of the slab geometry, called the Wadati-Benioff zone (Wadati, 1928; Benioff, 1949). Some subduction zones have two seismic planes, separated by a 20-40 km aseismic gap (Hasegawa et al., 1978; K. Wang, 2002; Yamasaki & Seno, 2003). These are typically referred to as a double seismogenic zones (DSZs, Figure 1.7). DSZs naturally pinch out as the two planes coalesce at depth (Hacker et al., 2003; Sippl et al., 2018; Florez & Prieto, 2019). The separation of the DSZs, and thus the thickness of the aseismic wedge, is dependent on the thermal structure of the slab – older (and therefore colder) slabs commonly display a thicker aseismic wedge than younger and hotter slabs (Brudzinski et al., 2007; Florez & Prieto, 2019). The depth at which the two

planes merge is thought to be controlled by the slab thermal parameter (Wei et al., 2017; Florez & Prieto, 2019), where colder slabs have DSZs which extend to greater depths (e.g. Tonga's cold slab DSZ extends to approximately 300 km).

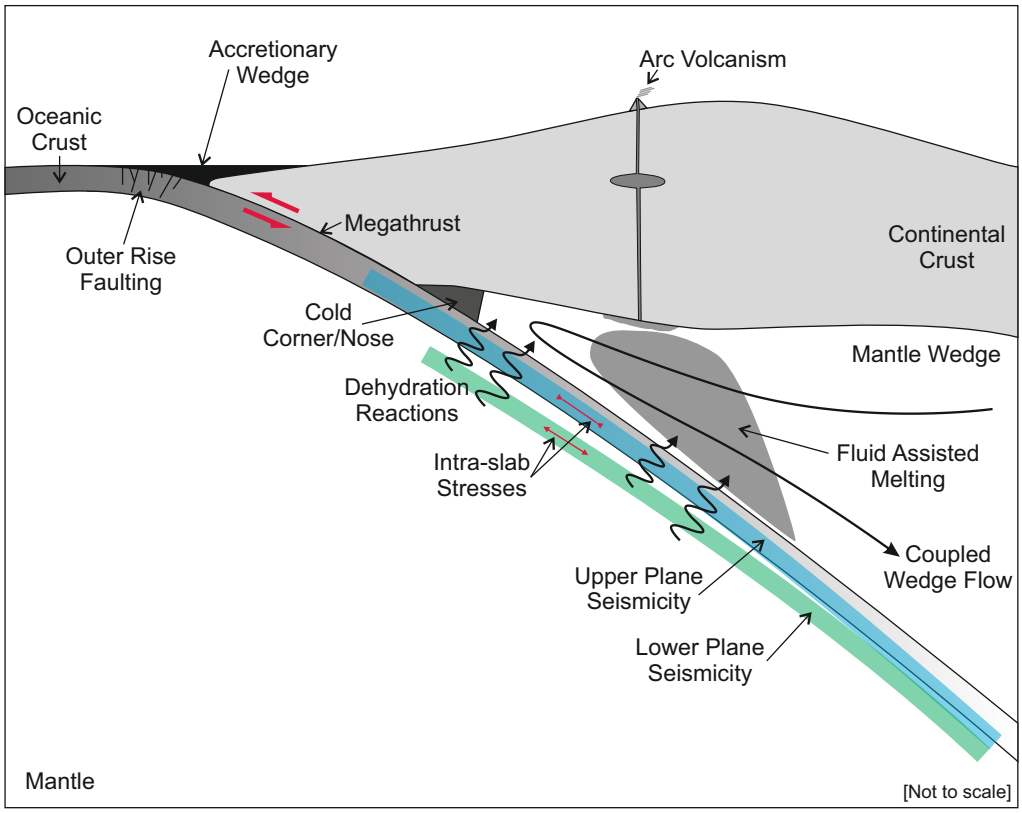

Figure 1.7: Schematic subduction zone with a double seismogenic zone (DSZ), highlighting key characteristics discussed during the chapter and thesis. The blue domain represents upper plane seismicity, while the green domain indicates the approximate location of lower plane seismicity within the down-going slab, often attributed to the breakdown of lawsonite and serpentinite, respectively (see Section 1.3.2.1). Adapted from van Keken and Wilson (2023).

Brudzinski et al. (2007) conducted a global study to address whether DSZs are widespread, and concluded that every subduction zone has at least a segment expressing an upper and lower band of seismicity. This has later been corroborated by the work of Florez and Prieto (2019), who relocated and analysed 32 slab segments globally. The presence of DSZs in all subduction zones indicates that the mechanism driving intermediate-depth seismicity must be present globally regardless of plate thermal structure, convergence rate and stress state (Brudzinski et al., 2007). However the heterogeneous nature of seismic activity presents a challenge for developing a widely compatible petrological and dynamic framework for subducting slabs (Sandiford et al., 2019). Many mechanisms have been proposed to explain the presence of intermediate-depth seismicity, and its manifestation as DSZs, since brittle failure should not be occurring at these depths. Proposed models

include the dehydration of hydrothermally altered oceanic lithosphere (Hacker et al., 2003), shear instabilities (Hobbs & Ord, 1988; Liu & Yao, 2020), and the bending/unbending of the subducting slab (Sandiford et al., 2020). These are discussed in Sections 1.3.2.1, 1.3.2.2 and 1.3.2.3, respectively.

1.3.2.1 Dehydration reactions

Dehydration reactions have been proposed as a facilitation mechanism for intermediate-depth earthquake nucleation, due to their ability to reduce fault and material strength (Sibson, 1977) via dehydration embrittlement (Murrell & Ismail, 1976; Kirby et al., 1996; Jung et al., 2004; Wagner et al., 2020). As the slab subducts, hydrated minerals from sea-water percolation, assisted by outer rise faults (Figure 1.7) and sometimes fluid-rich sediments on the slab top (K. Wang et al., 1997), begin to metamorphose under the increased pressure-temperature conditions by expelling their fluid content (Kirby et al., 1996). This increases the local pore fluid pressure (PFP), which acts to reduce the stress and confining pressure the slab may be experiencing, and thereby invoking a reduced effective differential stress upon the material (Figure 1.8). Mechanical failure, and therefore an earthquake, is prompted according to the Mohr-Coulomb failure envelope (Sibson, 1977) in a pressure-temperature regime which should deform in a ductile manner (Wagner et al., 2020), due to the changes in the local stress regime. The distribution of seismicity, for instance the reduction in earthquake frequency with respect to depth and the higher density of earthquakes close to pertinent pressure-temperature conditions, strongly supports the importance of dehydrating hydrous minerals for intermediate-depth earthquake nucleation (Kirby et al., 1996; Peacock, 2001; Hacker et al., 2003; Yamasaki & Seno, 2003; Abers et al., 2013). The hydration of the mantle additionally encourages partial melting of the overlying mantle wedge, and associated explosive arc volcanism to occur (van Keken & Wilson, 2023).

Lower DSZ Reactions

Different mineralogical systems have been experimentally observed to exhibit embrittlement during dehydration, such as amphibolite (Hacker & Christie, 2011), chlorite (Murrell & Ismail, 1976), gypsum (Ko et al., 1997), serpentine (Rutter & Brodie, 1988) and tremolite (Kirby, 1987), when the permeability of the material proves inadequate to allow fluid pressure to decrease.

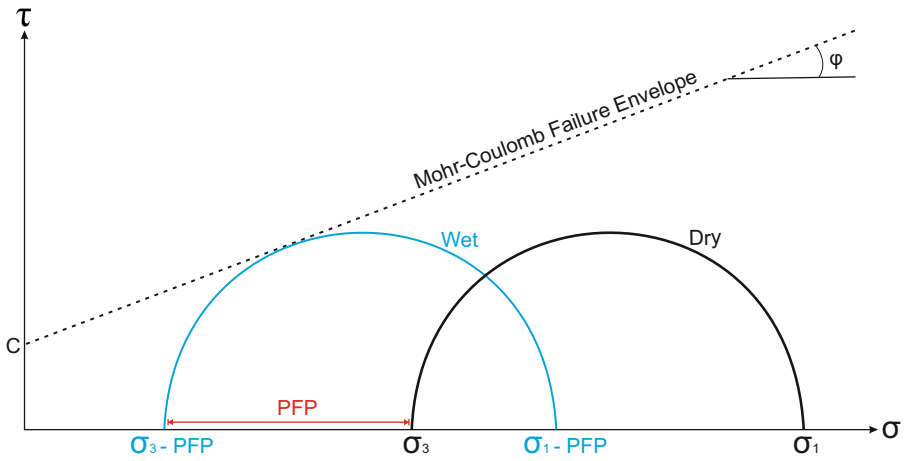

Figure 1.8: A schematic Mohr circle demonstrating the leftward shift of the dry total stress circle (black) – which represents the differential stress a material is under – due to an increase in pore fluid pressure (PFP). The new, wet, effective stress circle (blue) intersects the failure envelope (dashed line) indicating that brittle failure will occur. Shear stress (τ) and normal stress (σ) are on the y- and x-axes respectively, C represents the cohesion of the material and ϕ represents the angle of internal friction.

The upper mantle of the slab is likely hydrated – consisting of a serpentinite-dominated mineral assemblage, typically an altered harzburgite – largely due to infiltration of sea water at the outer rise. The dehydration of serpentinite, via an antigorite reaction under experimental conditions, causes an instantaneous stress decrease accommodated by shear fracturing (Raleigh & Paterson, 1965) and corresponds to the pressure-temperature conditions at locations of lower plane seismicity beneath north east Japan (Peacock, 2001). Seismicity which delineates the lower plane of the DSZ is therefore typically attributed to the breakdown of serpentinite (Peacock, 2001; Hacker et al., 2003; Sippl et al., 2018; Lu et al., 2021).

Upper DSZ Reactions

The upper plane of the DSZ could exist in the upper mantle of the down-going slab, and/or the crust depending on the temperature of the subduction zone – intermediate-depth earthquakes are observed in the crust and mantle of cold subduction zones slabs, whereas hot subduction zone slabs predominantly nucleate events sub-slab Moho (Abers et al., 2013). For cold subduction zones, the seismicity of the upper plane is proposed by Hacker et al. (2003) to result from lawsonite breakdown in the lower oceanic crust during eclogitisation, which is a reaction proven to be seismogenic by Okazaki and Hirth (2016). However, the presence of lawsonite is unlikely for younger, more buoyant, hot slabs such as Cascadia (Hacker et al., 2003). For hot subduction zones, the slab crust

pressure-temperature trajectory crosses a different set of reaction boundaries. Instead the slab crust might dehydrate to eclogite, via zoisite and antigorite, resulting in the slow release of water (Abers et al., 2013). The difference in slab temperatures and thus, reaction pathways, is likely to influence rate of seismogenesis, as the cold reaction pathway causes a net increase in solid plus fluid volume, whilst the hot reactions result in a net volume loss (Abers et al., 2013). The net volume increase from the blueschist/lawsonite reactions indicates a greater release of fluid than for the zoisite-antigorite-eclogite reactions, which could decrease PFP rapidly and enable brittle failure to a greater extent in cold slabs (Abers et al., 2013).

1.3.2.2 Shear instabilities

Shear instabilities (sometimes referred to as plastic instabilities) cause localised thermal runaway along a plane – typically a pre-existing shear zone from outer rise or transform faulting reactivated by viscous shear (Kelemen & Hirth, 2007). The plane is weakened through the interaction between shear heating and temperature-dependent rheology (Thielmann et al., 2015). Heat is generated at a greater rate than can be dissipated via conduction, allowing melt (Hosseinzadehsabeti et al., 2021), strain softening (Hobbs & Ord, 1988; John et al., 2009) and/or grain size reduction (Golding et al., 2012; Thielmann et al., 2015) to occur along the fault planes. This initiates a positive feedback cycle and can enable unstable, seismogenic slip at relatively low shear stresses (Ogawa, 1987).

Shear instabilities associated with strain softening will occur below a critical temperature, above which strain hardening processes dominate. Therefore for a given critical temperature and geothermal gradient of a subducting slab, there will exist a depth (approximately 800 km) beyond which shear instabilities are not possible due to the stability strain hardening provides (Hobbs & Ord, 1988). Since this mechanism appears to be functional to greater depths and occurs in the absence of increased PFP/without brittle failure (John et al., 2009), it is likely that shear instabilities may also be responsible for deep focus earthquakes (e.g. Ogawa, 1987; Wiens, 2001; Prakash et al., 2023).

Kelemen and Hirth (2007) suggest that shear instabilities nucleate in pre-existing shear zones from outer rise or transform faulting, and are reactivated via highly localised viscous creep. Kelemen and Hirth (2007) and Prakash et al. (2023) model thin olivine-rich and carbonate layers hosted in coarser grained peridotite respectively, and determine that unstable sliding is possible for these compositions under intermediate-depth earthquake

conditions.

Rather than suggest shear instabilities as an independent mechanism, researchers tend to propose that shear instability earthquakes likely occur alongside those caused by dehydration embrittlement (e.g. the upper band of DSZ seismicity, Figure 1.7) (John et al., 2009; Prieto et al., 2017; Prakash et al., 2023). However for subduction conditions which do not favour brittle failure due to dehydration reactions, a shear instability based mechanism is proposed to dominate (Prakash et al., 2023). Suggested locations for this are at depths greater than approximately 200 km (depending on the thermal state of the subduction zone) (Prakash et al., 2023), and slabs where the oceanic crust may not have been hydrated by outer rise faulting/sea-water penetration (Ranero et al., 2005; Wagner et al., 2020).

Shear instabilities have been recently proposed as an explanation for the nucleation of intermediate-depth earthquakes, including for the Hindu Kush nest (Poli et al., 2016), the M_w 4.8 Wyoming earthquake in continental lithosphere (Prieto et al., 2017), the M_w 8.0 Peruvian earthquake on 26th May 2019 (Liu & Yao, 2020) and for the lower plane of the Chilean DSZ (Lu et al., 2021). However alternative hypotheses for the Andean events, such as dehydration reactions, were ultimately favoured due to a lack of supporting temperature and velocity data. Despite the unpopularity of shear instabilities as a mechanism to explain intermediate-depth earthquakes, there are not sufficient data and experimental evidence to discount them as a viable option. Whether shear instabilities are a sustainable process at intermediate depths needs to be examined to a greater extent.

1.3.2.3 Intra-slab stresses

The relationships between slab seismicity, local/regional deviatoric stress and whole-scale subduction dynamics remain a challenge to unpick due to unresolved uncertainties, including the interplay of the metamorphic reactions and shear instabilities (discussed in Sections 1.3.2.1 and 1.3.2.2). Here I present two models which describe stress distribution in the subducting slab, without the consideration of either local perturbations or the effect of mineral reactions: the uniaxial stress model and the slab flexure model.

Early studies established a classic model relating intra-slab earthquake orientations to uniaxial stress and strain accommodation parallel to the down-going slab (Isacks & Molnar, 1969, 1971). Isacks and Molnar (1971) proposed that the predominant slab uniaxial stress

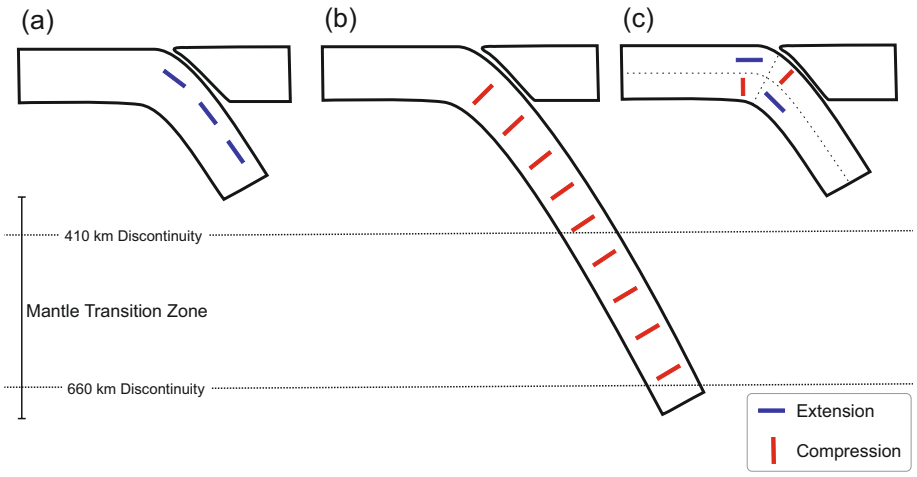

Figure 1.9: A schematic showing the uniaxial (a and b) and the flexural (c) intra-slab stress models, adapted from Isacks and Molnar (1971). The stress markers indicate approximate T-axes, whilst the dashed lines on (c) indicate the neutral planes of zero stress interpreted from Sandiford et al. (2020).

is tensile or compressional (Figure 1.9a and b) depending upon if the deepest portion of connected down-going slab exists in weak asthenosphere, where slab pull strongly exerts upon the slab (also observed by Rietbrock and Waldhauser (2004); Bloch et al. (2018)), or below the mantle transition zone, where resistive forces propagate up-dip (also observed by Gurnis et al. (2000); Billen et al. (2003)). However Apperson and Frohlich (1987) find that only 29% of their analysed earthquake focal mechanism catalogue, containing 853 CMT located events with a global distribution of hypocentres (>90 km deep), fit the slab parallel uniaxial stress hypothesis proposed by Isacks and Molnar (1971).

Furthermore, the simplicity of the uniaxial stress model also fails to explain the presence of DSZs, the upper and lower bands of which typically display opposing focal mechanisms (Figure 1.7). Updated focal mechanisms and models find the upper plane of a DSZ tends to express down-dip compression whilst the lower plane experiences down-dip tension (Engdahl & Scholz, 1977; Hasegawa & Sacks, 1981; Fujita & Kanamori, 1981; Brudzinski et al., 2007; Wei et al., 2017), this observation aligns with the stresses applied during slab unbending/flexure (Figure 1.9c) combined with dehydration embrittlement (Figure 1.7) in order to overcome the confining pressure (K. Wang, 2002; Sandiford et al., 2020).

Sandiford et al. (2019) used a flat slab configuration to assess the relationship between the increased number of slab bending points and the distribution of seismicity – they found a systematic link between increased seismicity and a greater slab curvature gradient. Additionally they observe an abrupt cessation of earthquakes at the $600-700$°C isotherm, where the brittle-viscous transition is expected (McKenzie, 1969), notably prevents the

full expression of the slab stress field at depth. Consequently, a slab which appears to be dominated by uniform down-dip tension may be experiencing compression below the 600-700°C isotherm without releasing a diagnostic seismic signal (Sandiford et al., 2019). This indicates that in order for bending/flexural related deformation to be seismogenic, the conditions for brittle deformation must already by present – either through shallower depth (reduced temperature-pressure conditions) or slab dehydration (local reduction in confining pressure).

Sometimes, on local data, a triple seismogenic zone can be observed, when unbending occurs in the presence of dehydration reactions to discretely form three planes under different pressure-temperature conditions (Igarashi et al., 2001). The upper plane is considered to be under an extensional stress regime and caused by eclogitisation reactions, whilst the middle and lower bands are thought to nucleate due to the accommodation of slab unbending (Igarashi et al., 2001; K. Wang, 2002). It is also thought that all double seismogenic zones are in fact under-developed triple seismogenic zones, where either the top or middle planes are less seismogenic either due to the balance between metamophic and unbending strain rates, or insufficient unbending strain (K. Wang, 2002).

1.3.2.4 Why relocate intermediate-depth earthquakes in subduction zones?

As shown in Sections 1.3.2.1, 1.3.2.2 and 1.3.2.3, the nucleation mechanism and the order/interplay of controls upon the location and distribution of intermediate-depth earthquakes, and thus intra-slab deformation, are still poorly understood (Hacker et al., 2003; Frohlich, 2006; Ferrand et al., 2017; Hosseinzadehsabeti et al., 2021; van Keken & Wilson, 2023). The primary limitation upon our understanding of these events is being able to accurately locate the hypocentres, and mapping those locations to the background rheology, geometry and conditions of the host slab. In subduction zones, the earthquake depth determination also needs to be at a higher resolution in order to assess the influence of rheological properties and intra-slab stress, as these change quickly over small vertical distances. Ultimately, it is important to continue researching the controls upon intermediate-depth earthquake nucleation and characteristics, as even though the hypocentres can be deep, they can present a significant seismic hazard to overlying population centres (Abe, 1972; Beck et al., 1998).

As a secondary reason, intermediate-depth earthquakes provide an excellent passive source to investigate other structures in the subduction zone. A good understanding of the source

location and parameters is essential when using earthquakes as sources for passive seismology, particularly for ray path calculation. One such structure which can be investigated with intermediate-depth earthquakes is the Mohorovičić discontinuity (McGlashan et al., 2008) – see Section 1.3.3 and Chapter 6 for further discussion.

For the reasons discussed above, I present in this thesis an intermediate-depth earthquake relocation approach to determine 1D (depth, Chapter 2) and 3D locations (Chapters 4 and 7) of events in subduction zones, in order to assist investigations into earthquake nucleation and provide insights into subduction zone geometry. See Section 1.4, for an overview of the thesis structure.

1.3.3 Moho depth

The Mohorovičić discontinuity (Moho) defines the boundary between the crust and the mantle (Mohorovičić, 1910), and can be identified seismically by observing a discrete increase in P and S wave velocity from 6.0-6.8 km/s and 3.7-3.9 km/s in the crust to approximately 8 km/s and 4.5 km/s in the mantle, and an increase in density from 2.7-2.9 to 3.3-3.4 g/cm^3 (Dziewonski & Anderson, 1981; Kennett & Engdahl, 1991; Kennett et al., 1995; Prodehl et al., 2013). The Moho depth is a critical parameter for defining geodynamic models (e.g. van Hunen et al., 2002), to understand the pressure-temperature conditions of the crust and upper mantle, gravitational measurements and resource distribution.

For subduction zones, alongside the slab top interpreted from intermediate-depth earthquakes (Hayes et al., 2018), the Moho depth is crucial to defining subduction zone geometry and the behaviour of the underlying mantle wedge. Furthermore, the mechanical nature of the Moho, which may be inferred from a reflector amplitude study (McGlashan et al., 2008), and the rheology of the lower crust versus upper mantle could be informative for understanding subduction zone dynamics and conditions.

Passive seismology and the application of receiver functions are classically used to determine Moho depth today, although controlled source seismic reflection/refraction surveys can also image the Moho (Prodehl et al., 2013). Receiver functions highlight near-to-receiver velocity structure interfaces which have converted P arrivals into SV waves (most prominently, the Moho), using an incoming teleseismic arrival. They are calculated by deconvolving the vertical component (or P) from the radial component (or SV), to re-

move the effect of the source-time function and near-source velocity structure (Langston, 1979). Deconvolving the vertical component from the transverse component provides signals which can be interpreted for anisotropy and dip (Langston, 1979; Farra & Vinnik, 2000). The resultant radial component receiver functions are typically stacked with move-out corrections to enhance the signal-to-noise ratio of key near-to-receiver conversion horizons (Farra & Vinnik, 2000) and migrated to the common conversion point (CCP) (Li et al., 2022). The travel times of the P to SV converted arrivals detected from the Moho can thus be used to determine Moho depth (Yuan et al., 2002), with the opportunity to analyse the signal amplitudes to infer discontinuity structure.

Using receiver functions to define Moho depth takes advantage of naturally occurring seismic sources (i.e. earthquakes), which is less costly than a planned controlled source experiment and will provide a greater coverage of data points globally (assuming a global coverage of seismometers). The limitations of receiver functions are the need for (1) a teleseismic source, receiver functions cannot be calculated if a study region lacks a seismically active zone within 30-90° epicentral distance (this is unlikely given the global distribution of seismic activity), and (2) for receivers located on the study region's surface. Alternatively, McGlashan et al. (2008) have developed an idea to use teleseismic *pmP* depth phases, near-source Moho reflectors, to define Moho depth. This removes the need for local receivers to determine the Moho, as only teleseismic receivers are necessary, however for *pmP* depth phases to occur, the study region will need to be seismically active at depths below the Moho.

Chapters 6 and 7 build upon the work of McGlashan et al. (2008) to generate regional Moho depth maps quickly and automatically, using teleseismic received *pmP* and *pP* phases detected on *ad-hoc* array data.

1.3.4 Study region – South American Subduction Zone

During this thesis, I demonstrate the methodologies using the South American Subduction Zone (SASZ) as a case study. The SASZ margin exists where the Nazca and South American plates converge, and extends from approximately 6°S to 45°S in latitude (Figure 1.10). The plates converge at a rate of ∼5.6–6 cm/yr (with the South American Plate overthrusting the Nazca Plate (Gripp & Gordon, 2002)) in the direction of ∼81–83°N (Trenkamp et al., 2002), which encourages increasingly oblique convergence north of Chile, where the subduction trench curves westward (Rodríguez et al., 2024). The down-going

Nazca plate in the SASZ has a number of bathymetric features which are thought to influence seismicity and slab geometry in the region, such as fracture zones and ridges (Espurt et al., 2008; Bilek, 2010; Gao et al., 2021), and two named flat slab sections (see Section 1.3.1.1) – the Peruvian and Pampean flat slabs (Flament et al., 2015). The buoyancy of the Nazca Ridge in particular is considered a major contributing factor to the development of flat slab subduction in Peru (Cross & Pilger, 1982; Pilger, 1981; Antonijevic et al., 2015; Schellart, 2020). The margin also has associated arc volcanism, and the locations of Holocene volcanoes are illustrated in Figure 1.10.

The SASZ is an ideal subduction zone to generate depth phase based catalogues for four reasons – (1) the region is rich in moderate magnitude, intermediate-depth events, (2) there is plentiful teleseismic data coverage, (3) a deep research record to provide results validation, and (4) a variety of open questions involving the subducting Nazca plate, mantle wedge and overlying South American plate which the catalogues can address. Open questions include, yet are not limited to: the geometry of the Peruvian flat slab and its relationship to nucleating intermediate-depth earthquakes; whether there are double seismogenic zones and if so what are their characteristics; where is the Moho and is it laterally variable?

Greater detail of the study region, and its subsets, are provided within the Chapters, along with the context of the research questions each Chapter is considering (Chapters 2, 6 and 7).

1.4 Overview

The aim of the thesis is to use teleseismic depth phase arrivals to improve upon regional intermediate-depth earthquake catalogues, investigate iterative updates to the presented relocation methodology, interpret the geological and geophysical implications of the event distributions in the new catalogues, and utilise the results generated to also establish a routine to regionally map crustal thickness.

Chapter 2 is a published paper (Blackwell et al., 2024), which establishes an initial approach to detect and identify teleseismic P, pP and sP arrivals using array processing techniques on *ad-hoc* medium-aperture arrays, and convert their relative times to event depth (1D relocation). Jack-knifing of the *ad-hoc* arrays additionally provides a basis to generate error estimations on the relocated event depths. The approach is entirely auto-

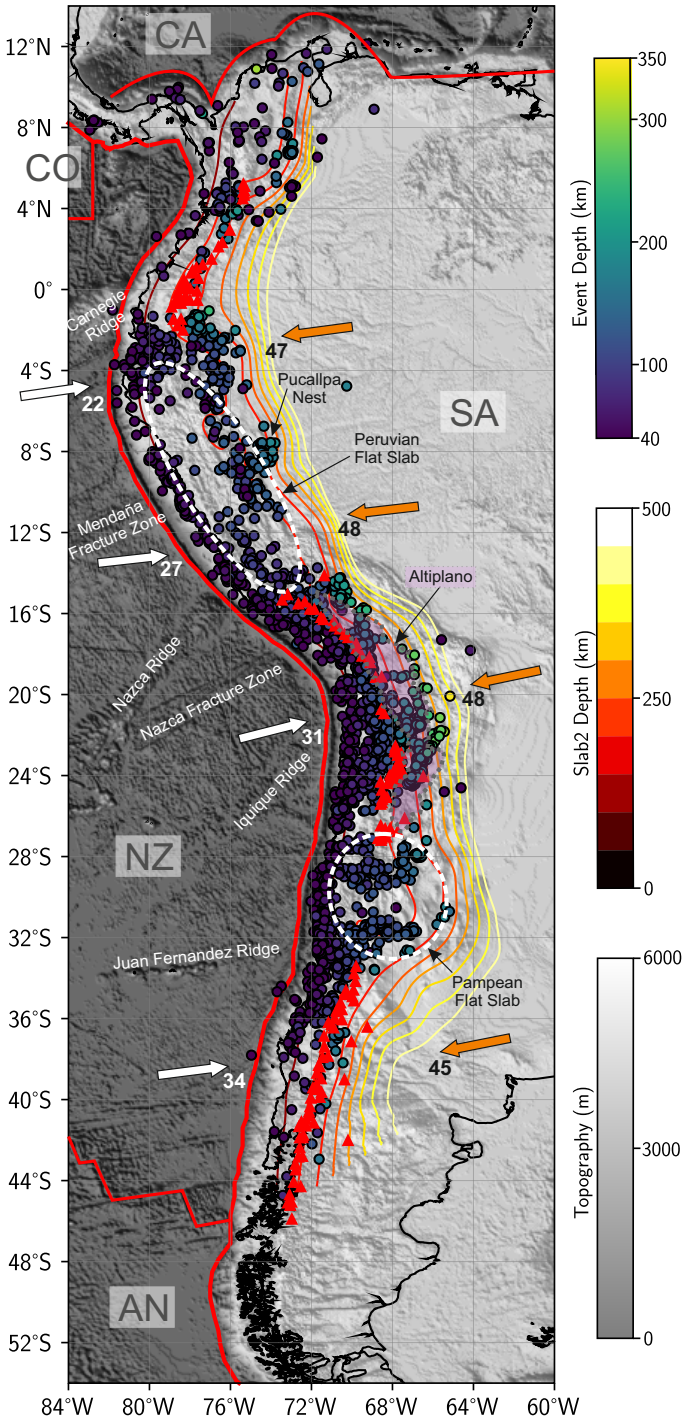

Figure 1.10: Map showing an overview of the South American Subduction Zone (SASZ). The thick red lines show where the tectonic plate boundaries exist between the Nazca (NZ), South American (SA), Caribbean (CA) and Cocos (CO) plates (Bird, 2003). Arrows indicate plate velocity in mm/yr at different latitudes for the Nazca and South American plates (Gripp & Gordon, 2002), and countours show the depth of the subducting Nazca plate according to the Slab2 model (Hayes, 2017). Red triangles represent the locations of Holocene volcanoes (Global Volcanism Program, 2024), and the Altiplano continental plateau located in northern Chile is highlighted (Zandt et al., 1994). Other pertinent bathymetric and slab features are also labelled (Zandt et al., 1994; Espurt et al., 2008; Bilek, 2010; Flament et al., 2015; Wagner & Okal, 2019).

mated and dynamic to both the event and the individual *ad-hoc* arrays, without the need for computationally expensive machine learning. Both northern Chile and Peru are used as study areas, with northern Chile serving as a validation region for the methodology. Reasons for the selection of the test regions are discussed in Section 1.3.4.

Chapter 3 is a brief chapter to outline how I expand upon the Chapter 2 relocation methodology to include S and sS phases, which will later be applied to the entirety of the SASZ alongside the original P, pP and sP routine to relocate events in Chapter 7. I believe this might be the first time a methodology which incorporates the automatic detection of both P wave and S wave coda depth phases for event relocation will be applied to the entire length of the South American Subduction Zone.

Chapter 4 investigates using the automatically detected depth phase picks for 3D event relocation. I integrate the phase arrival picks for P, pP and sP, with the International Seismological Centre (ISC) reported phases per event, and relocate the earthquakes using ISCloc (Bondár & Storchak, 2011) – the ISC inversion algorithm to solve for 3D location (Bondár & Storchak, 2011). After which I assess the improvement in terms of location and location error for both the ISC and Blackwell et al. (2024) (from Chapter 2) earthquake catalogues. By incorporating additional depth phases with the reported ISC phases before relocation, I increase the number of data points to ascertain good depth resolution and decrease locational error (specifically for the depth coordinate). The study area continues to be Peru and northern Chile for this chapter, and the new ISC integrated, 3D relocated catalogue allows updated interpretation to be discussed for the regions.

Chapter 5 tests a machine learning picker (PhaseNet by W. Zhu and Beroza (2019)) on phase-weighted beams to assess if (1) a machine learning picker could work on a teleseismic beam, and (2) if I could generate pick uncertainties. This work is motivated by the need to convert amplitude-based depth phase picks into absolute time, phase onset picks in Chapter 4, for the application of ISCloc (Bondár & Storchak, 2011). By displaying proof of concept, and showing that machine learning pickers can work on teleseismic, phase-weighted beams, I open up opportunities to convert amplitude-based picks from the automatic routine outlined in Chapters 2 and 3 to absolute onset times. This should encourage further integration of array-determined picks into global phase catalogues.

Chapter 6 leverages the generated data from the event relocation approach, to detect the depth phase – pmP – for Moho depth determination. In conjunction with pP, pmP

can inform us of the crustal thickness near to the event source. Chapter 6 describes an automatic methodology to generate regional crustal thickness maps quickly, and I validate the results against receiver function findings. I additionally consider the relative amplitudes of *pP* to *pmP*, to determine the mechanical nature of the Moho underlying Peru and northern Chile.

Finally, Chapter 7 applies all of the presented methodologies to the entirety of the SASZ to demonstrate their capability. Intermediate-depth events are relocated in 3D using *ad-hoc* array determined *P*, *pP*, *sP*, *S* and *sS* arrivals, combined with the globally reported ISC phase catalogues per event (following the methods presented in Chapters 2, 3 and 4). Furthermore, a regional Moho depth map is generated from the detection and identification of *pmP* arrivals, and a *pmP*/*pP* relative amplitude study conducted (following Chapter 6). The results from both the relocated event catalogue and the regional Moho depth map are analysed and discussed to provide insights into the SASZ, and the success of scaling-up the approaches to a larger region.

Chapter 2

Automatic relocation of intermediate-depth earthquakes using adaptive teleseismic arrays

2.1 Introduction

Intermediate-depth earthquakes – those with hypocentral depths between 60-300 km – occur in all actively subducting slabs (e.g. Frohlich, 2006) and, although they comprise only a small proportion of the total seismic moment release associated with subduction zones, they can present a significant seismic hazard of the overlying population centres (Abe, 1972; Beck et al., 1998). Despite this, they remain one of the least-well understood types of earthquake, with open questions as to what controls their occurrence, distribution, and nucleation (Hacker et al., 2003; Frohlich, 2006; Ferrand et al., 2017; Hosseinzadehsabeti et al., 2021). One of the principal issues limiting our understanding of such earthquakes is the difficulty in accurately locating these earthquakes, and their relationship to the rheology, geometry, and structure of the host slab. Determining accurate locations for such earthquakes, particularly in regions with very few local seismic instruments can be difficult, and subject to significant uncertainty. Earthquake depth, in particular, is of great importance, as both rheological properties and intraslab stress change fastest in the vertical direction, with the greatest complexity in seismogenic structure.

For global earthquake location, a vital observation offering both a direct and an independent constraint on the depth of an earthquake is the relative delay time of teleseismic

depth phases (Figure 2.1) – near-source surface reflections (pP, sP), which otherwise follow a similar raypath to the associated direct phase (P). The relative delay time of these depth phases is dependent on depth of the earthquake below the overlying surface and the near source velocity structure. Hence, in cases where the velocity structure is reasonably well known, the delay time offers a precise constraint on earthquake hypocentral depth, which is independent of the absolute travel time of any of the various phases. Therefore, depth determination using the relative arrival times is unaffected by any velocity structure variations outside of the near-source region, and additionally independent of the lateral location.

However, for smaller earthquakes ($M_w < 6$), depth phases are often difficult to identify – depth phase detection is hindered by their relatively low amplitude, and by the increased background 'noise' levels present in the direct phase coda, particularly for earthquakes in areas with complex near-source velocity structures. The recorded amplitude of the arrivals depends upon factors such as the moment magnitude, radiation pattern and the attenuation during transmission from source to receiver. Additionally, higher magnitude events at shallower depths are likely to have longer source durations and shorter relative delay times between the phases, which can result in the depth phases and the direct arrival overlapping and interfering with each other, further hindering identification.

One approach has been to enhance the detectability of depth phases by stacking waveform data where depth phases are coherent – an approach commonly employed using data from the limited number of small aperture arrays (typically <0.4° or 50 km) around the world (e.g., Heyburn & Bowers, 2008; Craig & Heyburn, 2015) via beamforming. Other approaches have tried to apply either time-compression or distance-dependent windowing of the waveform to allow the stacking of data from wide-aperture (typically these can be >9° or 1000 km) or global arrays (Woodgold, 1999; Murphy & Barker, 2006; Tibuleac, 2014; Craig, 2019; Fang & van der Hilst, 2019). However, with the increasing station density of long-term seismic networks, more recent approaches have been developed which construct 'medium' aperture (typically <5° or 556 km (Florez & Prieto, 2017)) seismic arrays, which suffer from neither the geographic sparsity of small-aperture arrays, nor the coherence limits of wide-aperture arrays. With the rapid increase in station density across many continental regions, the construction of large numbers of medium-aperture arrays is now possible for many, if not all, contemporary earthquakes, and offers a vital avenue to greatly increase the number of depth phases observed in global seismic catalogues, and to

greatly improve the location of intermediate-depth earthquakes, in particular.

Approaches to the accurate determination of earthquake depths tend to divide into two groups: those using the pre-identified arrival times of specific seismic phases (including depth phases; e.g., Engdahl et al., 1998; Bondár & Storchak, 2011; Münchmeyer et al., 2024), and those determining location parameters through the inversion of waveform data (over a window encompassing the depth phases; e.g., Craig et al., 2011; Devlin et al., 2012; Craig & Hull, 2024). In general, the latter has required significant computational and analytical resources, and has largely been restricted to studies of specific events, seismic sequences, or carefully-defined regions, whilst the former forms the basis for most global earthquake catalogues. Here, I instead aim to automate an innovative hybrid approach to waveform processing to greatly increase the number of depth phases for which relative travel times can be determined.

In this chapter, I demonstrate a dynamic and fully automated approach to re-locate the hypocentres of intermediate-depth earthquakes in depth using the relative delay times between the P wave and its associated depth phases (pP and sP). The approach leverages the increasing abundance of teleseismic data to allow the construction of adaptive teleseismic seismic arrays, which aim to image and detect clear depth phases for smaller-magnitude events. I start by illustrating my processing workflow (see Section 2.2) using an example earthquake from Peru, then presenting comparisons with previous depth-phase derived catalogues from northern Chile (see Section 2.3), before showing a regional case study based on the Peruvian subduction zone (see Section 2.4).

2.2 Relocation algorithm

To relocate intermediate-depth earthquakes automatically, I create dynamic medium-aperture *ad-hoc* arrays, independently generated to optimise usage of the available teleseismic data for each earthquake (see Section 2.2.3), detect and automatically pick the P, pP and sP phases from signal-to-noise enhanced vespagrams (see Section 2.2.4) and convert the pP-P and sP-P relative times to depth (see Section 2.2.5). This builds upon the methodology outlined in Florez and Prieto (2017).

The approach presented here can be used to create a high-resolution, regional intermediate-depth earthquake catalogue using depth phases. The primary aim is the determination of event catalogues for intermediate-depth earthquakes in subduction zones, but my approach

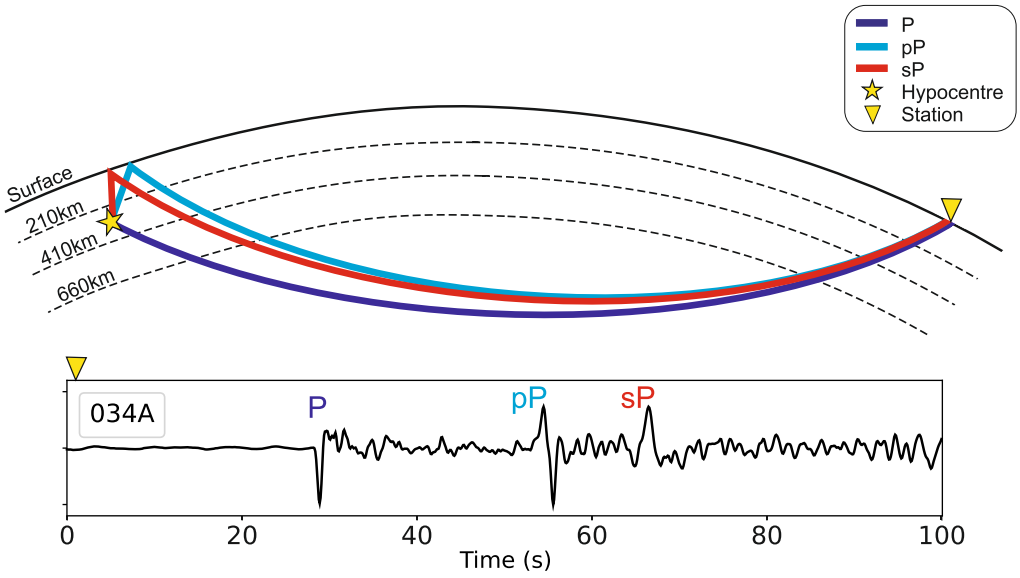

Figure 2.1: 2D schematic of the P, pP and sP ray paths from an earthquake hypocentre (star) to a teleseismic receiver (triangle), and an example vertical component, velocity waveform from station 034A of the TA network. The waveform is taken from the 23rd May 2010, m_b 6.2 event located at (13.98°S, 74.37°W).

maintains the scope to handle deeper earthquakes in the continental crust, provided a clear separation between the direct arrival and depth phases is present (Wimpenny et al., 2023). Globally, there are many regions which do not possess dense, local seismic networks and therefore lack near-field data for the constraint of earthquake location – a problem particularly prevalent in remote or oceanic subduction settings – and it is in these settings that I anticipate the method presented here will be particularly impactful. Figure 2.2 shows the workflow of my approach, which I will discuss in the upcoming sections.

2.2.1 Selecting events

To select candidate earthquakes for relocation, I start from a preliminary earthquake catalogue containing event locations, times, and magnitudes. For the examples in this section, I use the International Seismological Centre (ISC) catalogue post-1995, with a search box over Peru, a depth range of 40-350 km and a magnitude range of m_b 3.0 to 6.5. I begin with a catalogue which extends into magnitudes well below where I would typically expect to detect depth phases and with a larger depth range, in order to determine a lower magnitude limit for my approach (see Section 2.4.1), and test the ability of my approach to handle shallower and deeper depth data. For the upper magnitude limit, I choose a m_b 6.5 cut-off because I feel that more impact will be achieved by focusing on relocating smaller, less well constrained events – for earthquakes larger than this, depth phases are

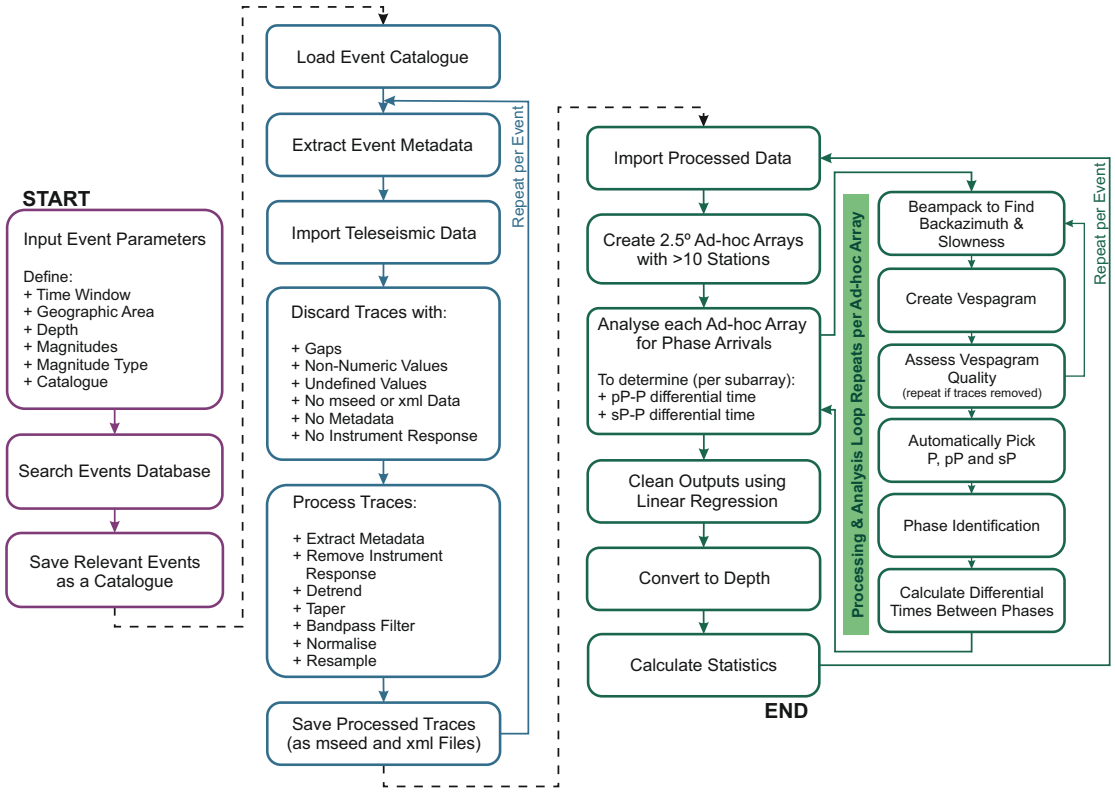

Figure 2.2: Workflow summarising the key steps of the method. Purple outlined boxes indicate processes related to assembling the event catalogue, blue outlined boxes indicate processes related to teleseismic data loading and pre-processing, and green outlined boxes indicate processes related to depth determination.

typically detectable in single-station data. Restricting the relocation of upper magnitude events also limits the application of a point source assumption, as larger earthquakes are more likely to consist of complex fault plane mechanics and multiple areas of slip.

2.2.2 Data and data processing

For a given earthquake from the event catalogue (Section 2.2.1) I take all available vertical component station data recorded on channels BH and HH at teleseismic distances (30-90° epicentral angle) from the initial location, from all of the open access FDSN data centres (see Data Availability section). I limit my station selection to those existing at teleseismic distances to allow sufficient time for the depth phase arrivals from intermediate-depth earthquakes to separate, whilst limiting the interference of upper mantle reflections and triplications.

Individual waveforms are limited to 200 seconds before the event origin time to 1500 seconds after, and subsequently checked and discarded automatically if there are incomplete traces, missing metadata or instrument responses. All remaining waveforms have their instrument response deconvolved, leaving the data recorded in units of velocity, are linearly detrended, tapered at 5% of the trace length, bandpass filtered between 1-10 seconds using a 3-corner Butterworth, two-pass filter, resampled to 10 Hz and normalised to their peak amplitude (see Figure 2.2). The final quality checked data will be dynamically grouped into medium-aperture *ad-hoc* arrays (see Section 2.2.3).

2.2.2.1 Determination of optimal filter parameters

I determine an optimum combination of bandpass filter (1-10 s) and seismic data (velocity) by testing five filter ranges on all three types of data (displacement, velocity or acceleration) for approximately 470 Peruvian intermediate-depth earthquakes and assessing the performance of my automatic phase picking routine (see Sections 2.2.4.4 and 2.2.4.5). The five test bandpass filter ranges were 0.5-15 s, 1-8 s, 1-10 s, 1-15 s, 15-20 s, and were initially selected based upon the source-time function wavelengths with respect to magnitude included in the SCARDEC database (Vallée & Douet, 2016). I ran the relocation algorithm from data processing (see Section 2.2.2) to phase identification (see Section 2.2.4.5) for each earthquake using all combinations of the test conditions, and recorded the number of phases identified per *ad-hoc* array (with a maximum of 3 for detecting P, pP and sP).

The results indicate that the automated phase picking routine is affected by the seismic

data type, demonstrating a significantly better performance using velocity data (Figure 2.3a), particularly towards the lower and upper bounds of the tested earthquake magnitudes. However the detection of depth phases for a given magnitude has a low sensitivity to the tested bandpass ranges, except the 15-20 second filter which is used to appraise sensitivity of the results given an unlikely filter (Figure 2.3b). It is apparent that the addition of waveforms with 10-15 second periods provides a marginal advantage for picking at magnitudes less than 5.4, and a marginal disadvantage at magnitudes greater than 5.4. Whilst filtering out waveforms in the range of 8-10 seconds reduces the mean number of phases picked between magnitudes 4.9 and 5.7. The 1-10 second filter provides a more consistent result over the entire range of magnitudes, and is therefore used for processing data for my relocation methodology. An adaptive filter dependent upon magnitude has been tested but offers little improvement over the best fitting filter for the range of magnitudes I am considering. More results from testing for the optimal filter parameters are included in the Appendix, see Figures A.1 and A.2.

2.2.3 Ad-hoc arrays

My approach, comparably to others (Tibuleac, 2014; Florez & Prieto, 2017; Craig, 2019; Fang & van der Hilst, 2019), relies on the application of array processing techniques to groups of teleseismic stations, to boost the signal-to-noise ratio of the depth phases, and increase the likelihood of detection. Craig (2019) stacks global teleseismic data using a kurtosis detected P wave arrival, whilst Fang and van der Hilst (2019) autocorrelate and beamform their global teleseismic traces using a simple moveout correction to a reference epicentral distance. Whilst both of these methods use a global distribution of data, there is limited scope to account for any 3D velocity structure variations which may exist locally to the receivers. Florez & Prieto (2017) and Tibuleac (2014) both beamform for a small number of fixed medium-aperture subarrays/wide-aperture super-arrays of teleseismic stations constructed for western USA; Florez & Prieto (2017) also construct arrays for western Japan. The use of defined arrays provides an opportunity to individualise beamforming to the local 3D velocity structure, by allowing data-driven determination of the local to array slowness and backazimuth parameters, resulting in an improved beam – see Section 2.2.4.1. However, the distribution of stations reporting at teleseismic distances for any given earthquake varies due to temporary deployments and the steady increase in stations over time. Hence, instead of defining a small number of fixed arrays, I incorporate

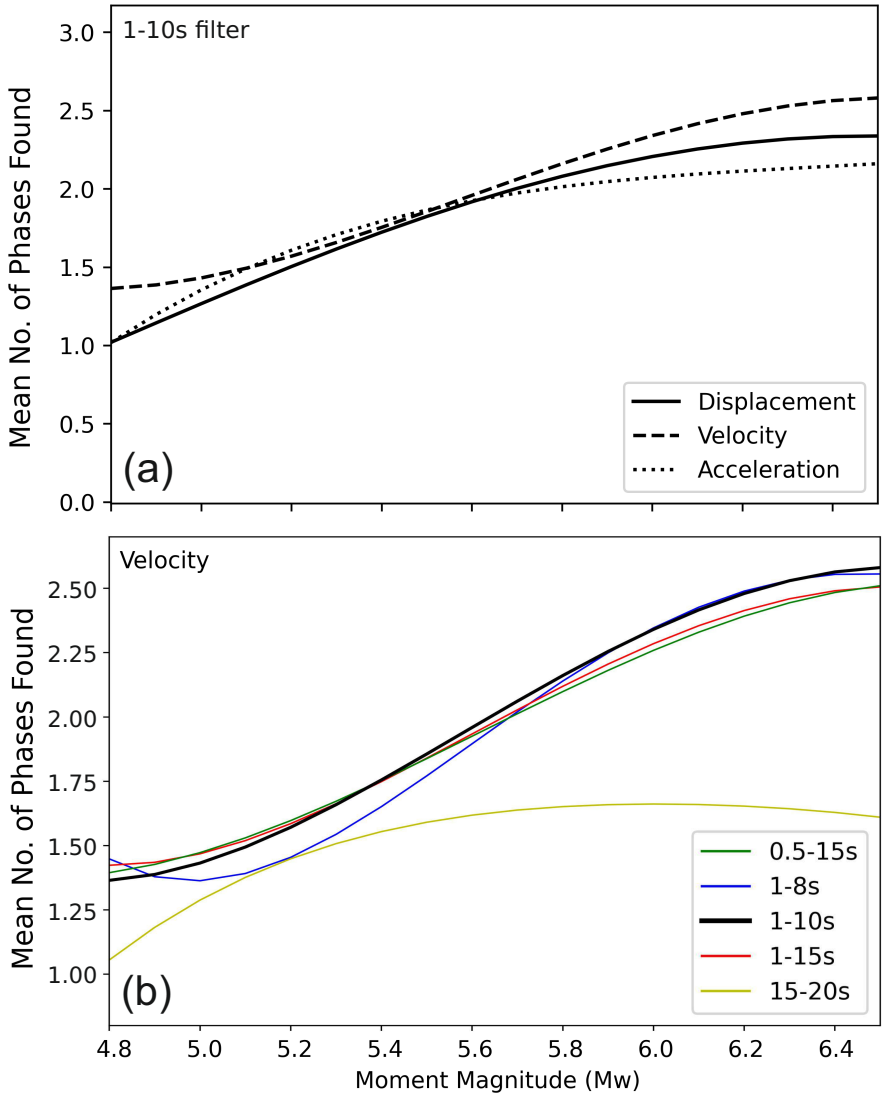

Figure 2.3: Mean number of phases (P, pP or sP) found per moment magnitude as per GCMT catalogue (Dziewonski et al., 1981; Ekström et al., 2012) whilst (a) applying a 1-10 seconds bandpass filter for three seismic data types – displacement, velocity and acceleration, and (b) applying 5 bandpass filters to velocity data.

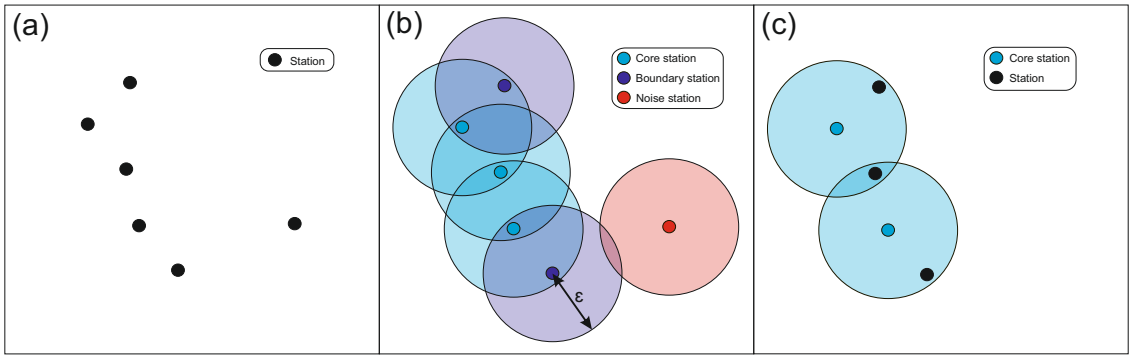

Figure 2.4: Cartoon illustrating how I dynamically create *ad-hoc* arrays from a population of stations. (a) initial set of stations to divide into *ad-hoc* arrays. b) how the DBSCAN clustering routine assigns core, boundary and noise labels to the stations, assuming that the minimum number of points required in the neighbourhood within a search radius ε of a core point is 3. (c) shows how the "noise" stations have been removed from the dataset, and only the mutually exclusive core stations are retained to create well-spaced and well-populated *ad-hoc* arrays using the Ball-tree routine.

an algorithm for the dynamic creation of an optimum suite of medium-aperture *ad-hoc* arrays from the initial teleseismic population of stations unique to each earthquake. I also determine the optimum beamforming parameters and automated picking threshold per *ad-hoc* array (see Sections 2.2.4.1 and 2.2.4.4).

I group stations with waveform data which has successfully passed my data quality control and pre-processing (see Section 2.2.2) into medium aperture *ad-hoc* arrays (see Figure 2.2) using a combination of two unsupervised machine learning algorithms – DBSCAN clustering and Ball-Tree nearest neighbour functions (Pedregosa et al., 2011) – in a process developed by Ward et al. (2023) (Figure 2.4).

DBSCAN clustering (Ester et al., 1996) categorises data points into either clusters or noise depending upon whether the point is part of a neighbourhood based on a set minimum density of points. The minimum density is defined using a given radius (ε) and a given minimum number of points, to remove stations which are not densely clustered enough to be considered for a medium aperture *ad-hoc* array (noise). The stations which are retained as part of a cluster are additionally categorised into core or boundary points (Figure 2.4b). Core points possess the specified minimum number of points within the given radius of itself (i.e. core stations in Figure 2.4 have 3 stations within their radius), whilst boundary points do not. The stations which are core or boundary points are retained for the Ball-Tree algorithm to divide into *ad-hoc* arrays.

I then use the Ball-Tree nearest neighbour algorithm (Omohundro, 1989) to identify the stations (core or boundary) located within the given radius from each core station, each

core station and its associated stations then become an *ad-hoc* array. The use of the Ball-Tree algorithm in this way results in overlapping *ad-hoc* arrays, where the core station of one *ad-hoc* array is contained within the radius of other core station's array clusters. A further process weeds out the excess *ad-hoc* array cores and associated stations, thus leading to a series of *ad-hoc* arrays where core stations are mutually exclusive and non-core stations can be shared (Figure 2.5). The data are then re-organised to reflect the newly found *ad-hoc* array groupings. I have tested this routine on regional and global distributions of seismic stations, with success on both counts.

I test the *ad-hoc* array creation process for a range of apertures (array diameter) from 167 to 2222 km (1.5 to 20°). Given a 1-10 second bandpass filter, 167 km is approximately the smallest *ad-hoc* array aperture I can consider for my target frequency, since the array aperture should be larger than the longest wavelength of interest in order to form a meaningful beam. If the wavelength is larger than the array aperture, the array has a limited wave number (or slowness) resolution and the array, essentially, acts as a single station (Schweitzer et al., 2012). This significantly limits array processing benefits such as an improvement in signal-to-noise ratio. Conversely using a wider array aperture increases the risk of larger velocity structure variations within the array, which increases the probability that higher frequency, shorter wavelength arrivals will stack incoherently. I observe that whilst the traces in the *ad-hoc* arrays coherently stack well between apertures of 167 km (1.5°) and approximately 1333 km (12°), there is a trade-off between the number of *ad-hoc* arrays created, the proportion of stations used, and the *ad-hoc* array aperture considered.

I find that *ad-hoc* arrays with a 278 km (2.5°) aperture strike the best balance between maintaining a plane wave assumption across the included stations (see Figure A.3 in the Appendix), and maximising the number of *ad-hoc* arrays that can be created from the station distribution available. Requiring at least 10 stations per array ensures the wavefield is sampled sufficiently and that there are enough traces in the array to enable acceptable signal-to-noise improvement. Note that the assigned array diameter represents a maximum aperture, the *ad-hoc* arrays created likely contain stations within a smaller area. For the remainder of the approach, I use 278 km as the maximum aperture for my arrays, require at least 10 stations in each array and set the geometric centre of each *ad-hoc* array as the 'reference station'.

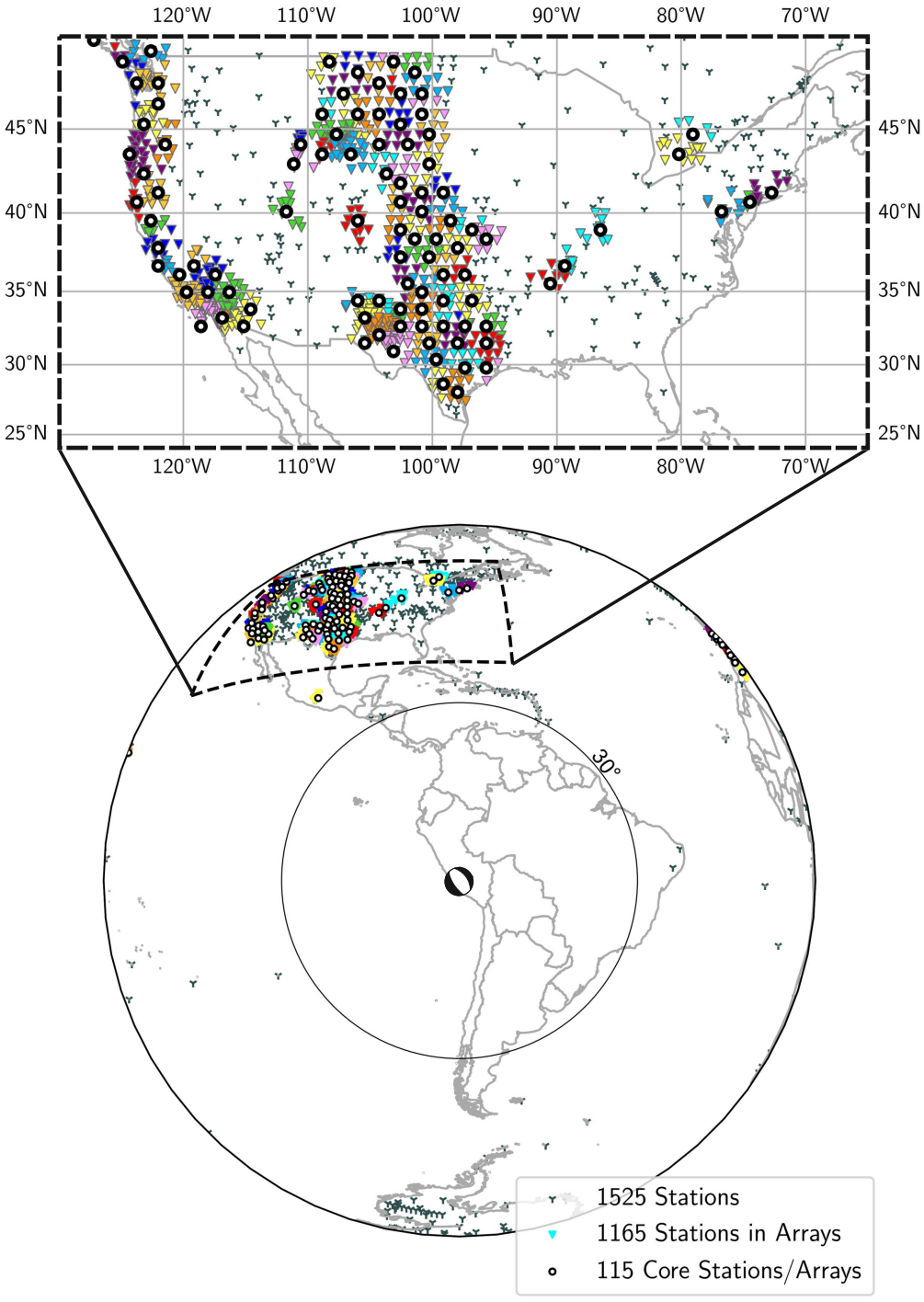

Figure 2.5: Example of the *ad-hoc* array creation process for a m_b 6.2 event from 23rd May 2010 located in the Peruvian flat slab portion of the Nazca plate, showing a global distribution of teleseismic stations and the subsequent *ad-hoc* arrays on the bottom, and a zoom in of the *ad-hoc* arrays created in the USA on the top. The core stations are shown as thick black circles and the associated *ad-hoc* array stations as coloured triangles (different colours correspond to different *ad-hoc* arrays). The unused stations (grey Ys) are those removed via the DBSCAN routine, prior to the Ball-Tree process. The earthquake focal mechanism is taken from the Global Centroid Moment Tensor Project (GCMT) (Dziewonski et al., 1981; Ekström et al., 2012).

2.2.4 Array processing

Once my station population has been divided into *ad-hoc* arrays (see Section 2.2.3), each *ad-hoc* array is then passed through an array processing and analysis loop, aiming to boost signal-to-noise sufficiently enough for the depth phases to be automatically picked, identified and their differential arrival times to be calculated (see Figure 2.2). The differential times found per *ad-hoc* array are collected together to determine a final hypocentral depth (see Section 2.2.5).

2.2.4.1 Determining optimum beamforming parameters

Beamforming involves the alignment, stacking and normalisation of an array of seismic traces to enhance the amplitude of smaller amplitude arrivals, such as depth phases. In this section I adopt P wave beamforming to determine the optimum backazimuth and slowness parameters directly from the *ad-hoc* array trace data, to be used when beamforming the depth phases later in Section 2.2.4.2. This process, as I show, is particularly important for the dynamic medium-aperture *ad-hoc* arrays I construct, as it compensates for the locally-variable velocity structure below each array. See Section 1.2.2 for a full explanation of the standard beamforming process, including Equation 1.1.

The beam is formed for a specific horizontal slowness and backazimuth, assuming the propagation of a plane wavefront across the array – this is a good approximation for the chosen array size. Theoretical values for the slowness and backazimuth can be calculated using the relative location of the earthquake source to the reference location, and assuming propagation along a great circle path, combined with ray tracing through an assumed 1-D velocity structure. Alternatively, a process such as F-K analysis or beampacking can be used to determine optimal, locally-calibrated values for arrivals from a given earthquake (Rost & Thomas, 2002; Florez & Prieto, 2017). Beampacking is the time domain equivalent to F-K analysis and searches over a grid of slowness and backazimuths for beamforming, to determine the values which produce the beam with maximum amplitude within a selected time window (typically centred on a specific phase arrival).

To directly extract the optimal slowness and backazimuth values from each *ad-hoc* array, I perform beampacking on a narrow time window centred on the predicted direct P wave arrival. The traces are trimmed to 17 second time windows around the predicted P arrival time calculated using the ak135 1-D Earth model (Kennett et al., 1995), and beamformed

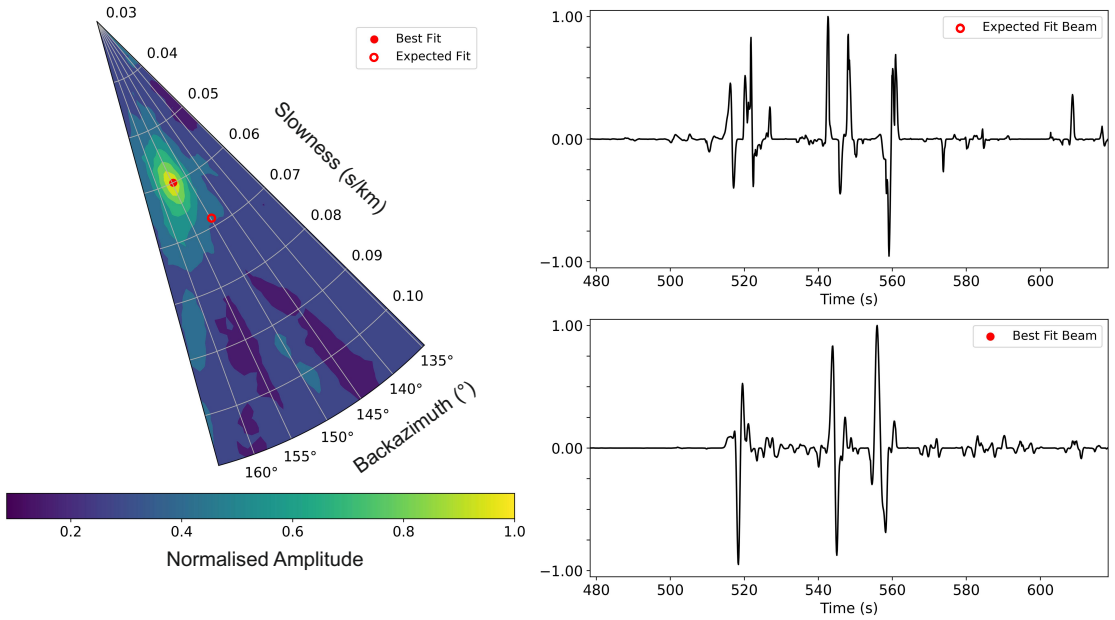

Figure 2.6: P wave amplitude during beamforming in polar coordinates (backazimuth and slowness) to determine the best-fit backazimuth and slowness parameters directly from the *ad-hoc* array traces. The open red circle shows the theoretical slowness and backazimuth found through calculation and the corresponding phase-weighted beam to the top right. The filled red circle shows the beampack derived values and the resultant phase-weighted beam to the bottom right, showing the importance of measured backazimuth and slowness values. Example from m_b 6.2 event from 23rd May 2010, *ad-hoc* array at 49.2° epicentral distance.

relative to the reference station of the *ad-hoc* array according to Equation **??**. The length of the time window has been found by trial and error, it aims to preserve the P arrival and exclude minimally separated depth phases from shallower events, whilst allowing a margin of error in the modelled P arrival time due to 3D velocity structure. I test a 30x30 grid of backazimuth and slowness values during my beampacking routine, the ranges of which are centred upon the theoretical backazimuth and slowness values. For backazimuth, the tested values range from the geodetic backazimuth value ±15° in 1° intervals, whilst slowness is tested from the modelled slowness value ±0.04 s/km in intervals of 0.001 s/km.

The maximum amplitude of each beam (assumed to be the P arrival) is extracted and mapped onto a polar grid, with slowness displayed along the radius and backazimuth given by the bearing (Figure 2.6). The beam providing the largest amplitude indicates the best fitting, optimal slowness and backazimuth for the event P arrival for the *ad-hoc* array, both values can be read directly from the plot.

I find that beams created using the data-derived, observationally-constrained backazimuth and slowness values account for near-receiver velocity structure variations and the resultant 3D raypath propagation effects, which significantly reduces impact from incoherent

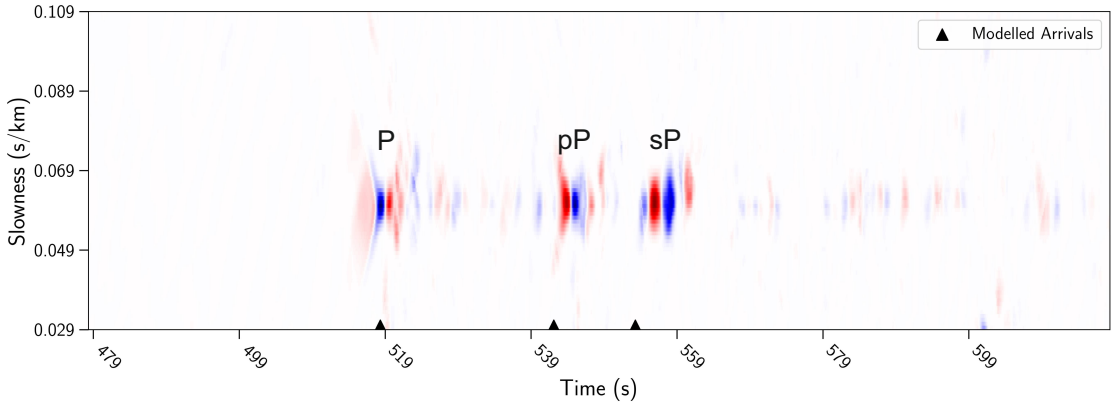

Figure 2.7: Normalised vespagram from an *ad-hoc* array located at an epicentral distance of 49.2°, for the m_b 6.2 event from 23rd May 2010. Phase arrivals are labelled.

noise, compared to the beams constructed with theoretically-derived parameters. The improvement between a beam constructed using parameters calibrated to produce maximum amplitude for the direct arrival, and one using the theoretical values can be seen in Figure 2.6 (an alternative display can also be seen in Figure A.4 located in the Appendix). The optimal backazimuth and slowness parameters found through beampacking are used for beamforming *ad-hoc* array traces in Section 2.2.4.2, to increase the likelihood of automatically detecting and picking depth phases.

2.2.4.2 Vespagrams

I use vespagrams to assess the quality of the *ad-hoc* array data for the automated picking routine (see Section 2.2.4.4, and Figure 2.2). Vespagrams are an array process which display a series of beams for a range of slownesses or backazimuths (Rost & Thomas, 2002).

My vespagrams highlight the time and slowness using a fixed backazimuth where phase arrivals are most coherent, by beamforming the *ad-hoc* array per slowness using Equation **??**. They are constructed using the same reference stations and best fitting slowness and backazimuth values found during beampacking (see Section 2.2.4.1). The resulting traces are stacked using phase weighting (Schimmel & Paulssen, 1997) with a power of 4 to amplify the signal relative to the noise, before being constructed into a vespagram (Figure 2.7).

The resulting plot allows for the identification of the most coherent beamform, which also illustrates the time of each phase arrival, assuming that the noise is diminished enough to allow the stacked phase arrival amplitudes to display significantly. Vespagrams for

each *ad-hoc* array are subject to quality control based on the clarity of signals along the expected slowness range and the overall noise content, with low quality vespagrams being removed from the relocation process (See Section 2.2.4.3). Remaining vespagrams, and their *ad-hoc* arrays, are passed to the automated picking routine (see Section 2.2.4.5).

2.2.4.3 Assessing vespagram quality

To limit the progression of poor quality *ad-hoc* arrays in order to assist the subsequent automatic picking routine (see Section 2.2.4.4), I apply two quality assessments to each *ad-hoc* array. The first assessment uses cross-correlation to consider the individual traces of the *ad-hoc* array relative to the beam formed using the optimal backazimuth and slowness parameters found in Section 2.2.4.1. The second check assesses the signal-to-noise of the entire vespagram by considering the highest amplitude phases and their slowness distribution.

In order to assemble a clean *ad-hoc* array beam, traces significantly different from the beam are identified using a cross-correlation approach, and removed (see Appendix A.5). Each time-shifted trace is trimmed around the expected P wave arrival and compared to the *ad-hoc* array P wave arrival of the beam. A cross-correlation coefficient of greater than 0.3 is required alongside a maximum time shift of 0.5 seconds for the trace to be deemed constructive to the *ad-hoc* array beam. Traces which fail to meet these criteria are discarded. Once a set of final traces is determined, the processing of the *ad-hoc* array is restarted (e.g. the beampacking derived slowness and backazimuth are re-determined). The cross-correlation check will not be repeated. The algorithm will pass over the check and continue to the construction of vespagrams for further data quality assessment. If fewer than 8 traces remain in the *ad-hoc* array after the cross-correlation check, the *ad-hoc* array will be removed from analysis.

For the second quality assessment, I check that the highest amplitude signals present in the vespagram align closely to the expected slowness found during beampacking, assuming that pP and sP phases travel at a similar slowness to the P arrival. Vespagrams lacking coherent arrivals both above the background noise level and at a consistent slowness will exhibit a greater standard deviation of their most coherent phases away from the expected slowness.

I implement this check by extracting the sample points (10 Hz sampling rate) on each

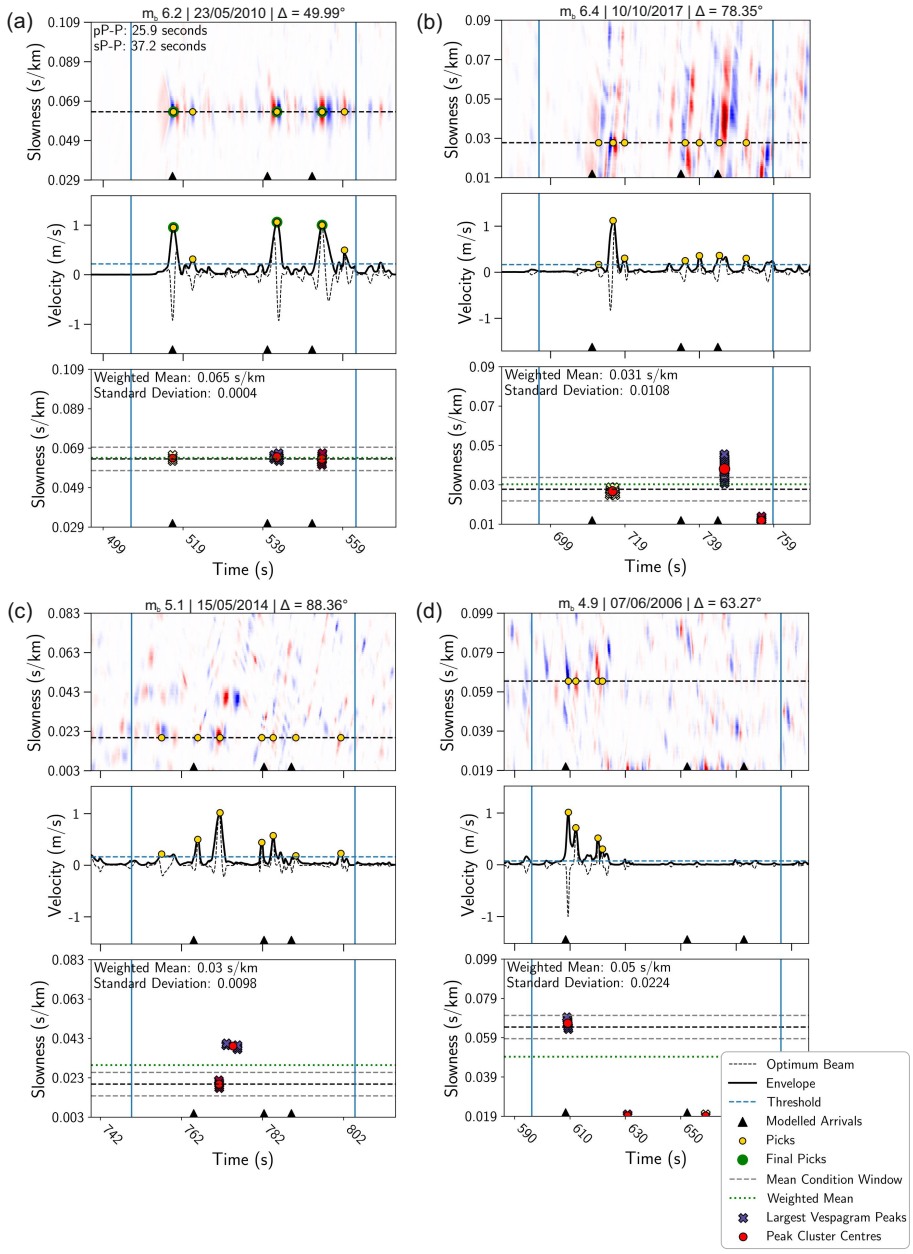

Figure 2.8: Four *ad-hoc* arrays from four different earthquakes demonstrating the determination of vespagram quality thresholds (see Section 2.2.4.3). Each set of three panels shows from top to bottom, the vespagram (see Section 2.2.4.2) with all picks in yellow (see Section 2.2.4.4), the optimum beam with picks and the corresponding DBSCAN vespagram quality test (see Section 2.2.4.3). The blue vertical lines indicate the time window used to assess data quality. *ad-hoc* array (a) is from the m_b 6.2 event from 23rd May 2010 at an epicentral distance of 48.99°. (b) the m_b 6.4 event from 10th October 2017 at an epicentral distance of 78.35 °. (c) the m_b 5.1 event from 15th May 2014 at an epicentral distance of 88.36 °. (d) the m_b 4.9 event from 7th June 2006 at an epicentral distance of 63.27 °.

vespagram (made up of beams stacked at 0.001 s/km slowness intervals) which possess an amplitude greater than 60% of the maximum value within a time window (98% of the modelled P to 102% of the modelled sP arrival time) incorporating the modelled arrival times for P, pP and sP, whilst retaining their slowness and time information. In a coherent vespagram, these points should gather around key phase arrivals approximately with a slowness found by the beampacking process (see Section 2.2.4.1) if the phases are derived from the P wave and its coda. I apply the DBSCAN clustering algorithm (Ester et al., 1996) to identify significant groups of coherent points (coloured crosses in lower panel for each event on Figure 2.8) and calculate the centres of the clusters (red points on Figure 2.8). The centres are used to determine mean slowness across the arrival clusters, weighted according to the size of the cluster, and the standard deviation of the cluster centres. In order to continue through to the relocation stage, a vespagram needs to exhibit a mean cluster slowness within 0.006 s/km of the beampacking slowness and a cluster centre standard deviation of less than 0.0105 s/km.

Ad-hoc arrays which form vespagrams that display high amplitude phase arrivals located within 0.006 s/km of the expected P arrival slowness found via beampacking (See Section 2.2.4.1) will pass the quality check (Figure 2.8a) and be automatically picked for P, pP and sP arrivals, if present, by the process described in Section 2.2.4.4. Figure 2.8 also shows examples of *ad-hoc* array vespagrams which fail the quality check – due to the standard deviation of the cluster centres about the threshold (b), a weighted mean slowness outside the bounds (c) and due to both the standard deviation and weighted mean (d).

After the cross-correlation and vespagram quality checks, the remaining *ad-hoc* arrays should have noisy traces removed to allow the cleanest beam to be stacked, and have demonstrated coherent vespagrams with respect to slowness. See Appendix A.6 showing the mean percentage of arrays removed per magnitude due to the quality assessments used for the Peruvian event catalogue defined in Section 2.2.1. For earthquakes with magnitudes below 4.7, the mean percentage of arrays removed is 86.4%, indicating a very low success rate and confidence when my relocation approach is applied to events with magnitudes lower than 4.7. Above magnitude 4.7, there is – unsurprisingly – a negative correlation between earthquake magnitude and the mean percentage of arrays removed as higher magnitude earthquakes tend to generate larger amplitude, more coherent signals. The quality assessments increase the probability that the automated picking routine (see Section 2.2.4.4) will succeed.

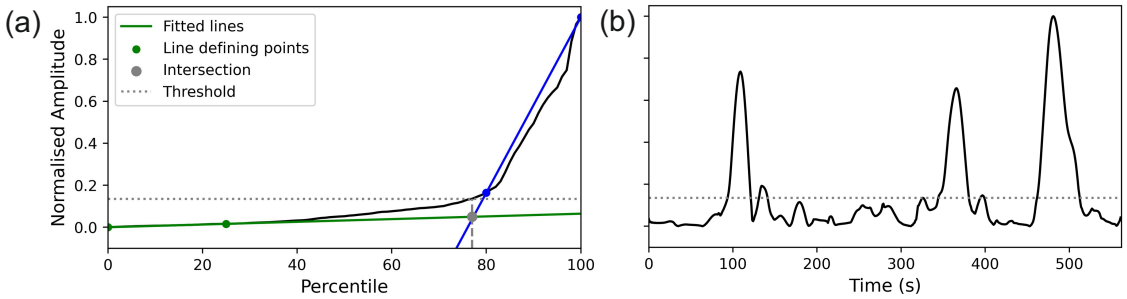

Figure 2.9: Example of the automatic picking threshold found for an *ad-hoc* array at an epicentral distance of 48.31° from the m_b 6.2 event on 23rd May 2010. (a) distribution of amplitude values for the *ad-hoc* array beam with respect to the percentile, the approximation of the beam with two lines, their intersection and the final threshold found. (b) threshold relative to the phase-weighted beam.

2.2.4.4 Automated picking routine

I take the *ad-hoc* arrays which have passed the vespagram quality check outlined in Section 2.2.4.2, and pick the *P*, *pP* and *sP* arrivals with an automated routine (Figure 2.2). The picks found via the automatic picking routine subsequently have phases assigned to them during the phase identification stage (see Section 2.2.4.5), before the differential times between *pP*-*P* and *sP*-*P* are calculated to convert for depth (see Section 2.2.5). I describe the automated picking routine in this section.

The routine uses the envelope of the phase-weighted beam created at the best fitting slowness (see Section 2.2.4.1) – I shall call this beam, the optimum beam. The approach identifies peaks along the optimum beam with a significant prominence above a dynamic threshold, calculated from the distribution of the beam amplitudes. The use of a dynamic threshold, as opposed to a window based approach, decreases dependence upon the velocity model and the modelled phase arrivals, however the risk of extra and/or misidentified picks increases. I handle this issue by applying a phase identification step, described in Section 2.2.4.5.

During the automated picking routine, the optimum phase-weighted beam for the *ad-hoc* array is trimmed, using arrival times determined through the ak135 1D Earth model (Kennett et al., 1995), to only include the expected *P*, *pP* and *sP* phases. The envelope of the trimmed beam is calculated and peaks with a prominence exceeding 15% of the maximum amplitude peak are identified.

The identified peaks are further filtered by a dynamic amplitude threshold, which is found using the distribution of amplitude in the trimmed envelope data. When the amplitudes

of the data are plotted against the percentile, there is a rapid increase in the amplitudes associated with the higher percentiles of the data which correspond to the coherent phase arrivals (Figure 2.9). I find the onset of the amplitude increase by approximating the pre- and post- increase slopes with lines and determining their intersect. The percentile associated with the intersect can thus be converted into its corresponding amplitude – the threshold amplitude (Figure 2.9). Any peaks found to be higher in amplitude than this threshold will be preserved as potential picks for phase identification (see Section 2.2.4.5).

2.2.4.5 Phase identification

During the automated picking routine (see Section 2.2.4.4) issues can arise in instances where an expected phase lacks sufficient amplitude to be observable (allowing for phase mis-identification) or more than three peaks are identified during the automatic picking routine (leading to ambiguity in phase identification). Here I develop a phase identification routine (see Figure 2.2 for placement of the routine in the overall approach, see Figure 2.10 for the phase identification workflow) to identify picks which correspond to the expected phases. If one of the *P*, *pP* or *sP* phases are missing from the vespagram, the routine will only identify the phases present. Unfortunately, this process is reliant upon a reasonable initial event depth (within ±40 km of the relocated depth) taken from the initial event catalogue (see Section 2.2.1), the velocity model and the resulting modelled arrivals.

Initially, the routine checks that the current set of picks are significantly greater in amplitude than the background noise of the data. I approximate the background noise amplitude by extracting 40 seconds of the optimum beam envelope recorded immediately before, yet not including the expected *P* wave arrival, and calculating the mean amplitude. For each pick, the ratio between the amplitude of the envelope at the pick and the calculated background noise must exceed 5 (following Florez and Prieto (2017)) to be considered significant enough to be continued as a phase pick candidate.

The routine subsequently considers each remaining pick relative to one another, calculating the differential times between all the possible pairs of picks. *Ad-hoc* arrays with single picks are no longer considered at this point. Differential times between the pairs of picks are then compared with the 1D modelled differential times for *pP*-*P* and *sP*-*P* determined using the ak135 velocity model (Kennett et al., 1995), and any pairs with a differential time within ±25% of the modelled *pP*-*P* or *sP*-*P* differential times are taken forward as reasonable candidates.

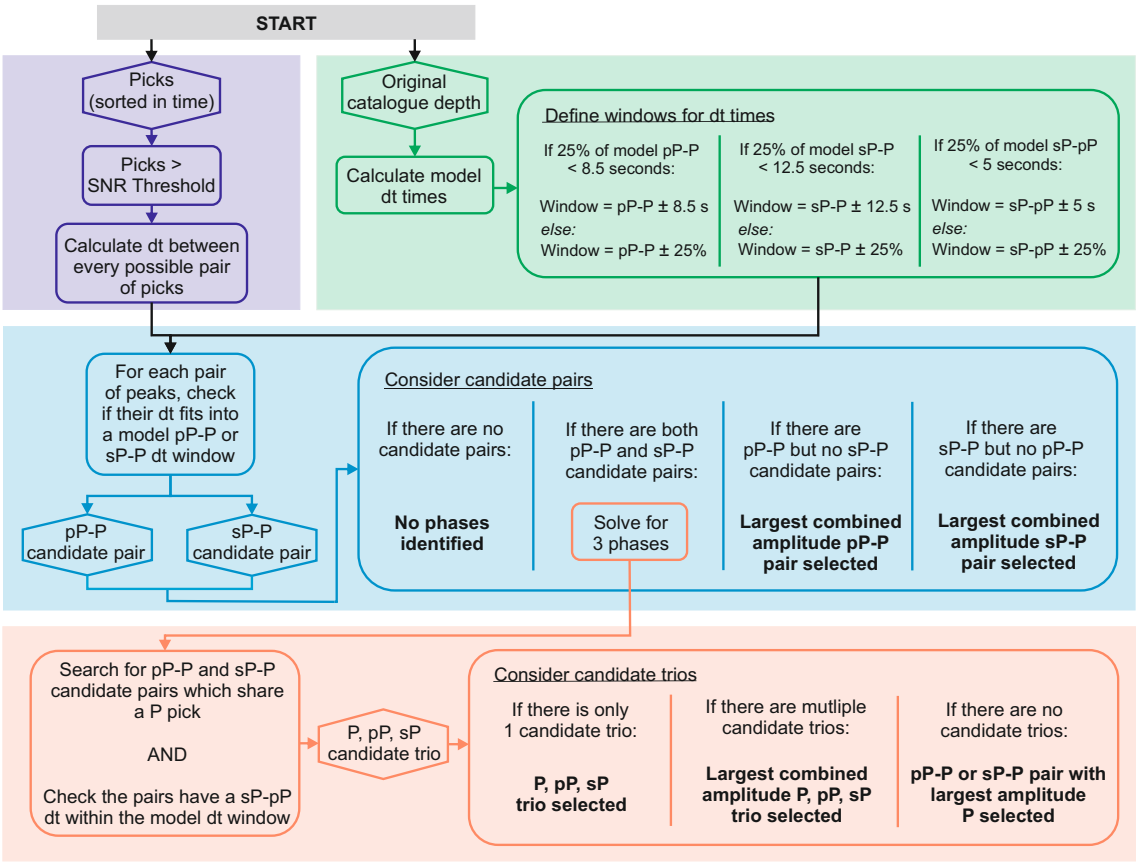

Figure 2.10: Phase identification workflow. Picks from the automatic picking routine are sorted into phases by comparing their differential times with the 1D velocity modelled differential times for *pP-P*, *sP-P* and *sP-pP*. Hexagonal boxes indicate products from a step in the workflow, and bold text shows the final phase selections.

For earthquakes at the shallow end of the depth range I consider, modelled differential times within ±25% for a given pair will provide a very small time margin. To address this issue I replace the margins with constant values of 8.5 and 12.5 seconds when the 25% margin becomes less than 8.5 seconds for *pP*-*P* and 12.5 seconds for *sP*-*P*, respectively. These constant margins are based upon the possible error in differential times assuming that the earthquake is within ±40 km from the initial catalogue depth (see Appendix A.7).

At this stage, the routine has pairs of picks which have been identified as candidates for either the *pP*-*P* pairing or the *sP*-*P* pairing, which need to be reconciled. If there are only candidates for either the *pP*-*P* or *sP*-*P* pairing, the largest combined amplitude pair is selected. If there are candidates for both pairings, I start by checking for a compatible set of *pP*-*P* and *sP*-*P* pairs by searching for matching *P* picks between the pairs, and for a reasonable separation in time for the associated *pP* and *sP* picks – a differential time within ±25% (or 5 seconds, if ±25% is less than 5 seconds) of the modelled *sP*-*pP* time. If only one complete *P*, *pP* and *sP* trio remains after this step, I select these as my final picks. If multiple trios remain, the complete set of picks with the largest combined amplitude is selected as the final picks. This assumes that the *P* arrival, and the depth phases, form the largest amplitude peaks. If there are candidates for both sets of pairs which cannot co-exist (i.e. their *P* arrivals do not match), the *P* candidate with the largest amplitude will be chosen preferentially and the associated depth phase selected. Note that the phase identification routine requires a *P*-arrival to output final picks – a requirement which would exclude *ad-hoc* arrays that are nodal or near-nodel on the *P* wave radiation pattern.

My process ensures that only good quality *ad-hoc* arrays with clear *P*, *pP* and/or *sP* arrivals are picked and identified. Finally I calculate the differential times between the final depth phases and their *P* arrival. I pass the *ad-hoc* array results through to the depth conversion stage (see Figure 2.2), where both the *pP*-*P* and the *sP*-*P* times, if found, will be used to determine an event depth (see Section 2.2.5).

2.2.5 Depth conversion

After processing all of the *ad-hoc* arrays for a given earthquake, the algorithm considers the results from each *ad-hoc* array (i.e *pP*-*P* and *sP*-*P* differential times) relative to one another. The *ad-hoc* array outputs are post-processed to remove obvious outliers and provide final depth statistics (see Figure 2.2).

To remove results from anomalous *ad-hoc* arrays, I calculate apparent depths for all of the *pP*-*P* and *sP*-*P* differential times (see Section 2.2.4.5) in order to directly compare *pP* and *sP* results and thus, create a larger population for identifying outliers. The depth conversion is a simple forward model. A range of test depths are defined from the initial catalogue depth (see Section 2.2.1) ±40 km, with 0.1 km intervals. For the *ad-hoc* array in question, the differential travel time for each test depth is forward modelled. The test depth with the smallest residual between the modelled and the determined differential times is determined as the best fit depth for this *ad-hoc* array. This is conducted independently for the *pP* and *sP* results of each *ad-hoc* array initially to achieve the distance-depth population.

I apply a linear regression to the resulting distance-depth population, whereby *ad-hoc* array depths which exceed the median ±1.3 of the standard deviation are removed from the dataset. These depths typically correspond to mis-picked and/or mis-identified phases, for the linear regression to be effective, I assume that there are more correct picks than mis-picks. I use the median as it is less susceptible to outlying data-points. Remaining *ad-hoc* arrays are used in a second forward model designed to determine depth per *ad-hoc* array by minimising the residual between the modelled differential times for both the *pP* and *sP* differential times. The median depth found from the *ad-hoc* array population using both the *pP* and *sP* differential times simultaneously provides the best indicator of the final earthquake hypocentre depth.

There is the option to use any 1D velocity model for the final depth determination. Throughout the depth conversion for the Peruvian data (see Section 2.2.2), I use a regionally modified version of ak135 1D velocity model (Kennett et al., 1995). To develop the model I take the 3D velocity cube for the region determined by Lim et al. (2018), extract the velocities above the location of slab indicated by the Slab2 model (Hayes et al., 2018) and average the velocities per depth interval. I then replace the upper portion of the 1D ak135 velocity model with the values determined from the regional 3D velocity cube. Alternatively, there is flexibility to pass the cleaned differential *pP*-*P* and *sP*-*P* times into an alternate depth inversion algorithm, such as ISCloc (see Chapter 4) developed by the ISC (Bondár & Storchak, 2011).

2.3 Validation

2.3.1 Single event

I test the relocation algorithm outlined in Section 2.2 on a magnitude 5.5 event from northern Chile which occurred on the 4th December 2008. This event is catalogued with a depth of 108.8 km by the ISC, and has previously been updated to a depth of 117 km by Florez & Prieto (2017) using 12 fixed medium-aperture arrays and a *pP* depth phase-based methodology in conjunction with the ak135 1D velocity model (Kennett et al., 1995). Using the same velocity model, and my adaptive *ad-hoc* array approach, I find a depth of 119.5 km from 86 *ad-hoc* arrays (Figure 2.11). The *ad-hoc* arrays demonstrate a strong *sP* arrival and, if present, a substantially weaker *pP* arrival, which has allowed the *sP-P* differential times to significantly weight the final depth determined. This likely accounts for the slight difference to the depth determined by Florez and Prieto (2017), whose approach only used *pP-P* delay times.

2.3.2 Regional catalogue comparison

To further assess the performance of my new earthquake relocation algorithm, I relocate the same earthquakes as presented in the regional catalogue of Craig (2019) from northern Chile. Craig (2019) stacked a global teleseismic dataset per candidate depth to identify the optimal depth to beamform depth phases, and hence determine hypocentre depth. As both studies use global teleseismic datasets and fix the latitude and longitude coordinates of the hypocentre during relocation, the results should be comparable. One key difference between this study and the study of Craig (2019) is the automation – this study uses a fully automated methodology, whilst Craig (2019) take a semi-automated approach, including automated stacking and phase picking using kurtosis, manual choices concerning the number of depth phases to pick, and by-hand quality control checks.

The compared earthquakes range from moment magnitudes of 4.8 to 6.4, and are found between 10 and 280 km depths (Figure 2.12). To ensure a thorough comparison, I have applied the same velocity model as Craig (2019) for the depth relocation step of the algorithm (see section 2.2.5). My relocation depths are in good agreement, demonstrating a mean difference in depth of 4.13 km and a strong alignment of the line of best fit to the the 1:1 ratio. There are a number of events with differing results, those with larger residuals are towards the lower end of the magnitude scale. I show two example events with

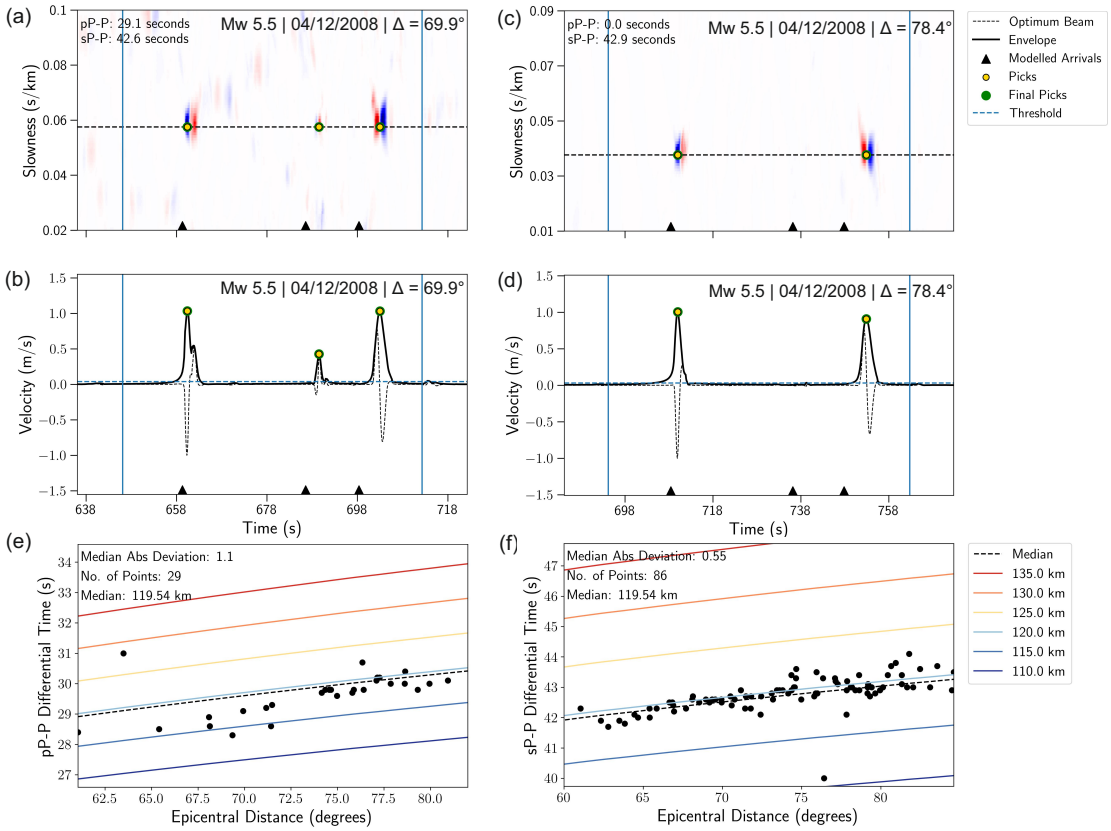

Figure 2.11: Example *ad-hoc* arrays, their automatic picks and differential times between phases for the Mw 5.5 event which occurred on 4th December 2008 in northern Chile, and plots illustrating all *ad-hoc* array differential times against epicentral distance to determine a final event depth. (a) and (b) are the vespagram and optimum beam respectively for an *ad-hoc* array at an epicentral distance of 69.9°, whilst (c) and d) are the vespagram and beam for an *ad-hoc* array at an epicentral distance of 78.4°. Blue vertical lines indicate the time window of data used for automatic picking. (e) and (f) show distance-differential time plots for *pP-P* and *sP-P* respectively. For this event the *sP* arrivals are clearly observed at each *ad-hoc* array, whilst the *pP* arrivals are significantly less apparent and smaller in amplitude. The differential times for *sP-P* seen in plot (f) are therefore more consistent with respect to epicentral distance than the pP-P times seen in (e), and noticeably weight the final hypocentral depth of 119.5 km.

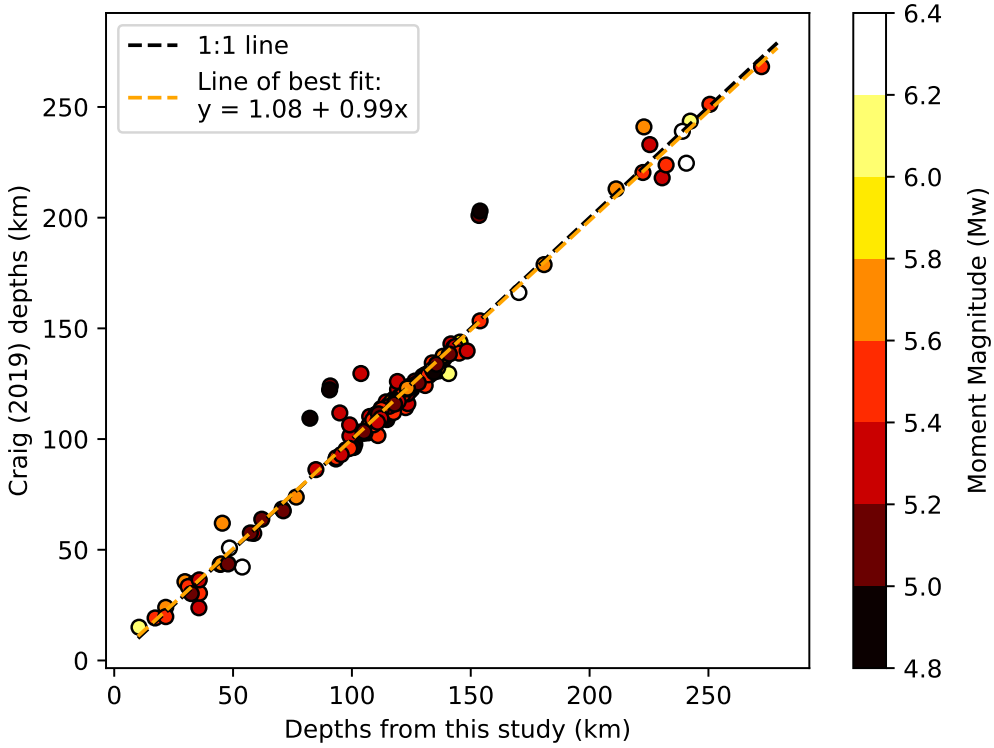

Figure 2.12: Depths of northern Chilean earthquakes as found by Craig (2019) against the depths found in this study.

differing depths in the Appendix (Figure A.8), which I believe are relocated well with my new approach, despite a disagreement in depth. These results demonstrate that my fully automated, computationally-efficient relocation approach for northern Chile is performing well compared to previous semi-automated and manually quality controlled routine. The catalogue comparison also demonstrates that my methodology can relocate events which are shallower than intermediate-depth earthquakes (<40 km). I have previously tested this with a moment magnitude 5.3 event in Algeria, with a depth of 31 km (Wimpenny et al., 2023). A map and two cross sections of the Chilean catalogue are in the Appendix, see Figure A.9.

2.4 Regional application – Peruvian flat slab

The Peruvian flat slab region is a zone of relatively shallow subduction located directly underneath Peru. It extends approximately 1600 km NW-SE and 300 km down-dip, plateauing at around 100 km depth (Hayes et al., 2018) before subducting further into the mantle at a 30° dip (Portner & Hayes, 2018). Its location has been recently refined and updated through integrating seismicity with tomography for the Slab2 model (Portner

& Hayes, 2018) – a global dataset of depth data for subducting slabs. However there is currently no regional intermediate-depth earthquake catalogue which incorporates the entire flat slab. A wholesale catalogue for the flat slab is likely to prove useful when it comes to trying to establish controls upon flat slab formation and intermediate-earthquake distribution, in addition to questions related to the slab geometry and structure.

I present results from a magnitude 4.7 event in Figure 2.13 to demonstrate the ability of the algorithm to successfully relocate small magnitude earthquakes and the potential to adapt the algorithm to push the lower magnitude bound further. The event has been relocated from a depth of 43.3 km provided by the ISC to 46.6 km using my approach. Notably there is an extra phase in Figure 2.13 (a) and (b) between the P and pP arrivals, also seen on several other *ad-hoc* arrays' data, which may be a pmP arrival. A pmP wave is a near-source Moho reflection which can be used relative to the pP arrival time (See Chapter 6) to determine crustal thickness (McGlashan et al., 2008). The detection of such phases highlights the potential for the relocation algorithm presented in this chapter to be adapted to boost the signal-to-noise ratios of alternative small amplitude arrivals, and automatically detect them for further analysis.

Additionally in Figure 2.14 I demonstrate the outputs of the m_b 6.2, 23rd May 2010 event. The vespagrams are from *ad-hoc* arrays located at 48.3° and 64.8° from the epicentre, and the new depth determined is 102.8 km from an initial depth of 99.6 km from the ISC. Note that with mean uncertainties of approximately 3 km (see Section 2.4.2), these depths are not significantly different.

2.4.1 Determining a lower magnitude limit

I determine an appropriate lower magnitude threshold for my approach using the Peruvian relocation results. The event catalogue tested contains earthquakes from m_b 3.0 to 6.5 from post-1995 taken from the ISC (see Section 2.2.1). By considering the number of relocated events relative to the total number of events in the catalogue, and the number of *ad-hoc* arrays with at least either a pP-P or sP-P differential time relative to the total number of *ad-hoc* arrays made per magnitude. I find a lower threshold of m_b 4.7, where the algorithm ceases to obtain consistent results due to a significant reduction in the number of high quality *ad-hoc* arrays (see Figure 2.15). Whilst depth phases can be found for smaller events, close inspection of the resulting vespagrams indicates that the true success rate of my routine rapidly decreases below m_b 4.7 – I find that coherent noise is typically

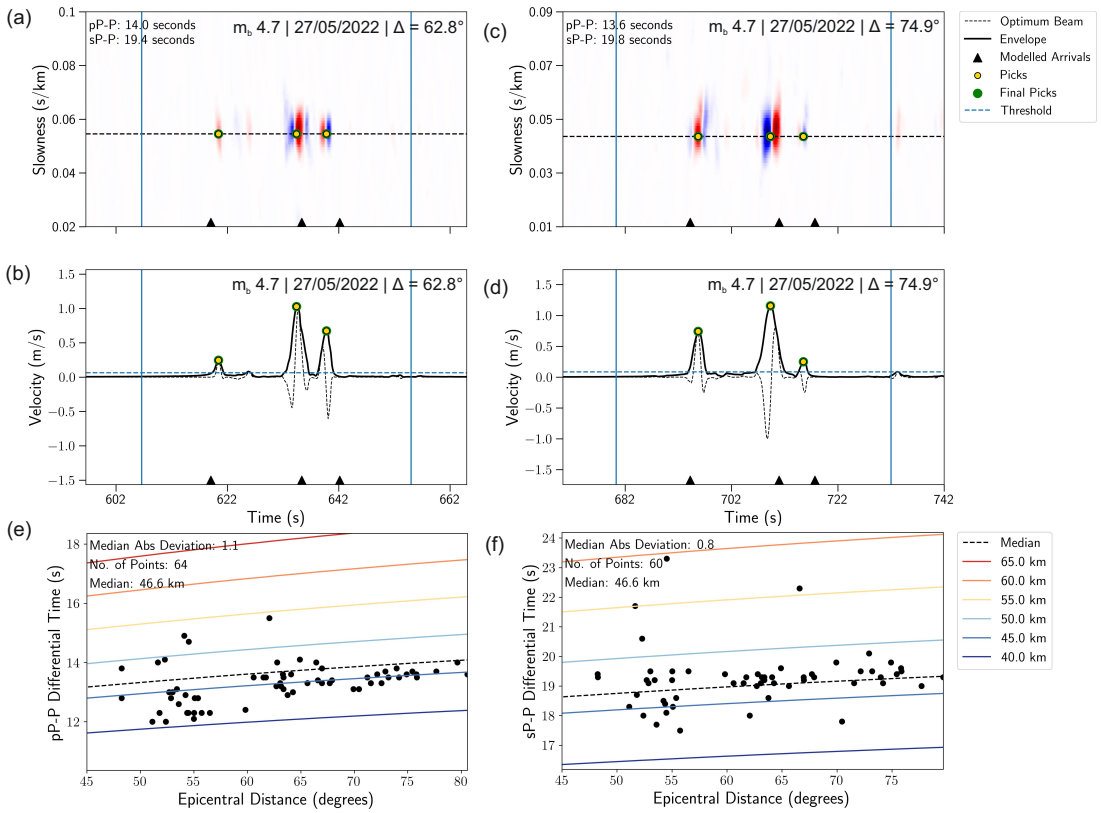

Figure 2.13: Example *ad-hoc* arrays, their automatic picks and differential times between phases for the m_b 4.7 event which occurred on 27th May 2022 in Peru, and plots illustrating all *ad-hoc* array differential times against epicentral distance to determine a final event depth. (a) and (b) are the vespagram and optimum beam respectively for an *ad-hoc* array at an epicentral distance of 62.8°, whilst (c) and (d) are the vespagram and beam for an *ad-hoc* array at an epicentral distance of 74.9°. Blue vertical lines indicate the time window of data used for automatic picking. (e) and (f) distance-differential time plots for *pP-P* and *sP-P* respectively. Plots (e) and (f) show that depth phase picks can be difficult to pick well automatically and gather consistent differential times, however a large number of data points (124) helps to combat the poorer picks.

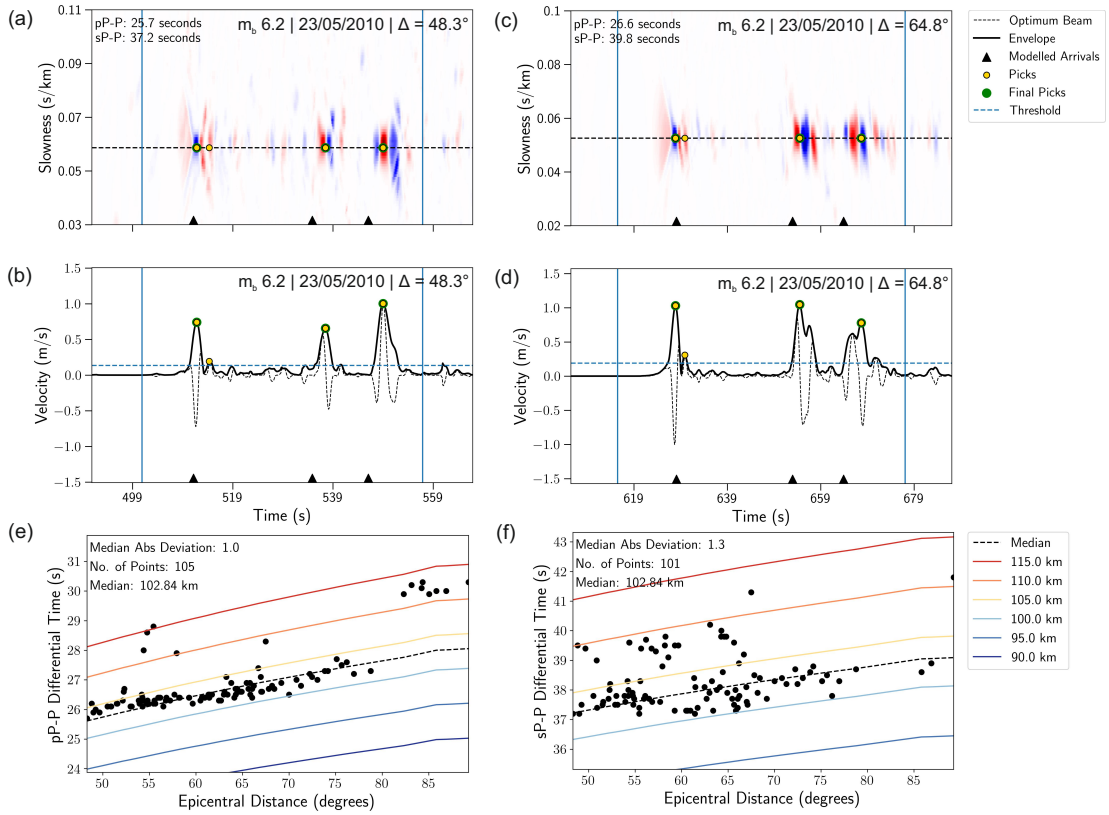

Figure 2.14: Example *ad-hoc* arrays, their automatic picks and differential times between phases for the m_b 6.2 event which occurred on 23rd May 2010 in Peru, and plots illustrating all *ad-hoc* array differential times against epicentral distance to determine a final event depth. (a) and (b) are the vespagram and optimum beam respectively for an *ad-hoc* array at an epicentral distance of 48.3°, whilst (c) and d) are the vespagram and beam for an *ad-hoc* array at an epicentral distance of 64.8°. Blue vertical lines indicate the time window of data used for automatic picking. (e) and (f) show distance-differential time plots for *pP-P* and *sP-P* respectively. On plot (e) the deeper picks determined from *ad-hoc* arrays at epicentral distances over 80° appear anomalous, these are located in Europe where perhaps the velocity model is not fitting the ray path well. Plot (f) shows that for this event *sP* picks can be more difficult to pick well automatically and gather consistent differential times. The cluster of *ad-hoc* arrays near a depth of 108 km occur due to a slight mispick as demonstrated by *sP* picks seen in (c) and (d).

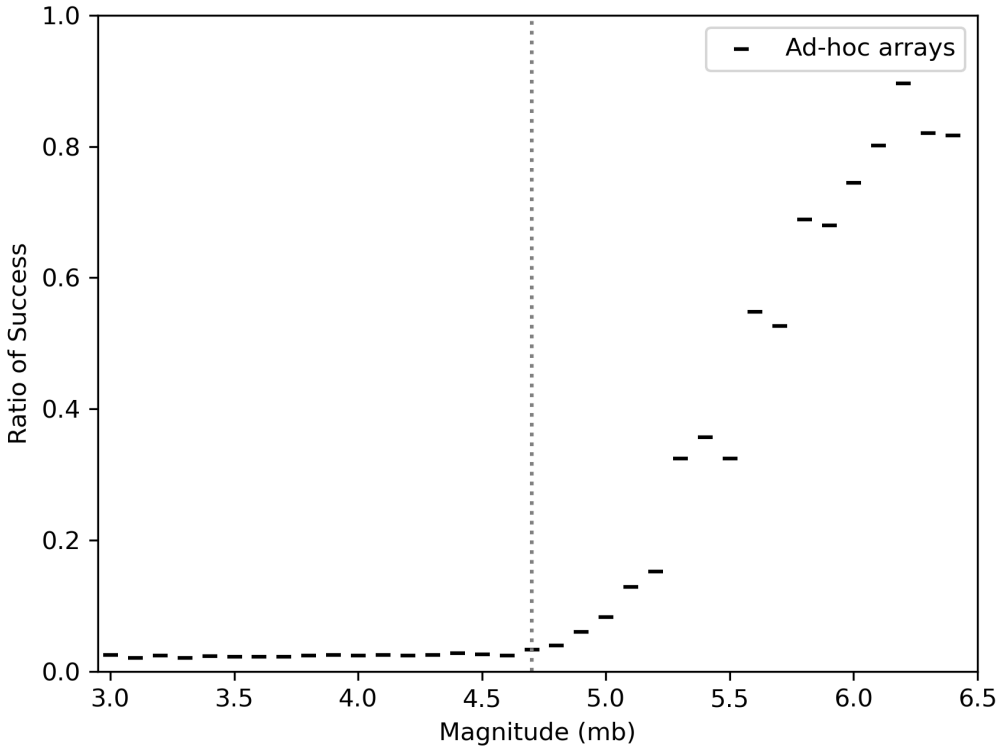

Figure 2.15: Determining the lower magnitude limit for my approach using the Peruvian catalogue containing 8796 earthquakes from m_b 3.0 to 6.5 which have occurred post 1995, taken from the ISC. Ratio of successful versus failed relocations for total *ad-hoc* arrays per 0.1 magnitude. The dashed line highlights my m_b 4.7 limit.

picked on the low number of *ad-hoc* arrays remaining after data quality checks, which skews how successful these events appear. I therefore suggest m_b 4.7 as an operational magnitude limit, and recommend inspection of formative lower magnitude events.

2.4.2 Assessing error

To provide a quantitative measure of the uncertainty present in the *pP-P* and *sP-P* differential times, which are later converted to depth, I jack-knife the traces of each *ad-hoc* array used to determine the final depth relocation of each earthquake.

For each *ad-hoc* array, I randomly remove one trace and pass the remaining traces through the processing and analysis loop. This tests the dependence of the *ad-hoc* array's results upon a single trace. Since the minimum number of traces permitted in an *ad-hoc* array is 8 (see Section 2.2.4.3), I jack-knife (Efron & Tibshirani, 1986; Korenaga, 2013) the traces and run the loop 8 times, before running the loop once more with all of the traces included to give a total of 9 runs per *ad-hoc* array. The same trace is not removed twice, therefore each *ad-hoc* array can have a maximum of 9 *pP-P* and 9 *sP-P* times, and therefore a

maximum of 18 associated depths.

After jack-knifing each *ad-hoc* array for a single earthquake, I post-process the results identically to the usual relocation routine and calculate the median absolute deviation of the remaining *ad-hoc* array distance-depth data points to assess how the differential times uncertainty translates to error in depth. This is repeated for every earthquake in the relocated catalogue, ensuring an event-specific uncertainty is determined for each relocated earthquake depth. I also preferentially use the median event depth found from the jack-knifed *ad-hoc* arrays as my final hypocentral depth – the larger number of data points typically provides a more precise depth and this value relates directly to the errors calculated.

For my regional catalogue, I remove events with zero error, thus removing events with their depths determined from a single *ad-hoc* array. I also remove events with an exact 40 km depth change from the original ISC catalogue, as these indicate events which cannot be relocated by my approach due to the ±40 km test depth limit used during depth conversion. I additionally limit the events to between m_b 4.7-6.5. The remaining events demonstrate errors ranging between 23.10 km and 0.05 km with a mean uncertainty of 3.13 km. For my final regional catalogue I choose to not include events providing errors greater than 20 km, the errors for the final catalogue vary between 0.05 and 18.40 km, with a mean uncertainty of 3.05 km – less than 5% of the events have errors >10 km. These uncertainties are illustrated as error bars on the Peruvian catalogue shown in Figure 2.16. The mean difference between the final catalogue depths and the initial ISC depths is 4.18 km, however the use of different velocity models will systematically factor into this variation – see Figure A.10 in the Appendix.

2.4.3 Relocated Peruvian catalogue

The final Peruvian catalogue demonstrates the automatic relocation of 620 earthquakes, and shows 3 broad zones of seismicity (Figure 2.16a) approximately between latitudes 1-7°S, 7-13°S and 13-19°S – the northern and southern most zones are located over the areas where the flat slab portion of the Nazca plate is transitioning into a steeper slab dip. The seismicity between 7-13°S includes the Pucallpa Nest, which is thought to be related to both the Mendaña Fracture Zone and a local slab sag (Wagner & Okal, 2019). The three cross sections (Figures 2.16b, c and d) aim to target these zones.

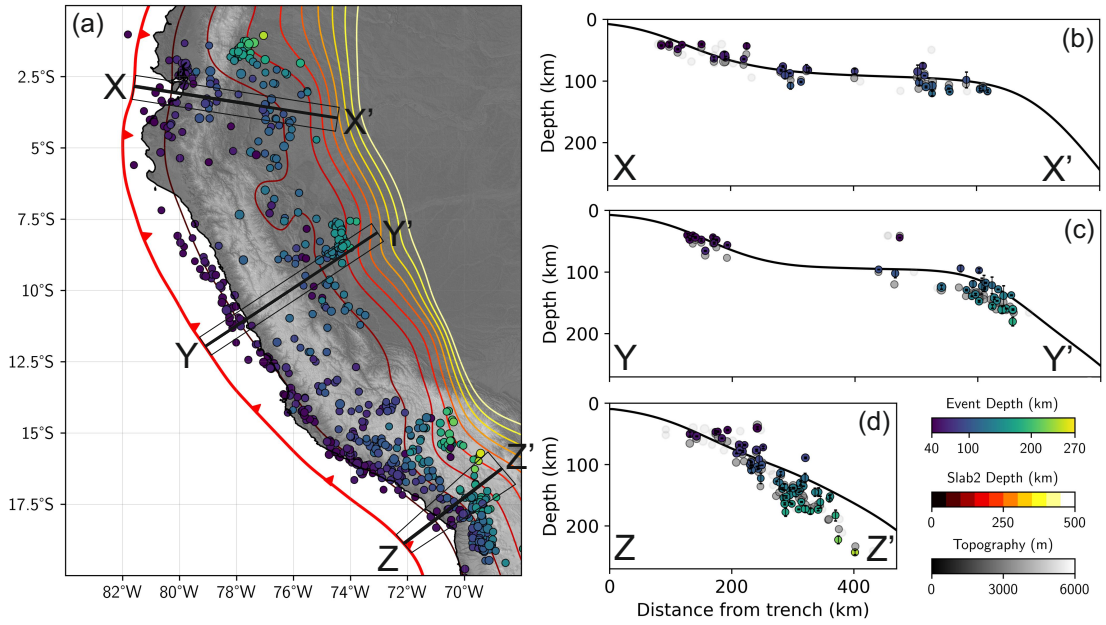

Figure 2.16: Peruvian flat slab catalogue with error bars determined though jack-knifing the *ad-hoc* arrays. The figure shows events with magnitudes between m_b 4.7-6.5, and have final relocated depths between 40-350 km with errors of less than 20 km. (a) is the map of Peru, with the relocated hypocentres (scaled in size to magnitude), example cross section locations and Slab2 contours plotted (Hayes et al., 2018). (b), (c) and (d) show the example cross sections with my relocated hypocentral depths in colour and with their error bars, the original ISC hypocentres which I relocated are in dark grey and also scaled in size to magnitude. ISC hypocentres which were not relocated by my approach are in pale grey.

These profiles (Figures 2.16b and 2.16c) demonstrate the flat slab, with intra-slab events occurring at the initial bend into the flat slab configuration approximately 100-300 km from the trench, and additionally when the slab bends again into the mantle between 450-750 km from the trench, with a largely aseismic stretch between the two bends. This observation supports the link between flexural bending of the down-going slab and the occurrence of intermediate-depth earthquakes due to the resultant intra-slab deformation (Sandiford et al., 2019). Figure 2.16d also looks to have two layers of seismicity within the Pucallpa Nest, approximately 600 km from the trench. This could indicate the presence of a double seismogenic zone in central Peru, however further analysis would be required to determine if the apparent layering is a real feature – see Sections 4.2.2 and 7.3.4 for updated Pucallpa Nest cross sections with bounce-point corrections included.

Figure 2.16d demonstrates the steeper slab dip which the flat slab transitions into north and south of Peru. Whilst the section does capture events occurring at variable slab dips in and out of the projection plane – note the two events at approximately 375-400 km from the trench at depths of 230-260 km – it is apparent that a new regional slab top deviating from Slab2 (Hayes et al., 2018) may be needed for the Peruvian portion of the Nazca plate. The tailored quantitative errors for each event determined from jack-knifing my *ad-hoc* arrays will help to inform future interpretations of the final catalogue.

2.5 Limitations

2.5.1 Assumed point souce

For a hypocentral depth to be relocated, there is an automatic assumption that the seismic signal is emitted from a discrete spatial point. In reality whilst this can be a sound assumption for smaller magnitude events, larger earthquakes will likely have spatiotemporal evolution of their ruptures and focal mechanisms. For example, the M_w 8.0 intraslab event which occurred in Peru on the 26th May 2019 demonstrated multiple rupture episodes (Hu et al., 2021) with two large slip areas approximately 120 km apart (Liu & Yao, 2020). Complex rupture propagations, and the spatial areas they cover, are not taken into consideration whilst relocating the earthquake depth. I limit the magnitude of the earthquake events I consider to $m_b < 6.5$ in order to avoid ruptures that appear complex at the frequencies used in my approach, and to assist the assumption of a simple point source.

2.5.2 Velocity model

Currently, the automated routine I have developed uses a 1D global velocity model modified to reflect regional variation in lithosphere velocity structure to predict phase arrivals, and invert the differential times for depth. The 1D velocity model does not take into account the near-source variance in crustal structure and topography the depth phases are experiencing with respect to receiver azimuth. To address this limitation I would need to incorporate a 3D velocity structure and ray tracing into the relocation algorithm.

However, the algorithm possesses the flexibility to outsource the depth conversion to an alternative inversion algorithm, which may use a 3D velocity structure during depth relocation – the phase picking routine is independent of the predicted phase arrival times and the phase identification routine has a modest margin of error built in to account for ray path errors. Additionally, the greater the epicentral distance of the station (i.e. further than 30°), the closer the depth phase bounce points exist to the event epicentre. This limits the velocity variations the depth phases experience relative to one another. Most teleseismic stations, and hence the *ad-hoc* arrays, are situated more than 30° from the event epicentre.

2.5.3 Shallow events

The ability to relocate shallow earthquakes depends upon whether there is sufficient separation between the direct arrival and its corresponding depth phases to allow the identification of distinct arrivals, which in turn is dependent upon the source duration (which broadly scales with earthquake magnitude). If the source duration of a shallow earthquake is small, the likelihood that the phases will separate enough to allow relocation to occur increases.

The relocation algorithm presented here has been designed to relocate earthquakes which occur between 40 and 350 km depth, however, I have observed robust relocations for depths sub-40 km. Whilst earthquakes with short source durations and depths down to ∼15 km have been relocated by the algorithm as it currently exists, some adaptations would be necessary to increase confidence in the phase identification routine for events sub-25 km deep.

2.5.4 Focal mechanism

In some cases the combination of station azimuth with takeoff angle results in a P wave ray path where the pierce point aligns with one of the event's nodal planes. When this happens there will be no detectable P arrival at the station due to the P wave radiation pattern. Without a P arrival, the relocation algorithm presented here cannot be used. *Ad-hoc* arrays containing data without a P wave arrival will be discarded by the phase identification routine (see Section 2.2.4.5), thus reducing the pool of *ad-hoc* arrays used to determine event depth.

Similarly, the detection of each individual depth phase depends upon the phase having a detectable amplitude, and is therefore limited in cases where the pierce point for that phase intersects with the radiation pattern nodal plane. Hence, even when P is clearly detectable, one or both of pP and sP may have small amplitudes, and be undetectable. This is the principal contributor to the complexity in my phase identification routine.

2.5.5 Station density

For a robust depth determination using my relocation algorithm, the formation of multiple *ad-hoc* arrays is required. For multiple *ad-hoc* arrays to be formed, I need a dense distribution of seismic stations, ideally spanning a range of distances and azimuths. Whilst the growth of seismic network coverage means future events will have a wealth of data recorded by the expanding open access seismic networks, historic events sometimes lack coverage. Events occurring pre-2000 struggle for data with a great enough station density for *ad-hoc* array formation under the criteria outlined in Section 2.2.3. The exceptions to the rule are events from the 1990s which contain dense, targeted station networks within teleseismic distances, such as the seismometers associated with the Southern California Earthquake Data Centre, or dense networks installed as part of temporary regional deployments. Yet even these events will suffer from a lack a backazimuthal variation if, for example, the nodal plane of the event focal mechanism aligned with the few existing *ad-hoc* arrays (see Section 2.5.4). Despite the occasional dense network available during the 1990s, older events are likely to suffer from the low density distribution of seismic data. The approach is unlikely to work pre-1990s due to a lack of global data.

2.5.6 Automation

I have consciously set high quality control measures in order to build confidence in the automated results. Consequently, clean coherent data may occasionally be discarded alongside poorer quality data. Equally, despite the high quality control measures, the occasional poor quality data *ad-hoc* array, or misidentified phase, may proceed through to the depth determination steps. I aim to capture the uncertainty of the new event depths based upon poorer quality data within the jack-knifing error estimations (see Section 2.4.2).

2.5.7 Maximum catalogue depth error

The phase identification routine and the depth conversion are designed to accommodate a maximum of 40 km error in the initial catalogue depth. The phase identification routine relies upon the predicted phase arrivals plus margins of error calculated from a potential 40 km error in the initial catalogue depth, and the forward modelled test depths are limited to $\pm$40 km of the initial catalogue depth. Any events which require an updated hypocentre depth that is greater than 40 km from the initial depth catalogue will not be correctly relocated, and hence would be excluded from a catalogue determined using my routine.

I use the ISC event catalogue as my initial catalogue as I expect that the event hypocentres they calculate are within 40 km of the depths I calculate using my algorithm, although I acknowledge that in rare cases, this may not be the case (e.g. Craig et al., 2023).

2.6 Conclusion

In this chapter, I present a fully automated, dynamic approach to constrain the depths of intermediate-depth earthquakes using depth phases. Depth phases are difficult to detect on single station seismic data, therefore I leverage the increasingly available global seismic data to construct adaptable *ad-hoc* arrays and apply array processing techniques, in order to significantly boost the detectability of both *pP* and *sP*. I use the differential times between the depth phases and their direct *P* arrival in conjunction with an appropriate 1D velocity model to determine hypocentral depth. Using this approach I am able to reliably generate regional catalogues containing events between m_b 4.7 and 6.5, and between depths of 40-350 km. I show regional catalogue results for the northern Chile and the Peruvian flat slab sections of the subducting Nazca plate, with strong agreement between my depths for northern Chile and those found by Craig (2019).

Chapter 3

Automatically detecting *S* and *sS* on teleseismic data

In Chapter 2, I demonstrated a method to use the direct P arrival and its associated depth phases, pP and sP, to relocate intermediate-depth earthquakes in depth. In this chapter I extend the approach to detect the direct S arrival and the corresponding sS depth phase. Below, I outline the adaptations made to the process, described in the previous chapter, required to work with S wave data.

3.1 Data

For integrating the S wave approach into the P wave based methodology established in Chapter 2, I use the same initial catalogue (Section 2.2.1) taken from the International Seismological Centre (ISC). For a given event in the catalogue, I take all of the available teleseismic (30-90° epicentral angle) horizontal component station data recorded on either BH or HH channels, from open access FDSN data centres. These data are subsequently checked to see if, for a given station, there are a trio of Z, N and E components (or Z and two horizontal components). If the trio includes two horizontal components not aligned to N and E (commonly called "1" or "2"), I rotate them into the N and E orientations using the component orientation stored in the metadata. Only stations with a final trio of Z, N and E component data and corresponding metadata will continue through the process, as this allows me to use the same *ad-hoc* arrays assembled for Z component data (Section 2.2.3), to simplify the workflow.

The remaining N and E component traces have their instrument response deconvolved into units of velocity, are linearly detrended, demeaned, have a 5% end taper applied, are bandpass filtered between 0.03-0.2 Hz using a 3-corner Butterworth filter, resampled to 10 Hz and normalised to their peak amplitude. Z component data are currently processed separately in accordance with the details outlined in Section 2.2.2.

I select a lower frequency filter than previously used for the P wave methodology (0.1-1 Hz), as I am now targeting longer period S wave arrivals with a lower dominant frequency. The 0.03-0.2 Hz band used here was guided by the work of both Molnar et al. (1973) and Langston (2014). Molnar et al. (1973) analysed the P and S spectra of 144 aftershocks which occurred near San Fernando in 1971, with magnitudes 0.5 to 4.5, to establish that S wave corner frequencies are systematically smaller than P wave corner frequencies. Although this was a local study, as part of the work, Molnar et al. (1973) compiled the spectral analyses from teleseismic studies (Hanks & Wyss, 1972; Molnar & Wyss, 1972; Wyss & Hanks, 1972; Wyss & Molnar, 1972) to generate a summary plot of teleseismic P versus S corner frequencies. The summary plot indicates a range of approximately 0.03-0.3 Hz for teleseismic S wave corner frequencies, and 0.04-0.5 Hz for teleseismic P waves. However two outlying data points from the same study lower the ranges, discounting these, the ranges shift to 0.05-0.3 and 0.1-0.5 Hz for S and P respectively. Given the age of the study, it is likely that broadband channels did not exist for seismometers, which may decrease the accuracy of the corner frequencies found.

The study conducted by Langston (2014) is more recent, and considers the coherency of both P and S wave signals across the TA network for teleseismic events in Chile, whilst varying inter-station distance and bandpass filters, using cross-correlation (Figure 3.1). This study therefore strongly aligns with my approach, as both consider teleseismic data from intermediate-depth earthquakes in Chile/mid-South American Subduction Zone, which are largely received in the US by the TA network. With an inter-station distance limited by the *ad-hoc* array aperture (2.5° or 278 km), I can consider which bandpass filter allows teleseismic direct arrivals to retain a cross-correlation coefficient of greater than 0.9, and thus, good coherency across the array.

For P waves, filters 0.05-0.1, 0.1-0.2, 0.2-0.4 and 0.4-0.8 Hz provide a coefficient of >0.9 at inter-station distances of 278 km. The final filter of 0.8-1.6 Hz gives a coefficient below 0.9 at all inter-station distances. The P wave results corroborate that my previous selection

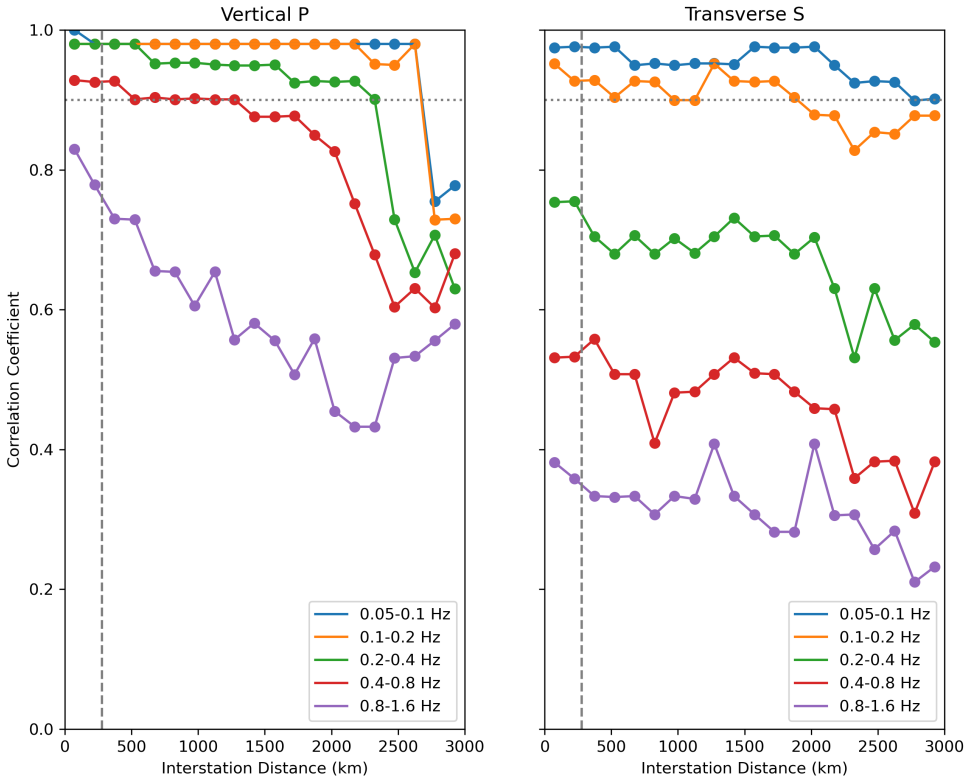

Figure 3.1: Plots of correlation coefficient versus interstation distance for teleseismic P and S waves from the M_w 6.2, 110 km deep Tarapaca event in Chile, adapted from Langston (2014). Grey dotted line indicates a correlation coefficient of 0.9, and grey dashed line indicates a 278 km interstation distance – the maximum possible for my *ad-hoc* arrays.

of a 0.1-1 Hz filter (Section 2.2.2.1) encourages coherent stacking across the *ad-hoc* array aperture. For teleseismic S waves, a cross-correlation coefficient greater than 0.9 for inter-station distances of 278 km or less occurs for the 0.05-0.1 and 0.1-0.2 Hz bandpass filters. The 0.2-0.4 Hz filter gives a coefficient of between 0.7 and 0.8, whilst coherency deteriorates rapidly (<0.6) for the tested 0.4-0.8 and 0.8-1.6 Hz filters. With both studies in mind, I select a bandpass filter of 0.03-0.2 Hz. The lower limit is extended to lower frequencies than the Langston (2014) study to acknowledge the possibility of lower corner frequencies, as indicated by Molnar et al. (1973). The upper limit is set using the upper limit indicated by the Langston (2014) study for coherent (>0.9 correlation coefficient) S waves across 278 km aperture *ad-hoc* arrays.

3.2 Methodology

I load in seismic data for stations which have processed Z, N and E components, and populate the relevant station attributes (e.g. coordinates, elevation). The available stations are subsequently grouped into the same *ad-hoc* arrays created using the Z component data (see Section 2.2.3 and Figure 3.2). This approach raises the likelihood that an S wave based *ad-hoc* array will fail to be processed, as the array clustering is not optimised for the horizontal component seismic dataset. Consequently, it is more likely that there will be less initial stations per array and thus, reduced resilience for quality control measures. However, using the same *ad-hoc* arrays simplifies the workflow, and allows direct comparison between the P wave and S wave *ad-hoc* array results.

The S wave methodology is also inherently linked to the success of the P wave *ad-hoc* arrays. The Z component, P wave targeting data is handled first in accordance with the approach discussed in Chapter 2. If the *ad-hoc* array passes the cross-correlation and vespagram quality checks for P wave picking, the *ad-hoc* array is forwarded to the S wave portion of analysis. Continued processing of the *ad-hoc* array for S wave data does not depend upon on the successful identification of P, pP and/or sP arrivals.

During the S wave processing for a given *ad-hoc* array, the station N and E component seismic data are rotated into radial and transverse using the beampack-determined best fitting backazimuth found from the P arrival. If a beampack determined backazimuth was not previously found during the P wave processing, the calculated backazimuth determined from ray tracing is used – this option is rare, with zero occurrences during the relocation

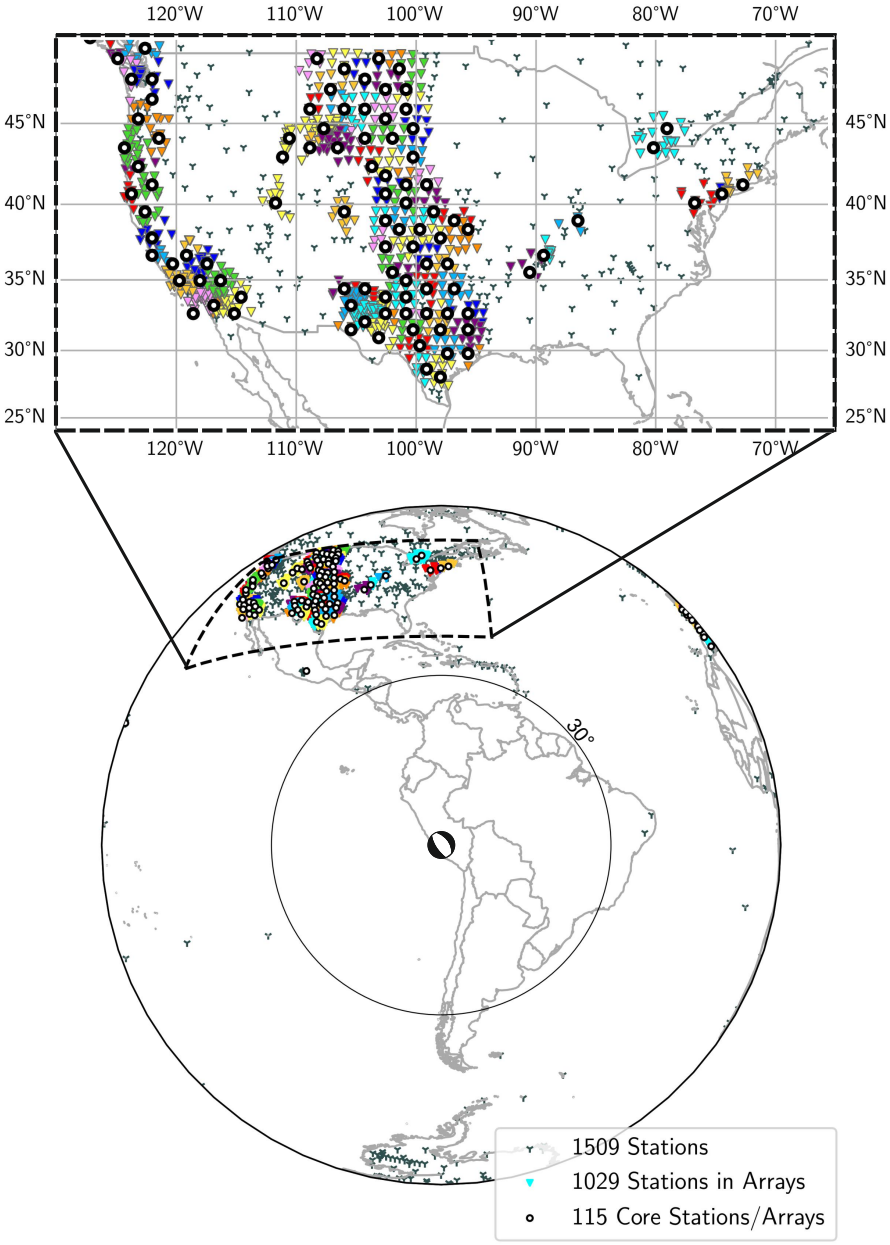

Figure 3.2: Example of the *ad-hoc* arrays for a m_b 6.2 event from 23rd May 2010, showing the distribution of teleseismic stations with 3-component data and their arrangement into the pre-designated *ad-hoc* arrays from P wave processing. A global view is shown on the bottom and and a zoom in of the *ad-hoc* arrays created in the USA on the top. The core stations found from the P wave processing are shown as thick black circles and the associated *ad-hoc* array stations as coloured triangles. The unused stations (grey Ys) are those removed due to their existence beyond the aperture of any of the pre-designated *ad-hoc* arrays. The earthquake focal mechanism is taken from the Global Centroid Moment Tensor Project (GCMT) (Dziewonski et al., 1981; Ekström et al., 2012). 113 *ad-hoc* arrays are assembled from the stations with Z, N and E components, whilst 115 were generated from only the Z component stations for P, pP and sP analysis.

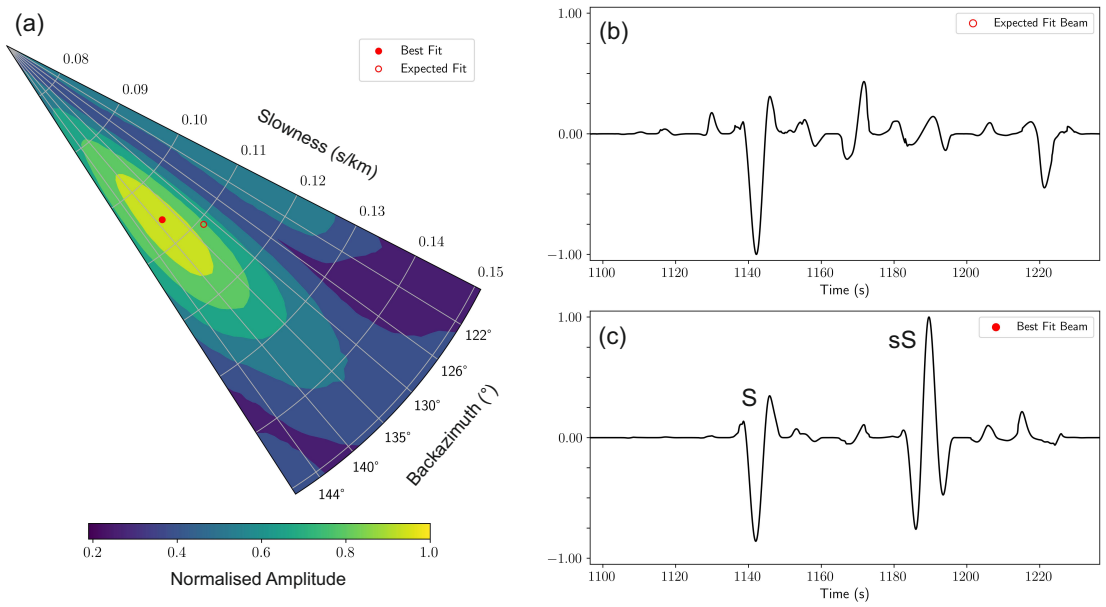

Figure 3.3: S wave amplitude during beamforming in polar coordinates (backazimuth and slowness) to determine the best-fit backazimuth and slowness parameters directly from the *ad-hoc* array traces (a). The open red circle shows the theoretical slowness and backazimuth found through calculation and the corresponding phase-weighted beam in (b). The filled red circle shows the beampack derived values and the resultant phase-weighted beam in (c), showing the importance of measured backazimuth and slowness values. Example from m_b 6.2 event from 23rd May 2010, *ad-hoc* array at 64.4° epicentral distance.

of the South American Subduction Zone catalogue (see Chapter 7). After the data are rotated into the ray path, I select and focus upon the transverse seismic dataset for the *ad-hoc* array, since this component will provide the clearest observations of tranverse propagating S wave arrivals.

Modelled arrival times for S and sS are calculated for the array geometric centre (retained from the P wave processing and analysis) using ray tracing in conjuction with the ak135 1D velocity model (Kennett et al., 1995) – these will be used to guide waveform trimming in upcoming steps. I then establish best fitting horizontal slowness and backazimuth values for the S arrival directly using the *ad-hoc* array data, by applying the beampacking approach from Section 2.2.4.1 to the S wave. Similarly to the Z component beams in Chapter 2, using the *ad-hoc* array derived beamforming values significantly enhances the wavelet arrivals for S and sS (Figure 3.3), and will assist the upcoming automatic picking routine.

With the data driven, best-fitting slowness and backazimuth values found, I construct phase-weighted beamforms for a range of slownesses to create a vespagram (Figure 3.4). The phase-weighted beams use an exponent of 4, and the slowness range tested is centred

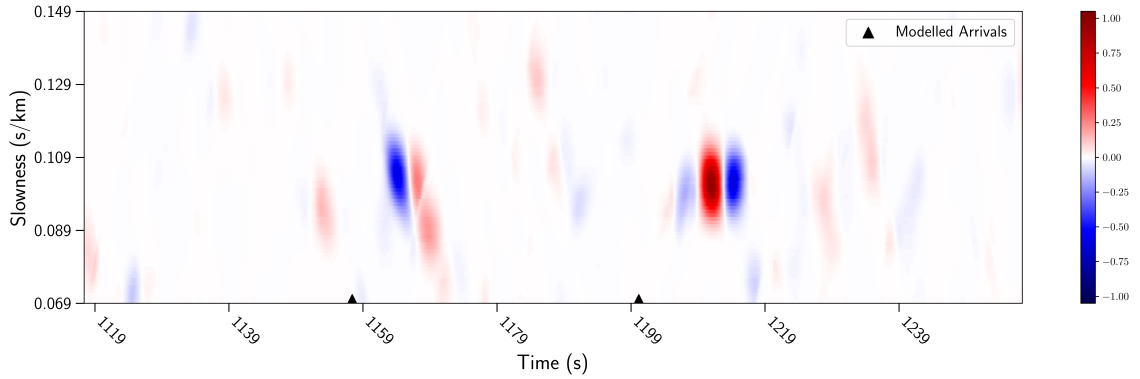

Figure 3.4: Example normalised, phase-weighted vespagram from m_b 6.2 event from 23rd May 2010, *ad-hoc* array at 66.1° epicentral distance.

on the beampack found slowness ±0.4 s/km in intervals of 0.001 s/km. These parameters are the same as those used in Chapter 2.

Here I check the quality of the beamforms, to decide if they are suitable to be continued into the phase detection steps of the workflow. Following Section 2.2.4.3 for P wave data, I apply a cross-correlation routine to compare the direct arrival (S) on the individual traces to the optimum beam (beamformed using the beampacking found, best-fitting backazimuth and slowness). Traces are trimmed around the modelled S arrival time with ±10 second margins, those which have a correlation coefficient <0.3 and a timeshift of >0.5 seconds are removed from the *ad-hoc* array. If 8 or more traces are retained for the *ad-hoc* array, the *ad-hoc* array will be continued to the next step of the processing and analysis loop. *Ad-hoc* arrays which do not meet this criterion are halted at this point in the workflow. Once again, these parameters are the same as those used in Chapter 2.

For *ad-hoc* arrays which have more than 8 traces after the cross-correlation routine, another quality control is applied, this time considering the entire vespagram and the coherency of the expected arrivals with respect to slowness. The routine is the same as the one applied to the P wave relocation approach in Section 2.2.4.3, where vespagram peaks which are >0.6 of the maximum vespagram amplitude are selected and analysed for clusters. If it is a good quality vespagram, I expect to see clusters of high amplitude peaks aligning along the beampack found slowness for the *ad-hoc* array – since the clusters should represent coherent phase arrivals. I check for this by identifying the centres of the high amplitude clusters and calculating their mean slowness and standard deviation in slowness space. If the mean slowness is within 0.006 s/km of the expected slowness, and the standard deviation of the cluster centres is <0.0105 s/km then I accept the *ad-hoc* array as passing

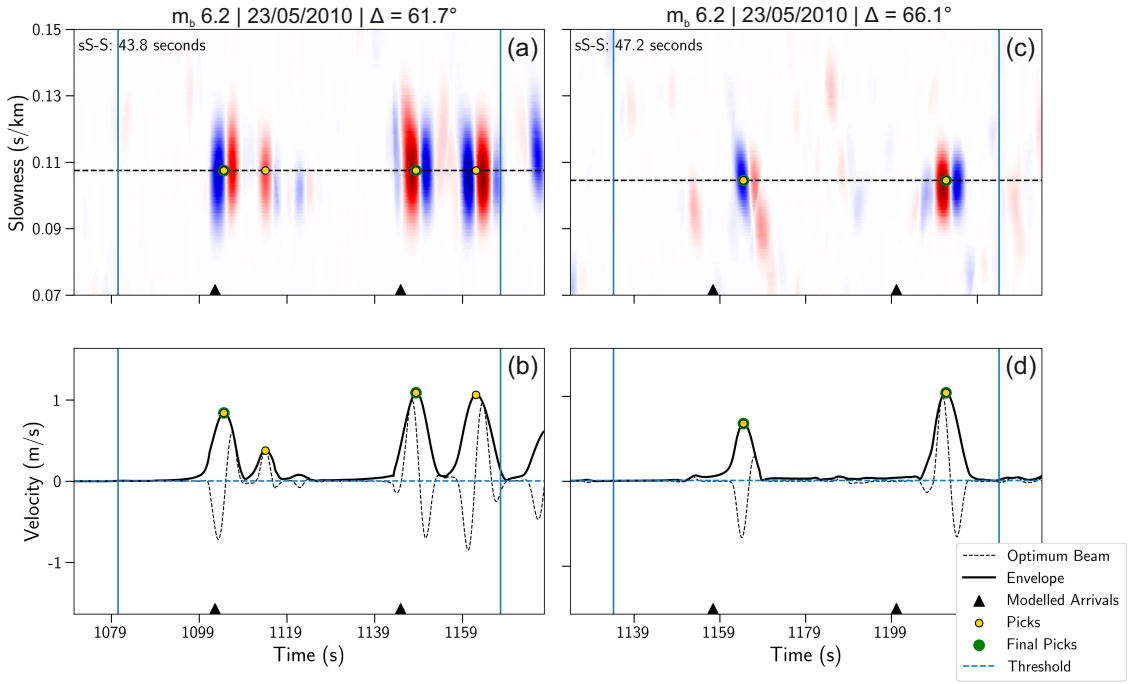

Figure 3.5: Example *ad-hoc* arrays, their automatic picks and differential times between phases for the m_b 6.2 event which occurred on 23rd May 2010 in Peru. (a) and (b) are the vespagram and optimum beam respectively for an *ad-hoc* array at an epicentral distance of 61.7°, whilst (c) and (d) are the vespagram and beam for an *ad-hoc* array at an epicentral distance of 66.1°. Blue vertical lines indicate the time window of data used for automatic picking.

the quality threshold. These criteria were discussed in Section 2.2.4.3. Given that S waves have longer periods and are therefore coherent over a larger range of horizontal slowness, these values might not be ideal for the S wave dataset. However, visual inspection of the vespagram quality check shows that the high amplitude clusters still centre upon the expected slowness, and are not weighting the mean towards the extreme slowness bounds. For now, I have not updated this criterion. *Ad-hoc* arrays which do not meet these criteria are not processed further.

The *ad-hoc* arrays that have managed to pass the quality checks are now considered for S and sS phase detection. Detection uses a dynamic, *ad-hoc* array tailored amplitude threshold based upon the amplitude distribution in the optimum beam waveform (Figure 3.6). This approach is identical to the one used for P, pP, and sP picking in Section 2.2.4.4, except I now consider the data between the modelled S and sS arrival times, with a 2% margin.

Any picks detected above the dynamic threshold and with a prominence greater than 0.15 of the maximum peak found in the beam are selected as candidates for my phases. The picks are subsequently run through a phase identification routine (Figure 3.7), similar to,

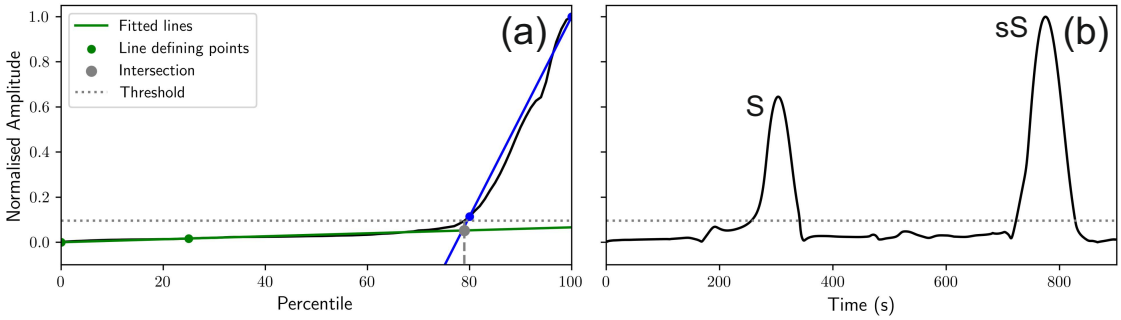

Figure 3.6: Example of the automatic picking threshold found for an *ad-hoc* array at an epicentral distance of 66.1° from the m_b 6.2 event on 23rd May 2010. (a) distribution of amplitude values for the *ad-hoc* array beam with respect to the percentile, the approximation of the beam with two lines, their intersection and the final threshold found. (b) threshold relative to the phase-weighted beam.

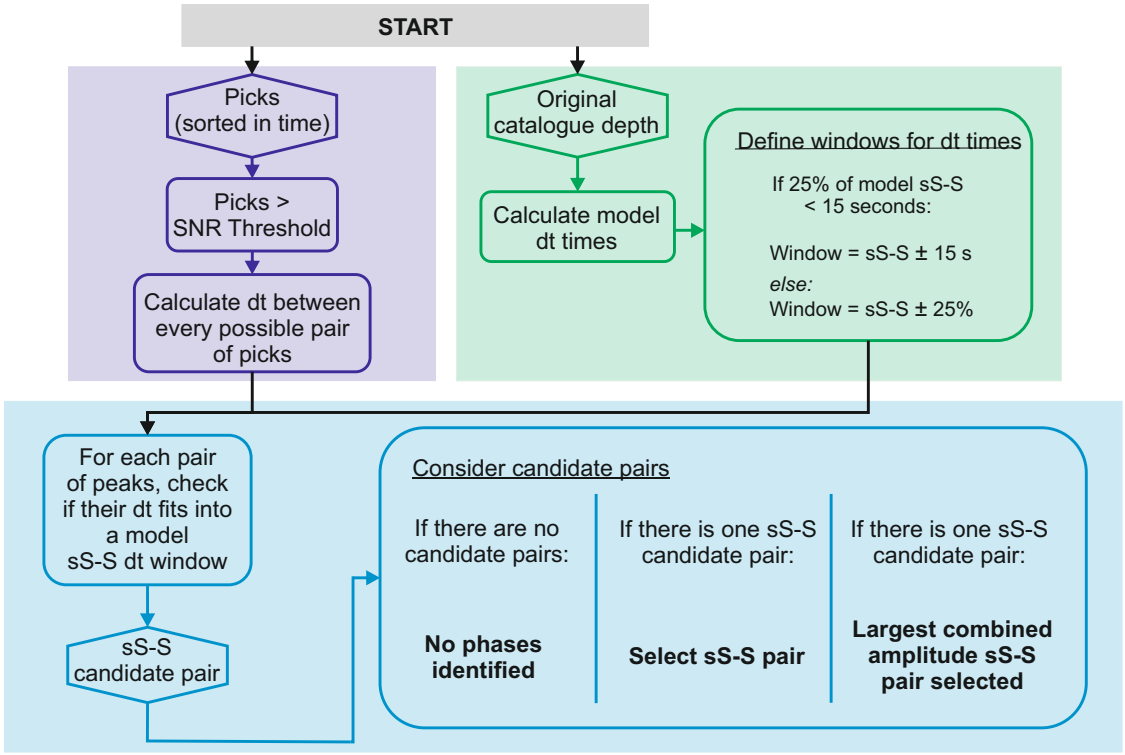

Figure 3.7: Phase identification workflow for S and sS. Picks from the automatic picking routine are sorted into phases by comparing their differential times with the 1D velocity modelled differential times for sS-S. Hexagonal boxes indicate products from a step in the workflow, and bold text shows the final phase selections.

yet entirely independent of the routine described in Section 2.2.4.5 for P wave data picks.

The phase identification routine relies upon a comparison between the observed and modelled differential times between S and sS, and only accounts for events within ±40 km of the relocated depth taken from the initial event catalogue. Initially picks are checked for a signal-to-noise greater than 5 (following Florez and Prieto (2017), and using the same approach as Chapter 2 except with the background noise calculated for 40 seconds immediately prior of the S arrival), in order to be considered as a final pick. The relative times between all these picks are subsequently calculated, and the picks considered as pairs for the remainder of the routine. For each pair of picks, the differential time is compared to the modelled differential time for the *ad-hoc* array using ak135 as the velocity model (Kennett et al., 1995), with any pairs with a differential time within ±25% of the modelled sS-S differential time (to account for unknown velocity structure) selected as a candidate pair.

If an earthquake is shallow, ±25% of a modelled differential time between sS and S will provide a very small time margin. To account for this, fixed time margins are used when the percentage margin is too small to be effective. For S waves I have adjusted this to ±15 seconds when 25% of the sS-S differential time is less than 15 seconds. The size of the fixed margin is based upon the possible error in differential times assuming that the earthquake is within ±40 km from the initial catalogue depth (see Appendix A.11). If there is a single candidate pair which compares favourably with the modelled arrivals, the two picks will be selected as sS and S. If more than one candidate pair is a reasonable fit for the *ad-hoc* array, the pair with the largest combined amplitude is selected. It is also very possible to have no candidate pairs, here the S processing will end for the given *ad-hoc* array.

The identified picks for S and sS are finalised, and their differential times calculated (Figure 3.5). These picks will be preserved and can either be used in a depth conversion algorithm similar to Section 2.2.5, or used in an alternative relocation algorithm. For a demonstration of how I use an alternative algorithm for earthquake relocation in 3D with P and S wave coda picks, see Chapter 7.

For the example earthquake (m_b 6.2 event on 23rd May 2010) in Peru, only 33 *ad-hoc* arrays are successfully picked for S and sS compared to approximately 100 for P, pP and/or sP (Figure 3.8). The reduction in success rate largely reflects the decision to use the same

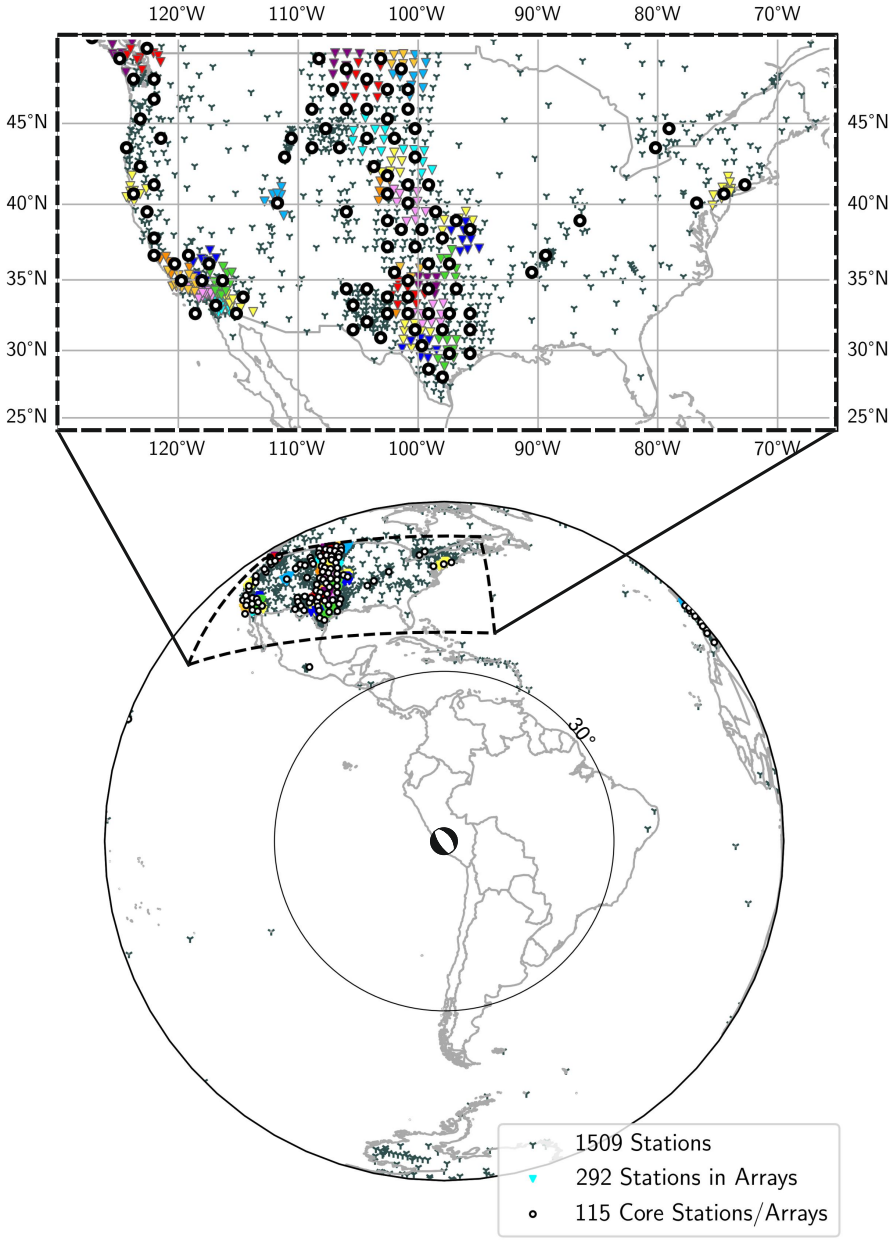

Figure 3.8: Distribution of *ad-hoc* arrays consisting of teleseismic stations with 3-component data which were successfully picked for S and sS (core stations with surrounding coloured triangles), for the m_b 6.2 23rd May 2010 Peruvian event. A global view is shown on the bottom and and a zoom in of the *ad-hoc* arrays created in the USA on the top. The core stations found from the P wave processing are shown as thick black circles and the associated *ad-hoc* array stations as coloured triangles. The unused stations are shown as grey Ys. The earthquake focal mechanism is taken from the Global Centroid Moment Tensor Project (GCMT) (Dziewonski et al., 1981; Ekström et al., 2012).

ad-hoc array arrangement as determined with the Z component dataset, resulting in many *ad-hoc* arrays having fewer stations contributing to the beamforms. When combined with targeting a more complex S waveform, which is more likely to fail the quality control measures, the *ad-hoc* arrays are significantly more sensitive to the criterion requiring more than 8 traces for further analysis. Chapter 7 discusses further the lower success rate and impact of S coda picking compared to the P coda, observed for the entire South American Subduction Zone.

Chapter 4

Assessing the impact of automatically-derived depth phases on global earthquake catalogues, and their relocation

Since 2009 the number of reported depth phases to the International Seismological Centre (ISC) have reduced from global seismic centres. This is likely due to their small amplitude coupled with limited picking resources at the centres. Consequently the number of depth phases defining ISC event locations has dropped from ∼8000-12,000 to ∼4000-7000 per month (Figure 4.1). The depth phase ray path (with a near-source surface reflection) constrains event depth, and acts to reduce the origin time-depth trade-off during relocation (Bondár & Storchak, 2011). Without the incorporation of depth phases, and assuming a lack of local network data, relocations will have a lower depth resolution. There has, therefore, been increased motivation to pick depth phases, either manually or automatically, to backfill the lack of reported depth phases and improve their event relocations.

Research into automatic and machine learning approaches to aid phase identification and picking is expanding (Ross et al., 2018; Woollam et al., 2022; Mousavi & Beroza, 2023). These methodologies are advantageous when handling larger quantities of seismic data efficiently, and for identifying phase arrivals which have previously proved difficult to manually pick on single station traces. Whilst developments in automatic methodologies

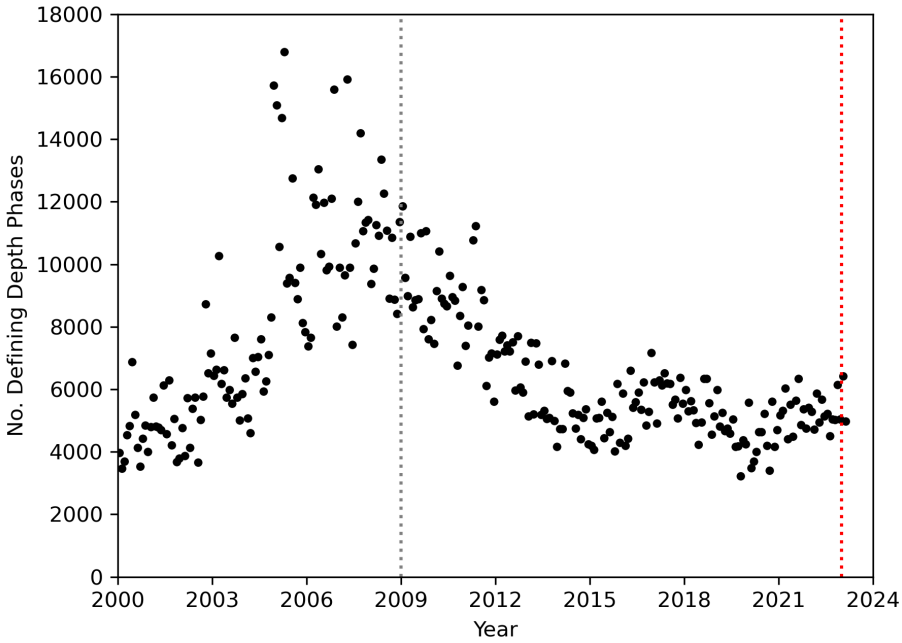

Figure 4.1: Number of depth phases (*pP*, *sP*, *pwP*, *sP* and surface reflected core phases) defining ISC event locations against the year the event occurred (ISC, personal comms.). Grey dotted line highlights the beginning of 2009, where numbers begin to decline. Red dotted line shows the beginning of 2023, where the reviewed ISC catalogue approximately ends at time of writing.

have largely focused upon detecting P and/or S wave arrivals, there is also a corner of research which has been refining the detection of *pP* and *sP* depth phases (Letort et al., 2016; Fang & van der Hilst, 2019; Craig, 2019; Münchmeyer et al., 2024; Blackwell et al., 2024). With the growth in techniques to automatically detect phase arrivals on seismic data, and specifically the burgeoning interest in using depth phases to refine event locations, it has become paramount to investigate the influence of automated depth phase results upon earthquake hypocentral locations in global catalogues.

In Chapter 2 I developed a new approach which leverages the growing (tele)seismic data, by assembling and processing *ad-hoc* arrays to increase the signal-to-noise ratio of the phases, and automatically pick the *ad-hoc* arrays for *P*, *pP* and *sP* arrivals expressly for event depth improvement in Peru and northern Chile (Blackwell et al., 2024). However, the methodology failed to account for 3D velocity structure (instead using locally derived 1D velocity models), bounce point and station elevation corrections when using the phase arrivals to determine event depth. These are significant assumptions to apply to regions in South America, given the local Andean mountain range and associated crustal geometries (Craig, 2019). By using a different relocation algorithm, such as ISCloc (Bondár & Storchak, 2011), these assumptions can be taken into account. ISCloc (Bondár & Storchak,

2011) is an algorithm used by the ISC to relocate earthquakes in 3D and determine location uncertainty, developed by Bondár and Storchak (2011), which uses globally reported phase arrivals in combination with the ak135 1D velocity model (Kennett et al., 1995) for an iterative linearized inversion.

In this chapter, I test the consequences of adding automatically-derived depth phases, determined for Peru and northern Chile (in Chapter 2), to established global phase catalogues upon the 3D relocation of the events, using ISCloc (Bondár & Storchak, 2011). I aim to see an improvement upon the results of the previous catalogue generated in Chapter 2, and the benefits of augmenting a global phase catalogue with *ad-hoc* array determined depth phases.

4.1 Methodology

4.1.1 Automatically deriving depth phases using array processing

I use the methodology presented in Chapter 2 to determine P, pP and sP phases from array processed data, with the aim to boost signal-to-noise ratios of typically very small amplitude arrivals on single station data. See Section 2.2 for details concerning data preprocessing, the creation of *ad-hoc* arrays and how array processing is applied to detect depth phases.

Previously, the differential times between the final pP-P and sP-P picks for all of the *ad-hoc* arrays for a given event are used to forward model a best-fitting earthquake depth, with an accompanying error found through jack-knifing the *ad-hoc* array traces. The conversion of the *ad-hoc* array determined phases into depth lacks features such as a bounce point and station elevation corrections, the ability to relocate in 3D space, and it only inputs the phases identified from the *ad-hoc* arrays. Given the vast catalogue of phase arrivals which exist globally for earthquakes, it seems pertinent to incorporate the new *ad-hoc* array phases with the phases which are already documented in order to refine earthquake location further. To this end, during this chapter I integrate the *ad-hoc* array P and depth phase picks into the ISC phase catalogue per event, and relocate the events using ISCloc (Bondár & Storchak, 2011).

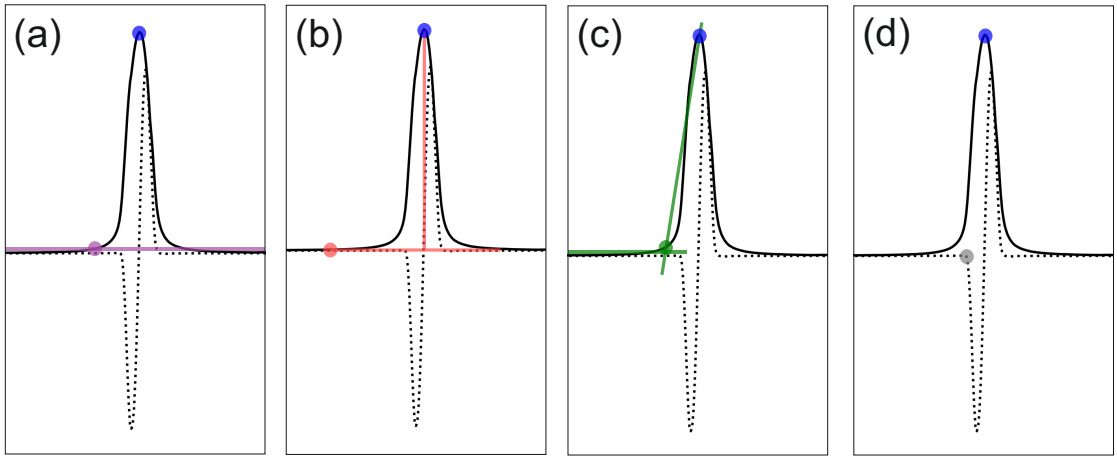

Figure 4.2: Four methods to correct amplitude P picks to onset picks. (a) Backstepping sample point by sample point backwards in time until below a noise threshold. (b) Finding the intersection of the envelope with a horizontal line projected at 0.9 of the P peak's height. (c) Finding the intersection between two lines approximating the peak onset and the pre-peak noise, and projecting to the envelope or trace. (d) Median P arrival calculated from slowness corrected reported P phases in the online ISC catalogue, projected to the trace. Dashed black line is the P arrival on a phase-weighted beam, the solid black line is the beam envelope, blue circles are the initial P amplitude pick on the envelope, and alternative coloured circles represent the onset pick for each method. Example beam from the 2010 June 26th event, m_b 5.4.

4.1.2 Conversion to onset times

Building on the previous work in Chapter 2, I use the vespagrams from each *ad-hoc* array, and the picks determined for P, pP and sP upon the beam formed using the best-fitting slowness and backazimuth. The picks are designed to be the amplitude peaks of the phases, as opposed to the phase onsets, which improves the ability to automatically and consistently pick phases, and proved unproblematic for using the relative arrival times of the phases to determine event depth. However, integrating the *ad-hoc* array-observed phases into a global catalogue requires a methodology to correct the amplitude picks to onset arrival times.

To correct the amplitude picks to onset times, the P wave onset needs to be identified, the time difference between the P onset and the picked P amplitude pick determined, and this time difference used as the time-shift correction for all three phases. A number of methodologies to geometrically determine the onset of the P arrival were tested on the envelope of the best-fitting optimum beam (Figure 4.2a-c), however significant inconsistencies failed to inspire confidence in this approach (see Figure 4.3).

Given that the aim of the work is to combine the *ad-hoc* array phase picks with those already reported in the ISC catalogue, I instead make use of the reported P wave arrivals

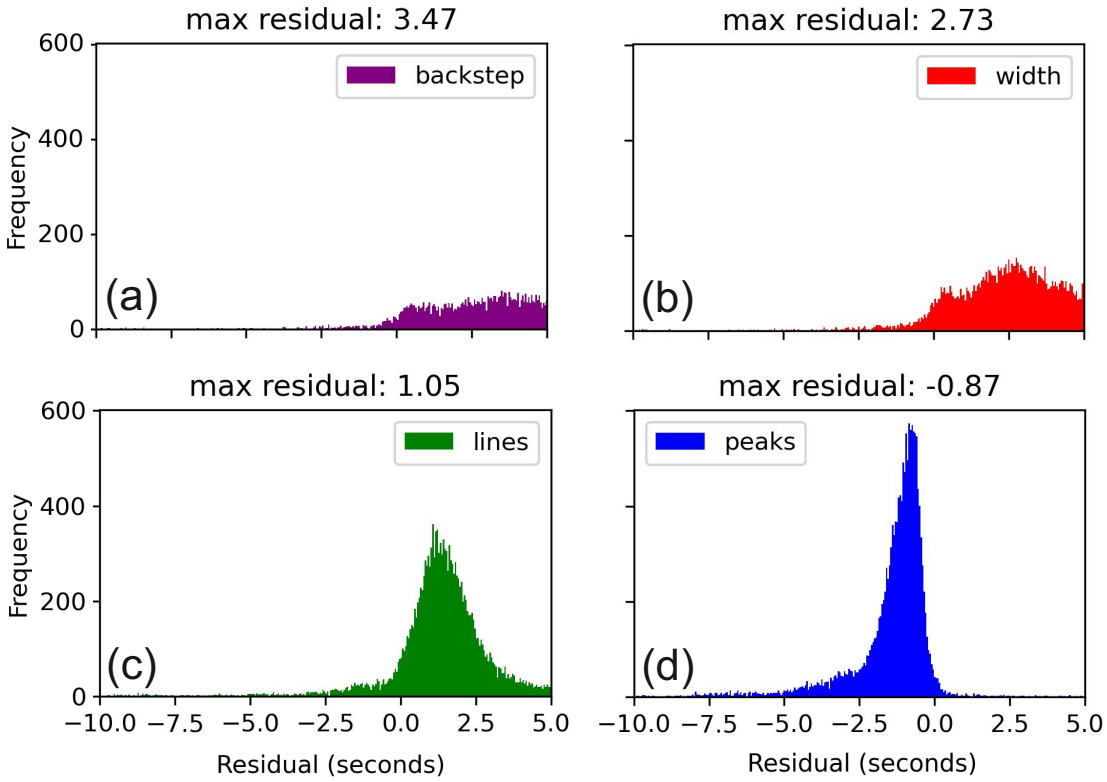

Figure 4.3: Plot of the residual between the slowness corrected, median ISC reported direct P arrival for an *ad-hoc* array and (a) the onset approximation using back-stepping from the peak to below a noise threshold, (b) the onset approximation using the intersection of the envelope with a horizontal line projected at 0.9 of the P peak height, (c) the onset approximation using two lines, and (d) the *ad-hoc* array determined peak amplitude pick. The plots demonstrate the inconsistency in using a geometric phase onset determination, and show that these are typically 1-3.5 seconds early compared to the slowness corrected, median ISC reported direct P arrival. (d) also shows that the mode difference between the amplitude pick and the ISC onset pick is 0.87 seconds for the data. These are calculated for the Peruvian and northern Chilean catalogues presented in Chapter 2, and the histograms are calculated at a 0.01 resolution.

already in the catalogue to inform my required time-shift. I therefore developed an approach to extract the stations with time-defining (location defining) P phases reported per event from the ISC online catalogue, associate the stations with the *ad-hoc* arrays created in Chapter 2 (Blackwell et al., 2024), slowness correct the phases to the geometric centre of the *ad-hoc* arrays and calculate the median P onset time. The difference between the ISC catalogue median P arrival time and the P amplitude pick from the *ad-hoc* array data is determined and used as the time-shift correction for the pP and sP phases. The ISC catalogue median P arrival is used as the corrected P onset time (Figure 4.2d).

The manner of the approach means that if there is not a P arrival reported by a station within an *ad-hoc* array, that *ad-hoc* array's picks cannot be corrected and thus used. This is a common occurrence for events >2022 at time of writing, as the ISC review process

runs 2 years behind the present. I therefore choose to only include events from 1995-2022 to achieve the best possible results. My tests on the previously relocated intermediate-depth earthquake catalogues derived for Peru and northern Chile (Blackwell et al., 2024), when removing events from >2022, indicate that 25.5% (8815 out of 34598) of all *ad-hoc* arrays fail due to a lack of reported P arrivals. This converts into 11.6% (137 out of 1179) events without any reported P arrivals in the ISC catalogue, with a mean magnitude of m_b 4.99. For a proof-of-concept test I feel that the failure rates are manageable given the large initial dataset, and note that my catalogue will likely have a higher magnitude of completeness than originally intended.

I observe that the ISC catalogue median P arrival can vary from the onset by up to 2 seconds when superimposed upon the *ad-hoc* array beam, this could be due to a number of reasons – manual picking error, loss in the resolution of the phase geometry when stacking the beam, or multi-pathing. I find a mode of 0.87 seconds between the median ISC reported P arrival and the *ad-hoc* array derived P amplitude pick, using the *ad-hoc* arrays from the Peruvian and north Chilean relocated catalogues from Chapter 2 (Appendix 4.3d). To cover the *ad-hoc* arrays without a recorded P arrival, it might be possible to use the mode to correct the *ad-hoc* array phases to onset times. Alternatively there is the possibility to use a machine learning picker to backfill *ad-hoc* arrays missing a recorded P onset (see Chapter 5). For this chapter, I limit my onset correction to the use of the manually reviewed ISC catalogue P phases to ensure high quality results.

4.1.3 Using ISCloc

The online ISC catalogue is dynamic, with the possibility of having new phases reported and added for an event after their original published ISCloc relocation. I therefore run ISCloc (Bondár & Storchak, 2011) twice, once with the ISC reported phases and once with the ISC reported phases plus the onset corrected *ad-hoc* array picks for P, pP and sP, to ensure a fair comparison between the 3D relocation outputs. I exclude ISC reported phases which are observed over 120° away from the ISCloc inputs to avoid complications with core depth phases, and I apply an inversion approach which seeds on the previously determined ISC location. In my inversions, I require 5 depth phases to secure depth resolution, and the ability to search/iterate without a fixed initial depth. This is important since the addition of *ad-hoc* array phases could make the difference between an event being relocated with a fixed depth or not, or even from being relocated at all.

4.2 Results

4.2.1 ISCloc comparisons

In this section I will compare the results from ISCloc when inputting the ISC reported catalogue phases versus the same input plus the *ad-hoc* array phase onsets for P, pP and sP per event. From henceforth, the online ISC catalogue phases will be referred to as the reported ISC inputs, and the ISC reported phases with the *ad-hoc* array phases will be referred to as the augmented ISC inputs. The aim is to assess how the addition of automatically-derived depth phases affects both the 3D relocation of a given event and the error statistics.

4.2.1.1 Number of defining phases

996 out of 1179 tested events had additional, *ad-hoc* array determined phases augmented to their initial ISC reported phase catalogues – an average of 47 phases were added (including direct P arrivals), with a minimum of 2 and a maximum number of 360, per event. Of these phase additions, an average of 29 depth phases were added to each event, with a minimum of 1 and a maximum of 238, and the sum total of depth phases across the events was increased by 49% (Figure 4.4a). More importantly, 5 depth phases were required per event to relocate it with a free, resolvable depth – the number of events which had too few depth phases reported to resolve depth, and thus depth was fixed, reduced by 35% (61 events) with the augmented inputs. Whilst this does not reduce the magnitude of completeness to which events are relocated without a fixed depth (m_b 5.5), it will improve the overall 3D relocation for the previously fixed events. For 137 events, I predicted that I do not have a means to correct my *ad-hoc* derived phases to absolute onset time, due to a lack of reported P arrivals within the aperture of my *ad-hoc* arrays (Section 4.1.2). Nevertheless, I observe that 183 events failed to have their phase catalogues augmented by my arrivals. This is because 46 of those 183 events have ISC reported P arrivals within at least one *ad-hoc* array, however, the *ad-hoc* arrays with the reported P arrivals do not align with the *ad-hoc* arrays with picks to correct.

After the application of ISCloc, 42,077 depth phases, with 11,406 (27% increase) new depth phases (Figure 4.4b), became time-defining (used to define the final 3D location), and therefore used in the algorithm to increase depth resolution. I had hoped that a greater number of my depth phases would become time-defining, however an inspection of the

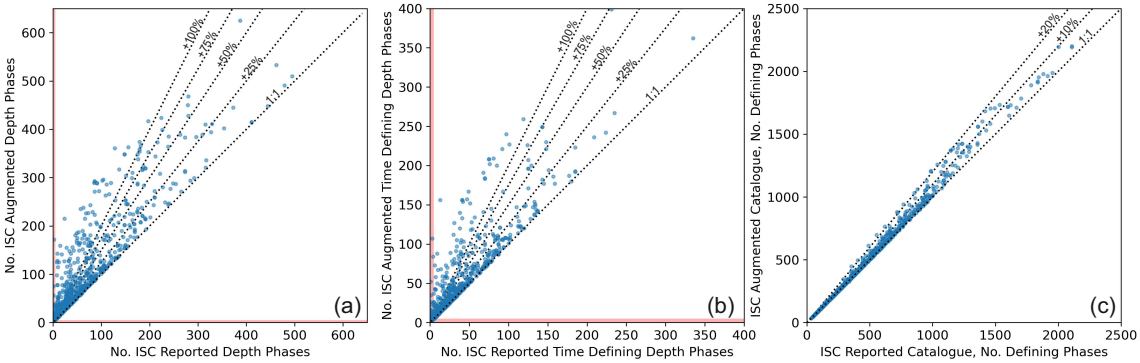

Figure 4.4: Plots showing the number of input depth phases (a), time-defining depth phases (b) and all time-defining phases (c) for the ISC reported catalogue versus the augmented ISC catalogue. Red bands highlight events with less than 5 depth phases.

results showed that my ISCloc results (ISC reported and ISC augmented) typically had less time-defining phases than the published ISC catalogue results. Therefore, I believe that the analysts at the ISC add significant value to the application of ISCloc, by interactively finding better fitting event locations which use a greater number of phases, than when ISCloc is used unsupervised. Despite this, Figure 4.4c demonstrates that the augmented ISC catalogue can increase the number of defining phases used to relocate the events by up to 25%. Figure 4.4a and b also illustrate that the events with lower numbers of depth phases experience the greatest impact from the addition of *ad-hoc* array derived phases, as numbers of (particularly time-defining) phases can increase by more than 100%, thus allowing greater depth resolution during the 3D relocation. I will assess the value of the *ad-hoc* array phase additions in terms of 3D relocation, the associated errors and the relation to event magnitude in the up-coming subsections.

4.2.1.2 Relocated depths and errors

ISCloc outputs two different depths, a traditional "Depth" which is determined using all of the time-defining phases and a "pP Depth" which is determined using only the differential times between time-defining depth phases and P arrivals. Whilst the "pP Depth" methodology solves in 1D and is more comparable to the original relocation methodology in Chapter 2, the "Depth" output factors in a larger number and range of phases which positively benefit the 3D event relocation. In this chapter I aim to assess the impact of the additional *ad-hoc* derived phases upon 3D earthquake relocations, rather than directly compare relative time, relocation approaches. Therefore I will be considering only the "Depth" output from ISCloc henceforth.

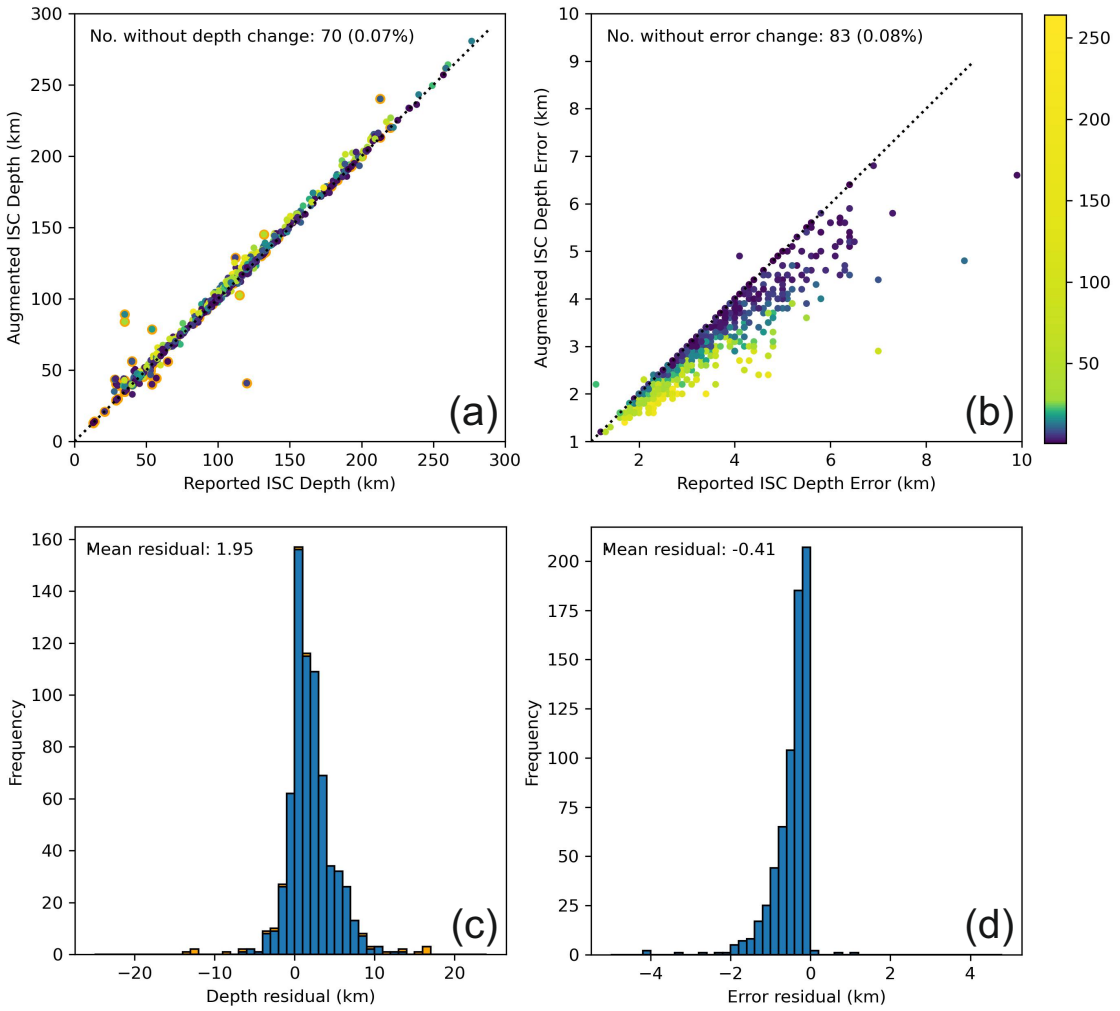

Figure 4.5: Comparison of depth and depth error between the reported ISC and augmented ISC inputs when applying ISCloc. (a) and (b) show the depth and depth error change when additional *ad-hoc* array phases are included. Both plots are coloured by number of additional time-defining phases, and (a) also has orange outlines for events which had fixed depths prior to the addition of phases. (c) and (d) are histograms showing the residual between the reported ISC and augmented ISC depths and depth errors respectively. (c) has orange bars indicating residual in depth when the fixed events are included. Events which did not have new time-defining phases from the augmented ISC input are not plotted.

Figure 4.5 shows the change in depth (a and b) and depth error (c and d) between the ISC reported inputs and the augmented ISC inputs, with scatter plots (coloured by the number of phases added by the *ad-hoc* arrays) and residual histograms. The depths tend to be deeper (mean residual of 1.95 km, not including depth fixed events) when the *ad-hoc* array phases are added to the input dataset, which is within the typical error range (1-7 km), and likely demonstrates the increase in depth resolution as a result of the additional depth phases. The events with the largest observed depth change are associated with depth fixing prior to the introduction of the *ad-hoc* array phases (orange in Figure 4.5a and c) – with the augmented phase catalogue a free depth for these events was determined. Whilst only a small change in depth is observed when adding *ad-hoc* array depth phases, it is the change in error which will provide greater insight into the relocation improvement. Figure 4.5b shows that depth error with the addition of *ad-hoc* array phases is reduced in 99.9% of events – although a correlation between absolute number of phases added and error change is weak (Figure 4.6). The mean reduction in depth error is 0.41 km using my test catalogues in Peru and northern Chile, with a maximum error reduction of 4.1 km observed. The few events with increased error using the augmented ISC catalogue input are typically caused by the depth becoming un-fixed due to the increase in number of depth phases, or the additional time-defining phases producing large time residual misfits to the final relocation. Given my location errors increase when an event becomes unfixed, it could be suggested that the errors defined for fixed events are overly conservative and need to be increased to align with the errors of events which are un-fixed in the future.

I also consider horizontal error reduction by calculating the area of the horizontal error ellipse, and notice that the addition of *ad-hoc* array phases minimally influences the horizontal error, with a mean reduction of 1.95 km square. Despite this, some outliers exist where the horizontal error decreased – notably there is a major outlier showing a reduction of 144 km squared. Further inspection of these examples show that time-defining sP additions with small time residuals allow significant horizontal error reduction when few depth phases exist in the ISC reported catalogue, and the location was already poorly constrained – the example with the 144 km squared reduction had an initial horizontal error area of >800 km. This suggests that horizontal and depth error improvement is more sensitive to sP than pP phases.

I additionally note that a reduction in depth error is strongly correlated with the percentage increase in time-defining depth phases, which interplays with magnitude, and not

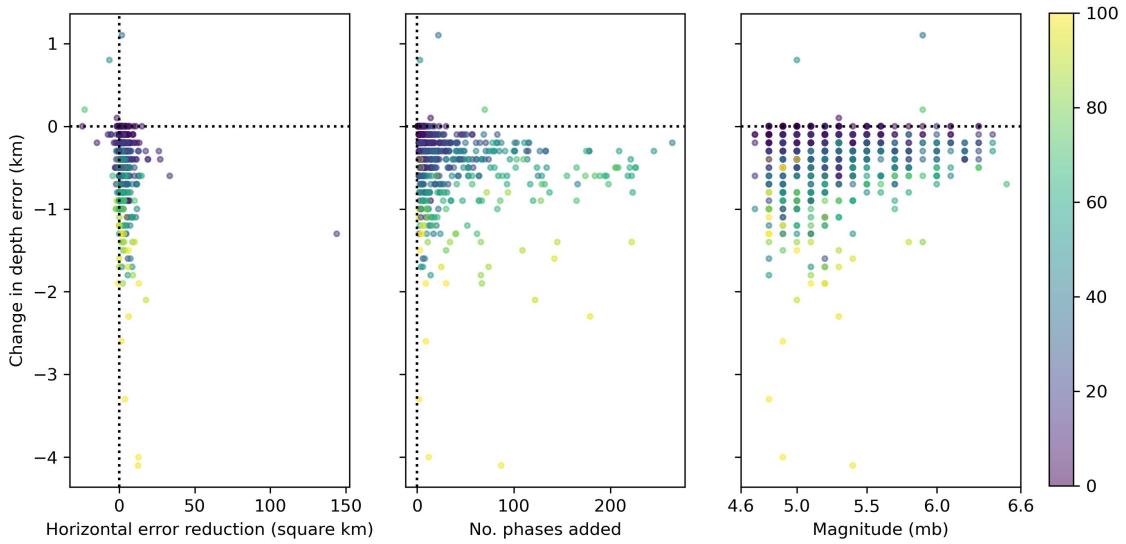

Figure 4.6: Change in depth error between the reported and augmented ISC catalogue results versus horizontal error ellipse reduction (a), the number of time-defining phases added by the *ad-hoc* arrays in the augmented ISC results (b), and magnitude (c). Scatter points are coloured by the percentage increase in time-defining depth phases. Events which did not have new time-defining phases from the augmented ISC input are not plotted.

necessarily related to an absolute number of additional phases (Figure 4.6b and c). Figure 4.6c indicates that lower magnitude earthquakes are more likely to experience a greater percentage increase in time-defining depth phases, if phases are able to be picked, which translates to a greater reduction in depth error. Therefore augmenting the catalogue with *ad-hoc* array derived phases has a greater impact upon the 3D relocations of events with low numbers of time-defining depth phases, which tend to be low magnitude events.

4.2.1.3 Sensitivity to sP

The outlier on Figure 4.6a showing a 144 km square horizontal error ellipse improvement indicated the importance of *sP* when reducing error, and implied a greater sensitivity towards *sP* additions than *pP* during event relocation.

To test this hypothesis I plot probability density functions for depth error from the augmented ISC results, and change in depth error between the augmented ISC and the reported ISC results in two ways. For both, the data are separated into two categories. (1) When the *ad-hoc* array depth phases add more time-defining *pP* than *sP* arrivals to an event, and vice versa (Figure 4.7a and b). (2) When *ad-hoc* arrays add a larger proportion of *pP* arrivals relative to the number of time-defining *pP* phases already in the event catalogue, than the equivalent proportion of *sP* phases, and vice versa (Figure 4.7c and d). I see from these plots that a greater absolute number and proportion of *sP* phase

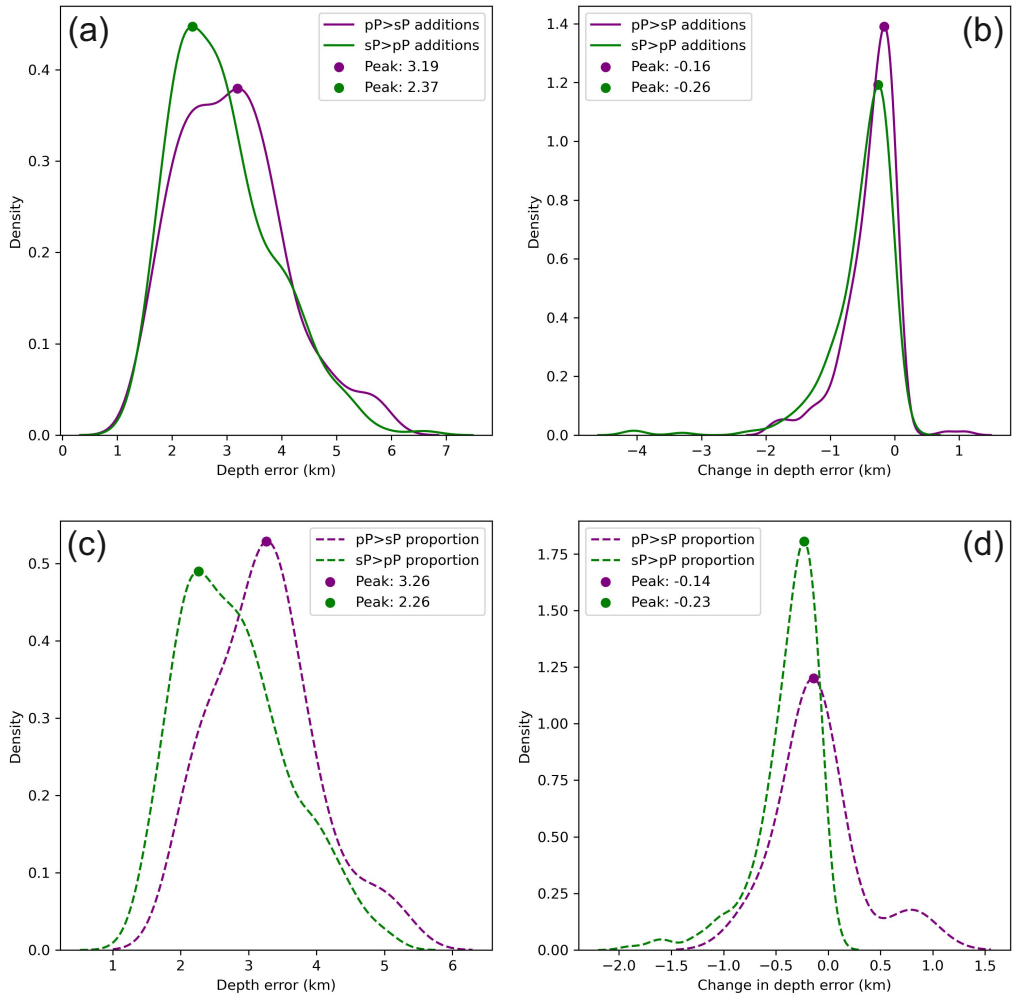

Figure 4.7: Probability density functions for the depth errors in the augmented ISC catalogue results, and change in depth error when compared to the reported ISC results. When *ad-hoc* arrays add more time-defining *pP* than *sP* phases to an event, or vice versa (a and b), and when *ad-hoc* arrays add a larger proportion of *pP* (relative to the number of time-defining *pP* phases) than *sP* (relative to the number of time-defining *sP* phases) phases to the event catalogue, and vice versa (c and d). Events which did not have new time-defining phases from the augmented ISC input are not plotted.

additions to *pP* lowers the depth error for events by a mode of 0.82 and 1.00 km respectively. A larger reduction in depth error between the reported and augmented results is also observed when a greater absolute number and proportion of *sP* to *pP* time-defining phases are added to the ISC augmented catalogue, although the improvement is slight at modes of -0.10 and -0.09 km respectively. It is clear that a reduction in depth error benefits from a larger number of *sP* phases, likely due to the low numbers in the reported ISC catalogue compared to the number of reported *pP* phases. Therefore my ability to boost the signal-to-noise ratio of *sP* using array processing, to supplement the reported ISC phase catalogue for a given event could help to improve the event locations in global catalogues to greater extent than *pP*.

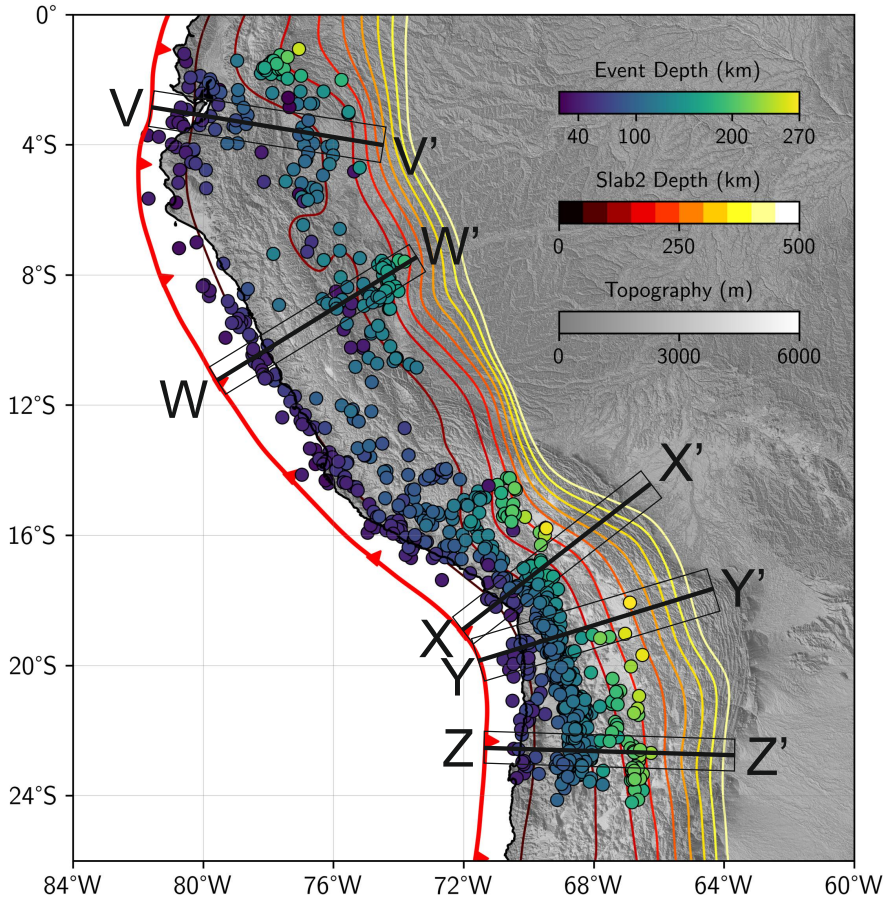

Figure 4.8: Map of Peru and northern Chile showing the 3D relocations of the earthquake hypocentres found using the augmented ISC phase catalogue. Events are coloured by depth, and example cross sections are marked which can be seen in Figures 4.9 and 4.10. Contours indicate the depth of the Slab2 model (Hayes et al., 2018).

4.2.2 Regional application

The previous sections have shown that a proportional increase in *P*, *pP* and *sP* phases – determined through *ad-hoc* arrays – decreases the number of fixed depth events, decreases depth error and that *sP* phase additions influence the reduction in depth error to a greater extent than *pP*. Whilst the reductions are typically small (mean reduction of 0.41 km), slight improvements in depth resolution across an event catalogue can allow updates in the interpretation of a seismogenic region.

I demonstrate the relocated augmented ISC event catalogue, in comparison to the relocated reported ISC and Blackwell et al. (2024)'s catalogues (from Chapter 2) for Peru and northern Chile (Figures 4.8, 4.9 and 4.10). It is apparent that the relocated catalogue from Blackwell et al. (2024)/Chapter 2 has been improved, in terms of depth location, as a result of using ISCloc for the depth determination. Independently determined event depths from the augmented ISC catalogue are indicating more discrete, linear features,

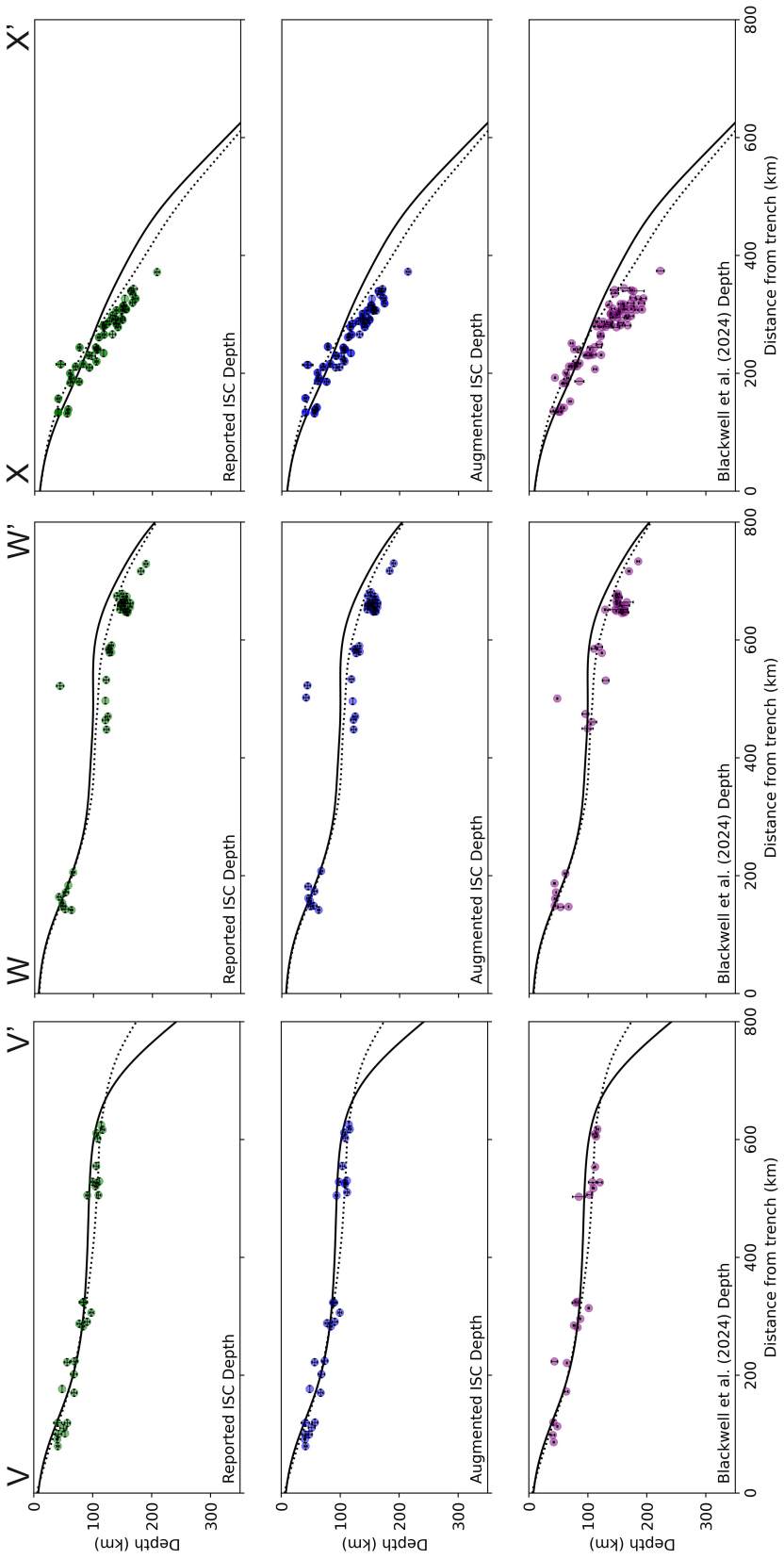

Figure 4.9: Cross sections of the Peruvian subducting slab with the earthquake hypocentres found using three different catalogues. Figure 4.8 shows the location of the sections on a map of Peru and northern Chile. Slab 1.0 (Hayes et al., 2012) and Slab2 models (Hayes et al., 2018) shown in dashed and solid black, respectively. Depth and horizontal error represented as error bars per event, although these are often within the size of the symbol.

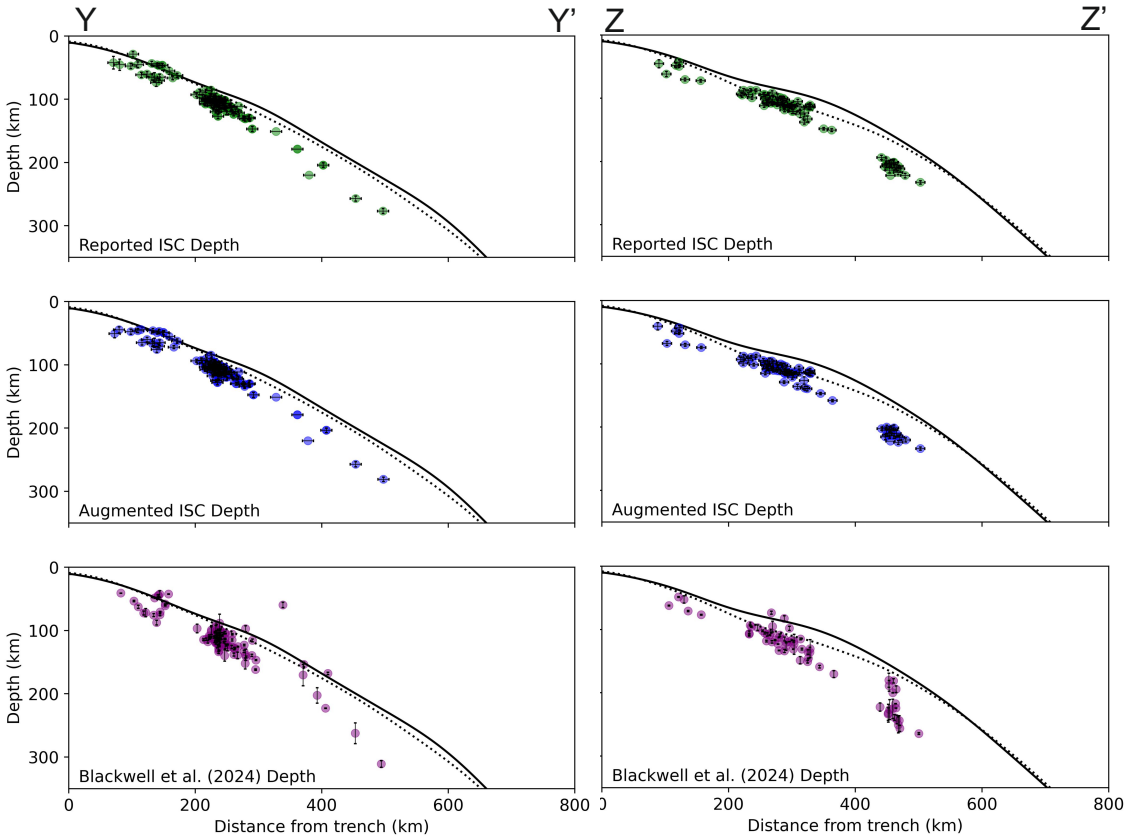

Figure 4.10: Cross sections of the Chilean subducting slab with the earthquake hypocentres found using three different catalogues. Figure 4.8 shows the location of the sections on a map of Peru and northern Chile. Slab 1.0 (Hayes et al., 2012) and Slab2 models (Hayes et al., 2018) shown in dashed and solid black, respectively. Sippl et al. (2018) northern Chilean microseismicity catalogue shown in the background as grey circles. Depth and horizontal error represented as error bars per event, these are often within the size of the symbol.

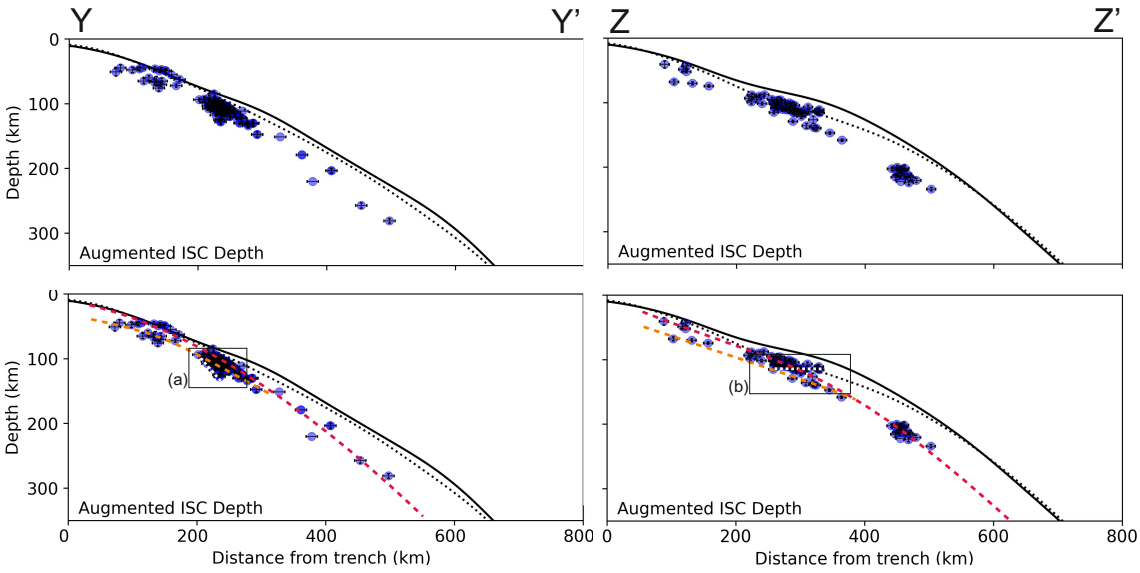

Figure 4.11: Interpreted cross sections of the Chilean subducting slab with the earthquake hypocentres found using the augmented ISC catalogue. Figure 4.8 shows the location of the sections on a map of Peru and northern Chile. Event depths shown in blue with error bars (often within the size of the marker), projected seismogenic slab geometry in dashed red, with orange dashed lines indicating an interpreted lower seismogenic plane. Bifurcating planes are interpreted in dashed white. Slab 1.0 (Hayes et al., 2012) and Slab2 models (Hayes et al., 2018) shown in dashed and solid black, respectively.

with a narrower seismogenic thickness than seen in the Blackwell et al. (2024) catalogue – for sections X-X' and Z-Z' on Figures 4.9 and 4.10, seismogenic thickness reduces by approximately a third. The improvement is likely to stem from the addition of bounce point and station elevation corrections built into the workflow of ISCloc, and inclusion of other (local to teleseismic) constraining phase arrivals. Bounce points refer to the coordinate location where the depth phases reflect off the free surface. If the free surface has significantly different topography, relative to the datum, which is not accounted for in earthquake relocation, then the depths of the events will appear too deep or shallow. Cross section V-V' in Figure 4.9 demonstrates the importance of a bounce point correction for determining event depth, as the Blackwell et al. (2024) data shows two events which are shallower than Slab2 at approximately 230 km from the trench, which are deepened by 10-20 km in both alternative ISCloc based catalogues. Cross section Z-Z' also shows a reduction in vertical smear from the Blackwell et al. (2024) catalogue at approximately 470 km away from the trench, to a tighter cluster of events centred upon the deeper location depths, indicating event deepening due to bounce point recognition.

There are a number of features which are of interest observed on the selected cross sections. These include the continued observation of a flat slab in central Peru (Portner & Hayes, 2018), the Pucallpa nest (Wagner & Okal, 2019; Sandiford et al., 2020) on section W-W'

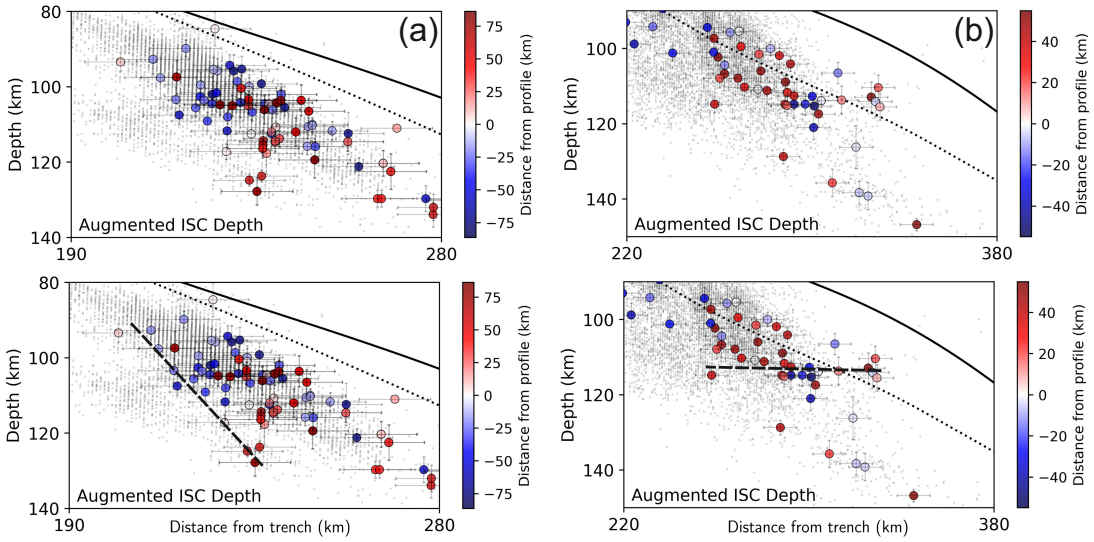

Figure 4.12: Zoomed-in Y-Y' and Z-Z' cross sections of the Chilean subducting slab, corresponding to the boxes shown in Figure 4.11. The earthquake hypocentres are found using the augmented ISC catalogue, with event hypocentres coloured by distance from the cross section plane and error bars. The both rows show the cross sections, with the bottom row showing the interpreted linear planes in dashed black. Slab 1.0 (Hayes et al., 2012) and Slab2 models (Hayes et al., 2018) shown in dotted and solid black, respectively.

at approximately 650 km from the trench, and the transition in slab dip to 20-30° towards northern Chile (Ye et al., 2020) which can all be seen more clearly with the augmented ISC catalogue on Figure 4.9. Other features are also observable on the Chilean cross sections, and highlighted in Figure 4.11, such as bifurcation of the hypocentres along a plane – for section Y-Y' the bifurcation occurs at approximately 250 km away from the trench and underneath the main seismogenic slab, whilst section Z-Z' suggests a bifurcation at approximately 300 km away from the trench and above the main seismogenic slab (Figure 4.11). These bifurcations could either be an artifact of creating a cross section, such as out-of-plane changes in slab dip, or a planar seismogenic hosting surface – such as splay faults or fluid migration associated with the thrusting of the subducting slab, similar to those seen by Nippress and Rietbrock (2007) and Fuenzalida et al. (2013) at shallower depths.

The planar hypocentral bifurcations on both cross sections fit poorly to the seismogenic slab geometry interpreted, and indicate through-going slab faults. However, Figures 4.12 show zoom-in boxes (a) and (b) from Figure 4.11 with and without the bifurcations interpreted, and with event hypocentres coloured by distance from the profile plane. From this perspective, there are few events anchoring the linear interpretations, they are within error of the double seismogenic zone planes, and their distances from the profile plane

imply that a consistent plane with a dimension of ∼160 km and ∼100 km is needed to satisfy the perceived trend. I also note that the seismicity defining each suggested plane has been active from at least 1999 to 2022. I therefore suggest that these planes, with my augmented catalogue, are not currently defensible.

It is also worth noting the need for a new slab interface to be interpreted for both Peru and northern Chile. For distances greater than 400 km from the trench, both the Slab 1.0 (Hayes et al., 2012) and 2 models (Hayes et al., 2018) indicate that subducting slab thicknesses of up to 50 km exists between the slab interface and the intermediate-depth earthquakes (Figure 4.11). Given that oceanic crust is typically approximated to 7 km, and intra-slab events occur in the slab crust and/or upper mantle (Section 1.3.2.1), a slab thickness of greater than 20 km (K. Wang, 2002) above an intra-slab earthquake implies a poorly fitting slab interface model, which needs deepening inland.

Additionally, the Chilean cross sections, when considered in tandem with local microseismicity data (Sippl et al., 2018), qualitatively support the presence of a double seismic zone, as suggested previously by Florez and Prieto (2019) and Sippl et al. (2018) for the region. I demonstrate how the upper and lower seismogenic planes of a double seismic zone could be fitted to the data in Figure 4.11, and I interpret a broad convergence zone where the planes cannot be resolved, which ranges from approximately 100-160 km in depth. This corroborates the previously hypothesised 80-120 km deep convergence depth for this latitude of the Nazca subducting slab using microseismicity observations (Sippl et al., 2018, 2023), and the 142.1 km ±8 km convergence depth found using relatively relocated global data (Florez & Prieto, 2019) and ak135 (Kennett et al., 1995). Variation between my augmented catalogue depths and the Sippl et al. (2018) catalogue is expected since my dataset is derived using a different velocity model, and therefore will suffer a translational offset in depth relative to the microseismicity catalogue.

To quantitatively investigate the presence of a double seismogenic zone I follow the work of Brudzinski et al. (2007), who use slab normal hypocentre locations above the point of double seismogenic zone convergence to determine if a two-layer, bimodal distribution exists. Figure 4.13 (a) and (b) show sections Y-Y' and Z-Z' with both the augmented catalogue event locations and the local Sippl microseismicity catalogue plotted (Sippl et al., 2018), and their lines of best fit. The lines of best fit are subsequently used to correct the event depths relative to the seismogenic slab geometry, and find the slab normal

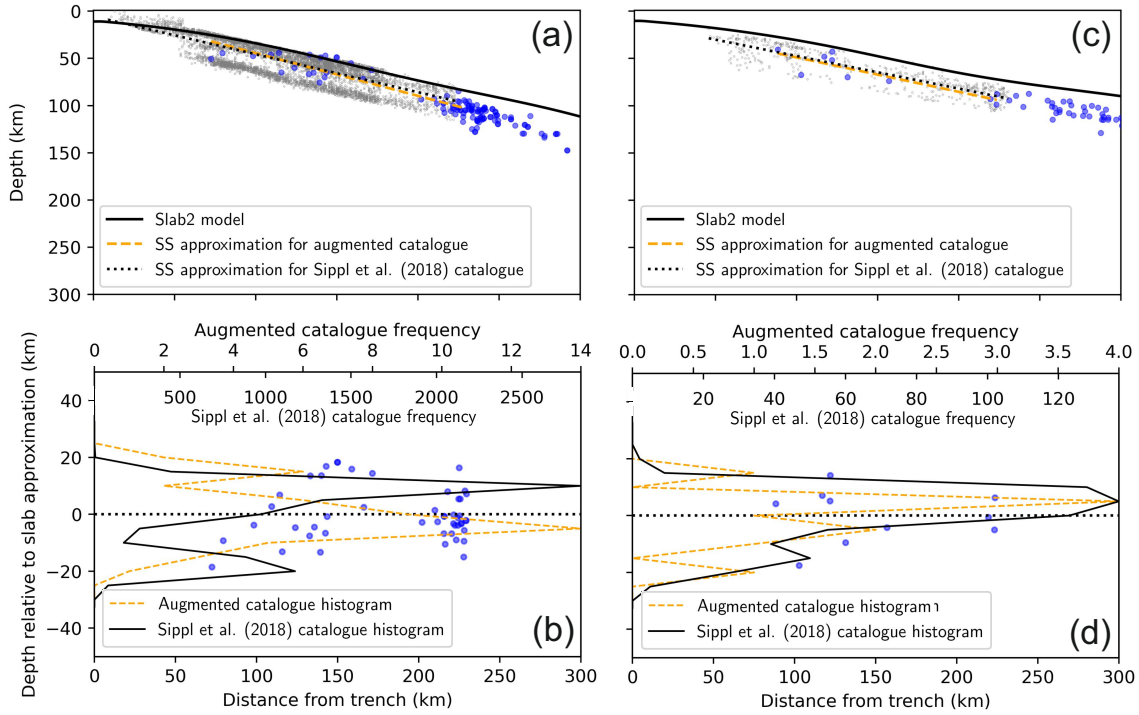

Figure 4.13: Zoomed-in Y-Y' (a) and Z-Z' (c) cross sections of the Chilean subducting slab, showing the augmented ISC catalogue (blue circles) and Sippl et al. (2018) catalogue (small grey circles) seismicity from the trench to 300 km inland, with seismogenic slab (SS) approximations for each catalogue. Slab 1.0 (Hayes et al., 2012) and Slab2 models (Hayes et al., 2018) shown in dotted and solid black, respectively. Histograms showing slab normal distributions of the augmented ISC and Sippl et al. (2018) catalogues for the Y-Y' (b) and Z-Z' (d) cross sections. Figure 4.8 shows the location of the sections on a map of Peru and northern Chile.

distribution of the hypocentres – seen in (b) and (d). The Sippl et al. (2018) catalogue here is limited to events categorised as either lower plane, upper plane or plate interface classes, in order to avoid loss of resolution from events which are not thought to form the double seismogenic zone. I note that these event categories, on the cross sections I inspect, end at approximately 230 km from the trench where plane convergence is expected, I therefore also limit the augmented ISC catalogue and calculate the linear lines of best fit only for events within 230 km of the trench.

The plots demonstrate that there is a clear bimodal distribution in both cross sections from the Sippl dataset (Sippl et al., 2018), with a 20-30 km seismogenic gap apparent, although the lower plane seismicity is under developed relative to the upper plane for both. The augmented ISC catalogue shows a weaker bimodal distribution in Figure 4.13b, with a more strongly defined upper plane and an approximately 20 km seismogenic gap. Whereas section Z-Z' on Figure 4.13d lacks enough events to define a confident histogram, yet still hints at bimodal distribution when considered in conjunction with the Sippl et al. (2018) catalogue slab normal distributions, despite offsets in both sections due to the use of different velocity models.

Whilst individually the augmented catalogue results are not conclusive enough to determine a double seismogenic zone, I believe that their results corroborate the presence of two planes seen in the Sippl et al. (2018) microseismicity data. My findings reflect the resolution of the global catalogue determined histograms in Brudzinski et al. (2007), where maximum frequencies of 15 or 16 earthquakes define the north east Japanese double seismic zone with an approximately 30 km aseismic gap. The confidence in the global catalogue observed double seismic zones is increased when compared to the histogram resulting from the local catalogue (with maximum frequencies of 182 events), similarly to my comparison to the Sippl et al. (2018) catalogue histograms.

The Brudzinski et al. (2007) approach allows us to assess the likely presence of a double seismogenic zone, however to characterise the geometry and plane seismicity to a greater degree of accuracy using global datasets, the approach of Florez and Prieto (2019) could be reproduced. Their use of relative relocation, following the double difference methodology, to define their earthquake catalogue allows the hypocentres to align along a coherent slab geometry. Thus enabling further analysis, such as investigating the controls upon the width of the aseismic gap and depth of double seismic plane convergence. For northern

Chile, Florez and Prieto (2019) determine an 11.1-11.7 ±4 km wide average aseismic gap, these values indicate that my augmented ISC catalogue and histogram driven results are too smeared to resolve a high accuracy measurement and likely mask a smaller aseismic gap. To continue research into the Chilean double seismogenic zone, I believe relative relocation of the event hypocentres is necessary to enhance the prevalent slab geometries and ascertain higher degrees of accuracy.

4.3 Conclusion

The 3D ISCloc event relocations based upon the augmented ISC phase catalogue (ISC reported phases with additional automatically-derived *P*, *pP* and *sP* arrivals) for Peru and northern Chile are shown to decrease depth error, and refine hypocentre location. Significant improvement is especially observed between my previous catalogue relocations (Blackwell et al., 2024) in Chapter 2 and those found using ISCloc, due to the acknowledgement of bounce point and elevation corrections, and solving for hypocentral location in 3D. It is clear that automatically determined phase arrivals, from array processed teleseismic data, are a useful and incipient resource to the wider community to improve earthquake locations and enhance interpretation. The greatest limitation of the presented approach is the conversion of the *ad-hoc* array determined amplitude picks to absolute phase onset times, I suggest an alternative method for this in Chapter 5 which could be used in future applications.

Chapter 5

Using PhaseNet to pick absolute travel times on teleseismic vespagram data

5.1 Motivation

Whilst researching the integration of automatically picked P, pP and sP arrivals into global phase catalogues, to assess their impact upon earthquake relocation (see Chapter 4), it became apparent that a mechanism to determine P onsets on my beamed teleseismic data would prove useful. This is because my picks are located at the peak amplitudes of arrivals, rather than at the onsets, which reduces the ability to compare my results with those found by the wider community. Consequently, to pool my arrival times with those reported by global agencies, a method to convert my amplitude picks to onset times is required.

Previously (as seen in Section 4.1.2) I have solved this by making use of reported P arrivals to the International Seismological Centre (ISC), however there are not always reported P arrivals within the aperture of a given *ad-hoc* array to rely upon for the conversion. Therefore, I lose a proportion ($\sim$25%) of automatically derived P, pP and sP picks which cannot be corrected to onset times. If I had the ability to quickly and efficiently determine P onsets for each *ad-hoc* array, my reliance upon phases reported by global agencies is removed. The obvious answer is to apply a machine learning algorithm, trained to pick arrival onsets from seismic data, on my beams. If I extend this idea further to include the

picking of P arrival onsets on vespagram data, I could calculate statistics concerning the machine learning picks with respect to slowness. External agencies may also find purpose for determining arrival onsets on vespagrams, in locations where array processing enables supplementary arrivals to be identified and reported to the ISC. In this chapter, I aim to test if I can apply machine learning pickers to my vespagrams and generate pick statistics, to discover if this is a reasonable and feasible line of research for the future.

Whilst a number of machine learning algorithms exist to pick P and S arrival onsets (Woollam et al., 2022; Mousavi & Beroza, 2023), few are trained upon teleseismic data (Münchmeyer et al., 2024). At this point, I am not too concerned with the positives and negatives of each algorithm, since I am simply attempting to test if a machine learning tool can pick P onsets on vespagrams. Therefore I select PhaseNet (W. Zhu & Beroza, 2019) as my candidate machine learning picker, knowing that the picker can be exchanged in the future if the approach is promising.

PhaseNet is a deep-neural-network-based P and S wave arrival picker which uses 3-component seismic data to ascertain probability distributions, and hence picks, for the arrivals. The model is trained, validated and tested on 779,514 locally recorded waveforms drawn from Northern California Earthquake Data Center (NCEDC) data which encompasses over 30 years of analyst labelled arrivals (W. Zhu & Beroza, 2019). I will use PhaseNet with single component (Z) teleseismic data, from an *ad-hoc* array located 52.33° away from the m_b 6.2, 23rd May 2010 event in southern Peru as an example.

5.2 Methodology

I build onto the workflow already defined in Chapter 2, where *ad-hoc* arrays are generated from teleseismic stations for a given intermediate-depth event, and the data are array processed. I join the workflow after the data for an *ad-hoc* array are quality checked, and extract the final set of *ad-hoc* array traces – this is where my PhaseNet methodology begins.

For each trace I trim 17 seconds of data around the modelled P arrival time (found using ray tracing (Crotwell et al., 1999) and the ak135 1D velocity model (Kennett et al., 1995)). As previously discussed in Chapter 2, a 17 second window ensures that the real P arrival is contained within the window, since the precision of the modelled arrival suffers from approximations. Similarly to Chapter 2, I use the windowed P traces to linearly beamform

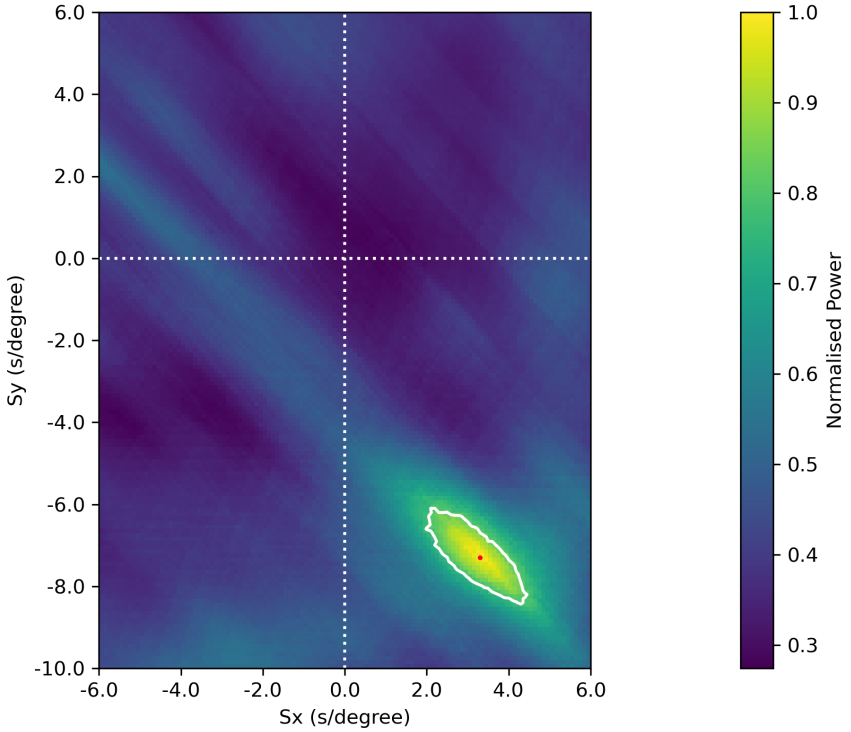

Figure 5.1: Normalised power for linear beamforms calculated using a horizontal slowness search grid. Red circle indicates the slowness parameters which generate the beam with the largest normalised power. White solid line identifies the 0.8 normalised power contour.

using a grid search through slowness and backazimuth space. Rather than directly using backazimuth as a search parameter, I instead use horizontal slowness to ensure a regular search grid, with the y- and x-component test ranges set to -10 to 6, and -6 to 6 seconds per degree, respectively. The test parameter space is not dynamic to the event, and is currently set to ranges suitable for my test event. For each beam calculated by the grid search, the normalised power of the beam is projected onto the relevant grid space in Figure 5.1.

Rather than apply PhaseNet (W. Zhu & Beroza, 2019) to every single beam calculated, I extract the resultant beams which exist within the 0.8 normalised power contour, resample them to 100 Hz (default sample rate defined by PhaseNet) and save them out in miniSEED format ready for picking. The resampling of the data is not ideal, given the traces have formerly been down-sampled to 10 Hz (Section 2.2.2), however initial tests with 10 Hz beams provided poorly constrained PhaseNet P picks – positive probability distributions ranging over 7 seconds, and defined picks over 0.5 seconds later than the 100 Hz results. The simplicity of the final beams encourages me to believe that in this case, the sampling

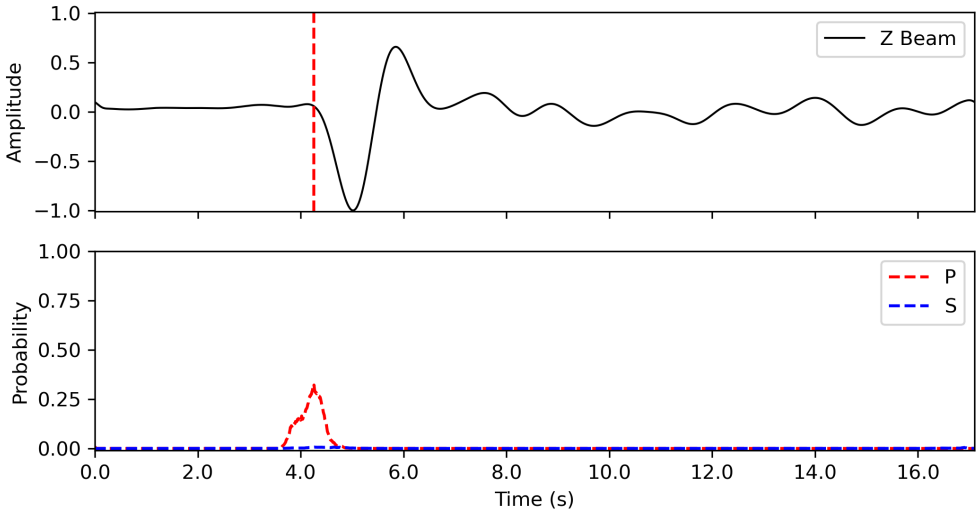

Figure 5.2: Beam with the largest normalised power (top) and probability distributions (bottom) for P and S arrivals as output by PhaseNet (W. Zhu & Beroza, 2019). Final P pick is shown by the vertical red dashed line on the top panel, at a relative time of 4.26 seconds.

rate changes will have minimal effect on (anti-)aliasing, whilst allowing sound PhaseNet outputs.

I apply PhaseNet (model 190703-214543, previously trained on NCEDC data) (W. Zhu & Beroza, 2019) to the saved beams, which outputs probability distributions for P and S arrivals (and noise). The peaks of the probability distributions are used to define an onset time for the relevant wave arrival. Figure 5.2 shows the outputs of PhaseNet for the largest power beam calculated (red circle on Figure 5.1). The P wave distribution indicates an uncertainty (approximately 1 second) associated with the pick due to the slight uplift in amplitude prior to the initial trough – this likely represents a spread which multiple analysts would also find when determining the onset. As hoped, the S wave probability distribution demonstrates little indication of an arrival within the 17 second trace.

There are a number of beams which did not receive a PhaseNet pick for P (Figure 5.3), this occurs when the probability distribution for P does not provide a peak above 0.3 – a default threshold set by the PhaseNet developers (W. Zhu & Beroza, 2019) – due to greater uncertainty associated with the precise onset time. The threshold can be adjusted, however it would require testing to select a new threshold (if a new threshold is needed).

After PhaseNet picked the P arrivals for the beams with normalised power within the 0.8 contour (Figure 5.1), I was able to calculate some basic statistics – maximum pick time,

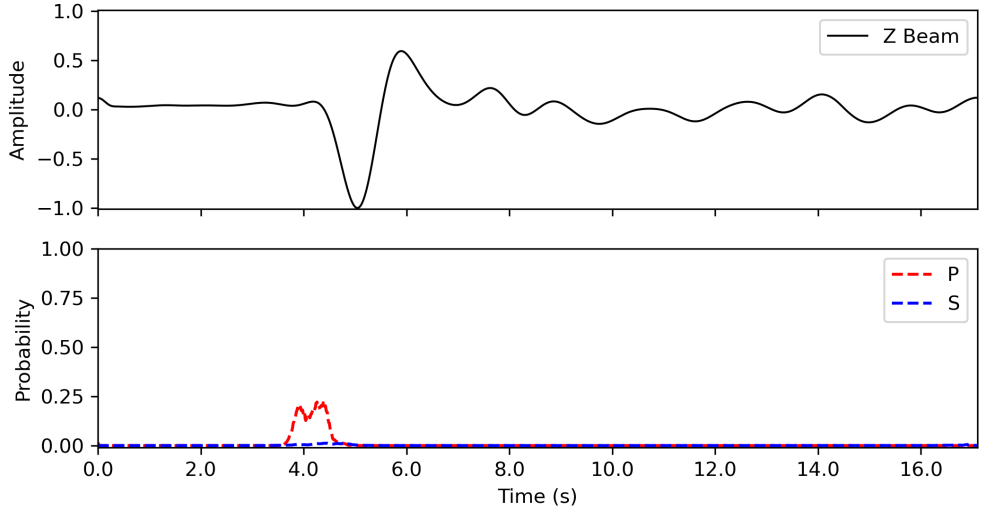

Figure 5.3: Beam (top) and probability distributions (bottom) for P and S arrivals as output by PhaseNet (W. Zhu & Beroza, 2019). No P pick is defined due to the peak of the probability distribution curve displaying at <0.3.

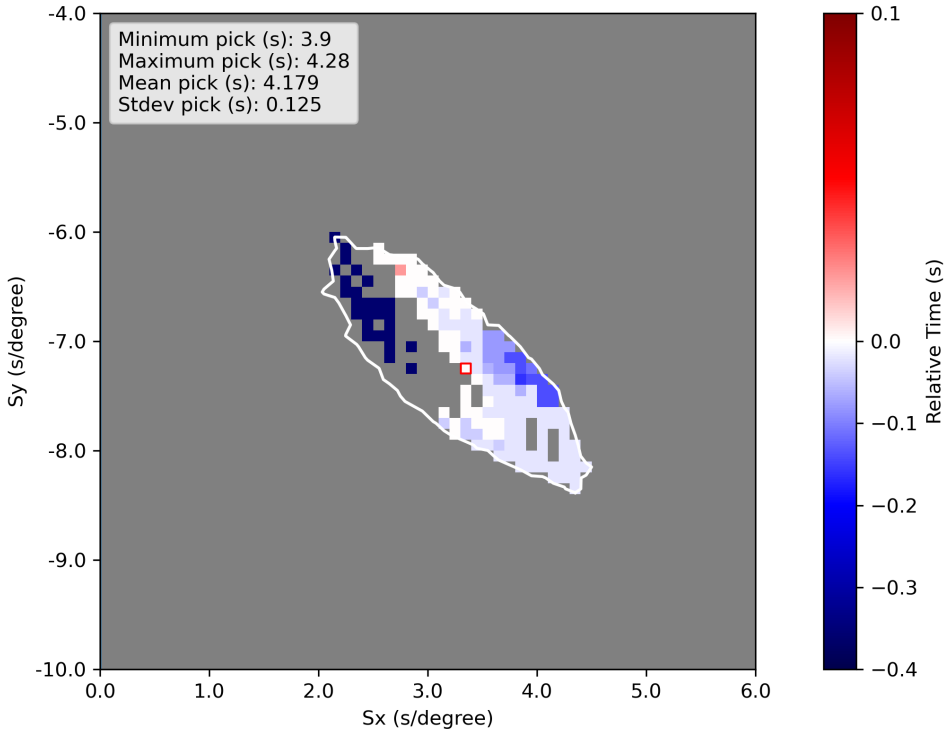

Figure 5.4: PhaseNet P picks (W. Zhu & Beroza, 2019), in seconds relative to the pick found from the beam with the largest power, plotted according to the slownesses for which the beams were constructed. The red square indicates the location of the beam with the largest power. Grey represents untested beams, either because their maximum normalized power is $\leq$0.8 or a PhaseNet pick was not determined (in cases where they fall within the white 0.8 relative power contour line).

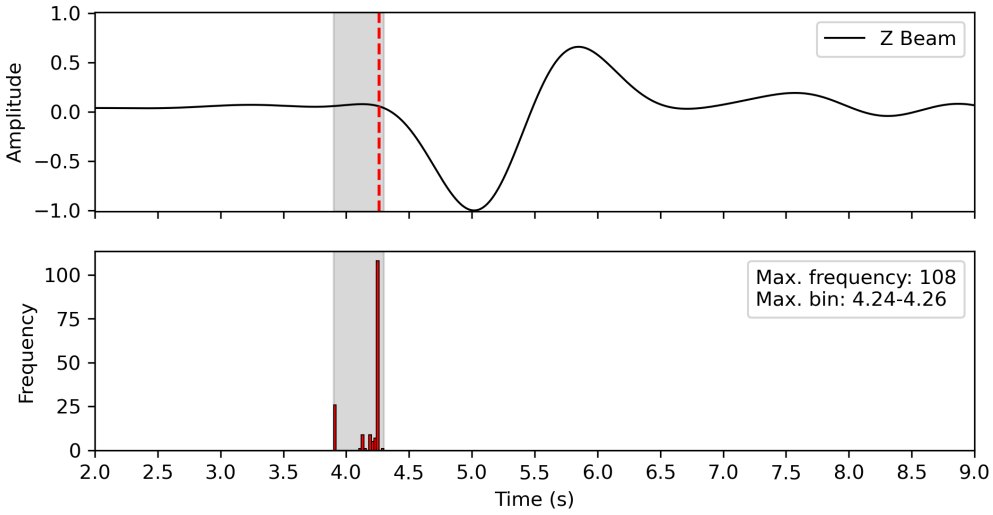

Figure 5.5: Beam with the largest normalised power (top) and histogram of pick times (bottom) for P and S arrivals as output by PhaseNet (W. Zhu & Beroza, 2019) all tested beams. Final P pick is shown by the vertical red dashed line on the top panel, at a relative time of 4.26 seconds. The histogram is constructed with 0.02 second bins.

minimum pick time, mean pick time and the standard deviation – and plot the relative pick time per beam onto the horizontal slowness grid (Figure 5.4). The beams without a pick time on Figure 5.4 had probability distributions with peaks lower than 0.3, as discussed with Figure 5.3. For my test event, the range for the P picks is 0.38 seconds, with a mean of 4.179 seconds and standard deviation of 0.125 seconds. Since PhaseNet relies upon probability distributions to identify picks, there is scope to incorporate the information provided by the distributions into an uncertainty measurement for a given pick, beyond its use as a quality threshold. To illustrate the range and frequency of the final P picks, Figure 5.5 shows a histogram of the pick times across all of the test beams in relation to the beam with the largest normalised power. It is evident from the pick distribution that the small amplitude rise before the main trough of the P arrival has bi-modally split the picks, however, overall all of the machine learning picks are good. This is particularly surprising given that PhaseNet is not designed for 0.1-1.0 Hz bandpassed, teleseismic data, further processed into high signal-to-noise beams.

5.3 Conclusion and future work

Using PhaseNet and an example teleseismic event in southern Peru, I have shown that multiple P wave beams with $\geq$0.8 maximum normalised power, calculated with a horizontal slowness search grid, can be picked by a machine learning algorithm and used to

generate pick statistics.

To expand the functionality of this approach, a number of further steps are required. I need to test if other earthquake events with variable source parameters (depth, magnitude, distance) also produce positive picks using a machine learning algorithm, since consistency across a broad range of events and resultant seismic data is important to establish a new application. Other machine learning seismic pickers should also be applied and the results compared to determine which algorithm works the best for this approach – this could include assembling a labelled training set of teleseismic data, to create a more relevant machine learning picking model for my purposes. Finally, given that the output of the machine learning pickers includes a probability distribution for each arrival, there is the potential to develop more meaningful statistical analysis of the picks which converts into a useful pick uncertainty.

In terms of future usage, I could apply this approach to adapt the results from the Chapter 2 amplitude pick based methodology into a set of community-comparable onset times. External agencies may also be interested in this approach, since the ability to automatically pick P onsets on vespagrams opens up an opportunity to use array processing to determine picks which are typically incoherent, and assign informed uncertainty estimates to the picks.

For now it is not critical to pursue this research further, since I have previously found an amplitude pick to onset pick conversion (see Chapter 4) which has a high enough success rate to allow me to compare my results to those reported by global agencies, and the required steps outlined above to fully appraise this methodology will take significantly more time than I have currently available.

Chapter 6

Crustal thickness determination using pmP phases identified from adaptive teleseismic array data

6.1 Introduction

The boundary between the Earth's crust and mantle is defined by the Mohorovičić discontinuity (see Section 1.3.3) – commonly referred to as the 'Moho' (Mohorovičić, 1910). This boundary can be identified seismically by observing a diagnostic change in P and S wave velocities, for P the velocities change from 6.0-6.8 km/s in the crust to approximately 8 km/s in the mantle (Prodehl et al., 2013). The depth at which the Moho exists is a crucial factor for many areas of Earth Sciences, such as seismic tomography, plate boundary/geodynamic reconstructions, isostatic compensation studies, geothermal and mineral physics predictions, and resource exploration. It is therefore important to accurately determine the depth of the Moho, and the roughness of the boundary, in order to better inform the research which relies upon the Moho as a constraint.

During the early 1900s, controlled-source seismology emerged as a technique to study intra-crustal layers and the Moho. This became the standard approach to investigate the uppermost layers of the Earth post World War II (e.g. Hodgson, 1946; Byerly, 1946; Willmore et al., 1952). However from the late 1970s onwards, the use of passive seismological techniques to study the Moho emerged with the use of receiver functions calculated from teleseismic (30°-90°) earthquake signals (Langston, 1979). From the 1990s the develop-

ment of mobile, high-quality broadband seismic instrumentation in large numbers assisted the relevancy of passive seismology, as temporary deployments in difficult environments and locations aided global seismometer coverage (Prodehl et al., 2013). The rise in passive seismology also meant that countries with strict regulations concerning active explosions now had an alternative method to study their crustal structure.

Typically receiver functions are used to identify P to SV conversions occurring at key velocity discontinuities in the Earth, most commonly the Moho. To create a receiver function, a seismogram with teleseismic arrivals has its radial component deconvolved by the vertical component, as an approximation of the source-time function, and usually stacked with other move-out corrected receiver functions, to identify P to SV converted phases (Farra & Vinnik, 2000). The deconvolution acts to remove the signal contribution of the source and near-source structure, to isolate the near-to-receiver converted phases (Langston, 1979). P to SV receiver functions rely on the idea that any S wave associated arrivals occurring prior to the direct S wave and alongside P coda arrivals must be converted energy (Wilson et al., 2006). The times of the P to SV phase arrivals can thus be used to determine the depth of the P to SV converting Moho (Yuan et al., 2002), with amplitudes carrying information on the discontinuity structure. It is also similarly possible to use S to P converted phases arriving as precursors to S, which can be used in cases where P to SV arrivals are difficult to determine (e.g. Farra & Vinnik, 2000).

Receiver functions have opened the door to study regions of the Earth with local seismometers who cannot use controlled source experiments, and have seismically active margins within teleseismic distances, to investigate the depth of the Moho locally. For regions without a local network of broadband seismometers, another method to determine the depth of the Moho using passive teleseimic signals was developed by Zhang and Lay (1993) and Zandt et al. (1994). The approach of Zandt et al. (1994) instead leverages the high density of broadband seismometers at teleseismic distances away from the study region to identify the *pmP* phase. The *pmP* phase is generated from a P wave reflecting off the underside of the Earth's crust (i.e. at the Moho) before travelling to a seismic station to be recorded. The caveat is that the study region will need to be seismically active sub-Moho for the *pmP* phase to be seen on teleseismic seismograms. Furthermore, the *pmP* phase will not be observable on seismograms for crustal events or for seismometers closer to the source than 30° epicentral distance due to the lack of separation between direct P arrival, *pmP*, and the *pP* depth phase (near-source, free surface reflection of P). The detection of

the *pmP* phase is useful to calculate the depth of the Moho, and thus crustal thickness, when considered in parallel with the *pP* depth phase arrival time, a process applied by McGlashan et al. (2008) to data sampling the Central Andes.

McGlashan et al. (2008) use 4 arrays in the USA to stack seismic data associated with events with magnitudes greater than Mw 5.8, and hypocentres deeper than 100 km. Array processing boosts the signal-to-noise ratios of the low amplitude *pmP* and *pP* phases to aid detection. The differential time between the two phases is subsequently converted to a Moho depth (associated to the reflection point between the source and array location), using a *P* wave velocity (*Vp*) of 6.2 km/s. The *Vp* was determined from a *Pg* distance-time plot for stations between 28°S-33°S.

In this chapter I extend the method outlined by McGlashan et al. (2008) by creating *ad-hoc* arrays from all available teleseismic stations per event, therefore utilising the increased number of broadband instruments deployed globally, to create stacks to identify *P*, *pmP* and *pP* arrivals and determine their differential times automatically. The method I apply directly follows on from the approach described in Chapter 2, where regional catalogues of intermediate-depth earthquake depths are created automatically using teleseismic *ad-hoc* arrays to detect the *P*, *pP* and *sP* phases.

6.1.1 Relocating intermediate-depth earthquakes using depth phases

Previously I have worked on a methodology in Chapter 2 which leverages the increasing density of teleseismic data density, to automatically relocate intermediate-depth events (Blackwell et al., 2024). The approach dynamically organises the available teleseismic stations for a given event into *ad-hoc* arrays, to optimise the available data, using a combination of the DBSCAN (Density-Based Spatial Clustering of Applications with Noise) and the Ball-Tree nearest neighbour algorithms (Pedregosa et al., 2011). Array processing techniques are subsequently applied to each array to enhance the detection and identification of the *P*, *pP* and *sP* phases, particularly the low signal-to-noise ratio depth phases. The calculated *sP*-*P* and *pP*-*P* differential times are converted to depth with a 1D velocity model and a final earthquake depth is determined. The approach can be used to quickly create a high-resolution, regional intermediate-depth earthquake catalogue using depth phases (Blackwell et al., 2024).

For this chapter, I build upon the results of the intermediate-depth earthquake relocation

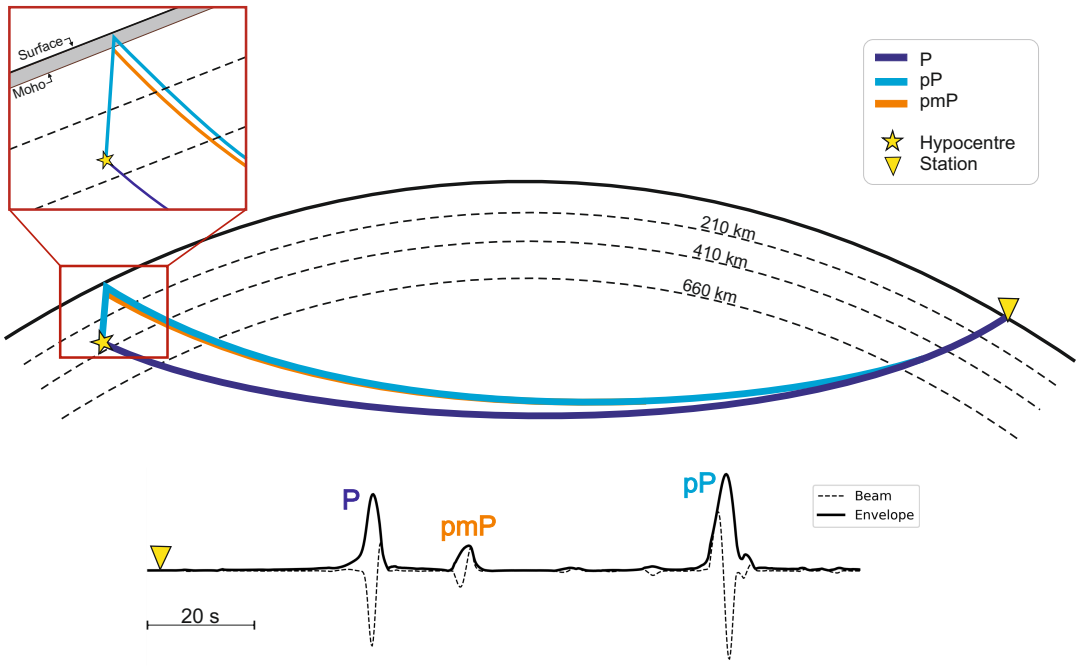

Figure 6.1: 2D schematic (top) of the *P*, *pmP* and *pP* ray paths from an earthquake hypocentre (star) to a teleseismic receiver (triangle), and an example vertical component (bottom), phase-weighted velocity array beam from a 2.5° aperture array located at 86.4° epicentral distance (array centre is (41.76°N, 4.99°W)) from the 8th October 2012, m_b 5.9 event located at (21.80°S, 68.87°W).

methodology found in Chapter 2, for Peru and northern Chile. I take the *ad-hoc* arrays found per event, their resultant phase-weighted vespagrams (Schimmel & Paulssen, 1997) and optimum beams (phase-weighted beams calculated using the best-fitting slowness and backazimuth for each *ad-hoc* array) to look for an additional low amplitude phase expected to arrive between *P* and *pP* – *pmP*.

The *pmP* arrival represents a *P* wave which radiated upwards from the hypocentre, reflected off the base of the crust at the Moho, and is received at a teleseismic station. Whilst a *pP* arrival follows a similar ray path, it instead reflects off the free surface before travelling to a teleseismic receiver. The delay time between the *pP* and *pmP* arrivals therefore relates to the thickness of the crust at approximately the bounce points of the *pmP* and *pP* waves (Figure 6.1). A summary workflow demonstrating how I detect and identify the *pmP* arrivals from my *ad-hoc* array data, and convert the differential times into a crustal thickness can be seen in Figure 6.2.

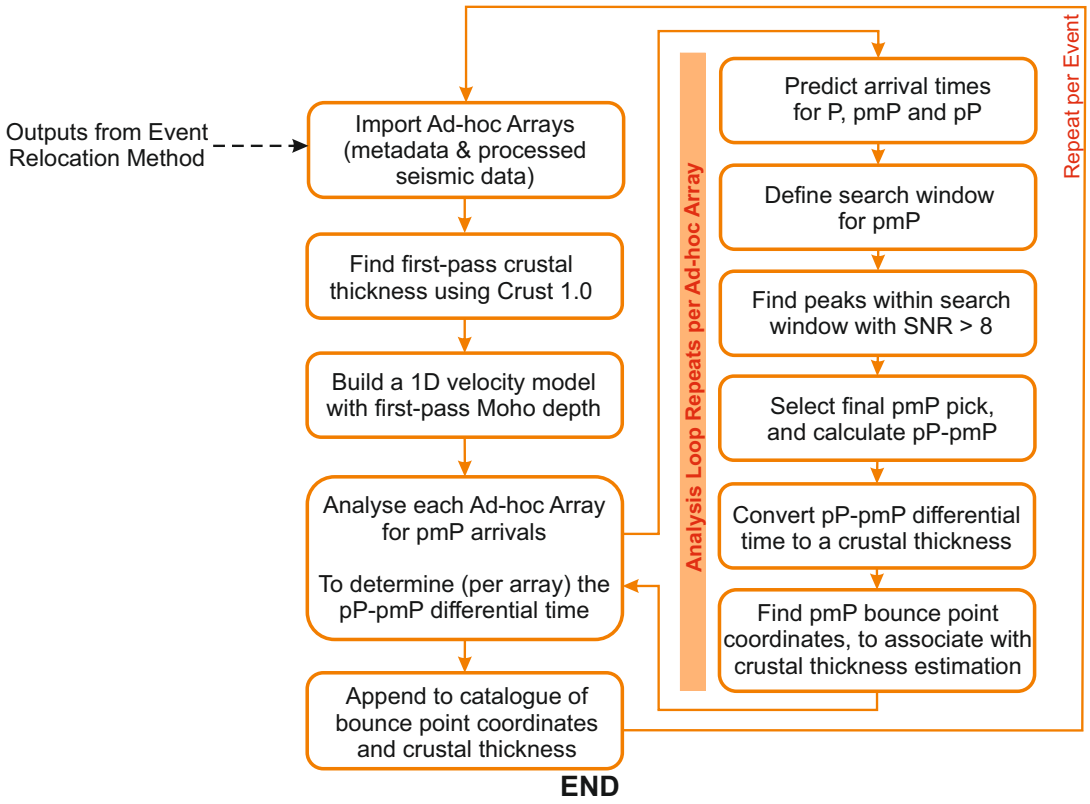

Figure 6.2: Workflow summarising the key steps of the method to detect *pmP* arrivals and convert the calculated *pP-pmP* differential time into a crustal thickness. Inputs to the method are obtained following the approach in Chapter 2

.

6.2 *pmP* Methodology

6.2.1 Automatic identification of *pmP*

Beginning with an intermediate-depth earthquake catalogue relocated using the methodology presented in Chapter 2, the formative *ad-hoc* arrays and their beamformed data, I identify events with viable P and pP picks. Events without a pP pick are discarded. For the purposes of demonstrating the methodology, I use the catalogues for Peru and northern Chile presented in Blackwell et al. (2024)/Chapter 2. These catalogues include events between 1995-2023, magnitudes m_b 4.7-6.5 and depths of 40-350 km with sufficient seismic data to be successfully processed (for selection criteria see Section 2.2.1).

For events with pP picks, I identify a first-pass crustal thickness for each earthquake by extracting the Moho depth from the Crust 1.0 model (Laske et al., 2013) at the epicentral coordinates. Ideally I would use the coordinates of the *pmP* phase bounce point for each *ad-hoc* array, however, I choose to use a single initial crustal thickness for an event which can be representative for all azimuthal directions at this stage. I use the first-pass crustal

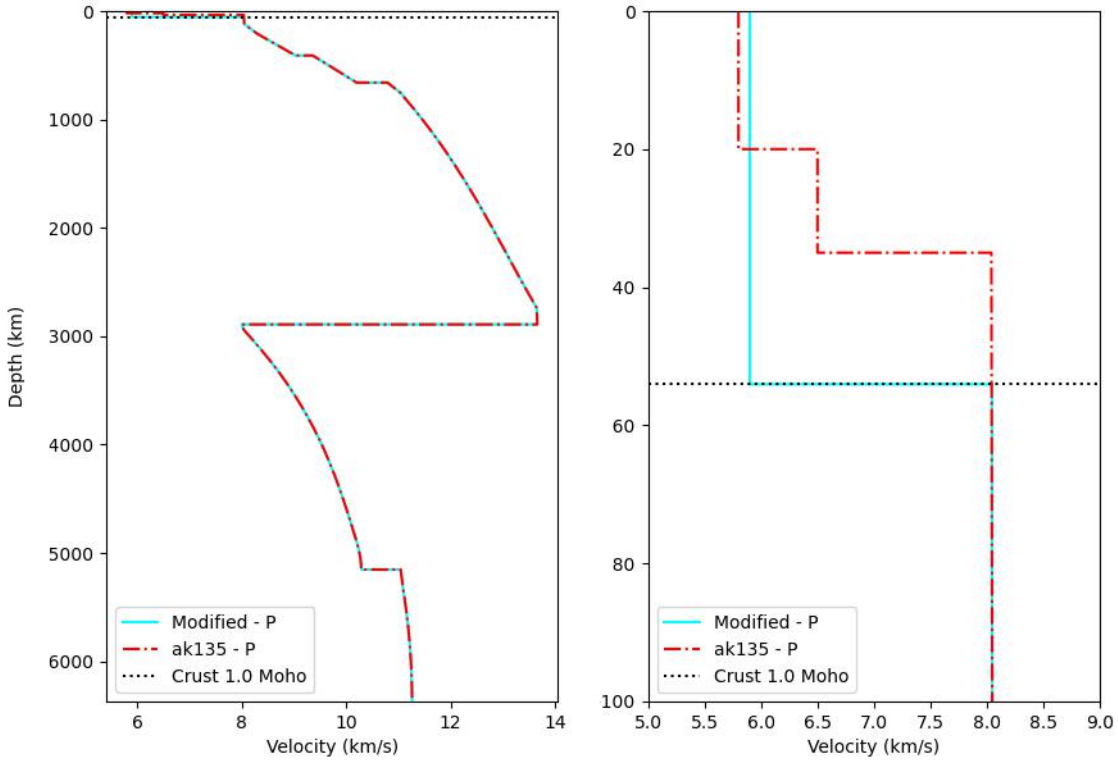

Figure 6.3: Comparison of the ak135 velocity model for P, with the modified version for the m_b 6.1 event which occurred on 15th April 2017 in northern Chile. The entire model and the upper 100 km can be seen on the left and right plots, respectively.

thickness to build a tailored 1D velocity model for each event, this ensures that my velocity model represents my initial Moho depth for where each event samples the Moho. I adjust the ak135 velocity model (Kennett et al., 1995) by replacing the Moho depth with the first-pass crustal thickness for the event, and inserting a uniform velocity layer for the crust above. I use 5.9 km/s as the P wave velocity (Figure 6.3), see Section 6.2.4 for further discussion on the choice of velocity model.

For a given event, I use the modified ak135 1D velocity model (Kennett et al., 1995) and the relocated hypocentral depth determined in Chapter 2 to predict the arrival times for the P, pmP, and pP phases (Crotwell et al., 1999) for each *ad-hoc* array. A time window-based approach is subsequently applied to automatically identify the pmP arrival from each phase-weighted beam for the different *ad-hoc* arrays. To define the centre of the time window, where I expect to see a pmP pick (assuming the Moho depth from Crust 1.0 (Laske et al., 2013)), I subtract the modelled differential time between the pP and pmP arrivals from the previously identified *ad-hoc* array pP arrival time. The difference between the pP and pmP phases should be entirely sensitive to the crustal structure, as opposed to the event depth or near-source velocity structure, and therefore less susceptible

to source location and velocity structure. Applying the modelled differential time to the already identified *pP* pick should limit the impact of the receiver-side structure variations, since the original *pP* phase picking routine depends upon receiver-side wave parameters extracted directly from the *ad-hoc* array data (see Section 2.2.4.1).

Around the centre of the time window, I apply a ±2.5 seconds of padding (see Section 6.2.3 for further information about the window size) which, according to the ak135 travel time tables (Kennett et al., 1995), equates to approximately ±8 km in crustal thickness (see Appendix A.12). If the ±2.5 second window edge becomes too close to the *P* or *pP* wave arrivals, the relevant window bound is limited to the wave arrival time plus or minus half of the *P* arrival duration, respectively. This is in effect to enforce sufficient phase separation between either *P* and *pmP*, or *pmP* and *pP* to enable confident identification. The *pmP* phases may arrive immediately after the *P* arrival if the event is shallow and/or the Moho is deep, and vice versa for *pmP* arrivals arriving shortly before *pP* waves for thin crust. The wavelength of the *P* arrival is calculated using a peak widths function (Virtanen et al., 2020) applied to the phase-weighted beam envelope of the *ad-hoc* array, where the wavelet width is found at a relative amplitude of 0.9. Finally, I search for arrival peaks with a prominence at least 0.05 of the maximum peak of the beam envelope, typically the *P* arrival, and select those which occur within the defined time window.

Using the window-based picking approach, I can expect to find none, one or multiple potential peaks. If zero peaks are found, I cannot return a crustal thickness for the *ad-hoc* array. Otherwise, I test whether the peaks are significant enough in terms of amplitude to be considered a phase arrival, by calculating their signal-to-noise ratios. I calculate the mean amplitude within a 40 second window immediately before the *P* wave arrival to use as the background noise level. The ratio between the amplitude of the envelope for a given pick and the calculated background noise must exceed 8 to be considered as a *pmP* pick candidate.

If only a single pick remains after the signal-to-noise ratio check, that pick is selected as the *pmP* arrival. If a number of picks remain post the signal-to-noise ratio check, the peak with the highest signal-to-noise ratio is selected as the final *pmP* pick. Whilst I recognise that the signal-to-noise ratio is not a good diagnostic feature for choosing a *pmP* depth phase, I expect that other phases which may arrive between the *P* and *pP* arrivals are likely to exhibit smaller amplitudes since they originate from lower impedance contrasts,

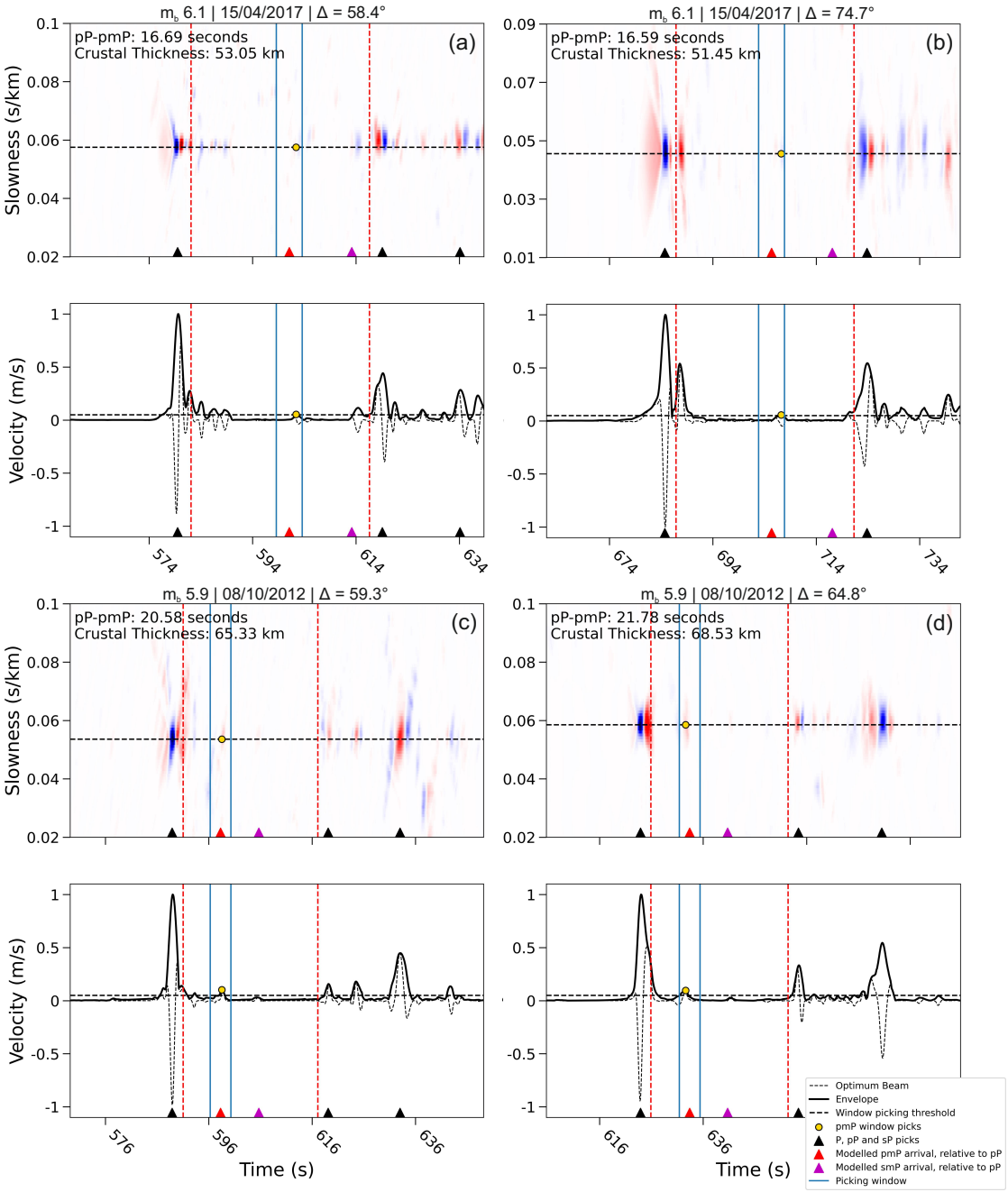

Figure 6.4: Example *ad-hoc* arrays for the m_b 6.1 event which occurred on 15th April 2017 and for the 8th October 2012, m_b 5.9 event located in northern Chile, with their automatic *pmP* picks. Vespagrams and optimum beams are shown for *ad-hoc* arrays at an epicentral distance/backazimuth of 58.4°/168.3° (a) and 74.7°/142.7° (b) from the 2017 event, and 59.3°/155.7° (c) and 64.8°/168.3° (d) for the 2012 event. The dashed red lines indicate the maximum and minimum *pmP* window bounds allowed, to ensure sufficient phase separation for clear phase identification. The blue solid lines show the 5 second *pmP* search window location, and the black dashed lines at a given slowness are the picking thresholds on the optimum beam plots.

and therefore, lower reflection coefficients. An exception to the rule could be an intra-slab earthquake P phase reflecting off the top of the subducting slab, however I would expect such a phase to have travel times very similar to the P arrival and rarely be significant in prominence on teleseismic broadband data. Figure 6.4 illustrates four example *ad-hoc* arrays with *pmP* picks from two earthquakes, to demonstrate my methodology.

6.2.2 Determining crustal thickness

To determine a crustal thickness using the identified *pmP* arrivals, I supply a range of test Moho depths and forward model the expected differential arrival times for *pP-pmP*. These are subsequently compared to the observed *pP-pmP* relative arrival times from my *ad-hoc* array data.

The test Moho depths range from ±15 km around the first-pass crustal thickness depth from Crust 1.0 (Laske et al., 2013), and step in intervals of 200 m. If the test range extends below the event depth, the test range is truncated to the event depth. Similarly, if the test range extends above the surface of the earth, it is truncated to 0 km depth.

For each test Moho depth, a simplified velocity model is built using the same approach as described in Section 6.2.1. The arrival times of *pmP* and *pP* are thus predicted using the new velocity model and ray tracing (Crotwell et al., 1999) for each *ad-hoc* array, and the differential time calculated. The test Moho depth which provides the smallest residual between the predicted and observed *pP-pmP* differential times is selected as the best-fitting Moho depth, and therefore provides the crustal thickness at approximately the *pmP* bounce point.

To find the refined *pmP* bounce points, I use the newly determined crustal thickness and its associated velocity model to predict the coordinates where the P wave ray path pierces the Moho. I associate the crustal thicknesses determined with the *pmP* bounce point coordinates, and construct a final catalogue of crustal thicknesses.

6.2.3 Search window length determination

A number of search window lengths were tested for the purpose of identifying *pmP* arrivals more accurately and consistently. Figure 6.5 demonstrates the importance of the window size, by showing the difference between the *pmP* picks detected when applying a ±2, 2.5 or 3 second window bound. If the window is too large, the risk of incorporating and

mis-identifying P wave coda (Fig 6.5a and b) or intracrustal reflections as pmP arrivals becomes greater. However if the window is too small, velocity model and first-pass crustal thickness discrepancies become more impactful, and the likelihood that a valid pmP arrival is included in the search window is reduced (Figure 6.5c and d). I, therefore, use a ± 2.5 second window to detect pmP.

6.2.4 Velocity model determination

Initially I attempted to use the weighted mean (6.22 km/s) calculated from the Crust 1.0 velocity model (Laske et al., 2013) as the uniform crustal velocity, above an ak135 (Kennett et al., 1995) mantle. However, testing conducted on the Chilean data demonstrated that the Crust 1.0 velocity model underestimates the P wave traveltime in regions with thicker crust (Figure 6.6a). This becomes problematic when my pmP search window is dependent upon the predicted arrival time for pmP, and consequently I found that valid pmP arrivals were not included in the search window. Since data points illustrating regional thickening of the crust are important for creating a new Moho depth map, I needed to find a solution which allowed the identification of pmP arrivals generated by a deeper Moho, with slower than expected crust. The two options were to widen the search window – however, as seen in Figure 6.5, a wider window allows greater mis-identification of P wave coda as a pmP arrival – or find a better fitting velocity model.

In accordance with previous studies (Yuan et al., 2002; McGlashan et al., 2008; Ryan et al., 2016), I tested a range of constants to use as a uniform crustal P wave velocity, ranging from 5.9-6.2 km/s in steps of 0.1 km/s. I found that all velocities tested produced significant numbers of data points, which upon inspection, pick pmP arrivals consistently. I therefore select $Vp = 5.9$ km/s, as this velocity generated the greatest number of pmP picks, including those in the regionally thicker crust (Figure 6.6b).

6.3 Results

6.3.1 North-mid Andean Moho depth

The north-mid Andean crust (Ecuador-Peru-Bolivia-Chile, 0°-24°S) is rarely studied cohesively, with many studies focussing on the latitudes between 14°S-24°S where the Altiplano (also known as the Andean Plateau) exists (e.g. Dorbath et al., 1993; Zandt et al., 1994; Allmendinger et al., 1997; Giese et al., 1999; McGlashan et al., 2008; Ryan et al., 2016),

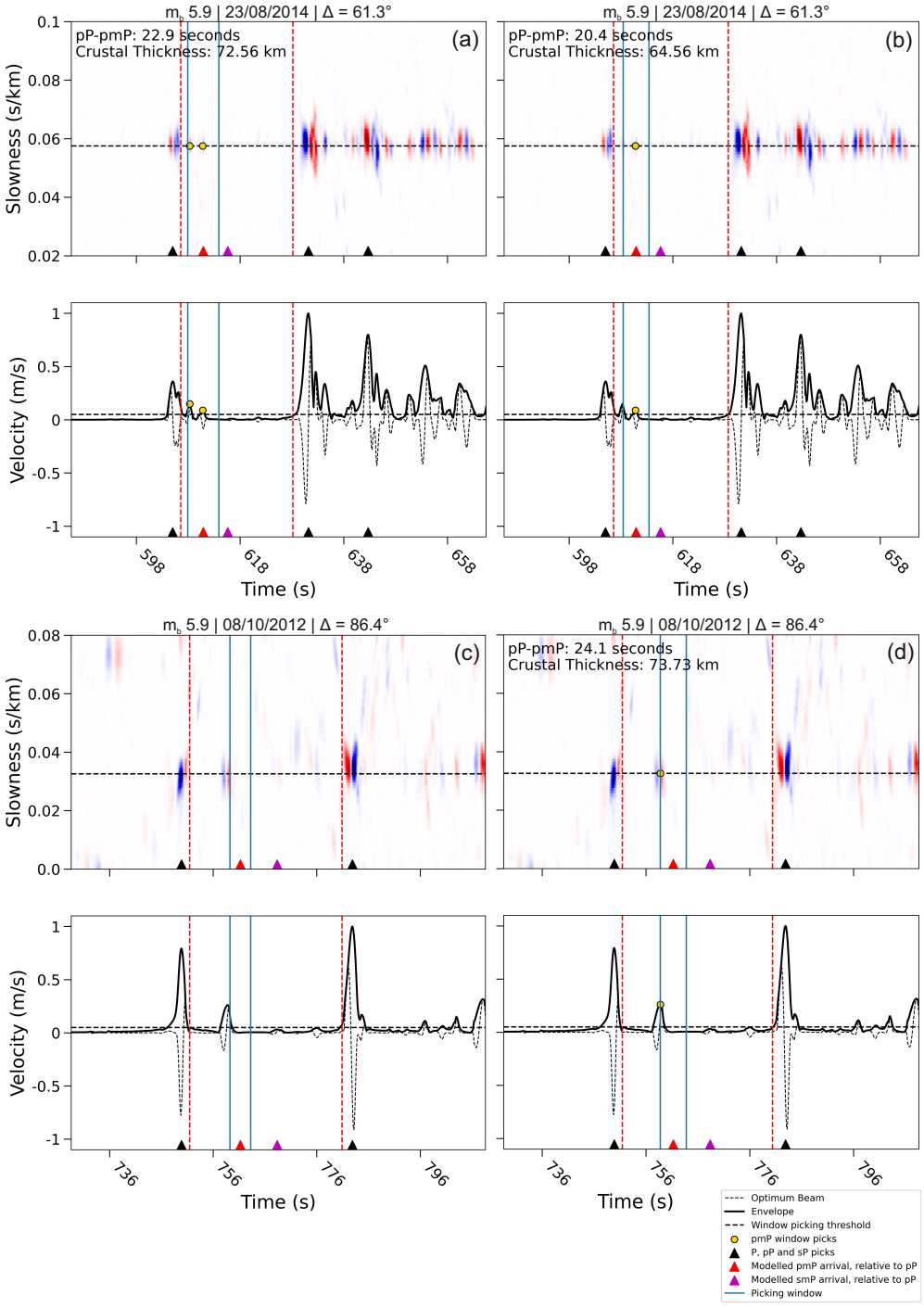

Figure 6.5: Example *ad-hoc* arrays for two events in northern Chile, to demonstrate the significance of the *pmP* search window length. Vespagrams and optimum beams are shown for 2 *ad-hoc* arrays, (a) and (b) are an array at epicentral distance = 61.3° (23rd August 2014 event), whilst (c) and (d) are showing an array at epicentral distance = 86.4°(8th October 2012 event). (a) uses a ±3 second search window, whilst (b) uses a ±2.5 second window – the smaller window avoids mis-identifying *P* wave coda as a *pmP* arrival. (c) uses a ±2 second window, whilst (d) has used a ±2.5 second window – the larger window allows a greater margin of error between the first-pass crustal thickness/predicted *pmP* arrival and the observed arrival time.

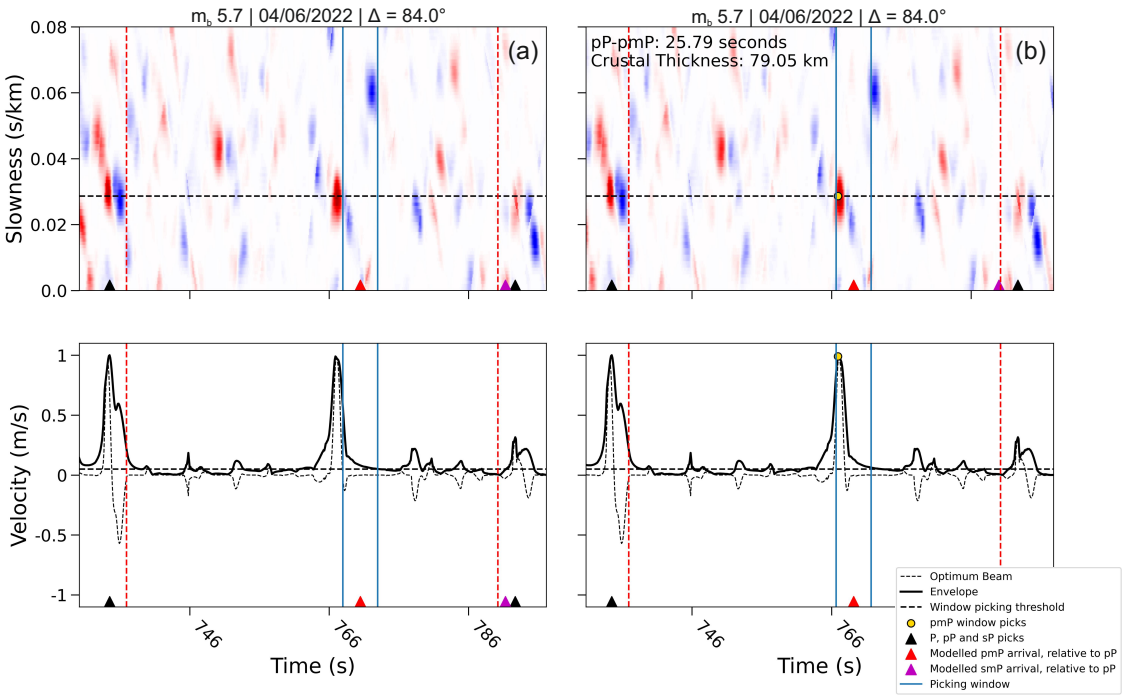

Figure 6.6: An example *ad-hoc* array for the m_b 5.7 event which occurred on the 4th June 2022, at an epicentral distance of 84.0° with a bounce point in a region of thicker crust (approx. 80 km). Vespagrams, optimum beams and automatic *pmP* picks are shown for a search window based upon (a) the Crust 1.0 (Laske et al., 2013) mean velocity (6.22 km/s), and (b) a 5.9 km/s constant crustal *P* velocity. It is clear that the Crust 1.0 based model provides a *pmP* search window which is too delayed to capture the *pmP* arrival.

and few extending northwards into Peru (e.g. James & Snoke, 1994; Condori et al., 2017). This is likely due to the more complex nature of the Altiplano and its role in understanding the geodynamic past of this segment of the Nazca-South American plate subduction zone, compared to the relatively flat and feature-less Peruvian Moho above flat slab subduction (Ma & Clayton, 2015; Hayes et al., 2018).

The Altiplano (see Figure 1.10) extends approximately 1800 km, has a maximum width of between 350-400 km, an elevation of ca. 4000 m and is the second largest plateau in the world based on height and extent (second to Tibet) (Dorbath et al., 1993; Allmendinger et al., 1997). Uplift began 25 Ma ago coevally with an increased convergence rate at the subduction zone, and the associated crustal shortening recorded at the surface is thought to account for 70-80% of the observed crustal thickness (Allmendinger et al., 1997). The remaining thickening is attributed to a combination of lithospheric underplating, magmatic intrusion, thermal uplift, and/or upper mantle hydration (Allmendinger et al., 1997; Giese et al., 1999). The elevation of the plateau is also thought to be supported by lithospheric thinning, due to the removal of denser eclogite from the lower crust and mantle lithosphere (Garzione et al., 2006). Furthermore the Altiplano displays low seismic velocities in the

crust (Dorbath et al., 1993; Swenson et al., 2000), which is consistent with my observations when selecting a suitable velocity model (see Section 6.2.4), and a strong crustal anisotropy which Zandt et al. (1994) interpret as a thick, largely felsic crustal root. There are two domains which flank the Altiplano – the Eastern Cordillera, a fold-thrust defined domain, and the Western Cordillera, a volcanic domain lined with stratovolcanoes (Garzione et al., 2006; Ryan et al., 2016) – which display differing seismic characteristics (Dorbath et al., 1993; Giese et al., 1999).

I test my methodology (Section 6.2) on the north-mid Andes, using the relocated intermediate-depth earthquake catalogues and *ad-hoc* arrays for Peru and northern Chile created by Blackwell et al. (2024) in Chapter 2. I identify 2124 *pmP* arrivals, which define *pmP* bounce points reflecting off the Moho and crustal thickness measurements, including across the Western Cordillera, Altiplano and Eastern Cordillera. I linearly interpolate between the crustal thickness measurements in order to create a map indicating Moho depth (Fig 6.7a) across the north-mid Andes (0°-24°S).

The Moho depth map indicates a regional thickening of the crust inland from the western coast, increasing from approximately 20 km to 70-75 km thick in southern Peru and northern Chile. The thickened crust forms a NW-SE spine, which correlates well with the location of the Altiplano, and appears to taper and thin to the east. However I have a limited number of data points to constrain Moho depth on the eastern side of the Altiplano.

In comparison, the Moho depth around the west side of the Altiplano is well constrained in northern Chile and southern Peru by my *pmP* bounce points, whilst the north of Peru is largely unconstrained between approximately 4°S-13°S, and 500 km inland. The likely cause of this is the lack of intraslab seismicity within the flat slab portion of the down-going Nazca plate, which reduces the sampling rate of the overlying crust. From the results I have determined in northern Peru, a broad thickening of the crust inland from the east coast is also apparent, with a shallower overall Moho depth (approximately 40-50 km) than observed in the northern Chile. The broad thickening correlates well with the location of the Andes mountain range.

6.3.2 Receiver function validation

I validate the crustal thicknesses found using my *pP-pmP* relative time methodology, by comparing my results to the crustal thicknesses calculated in Peru and northern Chile

with receiver functions by Yuan et al. (2002), Ryan et al. (2016) and Condori et al. (2017) (see Figure 6.7b).

Yuan et al. (2002) used 642 receiver functions from 170 stations to estimate the thickness of the Moho in the central Andes (17°S-25°S) using a combination of short period, temporary (approx. 3 months) station and longer term (more than a year), broadband station data. They found a thickening in the crust from 35 to 70 km from the fore-arc to the Altiplano, with the thickest crust to the north of the Altiplano. Further thinning to the east was also indicated, away from the apex of the Altiplano, to approximately 30 km. The receiver functions were stacked in a 1x1° grid, resulting in a resolution of 1° for the final results.

Ryan et al. (2016) took 343 teleseismic events recorded on the CAUGHT temporary array and 38 additional stations between 10°S-22°S latitude in Chile and Bolivia to construct a Moho map for the central Andes. Broadly they find that there is a wide spine of thickened crust below the Altiplano, with Moho depths of 65-75 km from south to north-west. The Altiplano decreases in thickness eastwards to approximately 35 km thick. These findings agree with those found by Yuan et al. (2002). The Moho depth map produced indicates smooth transitions between the varying crustal thicknesses west to east and north to south, whilst comparison to modelled Airy isostatic thickness indicates small, local anomalies where the crust is thinner or thicker than expected (Ryan et al., 2016). Ryan et al. (2016) suggest uneven climate induced exhumation, and lithospheric delamination for the variation in isostatic compensation regionally. Yuan et al. (2002) also suggest partial removal of the crust via delamination from the entire Altiplano, after comparing expected elevation (Bougueur anomaly) to the observed elevation.

Condori et al. (2017) calculated a total of 981 receiver functions from a combination of 28 permanent broadband stations, 12 temporary broadband stations from the SisNort network and one CTBTO (Comprehensive Nuclear-Test-Ban Treaty Organisation) seismic station located in Peru. They find that the crustal thickness varies from west to east – the crust is approximately 25 km thick on the west coast, to 55-60 km thick underneath the Andes and thinning to 35-40 km in the Amazonian Basin further to the east.

Our results show similar findings for the north-mid Andes – a thicker, broad spine of crust following the Andes/Antiplano from north-west to south (see Section 6.3.1). To quantitatively compare the receiver functions to my *pmP* determined results, I linearly interpolate each of the three sets of receiver functions and Crust 1.0 data points (Laske

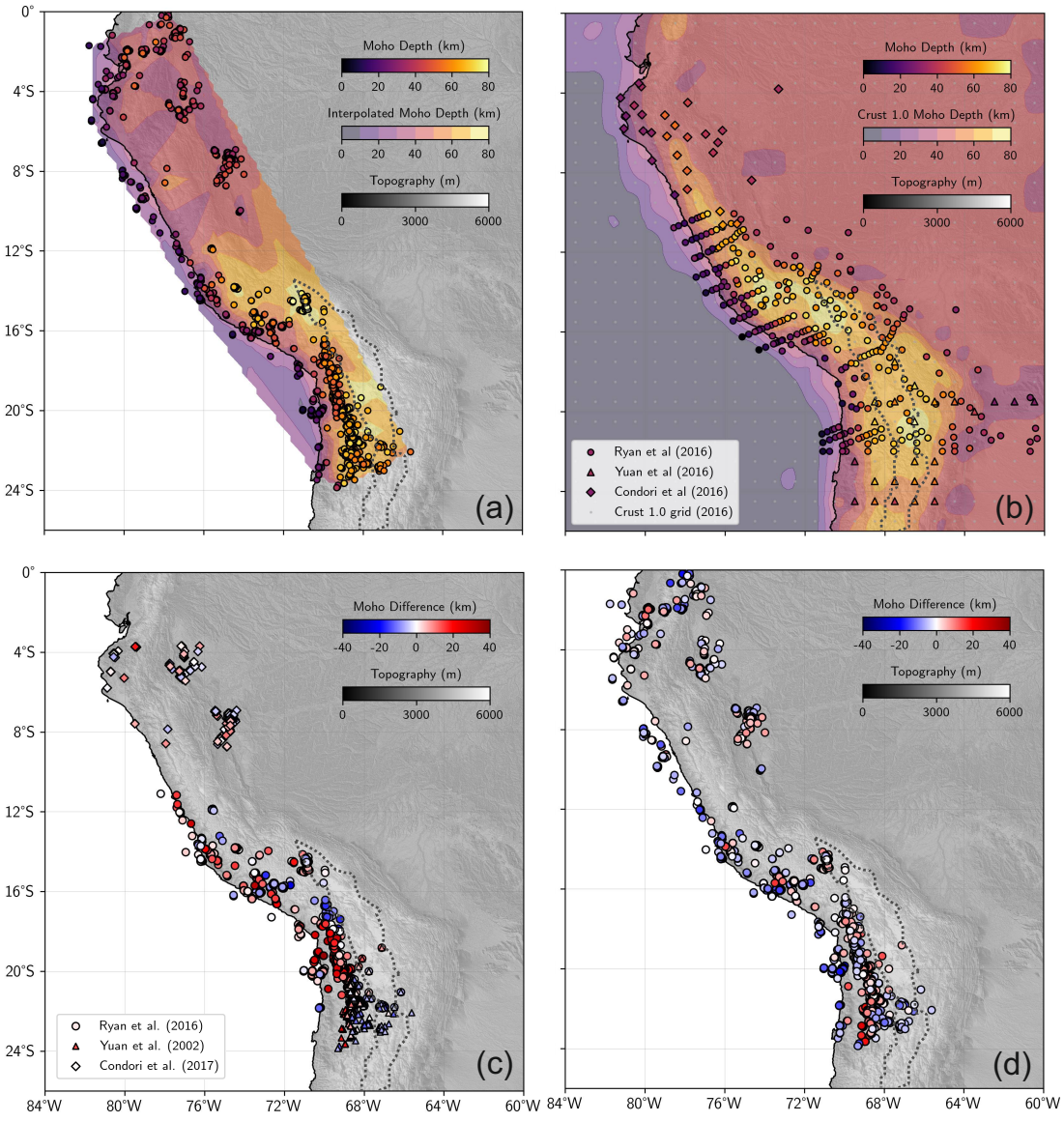

Figure 6.7: (a) Bounce point locations and associated Moho depths of the identified *pmP* arrivals for the north-mid Andes, and the linear interpolation. (b) Receiver function locations and associated Moho depths from previous studies (Yuan et al., 2002; Ryan et al., 2016; Condori et al., 2017), with a linear interpolation of Crust 1.0 (Laske et al., 2013). (c) Moho depth differences between the linearly interpolated receiver function results and the *pmP* crustal depths from this study. (d) Moho depth differences between the linearly interpolated Crust 1.0 model and the *pmP* crustal depths from this study. Altiplano crust is outlined in a grey dotted line on all panel (Zandt et al., 1994).

et al., 2013), extract the Moho depths of the interpolations at the *pmP* bounce point coordinates (for the results which exist within the receiver function interpolations), and directly examine the difference in depth. Figures 6.7 and 6.8 summarize the findings from this comparison.

It is clear that the Moho depth results from this paper broadly correlate with those found previously. However there are up to ±40 km differences, particularly for the Ryan et al. (2016) data set, along the coastline, and the *pmP* determined depths tend to be 2.5-7.5 km deeper than those of the previous studies (Figure 6.8). The largest discrepancies exist on the border of Peru and Chile along the coastline, where my *pmP* based results indicate a thicker Moho depth of approximately 40-50 km, whilst Ryan et al. (2016) find crustal thicknesses of 10-30 km. The discrepancies could be due to poor handling of Moho gradient by both the *pmP* bounce point methodology presented here and receiver function stacking (L. Zhu & Kanamori, 2000), mis-identification of interfaces on the receiver function stacks/mis-picks on my beamforms, and differing velocity models for conversion of the time domain to depth. Ryan et al. (2016) use a regional 3D velocity model derived from ambient noise above 60 km depth, and IASP91 1D global model (Kennett & Engdahl, 1991) sub 60 km, whilst I use the ak135 1D global model (Kennett et al., 1995) with the simplified crust.

I show example *ad-hoc* arrays which have the largest Moho depth differences between their *pmP* derived crustal thicknesses and those found by the receiver function studies and Crust 1.0 (Fig 6.9). I believe examples (a-c) demonstrate strong *pmP* picks which support my Moho depth determinations. However for (d), it is possible that the peak at 619 s is the actual *pmP* arrival, and I mis-identified it using my methodology. If the other pick had been identified as *pmP*, the Moho depth for *ad-hoc* array would have been 34.90 km and the discrepancy with Crust 1.0 only 4.67 km. I do not currently have a process which removes bounce points with Moho depths which do not appear to fit other local data points, rather I rely upon the linear interpolation to smooth out anomalous measurements. This is possible due to the high numbers of *pmP* picks.

6.3.3 Moho depth resolution

To determine the thickness of the crust, waves which reflect off or pass through the Moho are used (e.g. for us, *pmP* waves, for others, receiver function conversions). The area of the Moho that the waves sample can be simply approximated using knowledge of the

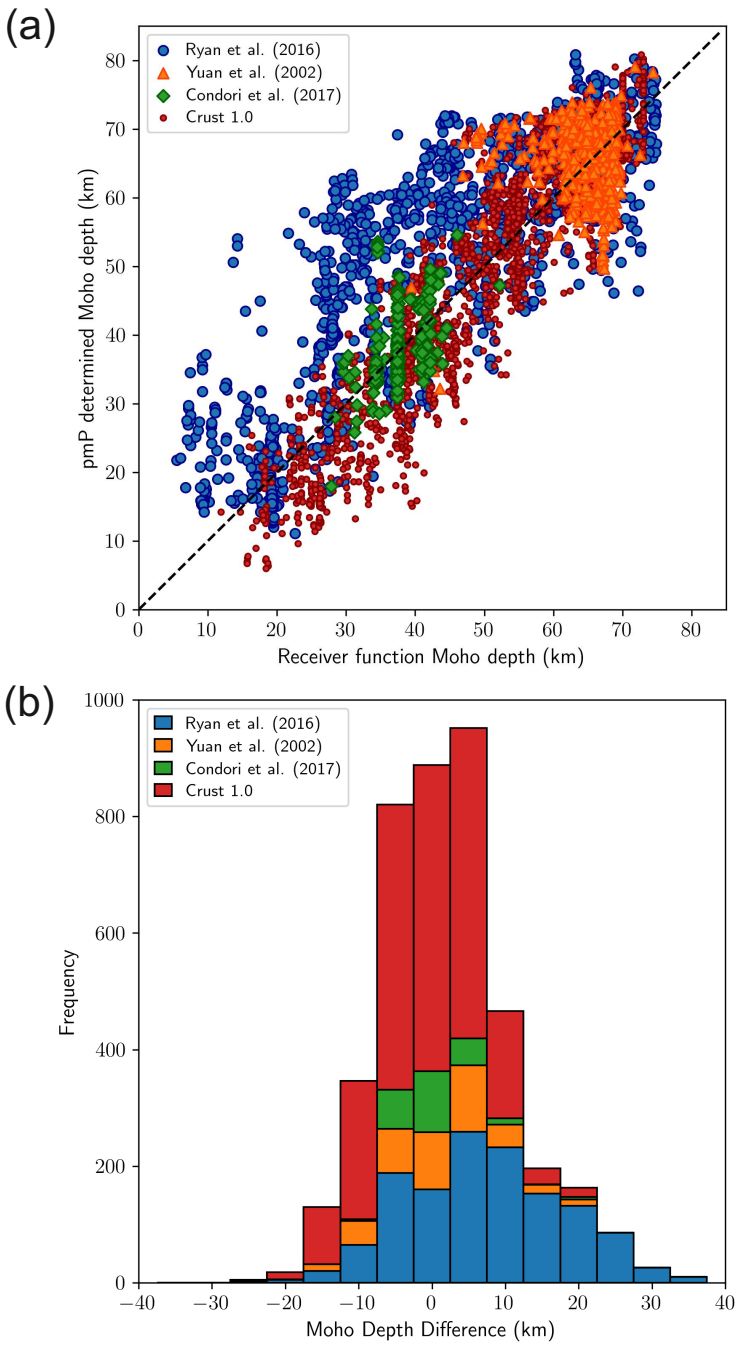

Figure 6.8: (a) Receiver function and Crust 1.0 Moho depths compared to the Moho depths found during this study, and (b) a stacked histogram demonstrating the frequency of the variance between the validation datasets and the results from this study.

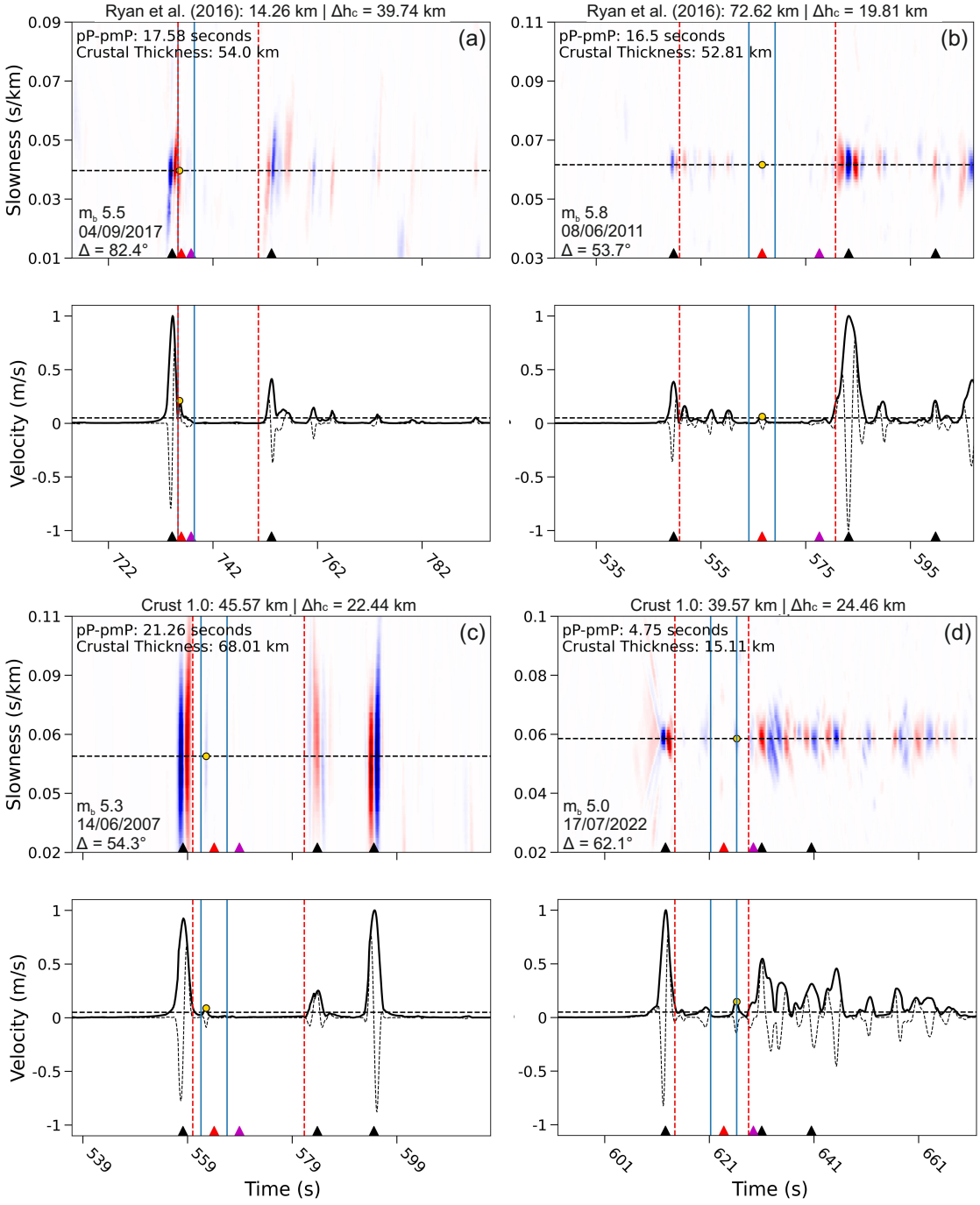

Figure 6.9: Example results from *ad-hoc* arrays, with their vespagrams (top) and optimum beams (bottom), for data points which have large discrepancies with the validation datasets. Comparison Moho depths and their dataset are labelled above each plot. (a) Results for 4 September 2017 (epicentral distance = 82.4°). (b) Results for 8 June 2011 (epicentral distance = 53.7°). (c) Results for 14 June 2007 (epicentral distance = 54.3°). (d) Results for 17 July 2020 (epicentral distance = 62.1°).

Fresnel zone. Assuming the wave is travelling perpendicularly to the Moho, I can calculate the Fresnel zone using crustal thickness, event depth, a resolution of 1/4 wavelength and the ray path geometry (see Appendix A.13).

For Yuan et al. (2002), bins of 1x1° were used to stack the receiver functions, which is larger than the predicted Fresnel zone, and therefore their Moho depth resolution is 1°. Meanwhile Ryan et al. (2016) use common conversion point stacks in bins of 50x50 km (roughly 0.4x0.4°). However, a quick calculation of each receiver function's Fresnel zone indicates that the sample area could be up to 1.2°.

For my work, the Fresnel zone of each *pmP* arrival observed between my 0.1-1.0 Hz bandpass filter can be up to 0.5°. In addition, I expect loss in my Moho depth resolution due to the stacking of *ad-hoc* array waveforms into beams, which needs to be taken into account. I find a maximum distance of 0.07° between the *pmP* bounce points which could be recorded in the same 2.5° array aperture (see Section 2.2.3), modelled for a 60 km crustal thickness. Therefore, despite the spread in source-side *pmP* bounce points, the sampling area for my *pmP* beamforms is estimated to have a maximum of 0.57°, which is significantly smaller than the receiver function results. I also have a greater lateral sampling density (this is irregular, however) of the Moho, achieved from using the bounce points surrounding an event location, over a potential backazimuth range of 360°. The smaller sampling area and increased number of data points sampling the Moho may help to highlight small-scale Moho roughness.

6.3.4 *pmP* and *pP* relative amplitudes

Although many *pmP* phases have been identified during my study, a large number of *ad-hoc* arrays failed to have a crustal thickness determined (approximately 93%). There are four possibilities for failure (besides an ill fitting selection window), all four stem from the *pmP* arrival not having enough prominence to be selected/pass the signal-to-noise ratio threshold, (1) the *ad-hoc* array is in close proximity to the nodal plane of *pmP* radiation pattern, (2) the local Moho roughness is scattering coherent *pmP* reflections, (3) the Moho does not have a great enough impedance contrast to reflect the *P* wave efficiently and/or (4) the *pmP* ray path is highly attenuating for varying reasons (Oliver et al., 1983; Cook, 2002; Zandt et al., 2004). Suggestions to explain the variability for reasons 2, 3 and 4 include compositional differences, such as ecologitization/hydration of the upper mantle, crustal delamination and lower crustal flow (McGlashan et al., 2008).

To investigate the nature of the Moho using the results of my methodology, I calculate the relative amplitudes of the detected *pP* and *pmP* arrivals per *ad-hoc* array. This aims to remove the influence of the source mechanism and retain amplitude information, which can be used to make inferences about the Moho reflector, given that both *pmP* and *pP* have the same angle of incidence at the Moho. Using the phase-weighted beams, I find a range of relative amplitude ratios between *pmP* and *pP* from 0.04-6.72, over both Peru and northern Chile, however after inspecting the data with large relative amplitudes, it is clear that data points with values above 1.72 are associated with noisy optimum beams with persistent, large amplitude *P* wave coda. Examples of *ad-hoc* arrays with relative amplitude values of 1.69, 1.72 and 1.73 can be seen in Figure 6.10 (bounce point locations can be seen in Appendix A.14). Whilst Figure 6.10a and b still have confident *pmP* picks, Figure 6.10c shows large signal amplitudes between the *P* and *pP* arrivals which discredits a *pmP* pick on the vespagram. I therefore choose to remove *pmP* arrivals, and resultant crustal thicknesses, which have been derived from vespagrams demonstrating a *pmP*/*pP* relative amplitude greater than 1.72 as a quality control measure. Events which do not pass this measure are already removed from Figure 6.7.

I use the amplitude ratios found from the phase-weighted beams initially as a quality control, since they are used for the original *pmP* detection, and include a measure of coherency and therefore confidence in the arrivals. From henceforth, I will be considering the relative amplitude of the arrivals on linear beams to investigate the Moho, which range from 0.08-2.74. I illustrate a range of relative amplitudes (showing both the phase-weighted and linear ratios for comparison) found from the vespagrams of a single earthquake event in Figure 6.11 as an example.

The majority of the relative amplitudes calculated are less than one (89.7%), indicating that typically the *pmP* wave reflection coefficient at the Moho is smaller than the *pP* reflection off the free surface. This is in agreement with the expected difference in the reflection coefficients of the free surface and the Moho, which I have modelled using the ak135 1D velocity model (Kennett et al., 1995) and Shuey's approximations (Shuey, 1985) for the Zoeppritz equations, with respect to incidence angle (Figure 6.12). Given that the amplitude ratio between *pmP* and *pP* is inherently overprinted by the expected difference in the surface and Moho reflection coefficients, I need to find a normalising factor in order to interpret where interface reflections are demonstrating an unexpected transfer of energy. I approach this by calculating the ratio between the reflection coefficients for the *pmP* and

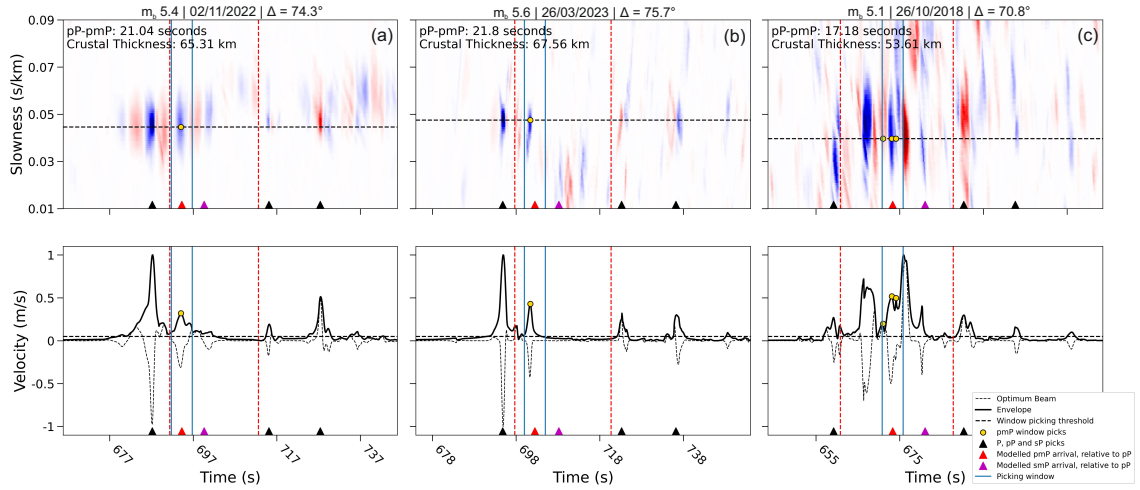

Figure 6.10: Example *ad-hoc* arrays, with their vespagrams and optimum beams, demonstrating the 1.72 upper bound on the usability of the phase-weighted relative amplitudes between *pmP* and *pP*. (a) Shows *ad-hoc* array 74.3° epicentral distance from the 2nd November 2022 event with relative amplitude of 1.69. (b) Shows *ad-hoc* array 75.7° epicentral distance from the 26th March 2023 event with relative amplitude of 1.72. (c) Shows *ad-hoc* array 70.8° epicentral distance from the 26th October 2018 event with relative amplitude of 1.73.

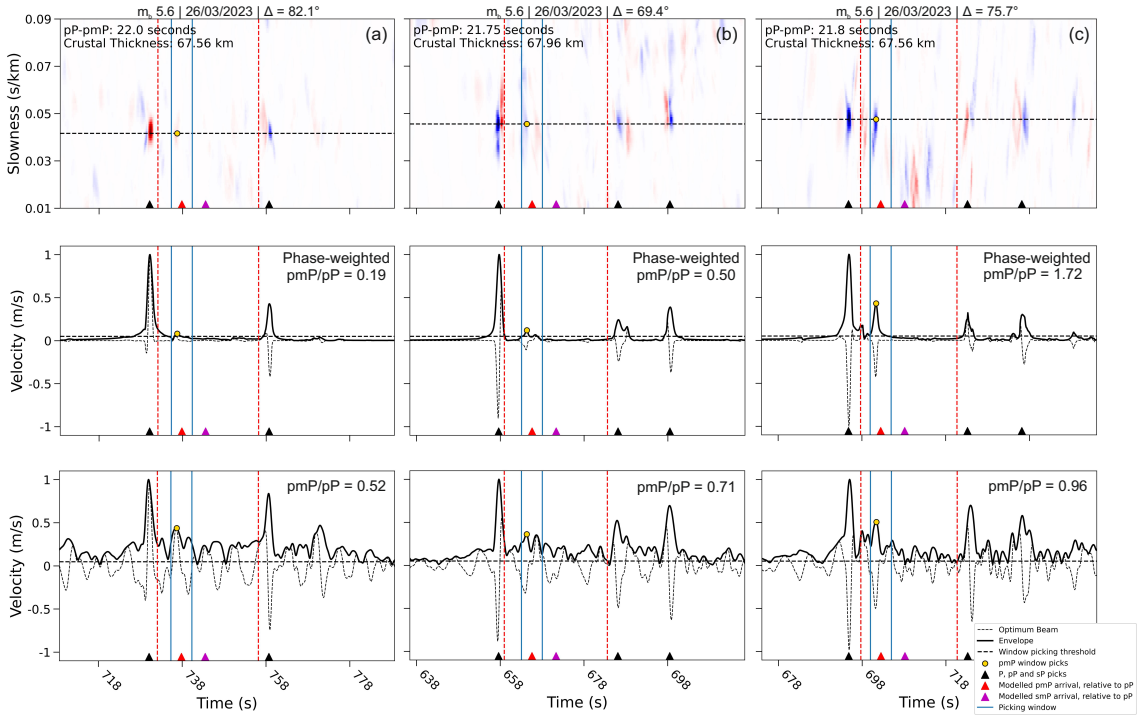

Figure 6.11: Example *ad-hoc* arrays, with their vespagrams (top), phase-weighted optimum beams (middle) and linear optimum beams (bottom), demonstrating the range of the relative amplitudes between *pmP* and *pP* for a single event from 26th March 2023. (a) Shows *ad-hoc* array 82.1° epicentral distance with relative amplitude of 0.19. (b) Shows *ad-hoc* array 69.4° epicentral distance with relative amplitude of 0.50. (c) Shows *ad-hoc* array 75.7° epicentral distance with relative amplitude of 1.72.

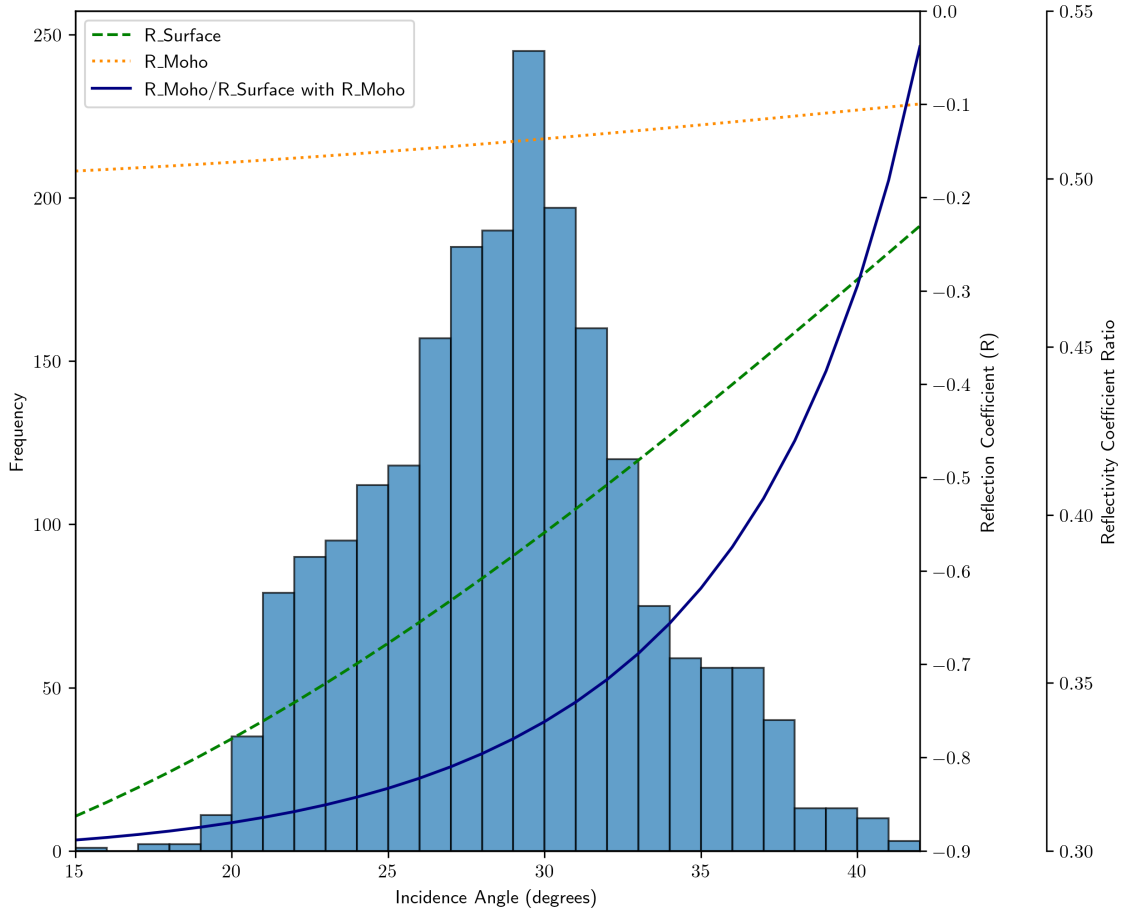

Figure 6.12: Histogram of the angles of incidence for the depth phase bounce points, overlain by the modelled reflection coefficients (R) for the free surface and the Moho using parameters from the ak135 1D velocity model (Kennett et al., 1995), and the ratio of the modelled Moho to free surface reflection coefficients (reflectivity coefficient ratio).

pP ray paths, using my modelled free surface and Moho reflection coefficients as a function of incidence angle, and the incidence angle of each depth phase bounce point for which I have results (Figure 6.12). For each pmP/pP data point, I select the modelled reflectivity coefficient ratio corresponding to the incident angle calculated for the pP bounce point, and use it as the normalising factor for that pmP/pP amplitude ratio. Therefore each pmP/pP data point is normalised individually, to account for variable incident angles. I find a range of normalised relative amplitude values between 0 and 5.4. A simple parameter test indicates that a pmP/pP relative amplitude of approximately 5 is a reasonable value to expect when varying the ak135 velocity model (Kennett et al., 1995) bounds between ± 0.1.

With the removal of the differing interface reflection coefficients and their influence upon the pmP/pP relative amplitudes, I can look to interpret variation in the nature of the Moho and crust at locations that my data points sample. In general, particularly small

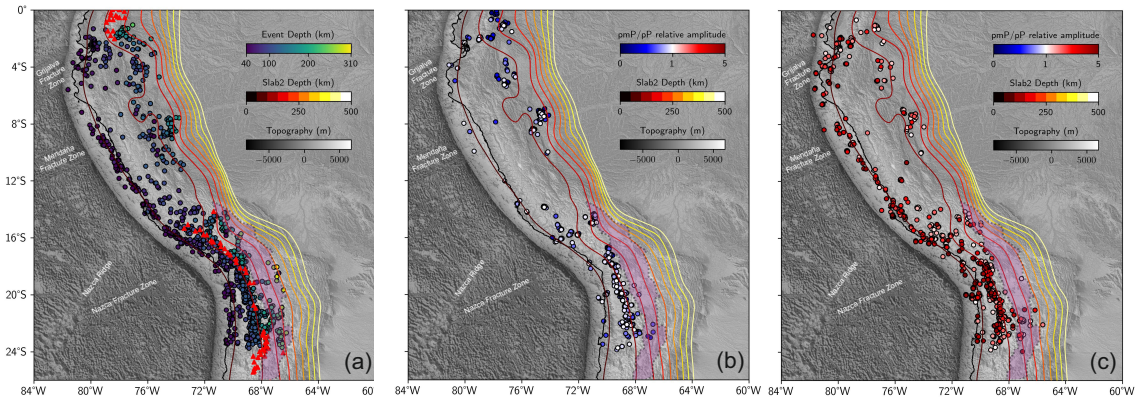

Figure 6.13: Spatial distribution of the earthquake catalogue used to find *pmP* arrivals (a), and *pmP*/*pP* relative amplitudes calculated at the *pmP* Moho bounce points ((b) for relative amplitudes <=1 and (c) >1). Holocene volcanoes (Global Volcanism Program, 2024) are additionally plotted on (a) as red triangles, and Altiplano crust (represented by a transparent pink polygon, outlined with a grey dotted line from Zandt et al. (1994)) and Slab2 contours (Hayes et al., 2018) are on all plots.

ratios may indicate a lack of sharp impedance contrast or greater interface roughness at the Moho. For the relative amplitude data points which equal approximately one, these represent locations where the observed ratio is as modelled, and likely the only amplitude difference between the phases prior to normalisation is caused by the reflection coefficients of the free surface and Moho. Although this is a simplified view, given that other energy losses such as geometric spreading and attenuation have not been corrected for, I am assuming that both phases experience the same ray path and therefore identical energy losses post re-entering the mantle. Finally, the large relative amplitude data points imply that the *pmP* waves are experiencing significantly less attenuation along their ray path than the *pP* waves, and greater reflection at the Moho. This could be a case where the crust is particularly attenuating for *pP* waves due to structural complexity, whilst the *pmP* wave is reflecting off a sharp Moho impedance contrast. It is also possible that there are other phases (intra-crustal reflections, or *smP*) coherently stacking with the *pmP* arrival.

On Figure 6.13, I find that my data points highlight significant areas of the Moho with similar *pmP*/*pP* ratios, and hence indicate spatially linked Moho properties. For example, broadly I observe high relative amplitudes along the coastline and on the western edge of the Altiplano between approximately 16°S-23°S, whilst low relative amplitude data points cluster to a greater extent inland over locations where the subducting slab exceeds approximately 100 km deep – a weak Moho is also noted here by Wigger et al. (1991) on seismic reflection profiles. By comparing the source locations of the earthquake data I have used to find *pmP* arrivals (Figure 6.13a) to the *pmP* bounce point locations (Figure 6.13b),

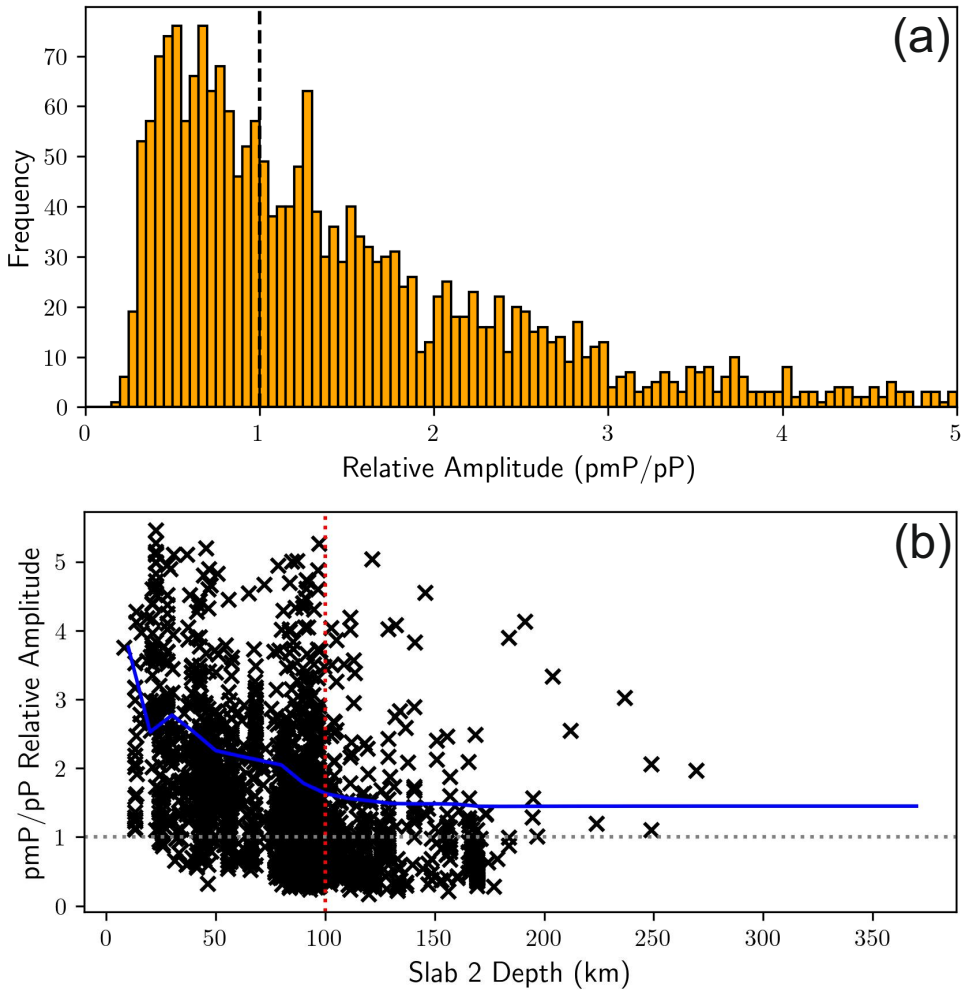

Figure 6.14: Histogram showing frequency of the normalised pmP/pP relative amplitudes calculated at the pmP Moho bounce points (a) and the relationship between the depth of the subducting slab, using Slab2 (Hayes et al., 2018), and normalised relative amplitude ratios (b). Red dotted line at 100 km depth, grey dotted line indicates a relative amplitude of 1, and blue solid line shows the rolling relative amplitude mean which flattens at approximately 100 km Slab2 depth.

I can also observe areas of the Moho where predicted pmP bounce points consistently fail to generate a detectable pmP arrival on teleseismic data – these events without identified pmP arrivals appear to be on the second Peruvian flat slab bend (downward into the mantle) and on the eastern edge of the Altiplano, and likely indicate a low impedance or rough Moho in these areas. Figure 6.14a illustrates the frequencies of normalised relative amplitudes found for the region, with a positive skew indicating generally larger numbers of low relative amplitude ratios.

Using these observations, I can hypothesise the controls upon the relative amplitude ratio distribution. The occurrence of high amplitude ratio data points along the coastline may reflect the thinner crust at the margins of the continental crust, and the shallower

intermediate-depth earthquakes in close proximity to the subduction trench. This combination may encourage a greater amount of coherent stacking between the *pmP* phase and intra-crustal interfaces, due to the smaller *pP*-*P* and *pP*-*pmP* differential times, to create an apparently large relative amplitude ratio.

Alternatively, there is a loose correlation between the depth of the subducting slab and whether the relative amplitude ratio between *pmP* and *pP* is smaller than one, particularly surrounding the Slab2 model (Hayes et al., 2018) 100 km contour. Figure 6.14b tests a correlation between slab depth and the overlying relative amplitude values, and I observe a diffuse negative gradient showing that the occurrence of larger relative amplitudes between *pmP* and *pP* is more likely restricted to crust overlying the slab when it is shallower than approximately 100 km. From this, I infer that the Moho has a larger impedance contrast when overlying the area where the slab is less than approximately 100 km deep in Slab2 (Hayes et al., 2018) and vice versa, assuming that the crustal attenuation is laterally unchanging. Unfortunately this is likely not true given the work of Haberland and Rietbrock (2001) and Jang et al. (2019). The diffuse nature of the gradient also infers that the controls upon this observation are not spatially sharp.

Slab dehydration reactions (Kirby et al., 1996; Hacker et al., 2003) could be responsible for creating a more diffuse Moho interface with a lower impedance contrast when the slab is deeper than approximately 100 km, since the ejected water lowers *P* wave velocity in the overlying mantle (Hyndman & Peacock, 2003; J. Wang et al., 2019). However, Syracuse et al. (2010) models that the slab in Peru and northern Chile dehydrates to 0.01 weight % water before 100 km depth, using the phase diagrams created by Hacker (2008).

Other pertinent conditions that exist around 100 km depth which could influence the Moho impedance include the presence of a cold, low attenuating mantle wedge nose (Jang et al., 2019; Hicks et al., 2023; van Keken & Wilson, 2023) with a sub-vertical boundary at ∼100 km slab depth where full upper mantle-slab coupling is thought to occur (Haberland & Rietbrock, 2001; Syracuse et al., 2010) in Chile and cold/dry mantle determined from low Vp/Vs ratios overlies the Peruvian flat slab (Lim et al., 2018). This would account for a faster velocity in the trenchward mantle wedge, where I am seeing high pmP/pP ratios which would increase the impedance of the Moho boundary and allow greater reflection of the *pmP* arrival, than eastward where the mantle wedge is likely coupled to the down-going slab.

Furthermore, the presence of a low velocity zone (approximately 10-20% reduction (Yuan et al., 2000)) within the crust underneath the Altiplano has been proposed using both wide-angle reflection profiles (Wigger et al., 1991) and receiver function data (Yuan et al., 2000), and inferred as high temperature rocks with small degrees of partial melting (Wölbern et al., 2009; Yuan et al., 2002). The Miocene-Holocene arc volcanism additionally exists throughout the Altiplano, which contributes to the low velocities observed in the area (Graeber & Asch, 1999). The presence of a low velocity zone underneath the Altiplano could influence pmP/pP relative amplitudes one of two ways – either the pP wave attenuates more as it traverses hot, slow, potentially partially melted crust to create a large relative amplitude ratio, and/or the pmP wave reflects poorly off the inefficient impedance contrast at the Moho (assuming dry, high velocity lower crust underneath the low velocity zone (Yuan et al., 2000)). The local inter-play of the crustal complexity and the reduction in Moho reflection coefficient could be why I observe both low and high relative amplitude ratios beneath the Altiplano.

There are data points which do not fit this broad trend. I suggest a number of reasons which could account for variation. (1) Lateral variability in slab water content, thermal environment, Moho roughness and crustal complexity could cause local fluctuations within a regional pattern. (2) The Slab2 model (Hayes et al., 2018) is regionally too shallow at distances greater than 250 km from the trench throughout Peruvian-northern Chile as observed in Chapters 2 and 4, which creates apparent discrepancies between the relative amplitude ratio data points and the 100 km Slab2 contour pattern. (3) There are bathymetric features on the down-going Nazca Plate (Nazca Ridge, Nazca Fracture Zone, Mendaña Fracture Zone and Grijalva Fracture Zone, see Figure 6.13b) which may have a higher water content than standard oceanic crust, thus driving greater upper mantle hydration and lowering the impedance contrast of the Moho/decreasing the pmP/pP amplitude ratio. (4) Crustal delamination may remove seismically fast lower crust (for example underneath the Altiplano, (Yuan et al., 2002; Ryan et al., 2016), and locally change the expected Moho impedance as a consequence. Overall, it is unlikely that a singular condition in the subduction zone is responsible for the trend I am observing, however, the presence of a cold mantle wedge over the Peruvian flat slab with a coupling depth of approximately 100 km seems likely to exert the strongest control on the reflectivity of the Moho interface, with secondary influence from dehydration reactions/slab hydration from bathymetric features, crustal delamination, partial melt in the crust/crustal complexity

and recent arc volcanism.

6.4 Conclusion

I previously used adaptive *ad-hoc* arrays to increase the signal-to-noise ratios of teleseismic *P*, *pP* and *sP* arrivals for intermediate-depth earthquakes in Peru and northern Chile (Chapter 2). I build on this work in order to automatically pick *pmP* arrivals using a window based approach, and calculate crustal thickness using the differential time determined between *pP* and *pmP*, in conjunction with the ak135 1D velocity model (Kennett et al., 1995). This enables me to quickly generate crustal thickness maps automatically for a region, with large numbers of data points and without the need for local seismometers, assuming that there are frequent sub-Moho earthquakes.

I find crustal thicknesses in northern Chile increase from approximately 25 km along the coast, to up to 80 km inland underneath the Altiplano, before reducing in thickness again to the east. My findings broadly corroborate previous crustal thicknesses determined through receiver functions, although discrepancies of up to 40 km exist. This may be due to the limitations of receiver functions when the Moho has a gradient, difficulties consistently identifying the Moho within a series of reflective interfaces, differing velocity models and the use of interpolation between the receiver function data points. Additionally, I determine that the sample area for my beamformed *pmP* arrivals (0.57°) is smaller than the compared receiver function areas (1-1.2°), which allows my methodology to demonstrate a greater resolution crustal thickness map than receiver function techniques for the region.

I also investigate if the relative amplitudes between the picked *pmP* and *pP* arrivals can provide information regarding the nature of the Moho, at a given sample point. I normalise the relative amplitudes to remove the overprint caused by differing surface and Moho reflection coefficients, and consider the spatial variation of data points indicating above and below expected amplitude ratios (ratio of 1 is expected, post normalisation). I find a spatial trend, whereby the data points overlying slab depths <100 km indicate higher than modelled relative amplitudes – which I interpret as a sharper impedance Moho, with more complex/attenuating crust. For the Moho above >100 km slab depths, I infer a reduction in relative amplitude due to the presence of a diffuse Moho interface. This trend is likely to be a product of a ∼100 km mantle wedge-slab coupling depth, which leads to cold, high velocity mantle wedge overlying sub-100 km depth slab. Deviations

from this observed pattern could be attributed to the interplay of bathymetric features on the down-going slab, crustal delamination, and spatial variations in slab water content and mantle wedge heterogeneity.

Chapter 7

South American Subduction Zone: a case study

7.1 Introduction

7.1.1 Preceding work

Previously, in Chapter 2, I have demonstrated an approach to relocate intermediate-depth earthquakes in 1D (depth) using array processing to automatically pick the direct P arrival and the associated depth phases (e.g. pP and sP). This approach was applied to northern Chile to validate the results with another intermediate-depth earthquake catalogue (Craig, 2019), and extended to generate a newly refined catalogue for the Peruvian flat slab.

The array processing results and 1D relocations for northern Chile and Peru were subsequently used in Chapter 6 to determine the depth of the Moho with pmP arrivals. The new Moho depth map for northern Chile and Peru corroborates a thickened plateau (the Altiplano) observed inland, which has a long axis aligned to the subduction trench (Yuan et al., 2002; McGlashan et al., 2008).

The earthquake location catalogues for northern Chile and Peru were refined further in Chapter 4, when the automatic P, pP and sP picks from Chapter 2 were combined with globally reported phases (taken from the ISC) and used to relocate the earthquakes in 3D with ISCloc (Bondár & Storchak, 2011). The 3D relocations which included the *ad-hoc* array determined automatic depth phase picks showed reductions in depth error for 99.9% of events, and the improved relocations allowed slab features, such as apparent seismicity

planes and DSZs, to be discussed for northern Chile. I also showed in Chapter 3, that the array processing approach in Chapter 2 can be extended to incorporate and automatically pick both the S and sS phases, yet have not demonstrated their incorporation into event relocation thus far.

Here, I apply all of the presented methodologies developed in the thesis to the entire South American Subduction Zone (SASZ) (see Section 1.3.4) to demonstrate their full capabilities. Previous chapters have discussed the Peruvian flat slab, and links between seismicity, Moho impedance, bathymetric features and arc volcanism (Chapters 2 and 6). By extending my approach to include the entire SASZ, and including new phases (S and sS), I aim to generate catalogues which can be used to assess further links between seismicity and the background geodynamic setting.

7.1.2 Chapter outline

The selection of the initial event catalogue for the SASZ is described in Section 7.2. I use the array processing methodology outlined in Chapters 2 and 3 to automatically detect and identify the P, pP, sP, S and sS phases in Section 7.3.1. These phases are then converted from amplitude picks to absolute onset picks, and combined with the globally reported phases for each event with the approach introduced in Chapter 4, in Section 7.3.3. As I have not previously introduced how S coda picks are converted, this will also be discussed in this section. ISCloc (Bondár & Storchak, 2011) is subsequently used to relocate the events in 3D using the combined phase catalogues, with the results shown in Section 7.3.4. Finally, the array processing results per event are analysed for pmP arrivals using the approach from Chapter 6, to determine a crustal thickness map for the entire SASZ in Section 7.4.

This Chapter represents the full deployment of all the techniques developed throughout the thesis, on a continent-scale dataset – a summary workflow of the methodologies applied to the SASZ, can be seen in Appendix A.15. The approaches have previously been described in Chapters 2, 3, 4 and 6, please refer to these for greater detail. I will demonstrate the methodologies upon an example earthquake (m_b 6.0 from 25th July 2016, located in Chile) to illustrate the approach processing and analysis steps.

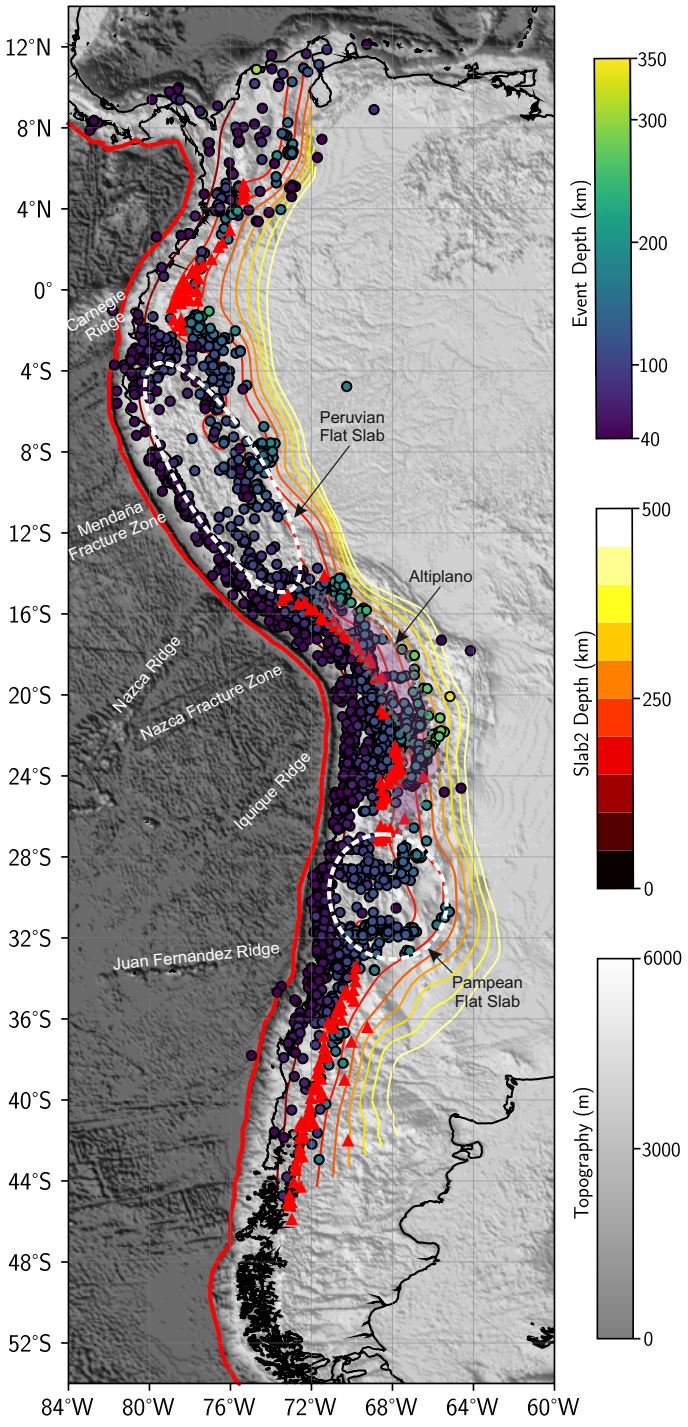

Figure 7.1: Map showing the initial earthquake catalogue used for the SASZ intermediate-depth earthquake relocation. The thick red line shows where the subduction trench exists, and red triangles represent the locations of Holocene volcanoes (Global Volcanism Program, 2024). Other bathymetric and slab features are labelled (Zandt et al., 1994; Espurt et al., 2008; Bilek, 2010; Flament et al., 2015).

7.2 Initial catalogue

The methodologies I have developed look to refine earthquake locations which have already been determined by an external agency. For my initial SASZ earthquake location catalogue, I searched for earthquakes in the ISC events catalogue which occurred:

1. between 01/01/1995 and 09/09/2024.
2. within a box defined by the coordinates: (58°S, 83°W), (14°N, 83°W), (14°N, 64°W), (58°S, 64°W).
3. between 40 to 350 km deep.
4. between m_b 4.7 to 6.5.

The results of this search form the initial catalogue for my earthquake relocation approach, and provides a list of events for which to acquire seismic data, and the accompanying metadata. The initial catalogue for the SASZ has 2877 events (Figure 7.1).

7.3 3D earthquake relocation

7.3.1 Data processing

For each earthquake in the initial catalogue taken from the ISC (see Section 7.2), all available BH or HH channel teleseismic data (recorded between 30-90° epicentral distance), and their metadata, are downloaded from open access FDSN servers using ObspyDMT (Hosseini & Sigloch, 2017). These data are then processed to prepare for the array-based approach used in Section 7.3.2.

The processing begins by discarding traces if they have gaps or missing data and rotating any horizontal components into the N and E orientations (if they are not already), using the component orientation stored in the metadata. The data then have their instrument response deconvolved into units of velocity, are linearly detrended, demeaned, have a 5% end taper applied, are bandpass filtered, resampled to 10 Hz and normalised to their peak amplitude. The bandpass filter applied depends on the component. Z component data is filtered between 0.1-1.0 Hz using a 3-corner Butterworth filter, whilst horizontal components are filtered between 0.03-0.2 Hz. For the duration of the seismic data processing, the Z components and horizontal components are handled independently, with horizontal

components for a station only being processed if the station has 3-component data.

7.3.2 Array processing

To determine the *P*, *pmP*, *pP*, *sP*, *S* and *sS* phases, for refining the event locations and calculating Moho depth (see Sections 7.3.3 and 7.4, and Chapters 2, 4, 6), array processing is used to boost the phase signal-to-noise ratios for automatic picking.

7.3.2.1 Creating *ad-hoc* arrays

Each event has their processed Z component seismic data grouped into *ad-hoc* arrays (see Section 2.2.3) using a combination of DBSCAN clustering and Ball-Tree nearest neighbour algorithms (Pedregosa et al., 2011). The DBSCAN algorithm searches for sufficiently dense station distributions to form arrays with at least 10 stations within a 2.5° aperture, and identifies a central core station per array. The nearest neighbour algorithm selects the stations within each core station's aperture to generate *ad-hoc* arrays. For the example event, which occurred on 25th July 2016 in Chile, there are 1789 stations with processed Z component data, which are clustered into 88 *ad-hoc* arrays containing 1229 of the available stations (Figure 7.2). Therefore, there are 560 stations with Z component data which were not incorporated into an *ad-hoc* array – these stations are located too sparsely to generate an array which fits the density parameters.

The Z component seismic data, for targeting *P* coda arrivals, are now arranged into *ad-hoc* arrays. However, for targeting *S* coda arrivals (*S* coda processing is optional throughout this workflow), the available 3-component stations are assembled into the same *ad-hoc* arrays. Typically there are less stations available with all 3 components, which can cause a number of 3-component *ad-hoc* arrays to have less than the required 10 stations or no stations at all. For the SASZ, 285,213 *ad-hoc* arrays are generated for the entire initial catalogue using Z component data, and only 89,024 *ad-hoc* arrays with 10 or more stations are re-created using 3-component data (31.2%). For the example event from the 25th July 2016, there are 88 *ad-hoc* arrays created from the Z component data, with only 72 from the 3-component data. Despite the reduction in *ad-hoc* array quantity, designing the *S* coda workflow to be dependent upon the *P* coda workflow significantly simplifies the approach.

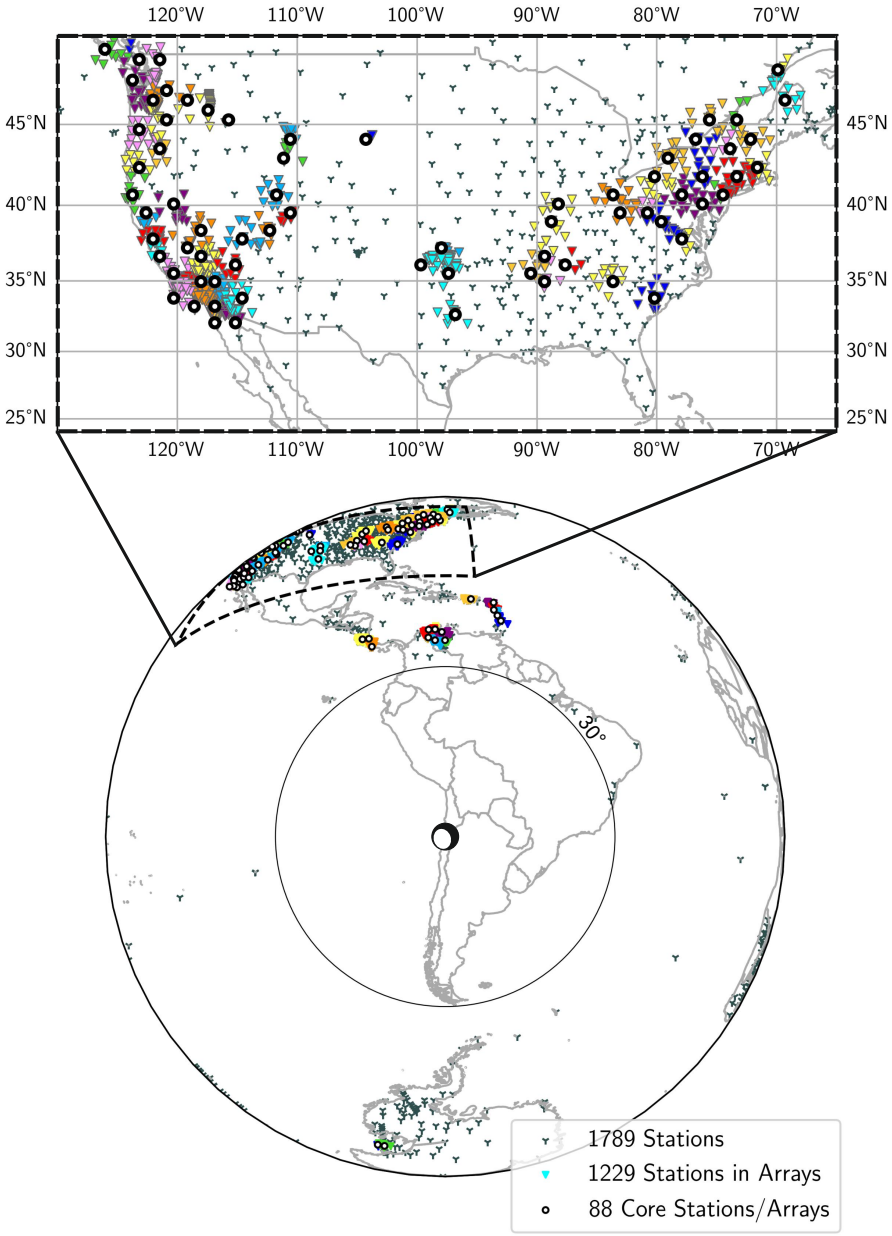

Figure 7.2: Example of the *ad-hoc* array creation process for a m_b 6.0 event from 25th July 2016 located in Chile, showing a global distribution of teleseismic stations with processed Z components and the subsequent *ad-hoc* arrays (bottom), and a zoom in of the *ad-hoc* arrays created in the USA (top). The core stations per *ad-hoc* array are shown as thick black circles and the associated *ad-hoc* array stations as coloured triangles. The unused stations (grey Ys) are those removed via the DBSCAN routine, prior to the Ball-Tree process. The earthquake focal mechanism is taken from the Global Centroid Moment Tensor Project (GCMT) (Dziewonski et al., 1981; Ekström et al., 2012).

7.3.2.2 Determining best fit backazimuth and slowness

After the *ad-hoc* arrays have been established, the approach can take advantage of array processing, as previously discussed in Chapters 2 and 3, to boost the signal-to-noise ratios of the small amplitude depth phases (*pmP*, *pP*, *sP* and *sS*). For both the Z and 3-component versions of each *ad-hoc* array, the best fitting backazimuth and slowness for the P and S waves are found directly from the station data by beampacking the arrivals. The Z component *ad-hoc* array data are trimmed around the ak135 (Kennett et al., 1995) modelled P arrival, and beamformed with a range of test slownesses (± 0.04 s/km in intervals of 0.001 s/km) and backazimuths ($\pm 15^\circ$ in 1° intervals) centred on the expected values calculated using ray tracing (Crotwell et al., 1999). The backazimuth and slowness which construct the largest amplitude beam are selected as the best fitting beamforming values.

For a 3-component *ad-hoc* array, the best fitting backzimuth found from the Z component data is used to rotate the horizontal components into radial and transverse orientations. If the Z component *ad-hoc* array fails to provide a beampack determined backazimuth, the ray path calculated backzimuth is used instead. Given that the approach intends to pick S and *sS*, the transverse (T) component is taken forward for further analysis. The best fitting slowness and backazimuth are searched for using the same beampacking approach applied to the Z component data, however this time the T component data is trimmed to include the ak135 (Kennett et al., 1995) modelled S arrival, and the test ranges straddle the expected S wave slowness and backazimuth.

Figure 7.3 shows examples of the beampacking parameter search to extract the best fitting slowness and backazimuth values for both P and S waves (filled red circles on a and d), and their resultant beams (c and f), for the same *ad-hoc* array. A comparison to the expected values is additionally provided (hollow red circle on a and d), and the beams they would construct (b and e). It is clear that using data derived beamforming parameters can significantly improve the wavelet geometry and signal-to-noise ratio of the depth phases, which improves the ability to automatically pick the phases.

7.3.2.3 Data quality control

At this point in the workflow, I apply two data quality tests to ensure that only *ad-hoc* arrays with clear, coherent arrivals are considered for automatic picking (see Sections

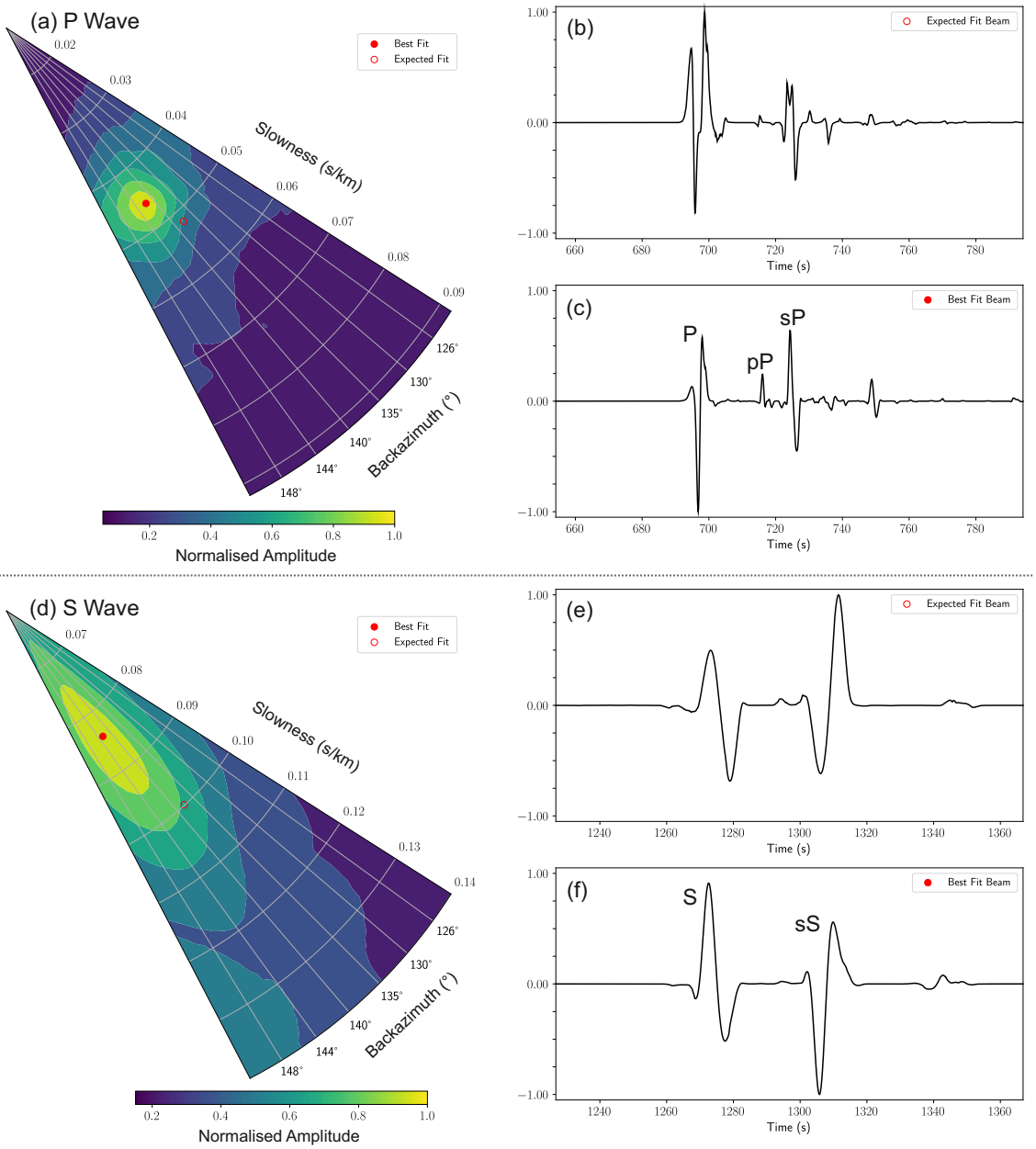

Figure 7.3: P and S wave amplitudes during beamforming in polar coordinates (backazimuth and slowness) to determine the best-fit backazimuth and slowness parameters directly from the *ad-hoc* array traces (a and d). The open red circle shows the expected slowness and backazimuth found through ray tracing and the corresponding phase-weighted beam in (b and e). The filled red circle shows the beampack derived values and the resultant phase-weighted beam in (c and f), showing the importance of measured backazimuth and slowness values. Example from m_b 6.0 event from 25th July 2016, *ad-hoc* array at 75.1° epicentral distance.

2.2.4.3 and 3.2).

The first test compares each trace in the *ad-hoc* array to the resultant optimum beam (created with the beampack determined slowness and backazimuth) using cross-correlation. If a trace has a cross-correlation coefficient less than 0.3 or requires a timeshift greater than 0.5 seconds to align the trace to the beam, then the trace is discarded. If the *ad-hoc* array has less than 8 traces after this test, the *ad-hoc* array is removed from further analysis. If the *ad-hoc* array has 8 traces or more, the *ad-hoc* array analysis begins again, to re-determine the best fitting slowness and backazimuth from the remaining traces, using the beampacking routine.

The second quality control test assesses the coherency of the arrivals in the *ad-hoc* array data, by considering their slowness vespagram. The vespagram beams are constructed using the same test slowness range used during the beampacking routine, and the beampack-determined backazimuth. On the resultant normalised vespagram, any peaks greater than 0.6 of the largest amplitude peak are selected, categorised into clusters using DBSCAN (Ester et al., 1996), and the cluster centres extracted. These cluster centres are expected to represent the P or S coda arrivals for the Z and T component *ad-hoc* arrays, respectively, and therefore, are expected to align along the beampack-determined slowness. If the clusters are prominent at an unexpected slowness on the vespagram, that is an indication that the *ad-hoc* array is too complex or poor quality to automatically pick. A set of criteria involving the cluster centres are outlined in Chapter 2 to identify poor quality vespagrams – if the mean slowness is within 0.006 s/km of the expected beampack-determined slowness and the standard deviation of the cluster centres is <0.0105 s/km, then I accept the *ad-hoc* array as passing the quality threshold. If these criteria are failed on either grounds, the *ad-hoc* array is discarded.

These quality control tests are separately applied to the Z and T component *ad-hoc* arrays for a given earthquake. However, for the T component *ad-hoc* array to be processed and analysed, the equivalent Z component *ad-hoc* array must have passed the quality standards set. Furthermore, since the T component *ad-hoc* arrays are arranged sub-optimally to match those created with the Z component data, and often have a reduced number of traces per *ad-hoc* array (hence a 68.8% reduction in *ad-hoc* arrays with more than 10 stations), the T component *ad-hoc* arrays are more sensitive to being discarded by the quality control tests.

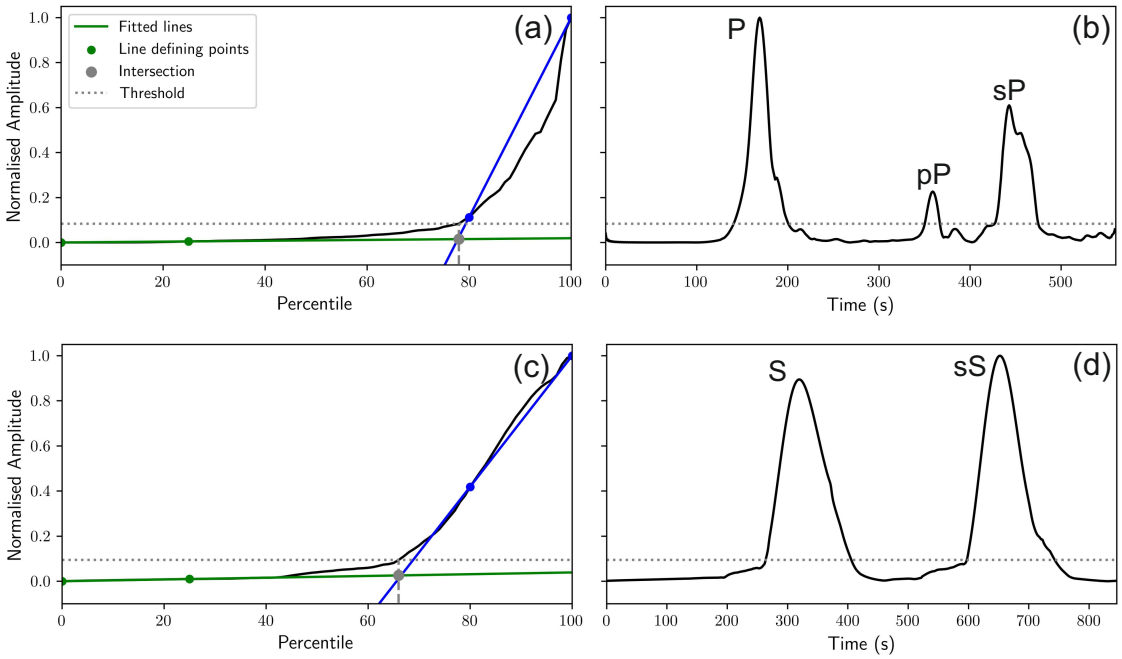

Figure 7.4: Example of the automatic picking threshold found for an *ad-hoc* array at an epicentral distance of 75.1° from the m_b 6.0 event on 25th July 2016. Distribution of amplitude values for the *ad-hoc* array beam with respect to the percentile, the approximation of the beam with two lines, their intersection and the final threshold found for the Z (a) and T (c) components (see Section 2.2.4.4 for more detail). Threshold relative to the phase-weighted beam for the Z (b) and T (d) components.

7.3.2.4 Automatic phase detection and identification

After the quality control routines have been applied, the *ad-hoc* array is eligible to be automatically picked using a threshold-based approach. The dynamic threshold for a given *ad-hoc* array is determined from the distribution of amplitudes in the optimum beam (see Section 2.2.4.4), by approximating the percentile (and thus, amplitude) after which larger amplitudes represent significant signal (Figure 7.4). Peaks which exist above this dynamic threshold, and have a prominence greater than 0.15 of the maximum peak found in the beam are selected as candidates for our phases.

These candidates are subsequently passed to a phase detection routine (see Sections 2.2.4.5 and 3.2) to determine the most likely trio of peaks for P, pP and sP from the Z component data, and the most likely pair of peaks for S and sS from the T component data, when compared to the ak135 (Kennett et al., 1995) modelled arrivals. The best fitting sets of P and S coda peaks are selected as the final phase picks (note that P and S candidate peaks are independently assessed, Figure 7.5), however if multiple trios or pairs of phases are appropriate for the phases, the largest combined amplitude sets are selected. Whilst pmP is not currently picked as an integrated part of this routine, the P coda vespagrams

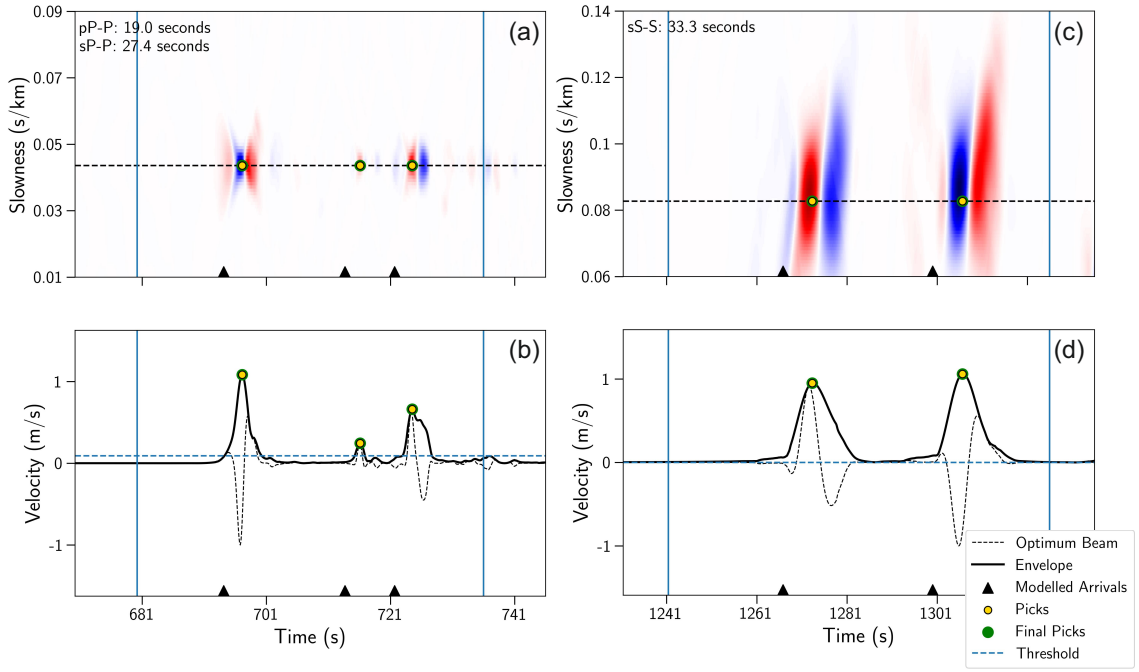

Figure 7.5: Example Z and T component *ad-hoc* arrays located 75.1° from the event, their automatic picks and differential times between phases for the m_b 6.0 event which occurred on 25th July 2016 in Chile. (a) and (b) are the vespagram and optimum beam respectively for the Z component *ad-hoc* array, whilst (c) and d) are the vespagram and beam for the T component *ad-hoc* array. Blue vertical lines indicate the time window of data used for automatic picking.

are used to detect *pmP* in a later portion of the workflow (see Section 7.4).

Each *ad-hoc* array for a given event is analysed as described in this section (Section 7.3.2), with each Z component *ad-hoc* array processed and analysed before the equivalent T component data. Figure 7.6 illustrates the success rate for the 25th July 2016 event, by showing which *ad-hoc* arrays produced phase picks for both the Z and T component data. The Z component data generated 88 *ad-hoc* arrays, resulting in 73 picked *ad-hoc* arrays (this could be *P* and either *pP* or *sP*, or all 3 phases). Whilst the T component data provided 72 *ad-hoc* arrays, using the previously defined Z component *ad-hoc* arrays, and 57 of those provided picks (both *S* and *sS*). The T component workflow suffers from a greater loss of data, due to the current requirement to construct the same *ad-hoc* arrays used for the Z component data, and link their processing to the success of the equivalent Z component *ad-hoc* array. In future, the T component workflow could be updated to process data independently of the Z component data to avoid this issue, although this would add to the processing time.

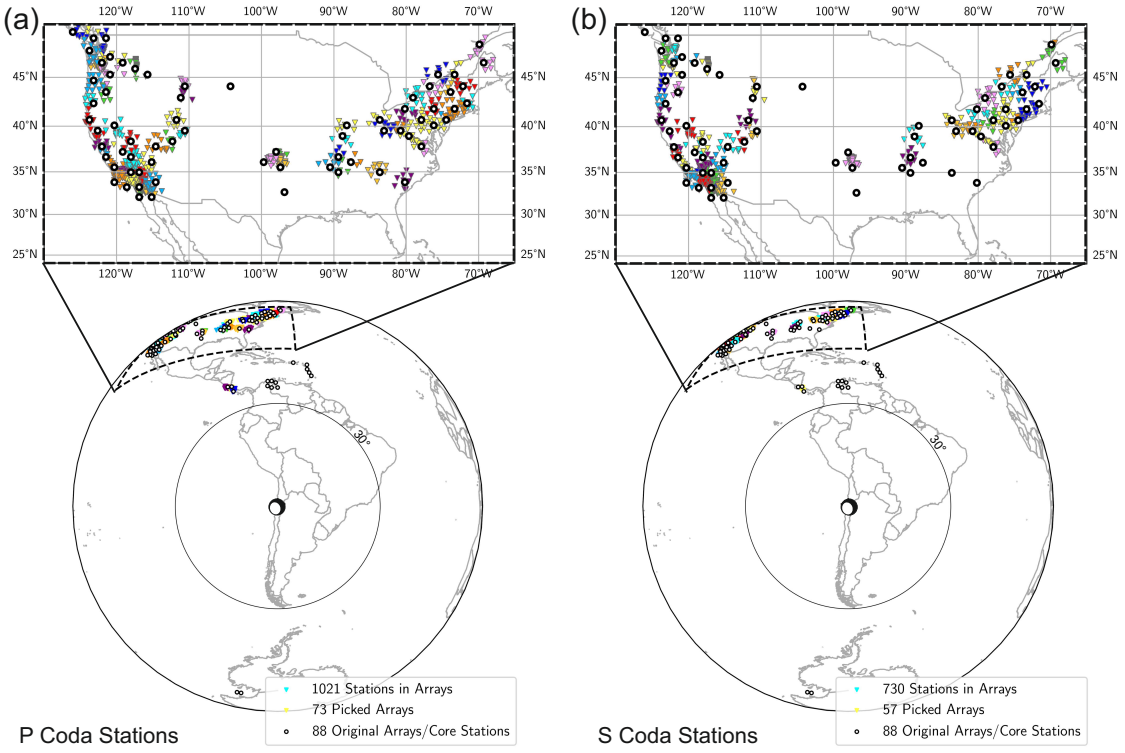

Figure 7.6: Global distribution of teleseismic stations in picked Z (P coda, a) and T (S coda, b) component *ad-hoc* arrays (bottom), and a zoom in of the USA *ad-hoc* arrays (top), from the m_b 6.0 25th July 2016 event. The initially created core stations per *ad-hoc* array are shown as thick black circles and the stations of picked *ad-hoc* arrays as coloured triangles. The earthquake focal mechanism is taken from the Global Centroid Moment Tensor Project (GCMT) (Dziewonski et al., 1981; Ekström et al., 2012)

7.3.3 ISCloc

For the SASZ, the *ad-hoc* array determined phases are combined with the ISC globally reported phase catalogues per event, to then relocate the event in 3D with the combined set of phases using ISCloc with a grid search-based inversion (Bondár & Storchak, 2011).

Before this can happen, the amplitude-based *ad-hoc* array picks need to be converted to absolute onset time. This is undertaken using the same approach as described in Chapter 4. For a given event, ISC reported direct P arrivals occurring within the *ad-hoc* array aperture are slowness corrected to the reference beamforming location for the *ad-hoc* array, and used to adjust the P coda amplitude picks. I purposefully limit this conversion to 2022 events and older, as the ISC will not have reviewed the phase catalogues and event locations which have occurred in the last 2 years (see Figure 4.1). Therefore the relocated catalogue will not include events from 2023 or 2024.

I extend this methodology to the S wave coda picks, using exactly the same approach, except ISC reported S arrivals are slowness corrected and used to convert the amplitude-based S and sS picks to onset times. Both corrections are limited by the availability of direct P and S arrivals within a given *ad-hoc* array aperture, with S coda arrivals rarely being converted as a result. The example earthquake from the 25th July 2016 only had 28.7% of *ad-hoc* arrays with S coda picks fail to be converted. However, 92.5% of all candidate T component *ad-hoc* arrays with picks fail to have a reported direct S wave arrival, resulting in 80.0% of events with S coda picks without a single converted phase. For comparison, only 25.0% of Z component *ad-hoc* arrays with picks fail to be converted to absolute time, which translates to 22.2% of events.

After the conversion of the *ad-hoc* array determined phases to absolute onset times, they are combined with the ISC reported phases to augment the phase catalogues per event. ISCloc (Bondár & Storchak, 2011) is subsequently used to relocate the event in 3D using the augmented phase catalogues, with associated hypocentral errors. This is repeated for all events with converted *ad-hoc* array determined picks.

7.3.4 Results

Figure 7.7 shows the new intermediate-depth earthquake catalogue for the SASZ, determined with the augmented ISC phase catalogues and ISCloc, with an example cross section to illustrate the differences between the earthquake locations with and without the *ad-hoc*

array determined phases, and when the phase catalogues are only augmented with the *P* coda picks.

1694 events have been augmented with 68,075 additional *ad-hoc* array derived phases, which provide a 50.0% increase in total depth phases (27.0% become time-defining (location defining)). As a result, there are 1046 events in the new SASZ intermediate-depth earthquake catalogue with free location solutions which incorporate *ad-hoc* array derived phases. Most events (784) fail to be relocated due to the need to convert the amplitude picks to onset times using reported direct phases (see Figure 8.1), especially for 2023/2024 events which are not currently considered for conversion (255 events with picks) – an alternative method independent of reported direct arrivals is presented in Chapter 5, to improve this in the future. 82 events also have had their number of depth phases increased to more than 5, which allows ISCloc to solve for depth when *ad-hoc* array determined phases are incorporated. The addition of *ad-hoc* determined phases has decreased the mean depth error by 0.47 km (see Appendix A.18) when compared to the reported ISC catalogue (relocated using ISCloc and the reported ISC phases, without any additional phases), with error reductions for 884 of the 1046 (84.5%) events.

The remaining cross sections are shown in Figures 7.8 and 7.9, with cross sections L-L', M-M' and O-O' illustrating previously identified slab features – the Pucallpa nest (L), and the diverging seismic planes (M, O) as discussed in Section 4.2.2. Cross section P-P' shows more examples of slab features, such as a clear aseismic gap in the upper 90 km of the plate between two planes of seismicity which further supports the presence of a DSZ in Chile (see Section 4.2.2), an aseismic gap in all seismicity between approximately 380-420 km from the trench, sub-horizontally aligned hypocentres at ∼190 km depth, and hypocentres sparsely clustered above the seismogenic slab at approximately 380 km from the trench (also observed on M-M' at ∼280 km, and N-N' in Figure 7.7b at ∼310 km from the trench). Finally Figure 7.9 shows cross section Q-Q', to highlight the seismicity in the Pampean flat slab and how the seismogenic slab thickness can be decreased when the *ad-hoc* array derived phases are incorporated into the earthquake relocation.

The cross sections also demonstrate the limited difference that including *S* and *sS* has had upon the event relocations. This is largely due to the relatively small number of *S* coda phases which were converted to absolute onset times, in order to use them with ISCloc (Bondár & Storchak, 2011). Only 830 *sS* phases were added to the reported ISC

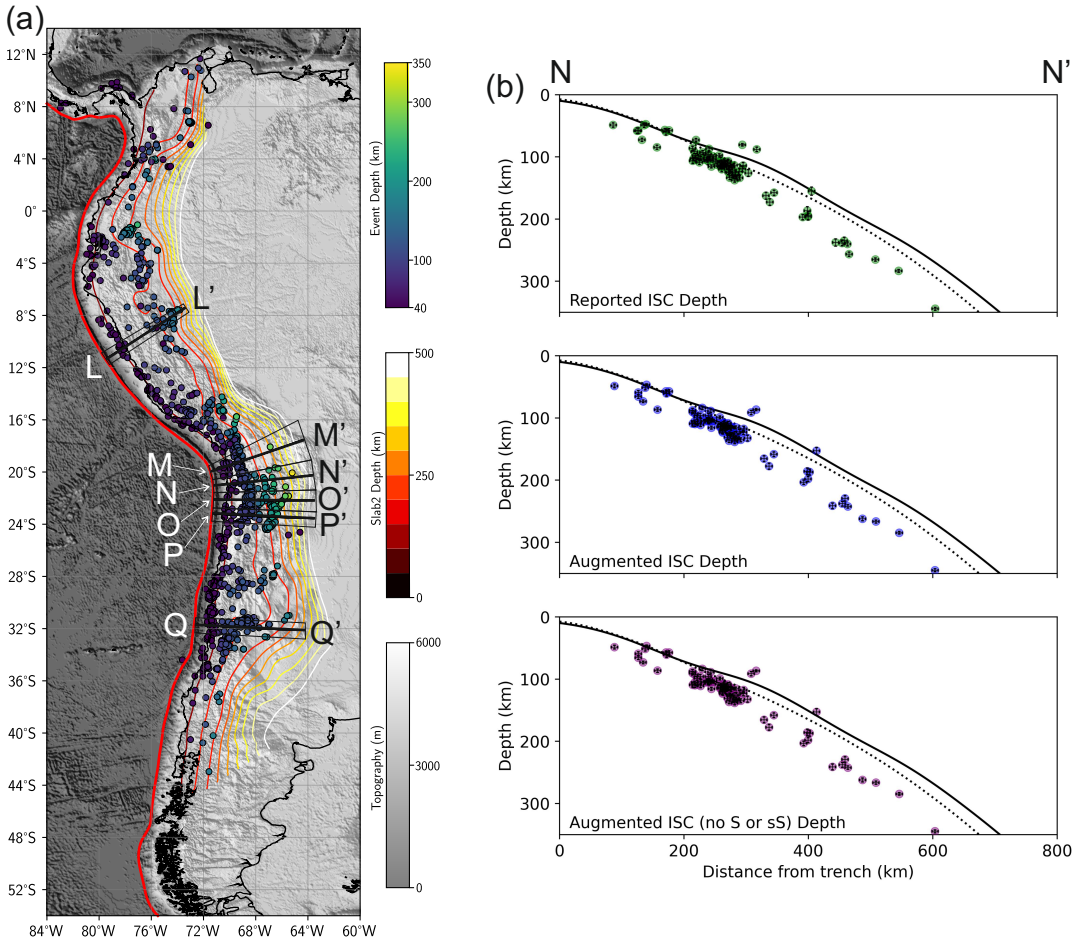

Figure 7.7: Map of the relocated intermediate-depth earthquakes (a), using the ISC augmented phase catalogues (which include *ad-hoc* array determined *P*, *pP*, *sP*, *S* and *SS* phases), with Slab2 contours (Hayes et al., 2018) and cross section locations. An example cross section is shown in (b) to show the difference between the earthquake catalogues determined using only the ISC reported phases (top), the ISC catalogue augmented with *P* and *S* coda picks (middle), and ISC catalogue augmented with only the *P* coda picks (bottom). Horizontal and depth error bars are plotted per event, they are often within the symbol diameter. Slab2 is plotted as a solid black line and Slab 1.0 is plotted as the dotted black line.

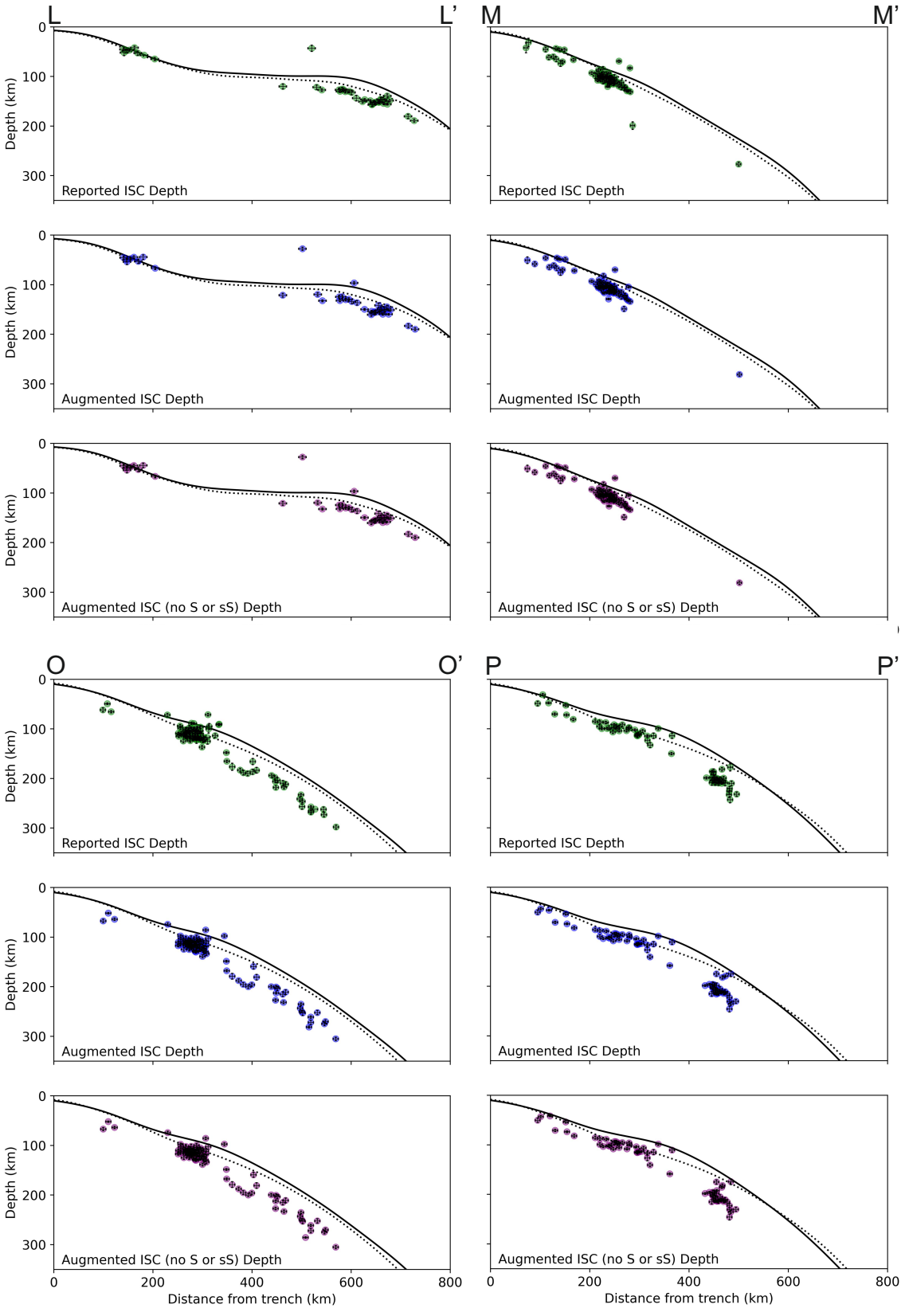

Figure 7.8: Example cross sections to show slab features, and the difference between the earthquake catalogues determined using only the ISC reported phases (top), the ISC catalogue augmented with P and S coda picks (middle), and ISC catalogue augmented with only the P coda picks (bottom). Horizontal and depth error bars are plotted per event, they are often within the symbol diameter. Slab2 is plotted as a solid black line and Slab 1.0 is plotted as the dotted black line. cross section locations visible in Figure 7.7.

phase catalogues, compared to 20,196 *pP* and 20,442 *sP* phases (see Appendix A.20, to compare phase additions). However, 238 *ad-hoc* array derived *sS* phases became time-defining for the ISCloc location solutions, this forms 52.7% of the total time-defining *sS* phases and indicates that whilst the final *sS* phases numbers are currently small, they are enhancing the reported ISC catalogue, although, the inclusion of *S* and *sS* does not currently translate to large depth error reductions. To demonstrate this quantitatively, the augmented catalogue using both *P* and *S* coda arrivals, and the augmented catalogue using only the *P* coda phases have the same mean depth error reduction relative to the reported ISC catalogue (0.47 km), and the nearly the same mean residual (2.50 and 2.52 km, respectively) between the augmented and reported ISC earthquake depths when *ad-hoc* array determined phases are incorporated (see Appendices A.18 and A.19).

Finally, the cross sections corroborate previous findings in Sections 2.4.3 and 4.2.2 that the global slab models are poorly fitting for the SASZ when considering the slab more than 400 km from the trench. For the entire region, particularly northern Chile, the Slab2 (Hayes et al., 2018) model needs to be deepened with respect to distance from the slab to prevent apparently thick down-going slabs of up to 50 km (Figure 7.8).

7.4 Moho depth determination

This section describes how the results from the 3D earthquake relocation (section 7.3) are leveraged to identify *pmP* arrivals (near-source *P* wave Moho reflection, and a pre-cursor to *pP* waves) and used to calculate Moho depth (see Chapter 6).

7.4.1 Inputs

The approach to detect *pmP* arrivals is the same as the method described in Chapter 6. Only Z component *ad-hoc* arrays which had a *pP* arrival picked during the array processing and analysis routine (Section 7.3.2) are considered during the approach, since *pmP* is a *P* coda arrival and several internal routines are dependent upon the *pP* arrival time.

Furthermore, by applying ISCloc (Bondár & Storchak, 2011), the algorithm inherently removes poorly fitting picks, which eliminates the need for a cleaning routine (previously used for 1D relocation in Section 2.2.5) for the *ad-hoc* array determined arrivals. However, for *pmP* detection, I use the direct outputs (vespagrams and picks) from the array processing and analysis routine which will include poorly fitting, outlying picks. I therefore

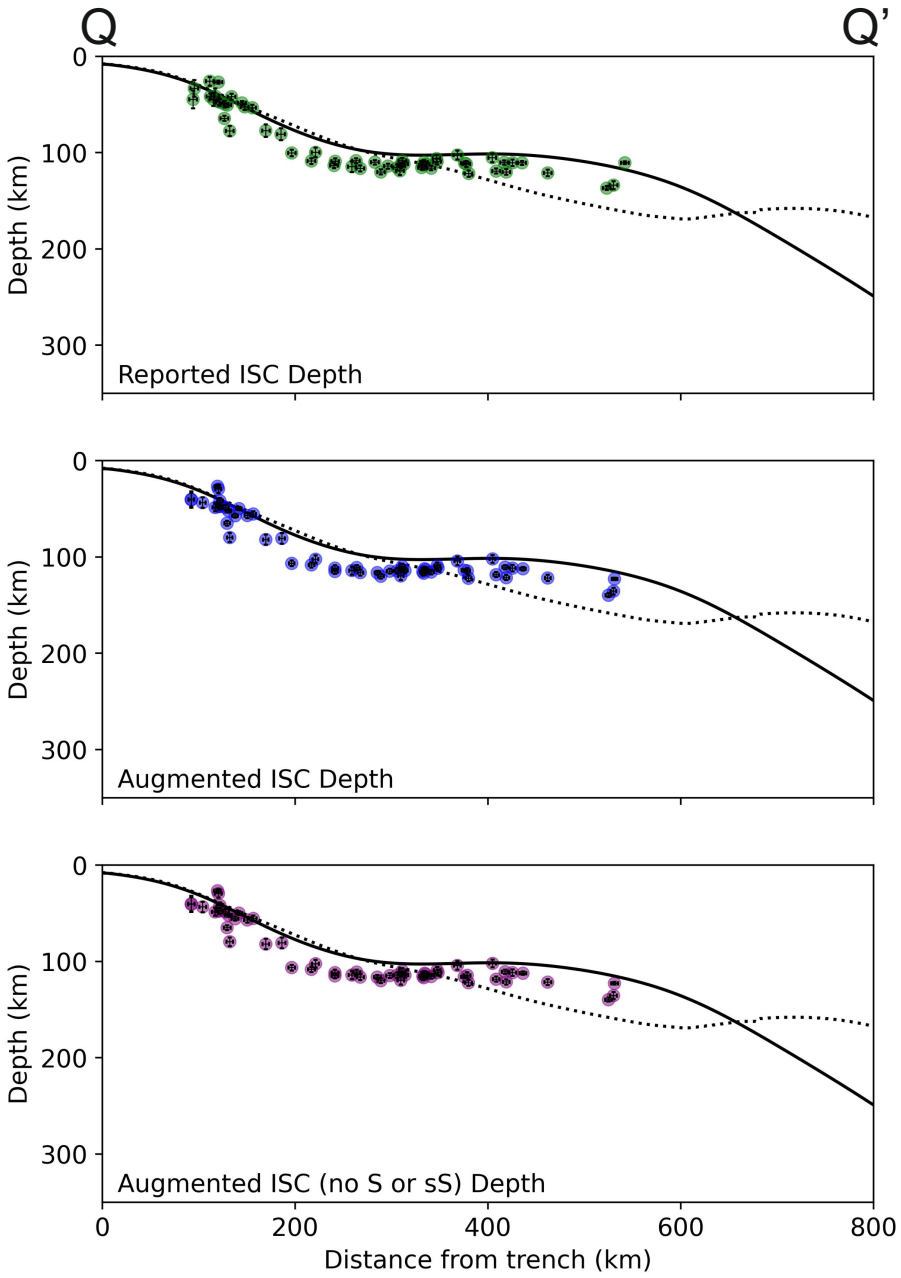

Figure 7.9: Example cross section to show slab features, and the difference between the earthquake catalogues determined using only the ISC reported phases (top), the ISC catalogue augmented with P and S coda picks (middle), and ISC catalogue augmented with only the P coda picks (bottom). Horizontal and depth error bars are plotted per event, they are often within the symbol diameter. Slab2 is plotted as a solid black line and Slab 1.0 is plotted as the dotted black line. cross section location visible in Figure 7.7.

apply the linear regression based cleaning routine used in Chapter 2 to remove anomalous *pP* picks, and hence *ad-hoc* arrays, from consideration.

An earthquake depth per input *ad-hoc* array is also required, to perform ray tracing calculations. For the 3D relocation used in Section 7.3, the amplitude picks identified during the array processing routine are converted to absolute onset times using reported *P* and *S* arrivals. This conversion relies on reported picks, which can cause good quality *ad-hoc* array data (especially all data from earthquakes in the last 2 years), and thus events, to be excluded from 3D relocation. For Moho depth determination using *pmP* arrivals, it is less important to have an accurate earthquake depth since the calculation uses the differential time between *pP* and *pmP*, and hence is independent of event depth. Therefore, to collate a larger number of *pmP* picks, I use the 3D relocated earthquake depth if available for an event, and if not, I use the original ISC determined event depth.

With the inputs of *pmP* detection established – cleaned Z component *ad-hoc* arrays with *pP* picks and corresponding source earthquake depths, either from the ISCloc relocation or the original ISC depth – the approach can begin.

7.4.2 pmP detection

Firstly for a given event, a first-pass crustal thickness is calculated for the epicentre using the Crust1.0 model (Laske et al., 2013), and a simplified velocity model to represent the 1D structure at the epicentre is built – this is the ak135 model (Kennett et al., 1995), truncated at the first-pass crustal thickness, and replaced with a constant *P* wave velocity of 5.9 km/s for the crust.

Each candidate *ad-hoc* array for the event is subsequently analysed for *pmP* arrivals, using a ±2.5 second search window on the phase-weighted optimum beam (Figure 7.10). The temporal placement of the search window is determined by calculating the modelled differential arrival times for *pmP* and *pP* (using the simplified 1D velocity model), and removing the differential time from the *ad-hoc* array identified *pP* pick. Any picks within the search window with a prominence greater than 0.05 of the *P* wave arrival and demonstrate a signal-to-noise ratio of greater than 8 are selected as *pmP* candidates. Here, there could be either zero, one or multiple pick candidates – if there are zero, there is no *pmP* pick for the *ad-hoc* array, if there is one pick it is selected as the *pmP* arrival, and if there are multiple, the pick with the greatest signal-to-noise ratio is selected.

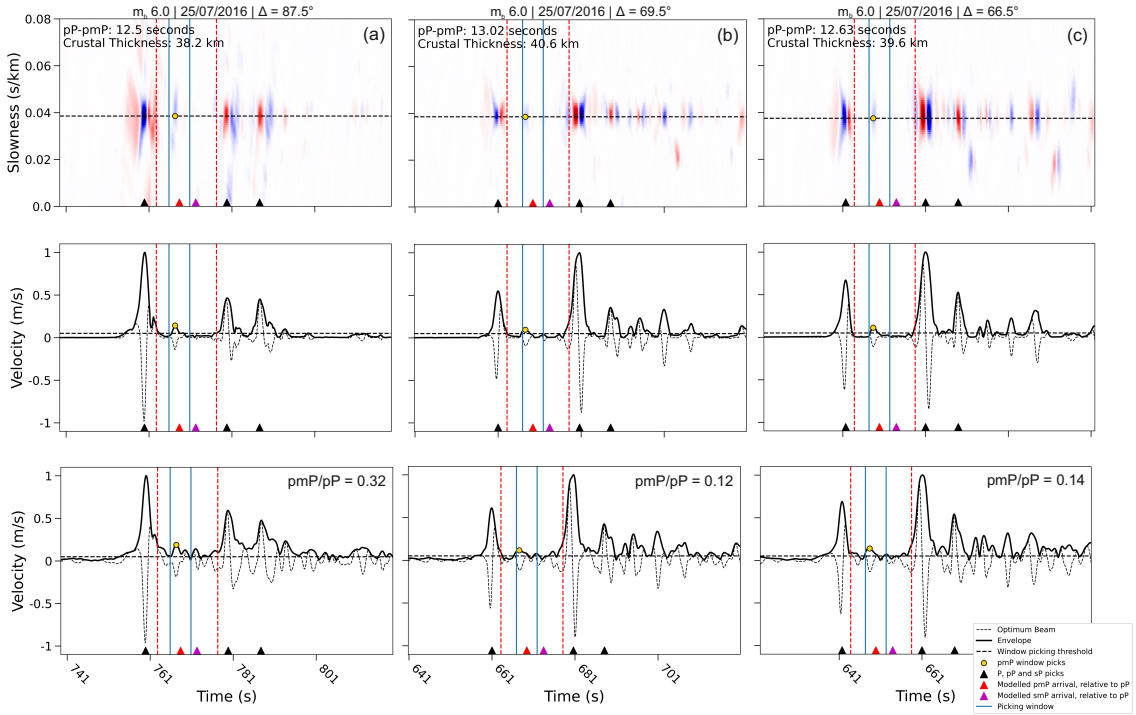

Figure 7.10: Example *ad-hoc* arrays, with their vespagrams (top), phase-weighted optimum beams (middle) and linear optimum beams (bottom) for a single event from 25th July 2016. (a) Shows *ad-hoc* array 87.5° epicentral distance with relative amplitude of 0.32. (b) Shows *ad-hoc* array 69.5° epicentral distance with relative amplitude of 0.12. (c) Shows *ad-hoc* array 66.5° epicentral distance with relative amplitude of 0.14. The bounce points for the *ad-hoc* arrays exist from east to west for (a) to (c). The red dashed lines indicate the time series which the *pmP* search window can exist within.

7.4.3 Conversion to crustal thickness

For each *ad-hoc* array with an associated *pmP* arrival, the differential time between *pP* and *pmP* is calculated and converted to a crustal thickness using a simple forward model. The test Moho depths range from ±15 km around the first-pass crustal thickness depth from Crust 1.0 (Laske et al., 2013), and step in intervals of 200 m. If the test range extends below the event depth, the test range is truncated to the event depth. Similarly, if the test range extends above the surface of the earth, it is truncated to 0 km depth. For each test Moho depth, a new 1D velocity model is generated to represent the test crustal thickness – using ak135 (Kennett et al., 1995) with a uniform 5.9 km/s crustal *P* wave velocity – and the modelled differential times for *pP* and *pmP* calculated. The test Moho depth with the smallest residual to the observed differential time is selected and associated locationally to the *pmP* bounce point coordinates.

The approach is repeated for each earthquake, and for every candidate Z component *ad-hoc* array to generate a catalogue of *pmP* bounce point coordinates and their determined crustal thickness/Moho depth. Following the method in Chapter 6, I remove events with a relative amplitude between the phase-weighted *pmP* and *pP* picked arrivals greater than 1.72. This removes accidentally picked complex *P* wave coda, which masks real *pmP* arrivals.

7.4.4 Results

For the SASZ, 2965 *pmP* picks were found from 27,362 candidate *ad-hoc* arrays (provided by 554 different earthquake events), to give a success rate of 10.8%. 285,213 *ad-hoc* arrays were initially created from Z component data, giving a success rate of 1.04% from start to end of the earthquake relocation and Moho depth determination approaches.

Figure 7.11 illustrates the locations of the 554 source events for the picked *pmP* arrivals (left), the Moho depth data points calculated using the *pmP* and *pP* arrivals (centre), and the linearly interpolated Moho depth/crustal thickness map for the SASZ (right). On the crustal thickness map, there is a clear spine of thickened crust which exists parallel to the subduction trench between approximately latitudes 8°S to 12°S, and reaching a maximum thickness of 80.8 km (which corroborates the crustal thicknesses previously found for Peru and northern Chile in Section 6.3.1). The crustal thickness is poorly constrained inland, due to the limited extent of intermediate-depth earthquakes, which inhibits measurements

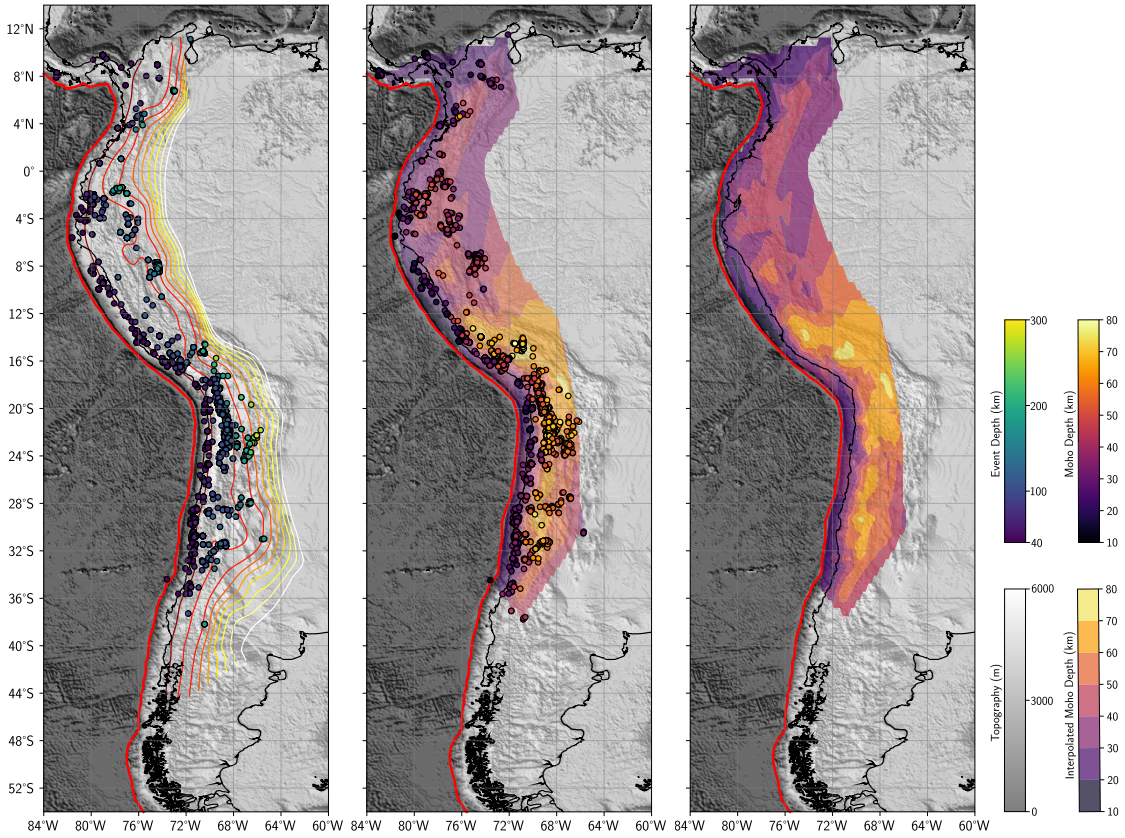

Figure 7.11: The 554 source earthquake events for the picked *pmP* arrivals, with Slab2 contours for the down-going Nazca Plate (Hayes et al., 2018) (left). The *pmP* bounce points and associated Moho depths calculated using the differential time between *pmP* and *pP* arrivals, with the Moho depth linear interpolation underneath (centre). The linearly interpolated Moho depth/crustal thickness map for the SASZ (right).

of the thickened crustal spine width. The observed spine fits well with the previously identified Altiplano (high elevation plateau) in northern Chile (Zandt et al., 1994), and the higher resolution map (than receiver functions, see Section 2.3) demonstrates the second order thickness variation as the Altiplano grades to thinner crust. The regional crustal thickness map could have positive implications for isostatic studies in the region, and research into the structural and arc volcanism complexity which exists in the crust.

Similarly to Section 6.3.4, I provide extra analysis of the *pmP* to *pP* relative amplitudes, extracted from the un-phase-weighted optimum beam (Figure 7.10) and normalised using a modelled *pmP*/*pP* amplitude per *pmP* pick, to investigate the mechanical nature of the Moho. In general, small ratios may indicate a lack of sharp impedance contrast or greater interface roughness at the Moho. For the relative amplitude data points which equal approximately one, these represent locations where the observed ratio is as modelled, and likely the only amplitude difference between the phases prior to normalisation is caused by the reflection coefficients of the free surface and Moho. Finally, the large relative amplitude

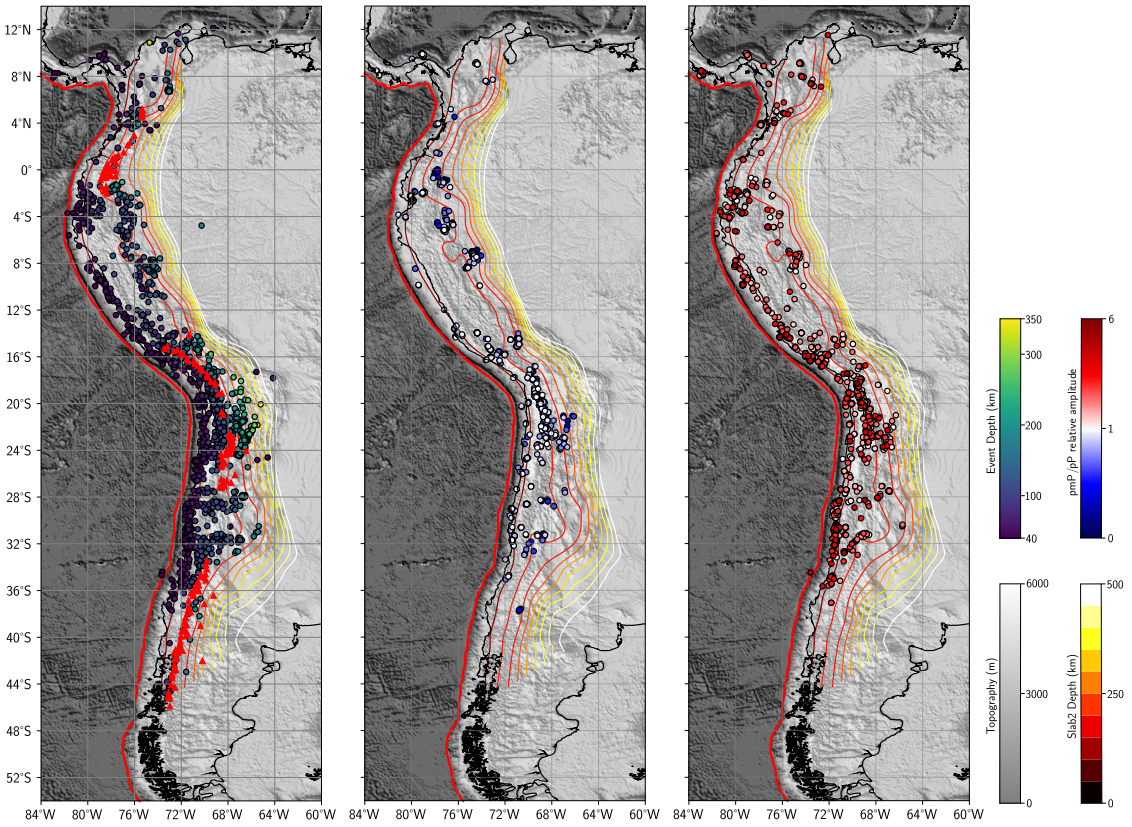

Figure 7.12: Locations of all 1693 possible source earthquakes for *pmP* analysis, using the 3D relocation if available or the original ISC location otherwise, alongside the locations of Holocene volcanism (Global Volcanism Program, 2024) with red triangles (left), the *pmP* bounce points with a normalised pmP/pP relative amplitude less than or equal to 1 (centre), and more than 1 (right).

data points imply that the *pmP* waves are experiencing significantly less attenuation along their ray path than the *pP* waves, and greater reflection at the Moho. This could be a case where the crust is particularly attenuating for *pP* waves due to structural complexity, whilst the *pmP* wave is reflecting off a sharp Moho impedance contrast.

Figure 7.12 shows the locations of all of the possible source earthquakes for *pmP* analysis, using the 3D relocation if available or the original ISC location if not, alongside the locations of Holocene volcanism (left), the *pmP* bounce points with a normalised pmP/pP relative amplitude less than or equal to 1 (centre), and more than 1 (right). Generally there is a mixture of pmP/pP relative amplitudes within close proximities of one another, indicating that Moho impedence varies on a local scale – likely influenced by arc volcanism, fluids and other discrete chemical factors, as opposed to a thermal control which requires a larger diffusive distance.

However, the Peruvian latitudes (0° to 16°S) of the SASZ appear to display a strong

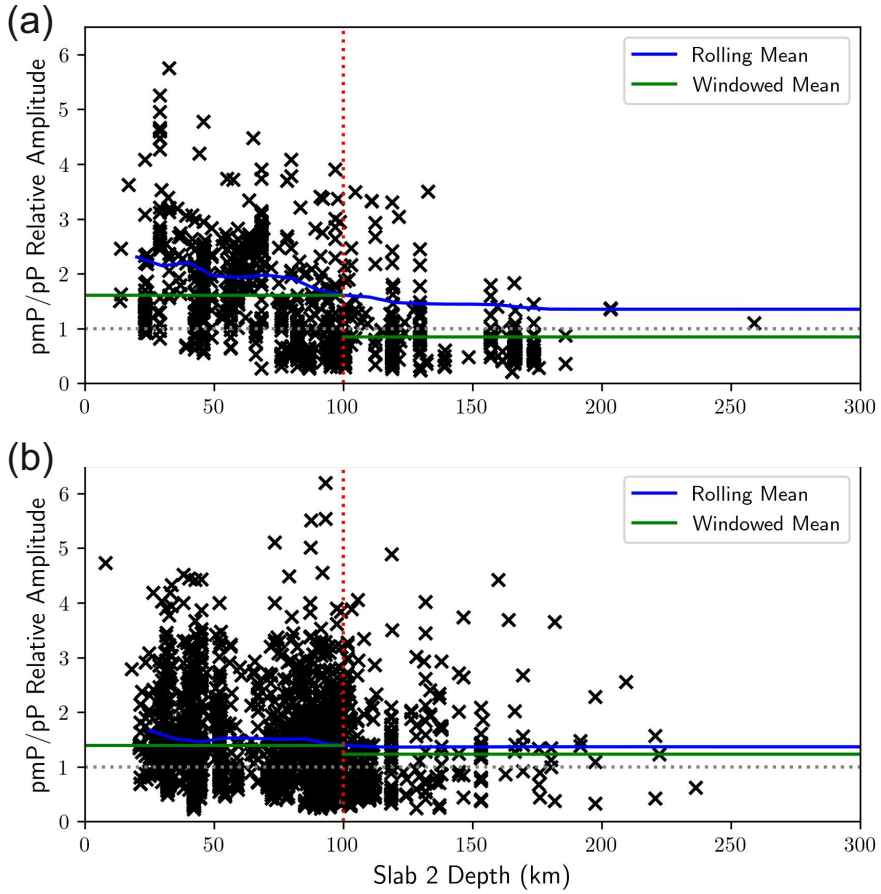

Figure 7.13: Normalised pmP/pP relative amplitudes plotted against the Slab2 depth at the same location, for the Peruvian latitudes (0° to 16°S, a) and the remaining latitudes (i.e. 12°N to 0° and 16°S to 45°S) on the SASZ (b). Vertical red dashed line indicates a 100 km slab contour, grey dotted line highlights a normalised relative amplitude of 1 (i.e. expected values), the blue line is a rolling mean and the green line shows the mean sub- and post- 100 km slab depth.

trend – few pmP/pP relative amplitudes show values less than 1 near to the trench, whilst abundant data points show pmP/pP relative amplitudes greater than 1. Inland, approximately around the 100 km deep contour for the Slab2 model (Hayes et al., 2018), pmP/pP relative amplitudes less than 1 are more abundant, and the number of data points with pmP/pP relative amplitudes greater than 1 decrease (also observed in Section 6.3.4). This hypothesis is tested by plotting the normalised pmP/pP relative amplitudes against the Slab2 depth at the geographical locations of the relative amplitude data points, for the Peruvian latitudes (0° to 16°S, Figure 7.13a) and the remaining latitudes for the SASZ (Figure 7.13b). These plots show that the Peruvian latitudes have a negatively correlating trend between normalised pmP/pP relative amplitude and the slab depth, which is more gradational (see the rolling mean) than the originally proposed discrete change from relative amplitudes greater than 1 to less than one over the Slab2 100 km deep contour (also tested in Chapter 6). However, there appears to be a relationship between the slab depth and the Moho mechanical strength, since the rolling mean of the normalised relative amplitude ratios settles into a constant lower mean between a slab depth of 100-120 km.

The gradational nature of the relative amplitude with respect to slab depth indicates a first order control over a larger distance, potentially thermally related. The lack of larger relative amplitudes towards the trench suggests higher pmP impedance at the Moho which decreases towards a slab depth of 100-120 km (assuming pP is experiencing a similar crust laterally). This could be caused by a colder, stagnant mantle wedge above the subducting flat slab where it has a depth shallower than 100-120 km, potentially identifying the location where the mantle begins to couple to the slab in Peru. Meanwhile, the same plot for the remaining latitudes of the SASZ pmP catalogue illustrates a lack of trend related to the slab depth. This could be related to the increased arc volcanism in these locations, or crustal delamination (Yuan et al., 2002), which may act to significantly overprint thermal controls locally, or perhaps the thermal control does not exist away from the Peruvian flat slab latitudes.

7.5 Conclusions

This chapter has demonstrated the application of both the 3D intermediate-depth earthquake relocation and Moho depth determination approaches, which rely upon *ad-hoc* array

determined *P*, *pmP*, *pP*, *sP*, *S* and *sS* phases, to the South American Subduction Zone (SASZ).

The resultant earthquake catalogue supports previously identified slab features, including the Pucallpa nest, a double seismogenic zone in Chile, and apparently linear seismic planes. The addition of *ad-hoc* array determined phases also decreases event depth errors for 80.8% of SASZ events. However, the addition and influence of the *S* wave coda phases is limited due to the sub-optimal organisation of 3-component seismic data into *ad-hoc* arrays, and a lack of reported *S* wave phases to the ISC to allow their conversion to absolute onset time.

The new regional Moho depth map for the SASZ corroborates the presence of the ∼80 km thick Altiplano in northern Chile, and illustrates to a higher resolution how the thickened crust grades to the north and south. Investigation into the relative amplitudes between *pmP* and *pP* at the *pmP* bounce points also reveals that whilst a first order thermal control may exist for the Peruvian flat slab Moho, indicating a cold mantle wedge above the slab when it is shallower than approximately 100 km, this trend does not persist elsewhere in the SASZ. Possible reasons for this may be that either the thermal trend is present elsewhere, yet is locally overprinted by the presence of arc volcanism and fluids, or that the thermal trend does not extend beyond the Peruvian flat slab due to the slab geometry controlling the location of cold mantle wedge.

Chapter 8

Discussion and Conclusions

In this chapter, I will briefly provide overviews of the previous chapters in Section 8.1, consider how they combine into a cohesive synthesis in Section 8.2 and discuss possible future direction in Section 8.3, before concluding the thesis.

8.1 Chapter overviews

8.1.1 Chapter 2: Automatic relocation of intermediate-depth earthquakes using adaptive teleseismic arrays

Chapter 2 introduced a new methodology to relocate intermediate-depth earthquakes, particularly targeting subduction zones events occurring between 40-350 km deep, and m_b 4.7-6.5. This approach takes advantage of the increasing availability of teleseismic stations to construct adaptive *ad-hoc* arrays and apply array processing techniques to their data in order to boost the signal-to-noise of the P, pP and sP arrivals. These arrivals are consequently able to be detected, identified and selected automatically using a dynamic threshold approach. The differential times between the depth phases (pP and sP) and their direct P arrival are used in tandem with a 1D local velocity model to convert to a new event depth, using a forward model. Jack-knifing is employed to determine suitable depth errors per relocated earthquake event, taking into account the dependence of each *ad-hoc* array result on a single contributing station trace. Relocations for events in northern Chile provide positive verification of the methodology, when analysed with comparable datasets (e.g. Craig (2019)). The approach is additionally applied to the Peruvian flat slab – a region without a cohesive previous intermediate-depth earthquake catalogue from

teleseismic data.

I find that my relocated earthquakes for both northern Chile and Peru corroborate features found by previous, local investigations, including the transitions of the slab from a continuously dipping geometry, to a flat region bounded by two clear slab bends, and back to a normal subduction configuration moving southward from northern Peru to northern Chile (Cahill & Isacks, 1992), the presence of the Pucallpa seismic nest (Wagner & Okal, 2019), and the observation that Peruvian seismicity intensifies in three broad latitude zones (Hasegawa et al., 1978). For Peru, the seismicity tends to exists on the bounding bends of the flat slab, with a largely aseismic flat section between – I interpreted this as supporting a flexural bending hypothesis for intermediate-depth earthquake nucleation, likely enabled through dehydration embrittlement. I also note the poor fit between the Slab2 model (Hayes et al., 2018) for the slab surface and the relocated hypocentres for both Peru and northern Chile, which indicates the need for a regional update.

The key limitations of the approach, are:

- An assumed point source – events are relocated assuming a single slip patch, hence I introduced an upper limit of m_b 6.5 for earthquakes to which I apply this technique.
- Use of a 1D velocity model – the approach uses a global 1D velocity model to convert the differential times to depth, and ignores local 3D velocity variations.
- The inability to relocate shallow events – the depth phases are unlikely to separate sufficiently from the direct arrival, depending on the event magnitude.
- Dependence upon the focal mechanism orientation – proximity of an *ad-hoc* array to a nodal plane will reduce the likelihood of recording arrivals.
- Station density – *ad-hoc* arrays will not be created if ten stations are not located within 2.5° of one another, leaving many less dense station installations outside the analysis.
- Automation – higher quality thresholds are imposed to ensure only good quality results influence the relocation, therefore some good quality results may be discarded alongside those of poor quality.
- Maximum catalogue depth error – the approach will only accommodate a ±40 km depth relocation from the original depth. Events which are more than 40 km deeper

or shallower than the original catalogue depth will not be relocated correctly. Events with exactly 40 km difference from the original catalogue are removed, as they are likely representing an artifact of this limit.

8.1.2 Chapter 3: Automatically detecting *S* and *sS* on teleseismic data

In Chapter 3, I demonstrate how S and sS arrivals could also be detected and identified using the approach from Chapter 2, with small modifications to target the longer period waves on transverse component data. The modifications include downloading 3-component seismic data, and rotating the horizontal components into radial and transverse, adjusting the bandpass filter to lower frequencies, and adapting the phase identification routine.

The arrivals are picked for the same *ad-hoc* arrays as those created using the single component, P coda approach seen in Chapter 2. This does mean that the success of the S coda picks is reliant upon, and limited by, the success of the P coda *ad-hoc* arrays. However, spatially linking together the P and S coda processing simplifies the phase results, and their ability to be incorporated into an external relocation algorithm (as seen in Chapters 4 and 7).

8.1.3 Chapter 4: Assessing the impact of automatically-derived depth phases on global earthquake catalogues, and their relocation

For Chapter 4, I developed a method to integrate the amplitude picks for P, pP, and sP (which also works for S and sS) into reported ISC phase catalogues, to be used in 3D event relocations using ISCloc. For each *ad-hoc* array, the approach requires a reported direct arrival within the array aperture, this is then slowness corrected to the geometric centre of the *ad-hoc* array and used to convert the peak P, pP, and sP picks into absolute onset times. Unfortunately, the dependence upon a reported phase in the global phase catalogues limits the success of the phase conversions, particularly S and sS, and is something which is addressed in Chapter 5. For the current approach (summarised in Appendix A.15), however, there is a high loss of data points during the conversion process (see Figure 8.1).

After the *ad-hoc* array determined phases are added to those in the reported phase list per earthquake event, I relocate the events using ISCloc (Bondár & Storchak, 2011) and analyse the improvement that the new phases provide in terms of locational error reduction. It is clear from this work that the addition of depth resolving phases reduces depth error in 99.9% of cases, with error reduction being particularly responsive to the addition

of *sP* phases.

The newly relocated Peruvian and northern Chile catalogue also demonstrates the benefits of 3D relocation, with the catalogue showing events which are now deeper than those described in Chapter 2 due to the addition of bounce point corrections, and generally more aligned along apparent slab features. One feature of the new catalogue I assessed is whether there is the presence of a double seismogenic zone (DSZ) in northern Chile – this is tested similarly to Brudzinski et al. (2007), using histograms of slab corrected hypocentral depths. I find that whilst a DSZ is hinted at, there are not currently sufficient data points to be confident on the basis of global seismic data alone.

8.1.4 Chapter 5: Using PhaseNet to pick absolute travel times on teleseismic vespagram data

Chapter 5 was motivated by the need to convert relative time, amplitude picks for *P*, *pP*, *sP*, *S* and *sS* from the approach outlined in Chapters 2 and 3 into absolute time for integration into existing global arrival catalogues (see Chapter 4). A methodology for the conversion is discussed in Chapter 4, however it results in a high failure rate due to its dependence upon reported direct arrivals. Therefore, in this chapter I investigate if a machine learning traveltime picker could successfully pick direct *P* arrivals on phase-weighted beams generated from my *ad-hoc* array data, to be used for peak to onset pick conversion.

I find that the pre-trained PhaseNet (W. Zhu & Beroza, 2019) machine learning model picks direct *P* waves on teleseismic data accurately, despite its training on local/regional seismic data from Californian earthquakes, although their associated probability is very low. In addition to this, I test if PhaseNet can pick multiple beams from a single *ad-hoc* array, generated under a horizontal slowness grid search, which can subsequently be used to define a pick error. PhaseNet succeeds in picking the direct *P* arrival on the best-fitting (optimum) beam, and a large proportion of the other test beams. I suggest that this Chapter acts as a proof of concept, and demonstrates that a machine learning picker has the potential to replace the current conversion of peak amplitude picks to absolute onset picks in Chapter 4, and perhaps the threshold based picking routine developed in Chapter 2, whilst providing associated picking errors. The low probability of the PhaseNet picks on the teleseismic array data, despite clear arrivals, strongly indicates that the model needs to be re-trained on appropriate teleseismic data to provide the greatest, highest confidence

success in this application.

8.1.5 Chapter 6: Crustal thickness determination using pmP phases identified from adaptive teleseismic array data

It is clear, from Chapters 2 and 3, that the foremost advantage of the developed approach for identifying depth phases is its ability to significantly boost the signal-to-noise of small amplitude arrivals. There are many other small amplitude, yet informative, phase arrivals which it may also be beneficial to detect, identify and apply to research questions. I look into leveraging the *ad-hoc* array P coda vespagrams for detecting pmP arrivals (near-source Moho reflected P wave) in Chapter 6.

By using the Crust1.0 global crustal thickness model (Laske et al., 2013), a 1D velocity model with a constant velocity crust, and the already identified pP arrivals from Chapter 2, I establish a search window for pmP. If a pmP phase is detected in the search window, its relative time to the picked pP arrival is used to forward model a best fitting crustal thickness (or Moho depth). When applied to an entire earthquake catalogue, in this case Peru and northern Chile, I automatically generate regional Moho depth maps and validate them against receiver function studies.

Again, there is a high failure rate for detecting pmP arrivals, due to their low amplitudes and likely overlap with the direct arrival. However each *ad-hoc* array with a pick provides a unique Moho sample point, which increases the data points defining the Moho depth. The resolution of each sample area is also smaller than those typically sampled by receiver functions, which may additionally provide greater insights into smaller order Moho structure.

I also analysed the relative amplitudes of pmP to pP to understand the mechanical nature of the Moho boundary, and find that pmP arrivals tend to display larger than expected amplitudes relative to pP when sampling the Moho above the shallow (<100 km deep) subducting slab, and this trend gradually reduces to showing Moho sample points with larger than expected pP amplitudes relative to pmP with respect to distance from the trench. I also observe significant overlaps to this trend, where higher and lower than expected pmP/pP amplitude ratios exist within a kilometer of one another. The first order trend may indicate the influence of a cold mantle wedge corner/nose, which increases the impedance experienced at the Moho between the crust and mantle. At approximately 100

km depth, the down-going slab may, therefore, be coupling viscously with the mantle wedge to eliminate the cold nose and decrease Moho impedance. The second order variation may demonstrate the interplay of arc volcanism, structurally complex crust and hydrated (and thus dehydrating) subducting slab features with the first order control.

8.1.6 Chapter 7: South American Subduction Zone: a case study

To demonstrate the capabilities of the techniques developed throughout the thesis, I apply all of the approaches discussed in Chapters 2, 3, 4 and 6 to a continental scale dataset – the South American Subduction Zone (SASZ) – to generate a new intermediate-depth earthquake catalogue (relocated in 3D) and regional Moho depth map. The chapter details how the different approaches interact with one another, and begins to draw together the observations from the preceding Chapters which focussed on Peru and northern Chile. Interpretation and discussion from this chapter are included in the synthesis, since the SASZ dataset overlaps and integrates all of the previous chapters.

8.2 Synthesis

I have developed a final workflow (see Appendix A.15) to create *ad-hoc* arrays from globally available teleseismic stations, apply array processing techniques to boost the signal-to-noise of small amplitude depth phases and pick *pmP*, *P*, *pP*, *sP*, *S* and *sS*. The final picks can either be relocated in 1D using the relative time to depth conversion routine demonstrated in Chapter 2 or relocated in 3D using ISCloc (Bondár & Storchak, 2011), as seen in Chapters 4 and 7.

The *ad-hoc* array processed data can be further leveraged to detect *pmP* arrivals automatically, which in turn can be used to constrain Moho depths when considered in conjunction with *pP* arrivals and a 1D velocity model. The workflow has been applied to the entirety of the South American Subduction Zone in Chapter 7 to generate a 3D relocated intermediate-depth earthquake catalogue using *P* and *S* coda picks, with associated location errors, and a Moho depth map for the region.

8.2.1 3D relocation improvements

The 3D relocation with ISCloc is a significant improvement upon the 1D, depth-only relocation model used in Chapter 2, since it incorporates a bounce point correction – a

vital step when working in a region with highly-variable topography, like the spatially variable Andes – and combines the *ad-hoc* array determined picks with globally reported phases catalogued by the ISC. The *ad-hoc* array determined phases augment the ISC phase catalogues, and add a greater number of depth phases to constrain depth and the associated depth error.

Chapter 4 demonstrated that the addition of these phases decreased event depth error in 99.9% of events, and enabled 30% more events to be solved freely for depth (this requires more than 5 depth phases to exist in the phase catalogue). Notably, events which had few initial depth phases in their ISC reported phase catalogues displayed the largest depth error reductions after the addition of *ad-hoc* array determined depth phases – especially the addition of *sP* (see Section 4.2.1.3). This shows that a proportional increase in a depth phase is more impactful to the relocation than an event which already had a high number of depth phases reported.

Error reductions from depth phase additions were also reflected in the 3D relocated SASZ catalogue presented in Chapter 7, where 84.5% events had their depth error reduced. A thorough analysis into the significance of *sS* additions on depth error reduction was not possible due to the limited numbers of phases which were converted to onset times, however the *ad-hoc* arrays boosted the number of location defining *sS* phases by 50.0%. Using a different approach (e.g. PhaseNet from Chapter 5) to convert amplitude picks to absolute onset times would help to incorporate more *S* coda data.

8.2.2 Limitations

The cohesive application of the approaches to the SASZ highlights areas where the workflow is currently limited. These include the incorporation of *S* and *sS* phases into the methodology introduced in Chapter 2, which is currently sub-optimal due to the dependence of the *S* coda/T component *ad-hoc* arrays upon the *P* coda/Z component *ad-hoc* array assembly and quality. Furthermore, the necessary conversion of the peak amplitude picks, found during the array processing routine, to phase onset times in order to combine my phases with those output by the community (e.g. the reported ISC phases) is severely limited. Currently, to adjust the picks, I need an ISC reported and reviewed (events older than 2023) direct phase arrival per *ad-hoc* array with identified phases. This results in high *ad-hoc* array failure rates (despite good quality data and picks). If none of the picked *ad-hoc* arrays for an event have a reported phase to use for the conversions, then the event

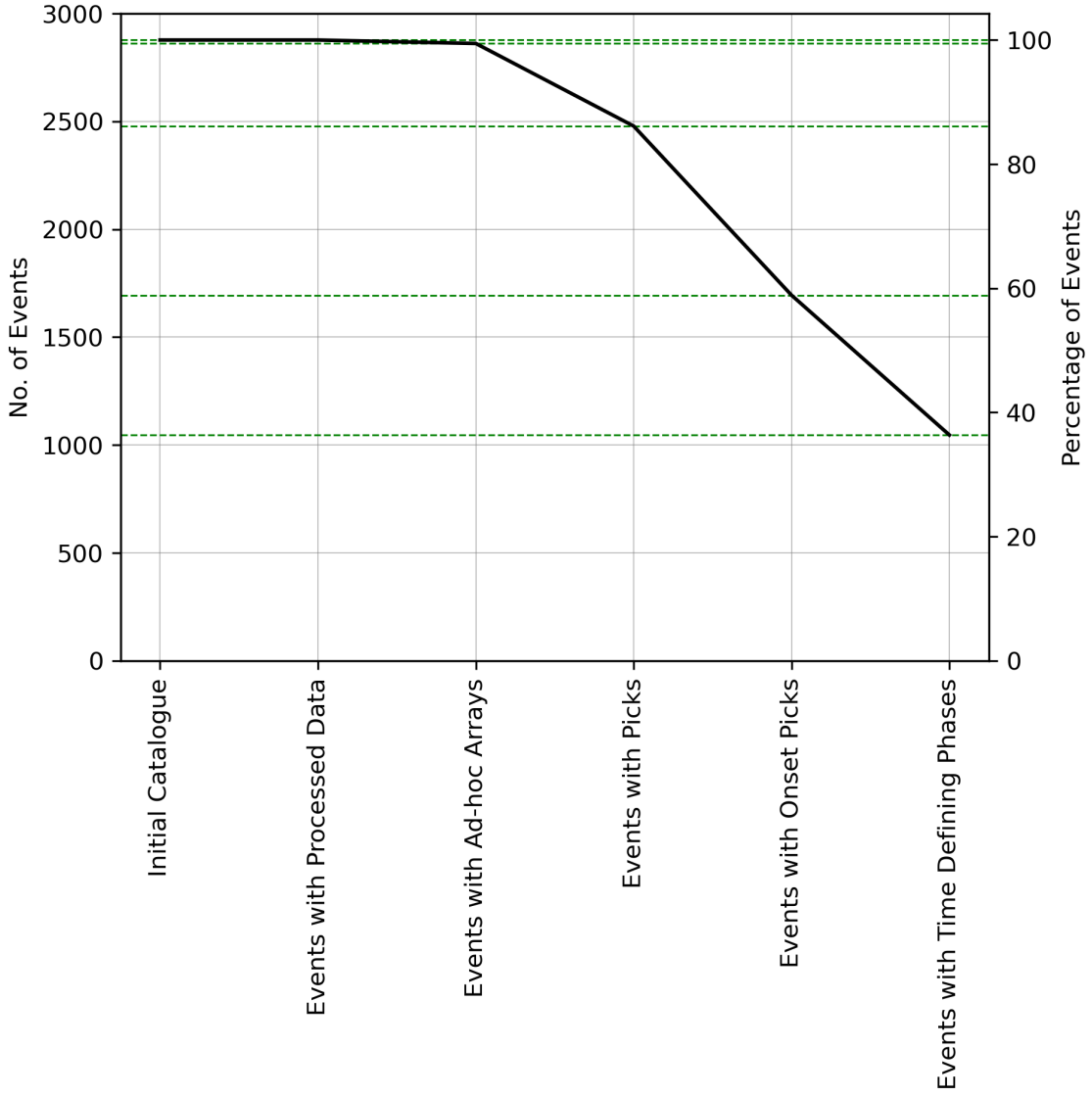

Figure 8.1: Plot showing the steps in the workflow where earthquakes fail to progress. Green dashed lines highlight the number of events remaining at each stage. The stage with the greatest event loss is the conversion of *ad-hoc* array determined picks to onset times.

fails. Figure 8.1 illustrates the number of events in the workflow per step, and highlights that the conversion of picks to onset times is the single largest point of event failure (27.3% of events) in the entire methodology. Chapter 5 offers a solution which should be included in future work (see Section 8.3.1), by applying PhaseNet to the individual *ad-hoc* arrays to obtain direct arrivals, thus aiming to eliminate dependence upon reported direct arrivals and their locations.

8.2.3 South American Subduction Zone interpretation

Despite limitations, a new 3D catalogue for the SASZ intermediate-depth earthquakes with errors is presented in Section 7.3.4 and corroborates previously observed features for

the region in Sections 2.4.3 and 4.2.2.

It is apparent that seismicity in the subducting slab tends to nucleate in regions aligned with the location of bathymetric features in the down-going plate, such as fracture zones and ridges (Bilek, 2010). This is likely due to the increased fluid content of the slab where these features exist, which encourages more dehydration reactions to occur and initiate slab failure – with the exception of the dehydrated Nazca Ridge (Kumar et al., 2016; Wagner et al., 2020). Additionally, such features could lead to a predisposed weakness to failure as a result of previous fractures existing in the slab. For example, the Mendaña fracture zone is thought to be the first order control on the Pucallpa seismic nest (Wagner & Okal, 2019), as seen in cross sections in Chapters 2, 4 and 7.

For the Peruvian flat slab, seismicity nucleates at the bends into and out of the flat slab portion, which exists at ∼100-120 km depth for a distance of ∼200 km, as observed on the new catalogue cross sections in Figures 2.16, 4.9 and 7.8. The stress concentrations focused around regions of slab bending are likely required to overcome the strength of the slab, and combined with the effects of ongoing dehydration embrittlement to produce seismicity (Sandiford et al., 2019). The apparently aseismic flat slab portion between the bends indicates that either dehydration reactions are limited in their occurrence, as the phases are stable at the existing pressure-temperature conditions (Kumar et al., 2016), or the slab is not experiencing enough stress to overcome the slab strength despite dehydration embrittlement.

The crustal thickness overlying the Peruvian and Chilean subduction zones (and the entire SASZ) is clearly constrained to the north and south by Moho depth maps developed in Chapters 6 and 7 using *pmP* (see Figures 6.7a and 7.11). The thickened crustal spine of the Altiplano (a large plateau in Chile, up to approximately 80 km thick) is shown to decrease in thickness into Peru and southern Chile. However, the Altiplano is not well constrained to the east due to the limited number of intermediate-depth events inland to act as passive sources. It is proposed by Ma and Clayton (2015) that the Moho geometry is reflected in the Peruvian flat slab geometry, due to hydrodynamic suction between the slab and continental crust – a factor which reduces the mantle wedge above the flat slab and decreases its connection to normal subduction mantle corner flow.

A relative amplitude analysis between *pmP* and *pP* in Sections 6.3.4 and 7.4.4 expands upon the investigation into the nature of the Moho and mantle wedge, and indicates that

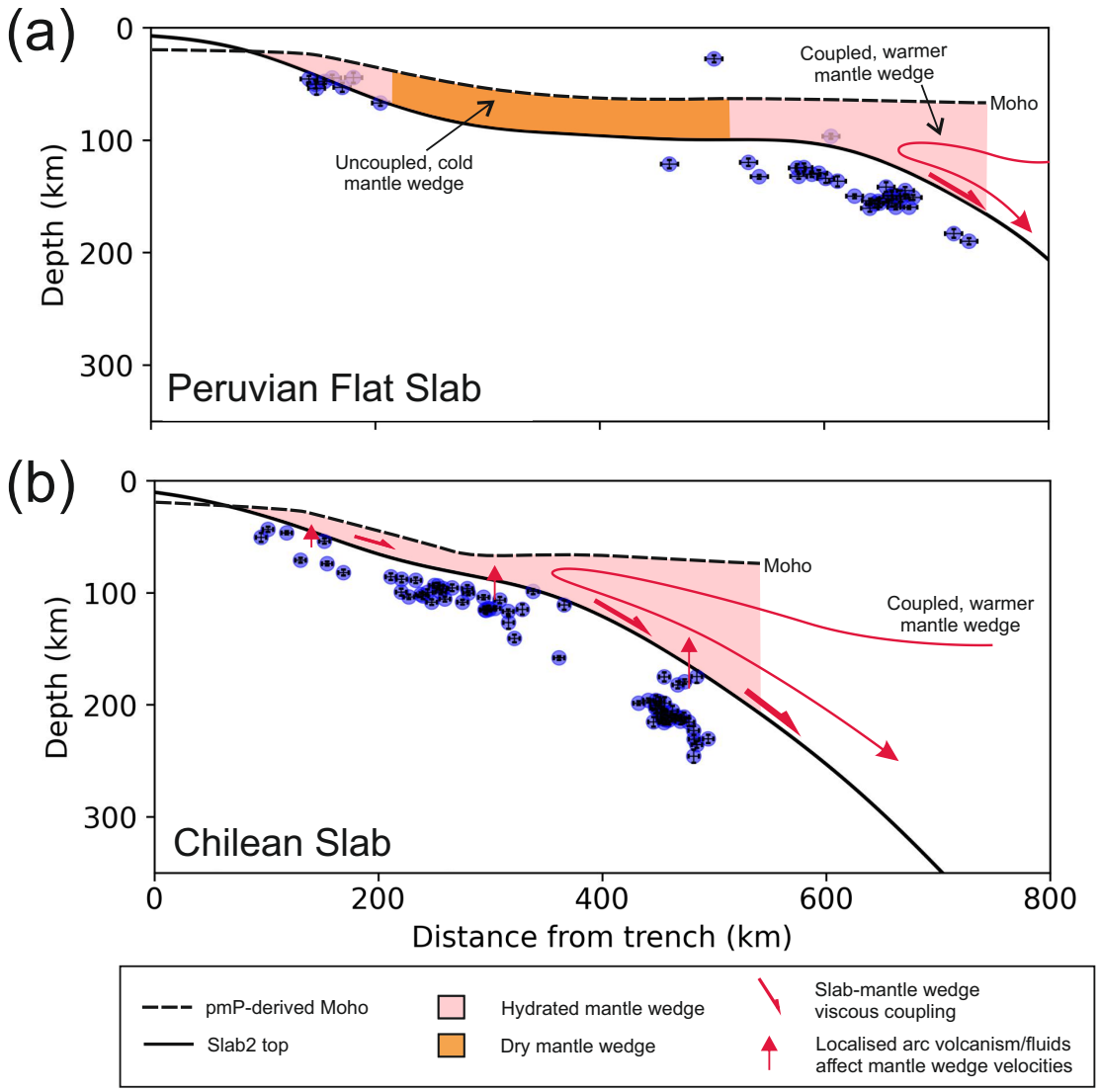

Figure 8.2: Plots of the L-L' (a) and P-P' (b) cross sections from Figure 7.7, with the SASZ augmented catalogue earthquake locations (blue circles and error bars) and *pmP* derived Moho depth (dashed black line) from Chapter 7. Mantle wedge interpretations are additionally illustrated. Slab2 is plotted as a solid black line, however this poorly fits my event locations, therefore I have plotted an inferred slab top with a sparsely dashed black line to demonstrate a more representative slab/wedge geometry.

the Peruvian flat slab has a high impendance Moho (high pmP/pP ratios) overlying the subducting slab when it resides at depths less than 100-120 km deep (i.e. the slab from the trench to the distal flat slab bend). The high impedance Moho transitions to a lower impedance interface (low pmP/pP ratios) when the slab is at greater depths than 100-120 km (i.e. when the flat slab begins to normally subduct into the mantle). The gradual transition with respect to distance from the trench/depth of the underlying subducting slab implies a diffusive thermal control, such as the presence of cold/higher velocity mantle wedge over the flat slab (assuming that pP is experiencing laterally similar crust, see Figure 8.2a).

Ma and Clayton (2015) observe a high velocity mantle wedge overlying the Peruvian flat slab, using a receiver function study, which decreases to normal expected values as the flat slab bends into the mantle and dehydrations reactions resume. Furthermore, Stachnik et al. (2004) interpret a viscous cold nose of mantle wedge at shallow subduction depths in the volcanically inactive Alaskan subduction zone, and conclude that the mantle wedge becomes cold and more viscous due to its exclusion from the mantle corner flow. These findings corroborate the interpretations from the Moho depth maps and pmP/pP relative amplitude studies (Sections 6.3 and 7.4.4), which propose that cold, dry, seismically fast mantle wedge overlies the Peruvian flat slab and that viscous coupling between the wedge and slab occurs at approximately 100-120 km depth, where the slab re-enters the mantle. The presence of a cold, dry mantle wedge above the Peruvian flat slab, as result of the hydrodynamic suction and the absence of dehydration reactions, also explains the lack of volcanism in Peru (Global Volcanism Program, 2024).

To the south of the Peruvian flat slab, the slab transitions smoothly into a steeper subduction angle without a discrete tear, supporting the observations of Cahill and Isacks (1992), and typically displays seismicity along its extent, within intermediate-depths. Results from the pmP/pP relative amplitude study at these latitudes are mixed, implying that either the mantle wedge is only seismically fast above the Peruvian flat slab, or that other factors with high lateral variability are overprinting the first order thermal trend in Chile. Given the Chilean slab does not tend to display aseismic extents down-dip, dehydration reactions and embrittlement are likely occurring at all intermediate-depths to hydrate the overlying mantle and locally reduce the mantle wedge seismic velocity (Cordell et al., 2019). Hydrated mantle will also enable the generation of partial melts for arc volcanism. Consequently, chemical effects related to partial melts from recent arc volcanism, fluids, and/or dehydration reactions will result in spatially variable Moho impedance in Chile (Figure 8.2).

Features such as apparent seismicity planes intersecting the slab and double seismogenic zones can also be observed in Chile using the relocated catalogues (Figures 4.10, 4.12, 4.11 and 7.8), similarly to those observed by Nippress and Rietbrock (2007) and Fuenzalida et al. (2013) at shallower depths. After investigation in Section 4.2.2, it is clear that the relocated intermediate-depth earthquake catalogues generated in this thesis do not have enough events to independently determine the authenticity of the observed features. By comparing to a locally determined catalogue, such as the one assembled by Sippl et

al. (2018), an increased level of confidence for the observed features can be ascertained – particularly for the presence of a double seismogenic zone in northern Chile (Section 4.2.2).

Histograms of slab plane-corrected event depths using both the 3D catalogue from Chapter 4 and a local microseismicity catalogue (Sippl et al., 2018) for northern Chile, following Brudzinski et al. (2007), indicate that a DSZ could exist in this portion of the slab as observed by Florez and Prieto (2019) (Figure 4.13). Cross sections (Figures 7.7, 7.8 and 7.9) seen along the length of the SASZ in Chapter 7 demonstrate that the DSZ is limited in extent (if present), and does not persist into Peru or southern Chile, where a single plane of seismicity is observed. K. Wang (2002) advocates that all DSZ are underdeveloped triple seismogenic zones, where each seismogenic layer (top to bottom) is defined by down-dip extension, compression and extension, with the upper two layers existing in close proximity (Igarashi et al., 2001). For northern Chile, an investigation into the event focal mechanisms could determine if the prospective DSZ layers demonstrate diagnostic intra-slab stresses, and corroborate the proposed influence of slab flexure, in the presence of dehydration embrittlement, to control the occurrence of slab seismicity (Igarashi et al., 2001; K. Wang et al., 1997; Sandiford et al., 2020). Further refinement of the relative event depths using a double difference approach, generating an improved slab plane for the slab depth correction, and incorporating focal mechanisms would provide better insight into slab features using teleseismic data.

8.3 Future work

There are a number of options to continue the progress of the research presented in this thesis, including methodology improvements, methodology additions and new applications.

8.3.1 Methodology improvements

A couple of further advancements to the approach would greatly expand the success of the earthquake relocation outcomes. Firstly, instead of linking together the fate of the P and S coda array processing routines, these steps should be separated. This could allow a new set of *ad-hoc* arrays to be created using only 3-component stations, and thus, maximise the 3-component station distribution available per event. The likelihood of S wave coda *ad-hoc* arrays having enough high quality traces to succeed the cross-correlation quality

criterion will consequently increase, and more S and sS phase arrivals will be output to guide the relocations.

The second improvement is updating the phase picking and/or the amplitude to onset conversion routines to machine learning, which has already been discussed in Chapter 5 and Section 8.1.4. If a new PhaseNet (W. Zhu & Beroza, 2019) model could be trained on teleseismic, array processed data to pick direct phase onsets then the conversion routine in Chapter 4 could be updated to reduce dependence upon the accuracy, consistency and location of reported direct phases. Or, if the model could be trained to pick the direct and depth phases on teleseismic array processed data, the threshold picking and identification routines outlined in Chapter 2 could be replaced and an onset conversion would no longer be necessary to integrate the results into a reported phase catalogue for relocation. This would require a large number of picks to be extracted from my *ad-hoc* array optimum beams, and manually checked to assemble a training dataset.

Münchmeyer et al. (2024) have trained a PhaseNet model to pick the pP and sP depth phases for earthquake relocation using 3-component single station data, yet the arrival probability curves remain considerably worse than P and S pickers, the array processing element of the workflow presented in this thesis could vastly enhance the success of machine learning pickers for depth phases (including sS).

8.3.2 Methodology extensions

My approach might offer further opportunity to interpret the down-going slab features. For example, it would be possible to relocate the final absolute earthquake catalogue (from ISCloc) to a relative location catalogue using a double difference algorithm. The refinement of the hypocentre locations relative to one another encourages the recognition of geometric features highlighted by the events, and could be of future interest for those wishing to build upon the work presented in this thesis. Future work along this line could also include defining a new regional slab top which fits the relocated 3D catalogue well, and reassessing the validity of ubiquitous double seismogenic zones using the updated slab tops.

A second extension to the presented approach could be a routine to determine focal mechanisms using the relative amplitudes between pP or sP and P (Pearce, 1977; Pearce & Rogers, 1989). Given that the intermediate-depth earthquake catalogues assembled during

this thesis are including m_b 4.7 events and GCMT focal mechanism solutions are limited to events with magnitudes greater than 5.0 (5.5 for rapid solutions), it would be good to provide the missing focal mechanisms for the smaller magnitude earthquakes.

The amplitudes of the depth phases and the direct arrival can be easily extracted from the current P wave coda *ad-hoc* array results, and a relative amplitude calculated – similarly to the work in Chapter 6 looking into the relative amplitudes of pmP/pP. It is then a case of running a forward model where the strike, dip and rake of a fault plane is varied between the possible ranges, the expected amplitudes of the radiating arrivals is calculated for a specific *ad-hoc* array location, and the observed and modelled relative amplitudes are compared. The fault plane parameters which provide the smallest cumulative residual or misfit between the observed and modelled relative amplitudes for all of the *ad-hoc* arrays for a given event would then be selected as the best fitting fault plane. From the best fitting fault plane, a focal mechanism can be defined for the event. This idea was briefly pursued during the course of the Ph.D, however, inconsistencies with the attenuation and energy partitioning corrections on the modelled arrival amplitudes limited its success in the time available.

8.3.3 New applications

Finally, there are new applications for the workflow presented in this thesis which could generate some exciting results. The relocated 3D catalogues could be correlated with thermal and/or slab bending models for the Nazca subduction zones to begin analysing the relationships between seismicity and the proposed nucleation mechanisms in Section 1.3.2.

However, most of all, the developed workflow could be applied to other subduction zones, where small to moderate magnitude earthquakes have previously been poorly relocated in depth and would significantly benefit from the increased depth resolution that depth phases provide, particularly if the there is a lack of local seismic stations (due to challenging, remote, or inaccessible terrain, or limited funding for a deployment). Furthermore, despite the approach targeting subduction zone intermediate-depth earthquakes, it can be very successful on intermediate-depth events in other tectonic settings – even on shallower, short source-time function events. For example I have previously used the approach to relocate a 31 km deep continental event in Algeria (Wimpenny et al., 2023).

Some adaptions may be required to download teleseismic data for alternative regions, especially if large influential station networks are missing from the FDSN framework (such as those based in Japan). It is important to bear in mind that sufficiently dense station data is required within telesesismic distances for the approach to work well, this should be considered before applying the approach to new regions.

8.4 Conclusions

This thesis demonstrates a new *ad-hoc* array-based approach to automatically identify and detect depth phases (*pP*, *sP*, *sS* and *pmP*) on teleseismic data, sourced from m_b 4.7-6.5 intermediate-depth earthquakes, and use them to determine accurate 3D event locations (with ISCloc (Bondár & Storchak, 2011)) and Moho depths. The application of depth phases for event relocation reduces the event origin time-depth trade-off, and enables crustal thickness calculations, without the need for near-to-source receivers. This offers an inexpensive alternative to investigate regions with remote and challenging terrain, and without a costly field campaign. By maximising the available teleseismic data per event and applying array processing techniques, the signal-to-noise ratio of low amplitude depth phases is improved to enable automatic picking. Therefore the approach also removes the need for intensive manual or semi-automatic processing, and computationally expensive analysis. Furthermore, I have demonstrated that the automated and adaptable methodology presented is scalable from regional to continental sized areas, without significant limits, using Peru, northern Chile and the South American Subduction Zone (SASZ) as case studies.

To relocate events in 3D using ISCloc (Bondár & Storchak, 2011), the *ad-hoc* array-determined phases (*pP*, *sP* and *sS*), alongside their direct arrivals (*P* and *S*), are integrated into existing global phase catalogues. This augments the global phase catalogue with depth constraining phases, which have been shown to reduce depth error in 99.9% of events in Peru and northern Chile with *P* coda *ad-hoc* array determined picks, and 84.5% events across the entire SASZ with *P* and *S* coda *ad-hoc* array determined picks. The final, new event catalogue (containing 1046 earthquakes, based upon 68,075 depth phase detections) and Moho depth map (using 2965 *pmP* detections) for the entirety of the SASZ, are believed to be the first continental-sized catalogues to use global phase catalogues augmented with both *P* and *S* coda array-determined picks, and *pmP* arrivals,

respectively.

Both high resolution results (the new earthquake catalogue and new Moho depth map) highlight a number of features for the SASZ. Notably across the entire SASZ, it is clear that the current Slab2 model (Hayes et al., 2018) poorly fits the newly-determined event locations, and is typically significantly shallower with respect to distance from the trench, relative to the event depths – a new slab top for the SASZ should be defined using the event catalogue in the future, to ensure analysis is not biased by a shallow slab top model.

For Peru, the seismicity congregates around the bends in the flat slab, inferring that slab flexure in combination with dehydration reactions is nucleating events. The lack of events within the aseismic flat section of the slab also indicates that dehydration reactions are minimal, likely due to unchanging pressure-temperature conditions, which results in a dry overlying mantle wedge. A *pmP* to *pP* amplitude analysis corroborates this finding, and also demonstrates a first order trend for the Peruvian flat slab, which suggests cold, seismically fast mantle wedge exists above the flat slab and transitions into warmer, seismically slower mantle at the distal slab bend. This is likely due to isolation of the mantle wedge above the flat slab from the mantle corner flow, and implies that viscous coupling between the mantle wedge and the down-going slab initiates at the distal bend.

Moving southwards, the new catalogue indicates a smooth transition from the Peruvian flat slab into a classical subduction zone geometry in northern Chile. Here a number of features are highlighted by the catalogue, including intersecting planes of seismicity and, potentially, a double seismogenic zone. With the global catalogue alone, the authenticity of these features is difficult to establish – by applying a double difference algorithm and calculating focal mechanisms for the events in the future, confidence in the features using a global catalogue could be increased. The *pmP* determined Moho in northern Chile corroborates the presence of a thick crustal plateau (the Altiplano) with a maximum thickness of approximately 80 km. The new Moho depth map shows that the Altiplano exists parallel to the subduction trench, and decreases in thickness to the north and south. The *pmP* bounce points used to establish Moho depth sample the Moho at a higher resolution than equivalent receiver function studies, therefore the resultant map provides new insight into Moho roughness and local variation.

In summary, the techniques presented enable the collation of regional to continental-scale, high resolution intermediate-depth earthquake catalogues and Moho depth maps, through

the automatic detection and application of *ad-hoc* array-determined depth phases (*pmP*, *pP*, *sP*, *sS*). This approach has led to new observations, analyses, and interpretations of the SASZ, and paves the way to significantly enhance our understanding of the links between seismicity and subduction dynamics.

Data Availability

All seismic data used in this study are openly available from:

BGR at `http://eida.bgr.de`, ETH at `http://eida.ethz.ch`

GEONET at `http://service.geonet.org.nz`

GFZ at `http://geofon.gfz-potsdam.de`

ICGC at `http://ws.icgc.cat`

INGV at `http://webservices.ingv.it`

IPGP at `http://ws.ipgp.fr`

IRIS at `http://service.iris.edu`

KNMI at `http://rdsa.knmi.nl`

LMU at `http://erde.geophysik.uni-muenchen.de`

NIEP at `http://eida-sc3.infp.ro`

NOA at `http://eida.gein.noa.gr`

ORFEUS at `http://www.orfeus-eu.org`

RESIF at `http://ws.resif.fr`

SCEDC at `http://service.scedc.caltech.edu`

TEXNET at `http://rtserve.beg.utexas.edu`

UIB-NORSAR at `http://eida.geo.uib.no`

USP at `http://sismo.iag.usp.br`.

Code and catalogues are available on request from the author.

References

Abe, K. (1972). Mechanics and tectonic implications of the 1966 and 1970 Peru earthquakes. *Physics of the Earth and Planetary Interiors*, *5*(C), 367–379. doi: 10.1016/0031-9201(72)90108-2

Abers, G., Nakajima, J., van Keken, P., Kita, S., & Hacker, B. (2013). Thermal-petrological controls on the location of earthquakes within subducting plates. *Earth and Planetary Science Letters*, *369-370*, 178–187. doi: 10.1016/j.epsl.2013.03.022

Allen, R. (1982). Automatic phase pickers: Their present use and future prospects. *Bulletin of the Seismological Society of America*, *72*(6B), S225-S242. doi: 10.1785/bssa07206b0225

Allmendinger, R., Jordan, T., Kay, S., & Isacks, B. (1997, 5). The evolution of the Altiplano-Puna Plateau of the Central Andes. *Annual Review of Earth and Planetary Sciences*, *25*(1), 139–174. doi: 10.1146/annurev.earth.25.1.139

Antonijevic, S., Wagner, L., Kumar, A., Beck, S., Long, M., Zandt, G., ... Condori, C. (2015). The role of ridges in the formation and longevity of flat slabs. *Nature*, *524*(7564), 212–215. doi: 10.1038/nature14648

Apperson, K., & Frohlich, C. (1987). The relationship between Wadati-Benioff Zone geometry and P , T and B axes of intermediate and deep focus earthquakes. *Journal of Geophysical Research: Solid Earth*, *92*(B13), 13821–13831. doi: 10.1029/jb092ib13p13821

Barazangi, M., & Isacks, B. (1976). Spatial distribution of earthquakes and subduction of the nazca plate beneath south america. *Geology*, *4*(11), 686–692.

Beck, S., Barrientos, S., Kausel, E., & Reyes, M. (1998). Source characteristics of historic earthquakes along the central Chile subduction zone. *Journal of South American Earth Sciences*, *11*(2), 115–129. doi: 10.1016/S0895-9811(98)00005-4

Benioff, H. (1949). Seismic evidence for the fault origin of oceanic deeps. *Bulletin of the*

Geological Society of America, *60*(12), 1837–1856. doi: 10.1130/0016-7606(1949)60[1837:seftfo]2.0.co;2

Betts, P., Mason, W., & Moresi, L. (2012). The influence of a mantle plume head on the dynamics of a retreating subduction zone. *Geology*, *40*(8), 739–742. doi: 10.1130/G32909.1

Bilek, S. (2010). Invited review paper: Seismicity along the South American subduction zone: Review of large earthquakes, tsunamis, and subduction zone complexity. *Tectonophysics*, *495*(1-2), 2–14. doi: 10.1016/j.tecto.2009.02.037

Billen, M., Gurnis, M., & Simons, M. (2003). Multiscale dynamics of the Tonga-Kermadec subduction zone. *Geophysical Journal International*, *153*(2), 359–388. doi: 10.1046/j.1365-246X.2003.01915.x

Billings, S., Kennett, B., & Sambridge, M. (1994). Hypocentre location: genetic algorithms incorporating problem-specific information. *Geophysical Journal International*, *118*(3), 693–706. doi: 10.1111/j.1365-246X.1994.tb03994.x

Bird, P. (2003). An updated digital model of plate boundaries. *Geochemistry, Geophysics, Geosystems*, *4*(3). doi: 10.1029/2001GC000252

Blackwell, A., Craig, T., & Rost, S. (2024, 9). Automatic relocation of intermediate-depth earthquakes using adaptive teleseismic arrays. *Geophysical Journal International*, *239*(2), 821–840. doi: 10.1093/gji/ggae289

Bloch, W., Schurr, B., Kummerow, J., Salazar, P., & Shapiro, S. (2018). From Slab Coupling to Slab Pull: Stress Segmentation in the Subducting Nazca Plate. *Geophysical Research Letters*, *45*(11), 5407–5416. doi: 10.1029/2018GL078793

Bondár, I., & Storchak, D. (2011). Improved location procedures at the International Seismological Centre. *Geophysical Journal International*, *186*(3), 1220–1244. doi: 10.1111/j.1365-246X.2011.05107.x

Brudzinski, M., Thurber, C., Hacker, B., & Engdahl, E. (2007). Global prevalence of double benioff zones. *Science*, *316*(5830), 1472–1474. doi: 10.1126/science.1139204

Byerly, P. (1946). The seismic waves from the Prot Chicago explosion. *Bulletin of the Seismological Society of America*(36), 331–348.

Cahill, T., & Isacks, B. (1992, 11). Seismicity and shape of the subducted Nazca Plate. *Journal of Geophysical Research*, *97*(B12), 17503–17529. doi: 10.1029/92jb00493

Condori, C., França, G., Tavera, H., Albuquerque, D., Bishop, B., & Beck, S. (2017). Crustal structure of north Peru from analysis of teleseismic receiver functions. *Jour-*

nal of South American Earth Sciences, *76*, 11–24. doi: 10.1016/j.jsames.2017.02.006

Cook, F. (2002, 1). Fine structure of the continental reflection Moho. *Geological Society of America Bulletin*, *114*(1), 64–79. doi: 10.1130/0016-7606(2002)114⟨0064:FSOTCR⟩2.0.CO;2

Cordell, D., Unsworth, M., Diaz, D., Reyes-Wagner, V., Currie, C., & Hicks, S. (2019). Fluid and Melt Pathways in the Central Chilean Subduction Zone Near the 2010 Maule Earthquake (35–36°S) as Inferred From Magnetotelluric Data. *Geochemistry, Geophysics, Geosystems*, *20*(4), 1818–1835. doi: 10.1029/2018GC008167

Craig, T. (2019, 2). Accurate Depth Determination for Moderate-Magnitude Earthquakes Using Global Teleseismic Data. *Journal of Geophysical Research: Solid Earth*, *124*(2), 1759–1780. doi: 10.1029/2018JB016902

Craig, T., & Heyburn, R. (2015). An enigmatic earthquake in the continental mantle lithosphere of stable North America. *Earth and Planetary Science Letters*, *425*, 12–23. doi: 10.1016/j.epsl.2015.05.048

Craig, T., & Hull, A. (2024). Extensional failure at the tip of a weak slab under slab pull – the 2023 Mw 6.4 Zacualpa, Guatemala, earthquake. *Seismica*, *3*(1). doi: 10.26443/seismica.v3i1.1190

Craig, T., Jackson, J., Priestley, K., & Ekström, G. (2023). A Cautionary Tale: examples of the mis-location of small earthquakes beneath the Tibetan plateau by routine approaches. *Geophysical Journal International*, *233*(3), 2021–2038. doi: 10.1093/gji/ggad025

Craig, T., Jackson, J., Priestley, K., & McKenzie, D. (2011). Earthquake distribution patterns in Africa: their relationship to variations in lithospheric and geological structure, and their rheological implications. *Geophys. J. Int*, *185*, 403–434. doi: 10.1111/j.1365-246X.2011.04950.x

Cross, T., & Pilger, R. (1982). Controls of subduction geometry location of magmatic arcs and tectonics of arc and back-arc regions. *Geological Society of America Bulletin*, *93*(6), 545–562. doi: 10.1130/0016-7606(1982)93⟨545:COSGLO⟩2.0.CO;2

Crotwell, H., Owens, T., & Ritsema, J. (1999). The TauP Toolkit: Flexible seismic travel-time and ray-path utilities. *Seismological Research Letters*, *70*, 154–160.

Davies, D., Kelly, E., & Filson, J. (1971). Vespa Process for Analysis of Seismic Signals. *Nature Physical Science*, *232*, 1971.

Devlin, S., Isacks, B., Pritchard, M., Barnhart, W., & Lohman, R. (2012). Depths and focal mechanisms of crustal earthquakes in the central Andes determined from teleseismic waveform analysis and InSAR. *Tectonics*, *31*(2). doi: 10.1029/2011TC002914

Diehl, T., Deichmann, N., Kissling, E., & Husen, S. (2009). Automatic S-wave picker for local earthquake tomography. *Bulletin of the Seismological Society of America*, *99*(3), 1906–1920. doi: 10.1785/0120080019

Di Stefano, R., Aldersons, F., Kissling, E., Baccheschi, P., Chiarabba, C., & Giardini, D. (2006). Automatic seismic phase picking and consistent observation error assessment: Application to the Italian seismicity. *Geophysical Journal International*, *165*(1), 121–134. doi: 10.1111/j.1365-246X.2005.02799.x

Dorbath, C., Granet, M., Poupinet, G., & Martinez, C. (1993). A teleseismic study of the Altiplano and the Eastern Cordillera in northern Bolivia: new constraints on a lithospheric model. *Journal of Geophysical Research*, *98*(B6), 9825–9844. doi: 10.1029/92JB02406

Dziewonski, A., & Anderson, D. (1981). Preliminary reference Earth model. *Physics of the Earth and Planetary Interiors*, *25*(4), 297–356. doi: 10.1016/0031-9201(81)90046-7

Dziewonski, A., Chou, T., & Woodhouse, J. (1981). Determination of earthquake source parameters from waveform data for studies of global and regional seismicity. *Journal of Geophysical Research*, *86*(B4), 2825–2852. doi: 10.1029/JB086iB04p02825

Efron, B., & Tibshirani, R. (1986). Bootstrap methods for standard errors, confidence intervals, and other measures of statistical accuracy. *Statistical science*, 54–75.

Ekström, G., Nettles, M., & Dziewoński, A. (2012, 6). The global CMT project 2004-2010: Centroid-moment tensors for 13,017 earthquakes. *Physics of the Earth and Planetary Interiors*, *200-201*, 1–9. doi: 10.1016/j.pepi.2012.04.002

Engdahl, E., Di Giacomo, D., Sakarya, B., Gkarlaouni, C., Harris, J., & Storchak, D. (2020a, 1). ISC-EHB 1964–2016, an Improved Data Set for Studies of Earth Structure and Global Seismicity. *Earth and Space Science*, *7*(1), e2019EA000897. doi: 10.1029/2019EA000897

Engdahl, E., Di Giacomo, D., Sakarya, B., Gkarlaouni, C., Harris, J., & Storchak, D. (2020b, 1). ISC-EHB 1964–2016, an Improved Data Set for Studies of Earth Structure and Global Seismicity. *Earth and Space Science*, *7*(1), e2019EA000897. doi: 10.1029/2019EA000897

Engdahl, E., & Scholz, C. (1977). A double Benioff Zone beneath the central Aleutians:

An unbending of the lithosphere. *Geophysical Research Letters*, *4*(10), 473–476. doi: 10.1029/GL004i010p00473

Engdahl, E., van der Hilst, R., & Buland, R. (1998). Global teleseismic earthquake relocation with improved travel times and procedures for depth determination. *Bulletin of the Seismological Society of America*, *88*(3), 722–743. doi: 10.1785/bssa0880030722

Espurt, N., Funiciello, F., Martinod, J., Guillaume, B., Regard, V., Faccenna, C., & Brusset, S. (2008). Flat subduction dynamics and deformation of the South American plate: Insights from analog modeling. *Tectonics*, *27*(3), 1–19. doi: 10.1029/2007TC002175

Ester, M., Kriegel, H., Sander, J., & Xu, X. (1996). A Density-Based Algorithm for Discovering Clusters A Density-Based Algorithm for Discovering Clusters in Large Spatial Databases with Noise. In *Proceedings - 2nd international conference on knowledge discovery and data mining, kdd 1996* (pp. 226–231).

Fang, H., & van der Hilst, R. (2019, 12). Earthquake Depth Phase Extraction With P Wave Autocorrelation Provides Insight Into Mechanisms of Intermediate-Depth Earthquakes. *Geophysical Research Letters*, *46*(24), 14440–14449. doi: 10.1029/2019GL085062

Farra, V., & Vinnik, L. (2000). Upper mantle stratification by P and S receiver functions. *Geophys. J. Int.*, *141*, 699–712.

Ferrand, T., Hilairet, N., Incel, S., Deldicque, D., Labrousse, L., Gasc, J., ... Schubnel, A. (2017). Dehydration-driven stress transfer triggers intermediate-depth earthquakes. *Nature Communications*, *8*. doi: 10.1038/ncomms15247

Flament, N., Gurnis, M., Müller, R., Bower, D., & Husson, L. (2015). Influence of subduction history on South American topography. *Earth and Planetary Science Letters*, *430*, 9–18. doi: 10.1016/j.epsl.2015.08.006

Florez, M., & Prieto, G. (2017, 6). Precise relative earthquake depth determination using array processing techniques. *Journal of Geophysical Research: Solid Earth*, *122*(6), 4559–4571. doi: 10.1002/2017JB014132

Florez, M., & Prieto, G. (2019, 4). Controlling Factors of Seismicity and Geometry in Double Seismic Zones. *Geophysical Research Letters*, *46*(8), 4174–4181. doi: 10.1029/2018GL081168

Forsyth, D., & Uyeda, S. (1975, 10). On the Relative Importance of the Driving Forces of Plate Motion. *Geophysical Journal of the Royal Astronomical Society*, *43*(1),

163–200. doi: 10.1111/j.1365-246X.1975.tb00631.x

Frohlich, C. (2006). *Deep earthquakes*. Cambridge university press. doi: https://doi.org/10.1017/CBO9781107297562

Fuenzalida, A., Schurr, B., Lancieri, M., Sobiesiak, M., & Madariaga, R. (2013). High-resolution relocation and mechanism of aftershocks of the 2007 Tocopilla (Chile) earthquake. *Geophysical Journal International*, *194*(2), 1216–1228. doi: 10.1093/gji/ggt163

Fujita, K., & Kanamori, H. (1981). Double seismic zones and stresses of intermediate depth earthquakes. *Geophysical Journal of the Royal Astronomical Society*, *66*(1), 131–156. doi: 10.1111/j.1365-246X.1981.tb05950.x

Gao, Y., Yuan, X., Heit, B., Tilmann, F., van Herwaarden, D., Thrastarson, S., ... Schurr, B. (2021, 11). Impact of the Juan Fernandez Ridge on the Pampean Flat Subduction Inferred From Full Waveform Inversion. *Geophysical Research Letters*, *48*(21), e2021GL095509. doi: 10.1029/2021GL095509

Garzione, C., Molnar, P., Libarkin, J., & MacFadden, B. (2006, 1). Rapid late Miocene rise of the Bolivian Altiplano: Evidence for removal of mantle lithosphere. *Earth and Planetary Science Letters*, *241*(3-4), 543–556. doi: 10.1016/j.epsl.2005.11.026

Geiger, L. (1910). Herdbestimmung bei Erdbeben aus den Ankunftszeiten. *Nachrichten von der Gesellschaft der Wissenschaften zu Göttingen, Mathematisch-Physikalische Klasse*, 331–349.

GFZ, & CNRS-INSU. (2006). *IPOC Seismic Network. Integrated Plate boundary Observatory Chile - IPOC*. `https://doi.org/10.14470/PK615318`. (Full author names: GFZ German Research Centre for Geosciences and Institut des Sciences de l'Univers – Centre National de la Recherche Scientifique (CNRS-INSU). Dataset/Seismic Network.) doi: 10.14470/PK615318

Giese, P., Scheuber, E., Schilling, F., Schmitz, M., & Wigger, P. (1999, 3). Crustal thickening processes in the Central Andes and the different natures of the Moho-discontinuity. *Journal of South American Earth Sciences*, *12*(2), 201–220. doi: 10.1016/S0895-9811(99)00014-0

Global Volcanism Program, S. I. (2024). *Volcanoes of the World, v. 5.2.7.* Retrieved from `https://volcano.si.edu/` doi: https://doi.org/10.5479/si.GVP.VOTW5-2024.5.2

Golding, N., Schulson, E., & Renshaw, C. (2012). Shear localization in ice: Mechanical

response and microstructural evolution of P-faulting. *Acta Materialia*, *60*(8), 3616–3631. doi: 10.1016/j.actamat.2012.02.051

Graeber, F., & Asch, G. (1999, 9). Three-dimensional models of P wave velocity and P -to- S velocity ratio in the southern central Andes by simultaneous inversion of local earthquake data. *Journal of Geophysical Research: Solid Earth*, *104*(B9), 20237–20256. doi: 10.1029/1999jb900037

Gripp, A., & Gordon, R. (2002). Young tracks of hotspots and current plate velocities. *Geophysical Journal International*, *150*(2), 321–361. doi: 10.1046/j.1365-246X.2002.01627.x

Gurnis, M., Ritsema, J., Van Heijst, H., & Zhong, S. (2000). Tonga slab deformation: The influence of a lower mantle upwelling on a slab in a young subduction zone. *Geophysical Research Letters*, *27*(16), 2373–2376. doi: 10.1029/2000GL011420

Gutscher, M., Spakman, W., Bijwaard, H., & Engdahl, E. (2000). Geodynamics of flat subduction: Seismicity and tomographic constraints from the Andean margin. *Tectonics*, *19*(5), 814–833. doi: 10.1029/1999TC001152

Haberland, C., & Rietbrock, A. (2001). Attenuation tomography in the western central Andes: A detailed insight into the structure of a magmatic arc. *Journal of Geophysical Research: Solid Earth*, *106*(B6), 11151–11167. doi: 10.1029/2000jb900472

Hacker, B. (2008). H2O subduction beyond arcs. *Geochemistry, Geophysics, Geosystems*, *9*(3). doi: 10.1029/2007GC001707

Hacker, B., & Christie, J. (2011, 9). Brittle/ductile and plastic/cataclastic transitions in experimentally deformed and metamorphosed amphibolite. In (pp. 127–147). American Geophysical Union (AGU). doi: 10.1029/gm056p0127

Hacker, B., Peacock, S., Abers, G., & Holloway, S. (2003, 1). Subduction factory 2. Are intermediate-depth earthquakes in subducting slabs linked to metamorphic dehydration reactions? *Journal of Geophysical Research: Solid Earth*, *108*(B1). doi: 10.1029/2001jb001129

Hanks, T., & Wyss, M. (1972). The use of body-wave spectra in the determination of seismic-source parameters. *Bulletin of the Seismological Society of America*, *62*(2), 561–589. doi: 10.1785/bssa0620020561

Hasegawa, A., & Sacks, I. (1981). Subduction of the Nazca plate beneath Peru as determined from seismic observations. *Journal of Geophysical Research*, *86*(B6), 4971–4980. doi: 10.1029/JB086iB06p04971

Hasegawa, A., Umino, N., & Takagi, A. (1978). Double-planed deep seismic zone and upper-mantle structure in the Northeastern Japan Arc. *Geophysical Journal of the Royal Astronomical Society*, *54*(2), 281–296. doi: 10.1111/j.1365-246X.1978.tb04260.x

Hayes, G. (2017). The finite, kinematic rupture properties of great-sized earthquakes since 1990. *Earth and Planetary Science Letters*, *468*, 94–100. doi: 10.1016/j.epsl.2017.04.003

Hayes, G., Moore, G., Portner, D., Hearne, M., Flamme, H., Furtney, M., & Smoczyk, G. (2018, 10). Slab2, a comprehensive subduction zone geometry model. *Science*, *362*(6410), 58–61. doi: 10.1126/science.aat4723

Hayes, G., Wald, D., & Johnson, R. (2012). Slab1.0: A three-dimensional model of global subduction zone geometries. *Journal of Geophysical Research: Solid Earth*, *117*(1), 1–15. doi: 10.1029/2011JB008524

Heyburn, R., & Bowers, D. (2008, 2). Earthquake depth estimation using the F trace and associated probability. *Bulletin of the Seismological Society of America*, *98*(1), 18–35. doi: 10.1785/0120070008

Hicks, S., Bie, L., Rychert, C., Harmon, N., Goes, S., Rietbrock, A., ... Kendall, J. (2023). Slab to back-arc to arc: Fluid and melt pathways through the mantle wedge beneath the Lesser Antilles. *Science Advances*, *9*(5), 1–14. doi: 10.1126/sciadv.add2143

Hobbs, B., & Ord, A. (1988). Plastic instabilities: implications for the origin of intermediate and deep focus earthquakes. *Journal of Geophysical Research*, *93*(B9). doi: 10.1029/jb093ib09p10521

Hodgson, J. (1946). Analysis of travel times from rockbursts at Kirkland Lake, Ontario. *Bulletin of the Seismological Society of America*(37), 5–17.

Hosseini, K., & Sigloch, K. (2017). ObspyDMT: A Python toolbox for retrieving and processing large seismological data sets. *Solid Earth*, *8*(5), 1047–1070. doi: 10.5194/se-8-1047-2017

Hosseinzadehsabeti, E., Ferré, E., Persaud, P., Fabbri, O., & Geissman, J. (2021). *The rupture mechanisms of intraslab earthquakes: A multiscale review and re-evaluation* (Vol. 221). doi: 10.1016/j.earscirev.2021.103782

Hu, Y., Yagi, Y., Okuwaki, R., & Shimizu, K. (2021). Back-propagating rupture evolution within a curved slab during the 2019 Mw8.0 Peru intraslab earthquake. *Geophysical Journal International*, *227*(3), 1602–1611. doi: 10.1093/gji/ggab303

Hyndman, R., & Peacock, S. (2003). Serpentinization of the forearc mantle. *Earth and Planetary Science Letters*, *212*(3-4), 417–432. doi: 10.1016/S0012-821X(03)00263-2

Igarashi, T., Matsuzawa, T., Umino, N., & Hasegawa, A. (2001). Spatial distribution of focal mechanisms for interplate and intraplate earthquakes associated with the subducting Pacific plate beneath the northeastern Japan arc: A triple-planed deep seismic zone. *Journal of Geophysical Research: Solid Earth*, *106*(B2), 2177–2191. doi: 10.1029/2000jb900386

Isacks, B., & Molnar, P. (1969). Mantle earthquake mechanisms and the sinking of the lithosphere. *Nature*, *223*(5211), 1121–1124. doi: 10.1038/2231121a0

Isacks, B., & Molnar, P. (1971). Distribution of stresses in the descending lithosphere from a global survey of focal-mechanism solutions of mantle earthquakes. *Reviews of Geophysics*, *9*(1), 103–174. doi: 10.1029/RG010i003p00847

James, D., & Snoke, J. (1994, 4). Structure and tectonics in the region of flat subduction beneath central Peru: Crust and uppermost mantle. *Journal of Geophysical Research: Solid Earth*, *99*(B4), 6899–6912. doi: 10.1029/93JB03112

Jang, H., Kim, Y., Lim, H., & Clayton, R. (2019). Seismic attenuation structure of southern Peruvian subduction system. *Tectonophysics*, *771*(September), 228203. doi: 10.1016/j.tecto.2019.228203

John, T., Medvedev, S., Rüpke, L., Andersen, T., Podladchikov, Y., & Austrheim, H. (2009). Generation of intermediate-depth earthquakes by self-localizing thermal runaway. *Nature Geoscience*, *2*(2), 137–140. doi: 10.1038/ngeo419

Jung, H., Greon, H., & Dobrzhinetskaya, L. (2004, 4). Intermediate-depth earthquake faulting by dehydration embrittlement with negative volume change. *Nature*, *428*(6982), 545–549. doi: 10.1038/nature02412

Kelemen, P., & Hirth, G. (2007). A periodic shear-heating mechanism for intermediate-depth earthquakes in the mantle. *Nature*, *446*(7137), 787–790. doi: 10.1038/nature05717

Kennett, B., & Engdahl, E. (1991). Traveltimes for global earthquake location and phase identification. *Geophysical Journal International*, *105*(2), 429–465. doi: 10.1111/j.1365-246X.1991.tb06724.x

Kennett, B., Engdahl, E., & Buland, R. (1995). Constraints on seismic velocities in the Earth from traveltimes. *Geophysical Journal International*, *122*(1), 108–124. doi: 10.1111/j.1365-246X.1995.tb03540.x

Kirby, S. (1987, 12). Localized polymorphic phase transformations in high-pressure faults and applications to the physical mechanism of deep earthquakes. *Journal of Geophysical Research: Solid Earth*, *92*(B13), 13789–13800. doi: 10.1029/jb092ib13p13789

Kirby, S., Engdahl, E., & Denlinger, R. (1996). Intermediate-depth intraslab earthquakes and arc volcanism as physical expressions of crustal and uppermost mantle metamorphism in subducting slabs. In *Geophysical monograph series* (Vol. 96, pp. 195–214). Blackwell Publishing Ltd. doi: 10.1029/GM096p0195

Kissling, E., Ellsworth, W., Eberhart-Phillips, D., & Kradolfer, U. (1994). Initial reference models in local earthquake tomography. *Journal of Geophysical Research*, *99*(B10). doi: 10.1029/93jb03138

Ko, S., Olgaard, D., & Wong, T. (1997). Generation and maintenance of pore pressure excess in a dehydrating system 1. Experimental and microstructural observations. *Journal of Geophysical Research: Solid Earth*, *102*(B1), 825–839. doi: 10.1029/96jb02485

Korenaga, J. (2013). Stacking with dual bootstrap resampling. *Geophysical Journal International*, *195*(3), 2023–2036.

Kumar, A., Wagner, L., Beck, S., Long, M., Zandt, G., Young, B., ... Minaya, E. (2016). Seismicity and state of stress in the central and southern Peruvian flat slab. *Earth and Planetary Science Letters*, *441*, 71–80. doi: 10.1016/j.epsl.2016.02.023

Langston, C. (1979). Structure under Mount Rainier, Washington, inferred from teleseismic body waves. *Journal of Geophysical Research*, *84*(B9), 4749–4762. doi: 10.1029/JB084iB09p04749

Langston, C. (2014). Coherence of teleseismic P and S waves across the transportable array. *Bulletin of the Seismological Society of America*, *104*(5), 2253–2265. doi: 10.1785/0120140075

Laske, G., Masters, G., Ma, Z., Pasyanos, M., & Livermore, L. (2013). EGU2013-2658 Update on CRUST1 . 0 : A 1-degree Global Model of Earth ' s Crust. *Geophysical Research Abstracts*, *15*, Abstract EGU2013–2658.

Lay, T., Kanamori, H., Ammon, C., Koper, K., Hutko, A., Ye, L., ... Rushing, T. (2012). Depth-varying rupture properties of subduction zone megathrust faults. *Journal of Geophysical Research: Solid Earth*, *117*(4), 1–21. doi: 10.1029/2011JB009133

Letort, J., Bollinger, L., Lyon-Caen, H., Guilhem, A., Cano, Y., Baillard, C., & Adhikari, L. (2016, 12). Teleseismic depth estimation of the 2015 Gorkha-Nepal aftershocks.

Geophysical Journal International, *207*(3), 1584–1595. doi: 10.1093/gji/ggw364

Li, T., Yao, J., Wu, S., Xu, M., & Tong, P. (2022). Moho Complexity in Southern California Revealed by Local PmP and Teleseismic Ps Waves. *Journal of Geophysical Research: Solid Earth*, *127*(2), 1–16. doi: 10.1029/2021JB023033

Lim, H., Kim, Y., Clayton, R., & Thurber, C. (2018, 9). Seismicity and structure of Nazca Plate subduction zone in southern Peru. *Earth and Planetary Science Letters*, *498*, 334–347. doi: 10.1016/j.epsl.2018.07.014

Liu, W., & Yao, H. (2020, 2). Rupture Process of the 26 May 2019 Mw 8.0 Northern Peru Intermediate-Depth Earthquake and Insights Into Its Mechanism. *Geophysical Research Letters*, *47*(4). doi: 10.1029/2020GL087167

Lu, P., Zhang, H., Gao, L., & Comte, D. (2021, 1). Seismic imaging of the double seismic zone in the subducting slab in Northern Chile. *Earthquake Research Advances*, *1*(1), 100003. doi: 10.1016/j.eqrea.2021.100003

Ma, Y., & Clayton, R. (2015). Flat slab deformation caused by interplate suction force. *Geophysical Research Letters*, *42*(17), 7064–7072. doi: 10.1002/2015GL065195

Manea, V., Manea, M., Ferrari, L., Orozco, T., Valenzuela, R., Husker, A., & Kostoglodov, V. (2017). A review of the geodynamic evolution of flat slab subduction in Mexico, Peru, and Chile. *Tectonophysics*, *695*, 27–52. Retrieved from `http://dx.doi.org/10.1016/j.tecto.2016.11.037` doi: 10.1016/j.tecto.2016.11.037

Manea, V., Marta, P., & Manea, M. (2012). Chilean flat slab subduction controlled by overriding plate thickness and trench rollback. *Geology*, *40*(1), 35–38. doi: 10.1130/G32543.1

McGlashan, N., Brown, L., & Kay, S. (2008, 12). Crustal thickness in the central Andes from teleseismically recorded depth phase precursors. *Geophysical Journal International*, *175*(3), 1013–1022. doi: 10.1111/J.1365-246X.2008.03897.X/3/175-3-1013-FIG010.JPEG

McKenzie, D. (1969). Speculations on the Consequences and Causes of Plate Motions. *Geophysical Journal of the Royal Astronomical Society*, *18*(1), 1–32. doi: 10.1111/j.1365-246X.1969.tb00259.x

Mohorovičić, A. (1910). Potres od 8. X 1909 (Das Beben vom 8. X. 1909). *Jahrbuch des meteorologischen Observatoriums in Zagreb (Agram) für das Jahr*, *1909*, 1–56.

Molnar, P., Tucker, B., & Brune, J. (1973). Corner frequencies of P and S waves and models of earthquake sources. *Bulletin of the Seismological Society of America*,

63(6-1), 2091–2104. doi: 10.1785/bssa0636-12091

Molnar, P., & Wyss, M. (1972). Moments, source dimensions and stress drops of shallow-focus earthquakes in the Tonga-Kermadec arc. *Physics of the Earth and Planetary Interiors*, *6*(4), 263–278. doi: 10.1016/0031-9201(72)90010-6

Mousavi, S., & Beroza, G. (2023). Machine Learning in Earthquake Seismology. *Annual Review of Earth and Planetary Sciences*, *51*, 105–129. doi: 10.1146/annurev-earth-071822-100323

Münchmeyer, J., Saul, J., & Tilmann, F. (2024). Learning the Deep and the Shallow: Deep-Learning-Based Depth Phase Picking and Earthquake Depth Estimation. *Seismological Research Letters*, *95*(3), 1543–1557. doi: 10.1785/0220230187

Murphy, J., & Barker, B. (2006, 8). Improved focal-depth determination through automated identification of the seismic depth phases pP and sP. *Bulletin of the Seismological Society of America*, *96*(4 A), 1213–1229. doi: 10.1785/0120050259

Murrell, S., & Ismail, I. (1976, 4). The effect of decomposition of hydrous minerals on the mechanical properties of rocks at high pressures and temperatures. *Tectonophysics*, *31*(3-4), 207–258. doi: 10.1016/0040-1951(76)90120-7

Nippress, S., & Rietbrock, A. (2007). Seismogenic zone high permeability in the Central Andes inferred from relocations of micro-earthquakes. *Earth and Planetary Science Letters*, *263*(3-4), 235–245. doi: 10.1016/j.epsl.2007.08.032

Ogawa, M. (1987, 12). Shear instability in a viscoelastic material as the cause of deep focus earthquakes. *Journal of Geophysical Research: Solid Earth*, *92*(B13), 13801–13810. doi: 10.1029/JB092IB13P13801

Okazaki, K., & Hirth, G. (2016, 2). Dehydration of lawsonite could directly trigger earthquakes in subducting oceanic crust. *Nature 2016 530:7588*, *530*(7588), 81–84. doi: 10.1038/nature16501

Oliver, J., Cook, F., & Brown, L. (1983, 4). Cocorp and the continental crust. *Journal of Geophysical Research: Solid Earth*, *88*(B4), 3329–3347. doi: 10.1029/JB088iB04p03329

Omohundro, S. (1989). Five balltree construction algorithms. *Science*, *51*(1), 1–22.

Peacock, S. (2001). Are the lower planes of double seismic zones caused by serpentine dehydration in subducting oceanic mantle? *Geology*, *29*(4), 299–302. doi: 10.1130/0091-7613(2001)029⟨0299:ATLPOD⟩2.0.CO;2

Pearce, R. (1977). Fault plane solutions using relative amplitudes of P and pP. *Geophysical*

Journal of the Royal Astronomical Society, *50*(2), 381–394. doi: 10.1111/j.1365-246X.1977.tb04179.x

Pearce, R., & Rogers, R. (1989). Determination of earthquake moment tensors from teleseismic relative amplitude observations. *Journal of Geophysical Research*, *94*(B1), 775–786. doi: 10.1029/JB094iB01p00775

Pedregosa, F., Michel, V., Grisel, O., Blondel, M., Prettenhofer, P., Weiss, R., ... Duchesnay, E. (2011). Scikit-learn: Machine Learning in Python Gaël Varoquaux Bertrand Thirion Vincent Dubourg Alexandre Passos PEDREGOSA, VAROQUAUX, GRAMFORT ET AL. Matthieu Perrot. *Journal of Machine Learning Research*, *12*, 2825–2830. Retrieved from `http://scikit-learn.sourceforge.net`.

Pesicek, J., Thurber, C., Zhang, H., Deshon, H., Engdahl, E., & Widiyantoro, S. (2010, 10). Teleseismic double-difference relocation of earthquakes along the Sumatra-Andaman subduction zone using a 3-D model. *Journal of Geophysical Research: Solid Earth*, *115*(10), 10303. doi: 10.1029/2010JB007443

Phillips, K., Clayton, R., Davis, P., Tavera, H., Guy, R., Skinner, S., ... Aguilar, V. (2012). Structure of the subduction system in southern Peru from seismic array data. *Journal of Geophysical Research: Solid Earth*, *117*(11), 11306. doi: 10.1029/2012JB009540

Pilger, R. (1981). Plate reconstructions, aseismic ridges, and low-angle subduction beneath the Andes. *Geological Society of America Bulletin*, *92*(7 pt 1), 448–456. doi: 10.1130/0016-7606(1981)92⟨448:PRARAL⟩2.0.CO;2

Poli, P., Prieto, G., Rivera, E., & Ruiz, S. (2016). Earthquakes initiation and thermal shear instability in the Hindu Kush intermediate depth nest. *Geophysical Research Letters*, *43*(4), 1537–1542. doi: 10.1002/2015GL067529

Portner, D., & Hayes, G. (2018). Incorporating teleseismic tomography data into models of upper mantle slab geometry. *Geophysical Journal International*, *215*(1), 325–332. doi: 10.1093/gji/ggy279

Prakash, A., Holyoke III, C., Kelemen, P., Kirby, S., Kronenberg, A., & Lamb, W. (2023). Carbonates and intermediate-depth seismicity: Stable and unstable shear in altered subducting plates and overlying mantle. *Proceedings of the National Academy of Sciences*, *120*(21), 2017. doi: 10.1073/pnas.2219076120

Prieto, G., Froment, B., Yu, C., Poli, P., & Abercrombie, R. (2017). Earthquake rupture below the brittle-ductile transition in continental lithospheric mantle. *Science*

Advances, *3*(3), 1–6. doi: 10.1126/sciadv.1602642

Prodehl, C., Kennett, B., Artemieva, I., & Thybo, H. (2013). 100 years of seismic research on the Moho. *Tectonophysics*, *609*, 9–44. doi: 10.1016/j.tecto.2013.05.036

Raleigh, C., & Paterson, M. (1965, 8). Experimental deformation of serpentinite and its tectonic implications. *Journal of Geophysical Research*, *70*(16), 3965–3985. doi: 10.1029/jz070i016p03965

Ranero, C., Villaseñor, A., Morgan, J., & Weinrebe, W. (2005). Relationship between bend-faulting at trenches and intermediate-depth seismicity. *Geochemistry, Geophysics, Geosystems*, *6*(12). doi: 10.1029/2005GC000997

Rietbrock, A., & Waldhauser, F. (2004). A narrowly spaced double-seismic zone in the subducting Nazca plate. *Geophysical Research Letters*, *31*(10), 2–5. doi: 10.1029/2004GL019610

Robinson, D., Sambridge, M., Snieder, R., & Hauser, J. (2013). Relocating a cluster of earthquakes using a single seismic station. *Bulletin of the Seismological Society of America*, *103*(6), 3057–3072. doi: 10.1785/0120130004

Rodríguez, E., Beck, S., Ruiz, M., Meltzer, A., Portner, D., Hernández, S., ... Charvis, P. (2024). Seismic imaging of the Northern Andean subduction zone from teleseismic tomography: a torn and fragmented Nazca slab. *Geophysical Journal International*, *236*(1), 593–606. doi: 10.1093/gji/ggad421

Ross, Z., Meier, M., & Hauksson, E. (2018). P Wave Arrival Picking and First-Motion Polarity Determination With Deep Learning. *Journal of Geophysical Research: Solid Earth*, *123*(6), 5120–5129. doi: 10.1029/2017JB015251

Rost, S., & Thomas, C. (2002). Array seismology: Methods and applications. *Reviews of Geophysics*, *40*(3), 2–1. doi: 10.1029/2000RG000100

Rutter, E., & Brodie, K. (1988, 5). Experimental "sytectonic" dehydration of serpentinite under conditions of controlled pore water pressure. *Journal of Geophysical Research: Solid Earth*, *93*(B5), 4907–4932. doi: 10.1029/jb093ib05p04907

Ryan, J., Beck, S., Zandt, G., Wagner, L., Minaya, E., & Tavera, H. (2016). Central Andean crustal structure from receiver function analysis. *Tectonophysics*, *682*, 120–133. doi: 10.1016/j.tecto.2016.04.048

Sandiford, D., Moresi, L., Sandiford, M., Farrington, R., & Yang, T. (2020, 8). The Fingerprints of Flexure in Slab Seismicity. *Tectonics*, *39*(8). doi: 10.1029/2019TC005894

Sandiford, D., Moresi, L., Sandiford, M., & Yang, T. (2019). Geometric controls on flat

slab seismicity. *Earth and Planetary Science Letters*, *527*, 115787. doi: 10.1016/j.epsl.2019.115787

Schaff, D., & Waldhauser, F. (2005). Waveform cross-correlation-based differential travel-time measurements at the northern California seismic network. *Bulletin of the Seismological Society of America*, *95*(6), 2446–2461. doi: 10.1785/0120040221

Schellart, W. (2020). Control of Subduction Zone Age and Size on Flat Slab Subduction. *Frontiers in Earth Science*, *8*(February), 1–18. doi: 10.3389/feart.2020.00026

Schepers, G., Van Hinsbergen, D., Spakman, W., Kosters, M., Boschman, L., & McQuarrie, N. (2017). South-American plate advance and forced Andean trench retreat as drivers for transient flat subduction episodes. *Nature Communications*, *8*(0316), 1–9. Retrieved from `http://dx.doi.org/10.1038/ncomms15249` doi: 10.1038/ncomms15249

Schimmel, M., & Paulssen, H. (1997). Noise reduction and detection of weak, coherent signals through phase-weighted stacks. *Geophysical Journal International*, *130*(2), 497–505. doi: 10.1111/j.1365-246X.1997.tb05664.x

Schweitzer, J., Fyen, J., Mykkeltveit, S., Gibbons, S., Pirli, M., Kühn, D., & Kværna, T. (2012). Seismic arrays. In *In new manual of seismological observatory practice 2 (nmsop-2)* (pp. 1–80). Deutsches GeoForschungsZentrum GFZ. doi: 10.1007/978-3-642-41714-6{_}191764

Shuey, R. (1985). Simplification of the Zoeppritz Equations. *Geophysics*, *50*(4), 609–614. doi: 10.1190/1.1441936

Sibson, R. (1977). Fault rocks and fault mechanisms. *Journal of the Geological Society*, *133*(3), 191–213. doi: 10.1144/gsjgs.133.3.0191

Sippl, C., Schurr, B., Asch, G., & Kummerow, J. (2018, 5). Seismicity Structure of the Northern Chile Forearc From ¿100,000 Double-Difference Relocated Hypocenters. *Journal of Geophysical Research: Solid Earth*, *123*(5), 4063–4087. doi: 10.1002/2017JB015384

Sippl, C., Schurr, B., Münchmeyer, J., Barrientos, S., & Oncken, O. (2023). The Northern Chile forearc constrained by 15 years of permanent seismic monitoring. *Journal of South American Earth Sciences*, *126*(March), 104326. doi: 10.1016/j.jsames.2023.104326

Stachnik, J., Abers, G., & Christensen, D. (2004). Seismic attenuation and mantle wedge temperatures in the Alaska subduction zone. *Journal of Geophysical Research: Solid*

Earth, *109*(10), 1–17. doi: 10.1029/2004JB003018

Storchak, D., Schweitzer, J., & Borman, P. (2003). Seismic Phase Nomenclature: The IASPEI Standard. *Seismological Research Letters*, *74*(6), 761–772. doi: 10.1007/978-3-030-10475-7{_}11-1

Swenson, J., Beck, S., & Zandt, G. (2000). Crustal structure of the Altiplano from broadband regional waveform modeling: Implications for the composition of thick continental crust. *Journal of Geophysical Research: Solid Earth*, *105*(B1), 607–621. doi: 10.1029/1999jb900327

Syracuse, E., van Keken, P., Abers, G., Suetsugu, D., Bina, C., Inoue, T., ... Jellinek, M. (2010). The global range of subduction zone thermal models. *Physics of the Earth and Planetary Interiors*, *183*(1-2), 73–90. doi: 10.1016/j.pepi.2010.02.004

Taramõn, J., Rodríguez-González, J., Negredo, A., & Billen, M. (2015). Influence of cratonic lithosphere on the formation and evolution of flat slabs: Insights from 3-D time-dependent modeling. *Geochemistry, Geophysics, Geosystems*, *16*(9), 2933–2948. doi: 10.1002/2015GC005940

Thielmann, M., Rozel, A., Kaus, B., & Ricard, Y. (2015). Intermediate-depth earthquake generation and shear zone formation caused by grain size reduction and shear heating. *Geology*, *43*(9), 791–794. doi: 10.1130/G36864.1

Tibuleac, I. (2014, 11). A method for first-order earthquake depth estimation using super-arrays. *Seismological Research Letters*, *85*(6), 1255–1264. doi: 10.1785/0220130212

Tovish, A., Schubert, G., & Luyendyk, B. (1978). Mantle flow pressure and the angle of subduction: Non-Newtonian corner flows. *Journal of Geophysical Research: Solid Earth*, *83*(B12), 5892–5898. doi: 10.1029/jb083ib12p05892

Trenkamp, R., Kellogg, J., Freymueller, J., & Mora, H. (2002). Wide plate margin deformation, southern Central America and northwestern South America, CASA GPS observations. *Journal of South American Earth Sciences*, *15*(2), 157–171. doi: 10.1016/S0895-9811(02)00018-4

Vallée, M., & Douet, V. (2016). A new database of source time functions (STFs) extracted from the SCARDEC method. *Physics of the Earth and Planetary Interiors*, *257*, 149–157. doi: 10.1016/j.pepi.2016.05.012

van Hunen, J., Van Den Berg, A., & Vlaar, N. (2002, 7). The impact of the South-American plate motion and the Nazca Ridge subduction on the flat subduction below South Peru. *Geophysical Research Letters*, *29*(14), 35–1. doi: 10.1029/2001GL014004

van Hunen, J., van den Berg, A., & Vlaar, N. (2004). Various mechanisms to induce present-day shallow flat subduction and implications for the younger Earth: A numerical parameter study. *Physics of the Earth and Planetary Interiors*, *146*(1-2), 179–194. doi: 10.1016/j.pepi.2003.07.027

van Keken, P. (2003). The structure and dynamics of the mantle wedge. *Earth and Planetary Science Letters*, *215*(3-4), 323–338. doi: 10.1016/S0012-821X(03)00460-6

van Keken, P., & Wilson, C. (2023). An introductory review of the thermal structure of subduction zones: I—motivation and selected examples. *Progress in Earth and Planetary Science*, *10*(1). doi: 10.1186/s40645-023-00573-z

Virtanen, P., Gommers, R., Oliphant, T., Haberland, M., Reddy, T., Cournapeau, D., ... Vázquez-Baeza, Y. (2020). SciPy 1.0: fundamental algorithms for scientific computing in Python. *Nature Methods*, *17*(3), 261–272. doi: 10.1038/s41592-019-0686-2

Wadati, K. (1928). Shallow and deep earthquakes. *Geophysical Magazine*, *1*, 161–202.

Wagner, L., Caddick, M., Kumar, A., Beck, S., & Long, M. (2020). Effects of Oceanic Crustal Thickness on Intermediate Depth Seismicity. *Frontiers in Earth Science*, *8*(July), 1–14. doi: 10.3389/feart.2020.00244

Wagner, L., & Okal, E. (2019). The Pucallpa Nest and its constraints on the geometry of the Peruvian Flat Slab. *Tectonophysics*, *762*(October 2018), 97–108. doi: 10.1016/j.tecto.2019.04.021

Waldhauser, F., & Ellsworth, W. (2000). A Double-difference Earthquake location algorithm: Method and application to the Northern Hayward Fault, California. *Bulletin of the Seismological Society of America*, *90*(6), 1353–1368. doi: 10.1785/0120000006

Wang, J., Xiao, Z., Liu, C., Zhao, D., & Yao, Z. (2019). Deep Learning for Picking Seismic Arrival Times. *Journal of Geophysical Research: Solid Earth*, *124*(7), 6612–6624. doi: 10.1029/2019JB017536

Wang, K. (2002). Unbending combined with dehydration embrittlement as a cause for double and triple seismic zones. *Geophysical Research Letters*, *29*(18), 1889. doi: 10.1029/2002GL015441

Wang, K., He, J., & Davis, E. (1997). Influence of basement topography on hydrothermal circulation in sediment-buried igneous oceanic crust. *Earth and Planetary Science Letters*, *146*(1-2), 151–164.

Ward, J., Nowacki, A., & Rost, S. (2020). Lateral Velocity Gradients in the African Lower

Mantle Inferred From Slowness Space Observations of Multipathing. *Geochemistry, Geophysics, Geosystems*, *21*(8). doi: 10.1029/2020GC009025

Ward, J., Thorne, M., Nowacki, A., & Rost, S. (2021). Automatic slowness vector measurements of seismic arrivals with uncertainty estimates using bootstrap sampling, array methods and unsupervised learning. *Geophys. J. Int*, *226*, 1847–1857. doi: 10.1093/gji/ggab196

Ward, J., Thorne, M., Nowacki, A., & Rost, S. (2023, 7). Upper Mantle Structure Beneath the Contiguous US Resolved With Array Observations of SKS Multipathing and Slowness Vector Perturbations. *Journal of Geophysical Research: Solid Earth*, *128*(7), e2022JB026260. doi: 10.1029/2022JB026260

Wei, S., Wiens, D., van Keken, P., & Cai, C. (2017). Slab temperature controls on the Tonga double seismic zone and slab mantle dehydration. *Science Advances*, *3*(1), 1–9. doi: 10.1126/sciadv.1601755

Weston, J., Engdahl, E., Harris, J., Di Giacomo, D., & Storchak, D. (2018). ISC-EHB: Reconstruction of a robust earthquake data set. *Geophysical Journal International*, *214*(1), 474–484. doi: 10.1093/gji/ggy155

Wiens, D. (2001). Seismological constraints on the mechanism of deep earthquakes: Temperature dependence of deep earthquake source properties. *Physics of the Earth and Planetary Interiors*, *127*(1-4), 145–163. doi: 10.1016/S0031-9201(01)00225-4

Wigger, P., Araneda, M., Giese, P., Heinsohn, W., Röwer, P., Schmitz, M., & Viramonte, J. (1991). The crustal structure along the central Andean transect derived from seimic refraction investigations. *Central Andean Transect Nazca Plate to Chaco Plains, Southwestern Pacific Ocean, Northern Chile, and Northern Argentina*, *6*, 13–19. doi: 10.1029/gt006p0013

Willmore, P., Hales, A., & Gane, P. (1952). A Seismic investigation of crustal structure in western Transvaal. *Earth*(42), 53–80.

Wilson, D., Angus, D., Ni, J., & Grand, S. (2006). Constraints on the interpretation of S-to-P receiver functions. *Geophysical Journal International*, *165*(3), 969–980. doi: 10.1111/j.1365-246X.2006.02981.x

Wimpenny, S., Craig, T., & Blackwell, A. (2023). Lower-Crustal Normal Faulting and Lithosphere Rheology in the Atlas Foreland. *Journal of Geophysical Research: Solid Earth*, *128*(12). doi: 10.1029/2023JB028090

Wölbern, I., Heit, B., Yuan, X., Asch, G., Kind, R., Viramonte, J., ... Wilke, H. (2009).

Receiver function images from the Moho and the slab beneath the Altiplano and Puna plateaus in the Central Andes. *Geophysical Journal International*, *177*(1), 296–308. doi: 10.1111/j.1365-246X.2008.04075.x

Woodgold, C. (1999). Wide-Aperture Beamforming of Depth Phases by Timescale Contraction. *Bulletin of the Seismological Society of America*, *89*(1), 165–177. doi: 10.1785/bssa0890010165

Woollam, J., Münchmeyer, J., Tilmann, F., Rietbrock, A., Lange, D., Bornstein, T., ... Soto, H. (2022). SeisBench-A Toolbox for Machine Learning in Seismology. *Seismological Research Letters*, *93*(3), 1695–1709. doi: 10.1785/0220210324

Wyss, M., & Hanks, T. (1972). The source parameters of the San Fernando earthquake inferred from teleseismic body waves. *Bulletin of the Seismological Society of America*, *62*(2), 591–602.

Wyss, M., & Molnar, P. (1972). Source parameters of intermediate and deep focus earthquakes in the Tonga arc. *Physics of the Earth and Planetary Interiors*, *6*(4), 279–292. doi: 10.1016/0031-9201(72)90011-8

Yamasaki, T., & Seno, T. (2003). Double seismic zone and dehydration embrittlement of the subducting slab. *Journal of Geophysical Research: Solid Earth*, *108*(B4), 2212. doi: 10.1029/2002jb001918

Yang, H., Liu, Y., & Lin, J. (2012, 12). Effects of subducted seamounts on megathrust earthquake nucleation and rupture propagation. *Geophysical Research Letters*, *39*(24). doi: 10.1029/2012GL053892

Ye, L., Lay, T., & Kanamori, H. (2020). Anomalously low aftershock productivity of the 2019 MW 8.0 energetic intermediate-depth faulting beneath Peru. *Earth and Planetary Science Letters*, *549*. doi: 10.1016/j.epsl.2020.116528

Yuan, X., Sobolev, S., & Kind, R. (2002). Moho topography in the Central Andes and its geodynamic implications. *Earth and Planetary Science Letters*, *199*(3-4), 389–402. doi: 10.1016/S0012-821X(02)00589-7

Yuan, X., Sobolev, S., Kind, R., Oncken, O., Bock, G., Asch, G., ... Comte, D. (2000). Subduction and collision processes in the Central Andes constrained by converted seismic phases. *Nature*, *408*(6815), 958–961. doi: 10.1038/35050073

Zandt, G., Gilbert, H., Owens, T., Ducea, M., Saleeby, J., & Jones, C. (2004, 9). Active foundering of a continental arc root beneath the southern Sierra Nevada in California. *Nature*, *431*(7004), 41–46. doi: 10.1038/nature02847

Zandt, G., Velasco, A., & Beck, S. (1994). Composition and thickness of the southern Altiplano crust, Bolivia. *Geology*, *22*(11), 1003–1006. doi: 10.1130/0091-7613(1994)022⟨1003:CATOTS⟩2.3.CO;2

Zhang, Z., & Lay, T. (1993). Investigation of upper mantle discontinuities near northwestern Pacific subduction zones using precursors to sSH. *Journal of Geophysical Research*, *98*(B3), 4389–4405. doi: 10.1029/92jb02050

Zhu, L., & Kanamori, H. (2000). Moho depth variation in southern California from teleseismic receiver functions. *Journal of Geophysical Research: Solid Earth*, *105*(B2), 2969–2980. doi: 10.1029/1999jb900322

Zhu, W., & Beroza, G. (2019). PhaseNet: A deep-neural-network-based seismic arrival-time picking method. *Geophysical Journal International*, *216*(1), 261–273. doi: 10.1093/gji/ggy423

Appendix A

Supplementary Material per Chapter

A.1 Chapter 2: Automatic relocation of intermediate-depth earthquakes using adaptive teleseismic arrays

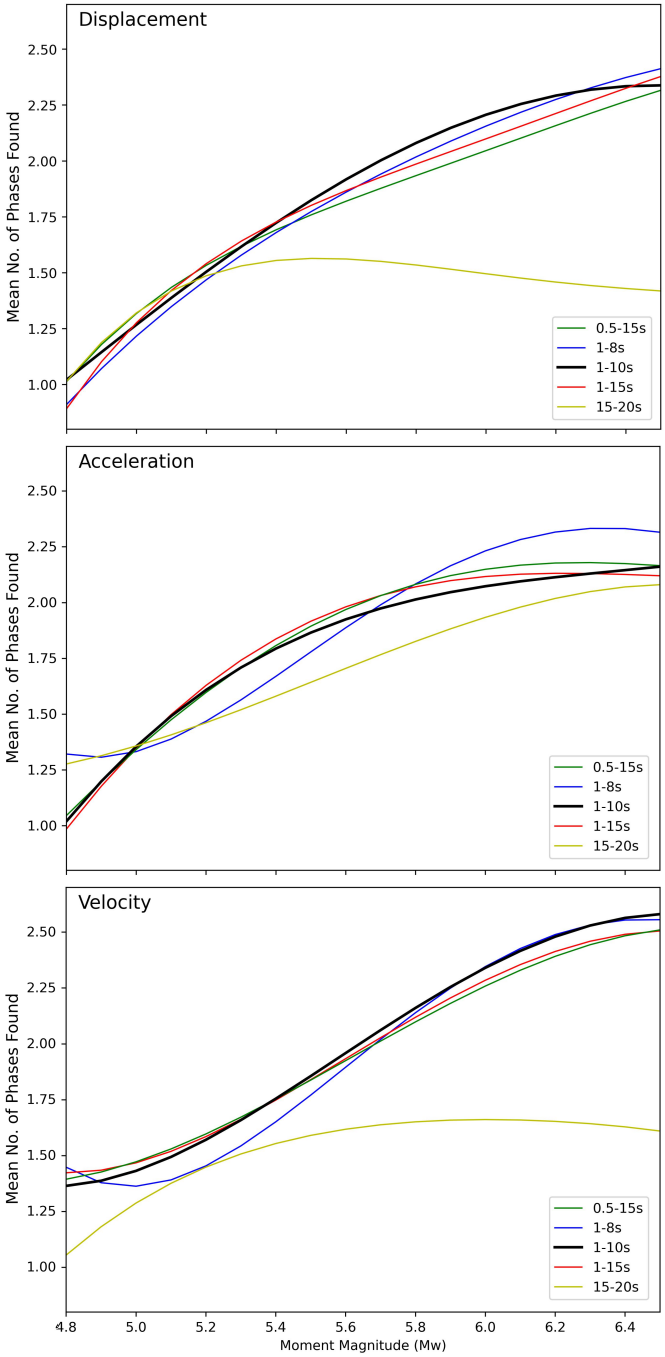

Figure A.1: Plot showing the mean number of phases (P, pP or sP) found per moment magnitude whilst applying five different bandpass filters for three seismic data types – displacement, acceleration and velocity.

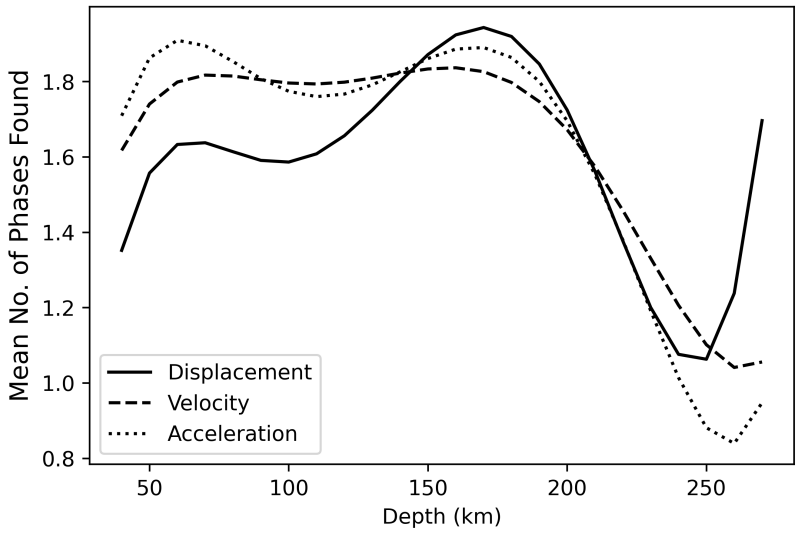

Figure A.2: Plot showing the mean number of phases (P, pP or sP) found per depth whilst applying a 1-10 s bandpass filter for three seismic data types – displacement, velocity and acceleration.

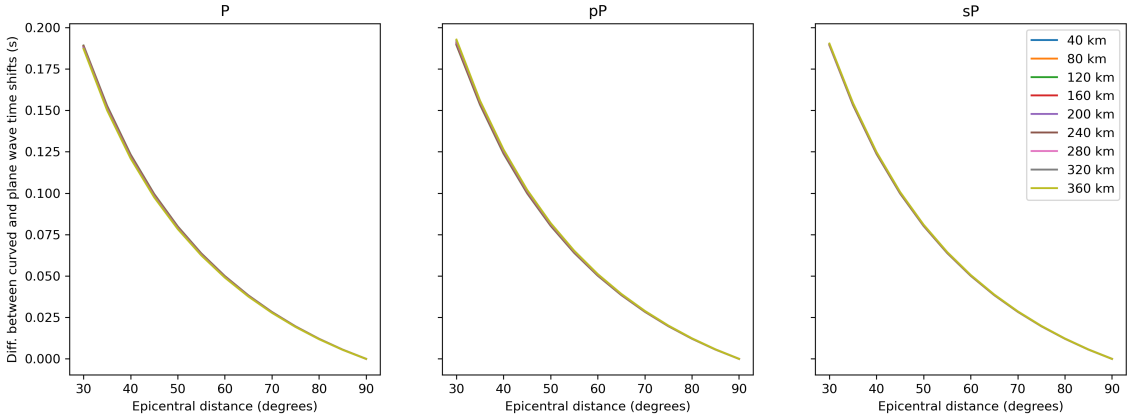

Figure A.3: Plots showing the difference between the plane and curved wavefront time-shifts required to beamform a theoretical station for P, pP and sP arrivals using the ak135 velocity model (Kennett et al., 1995). The theoretical station is 278 km away from the beamforming coordinates at approximately 045° bearing. A range of source depths from 40-360 km are tested using a backazimuth of 180°. All 3 phases are calculated to have less than 0.2 s difference between the plane and curved wavefront time-shifts which significantly decreases with epicentral distance. Results shown are calculated using software from Ward et al. (2023).

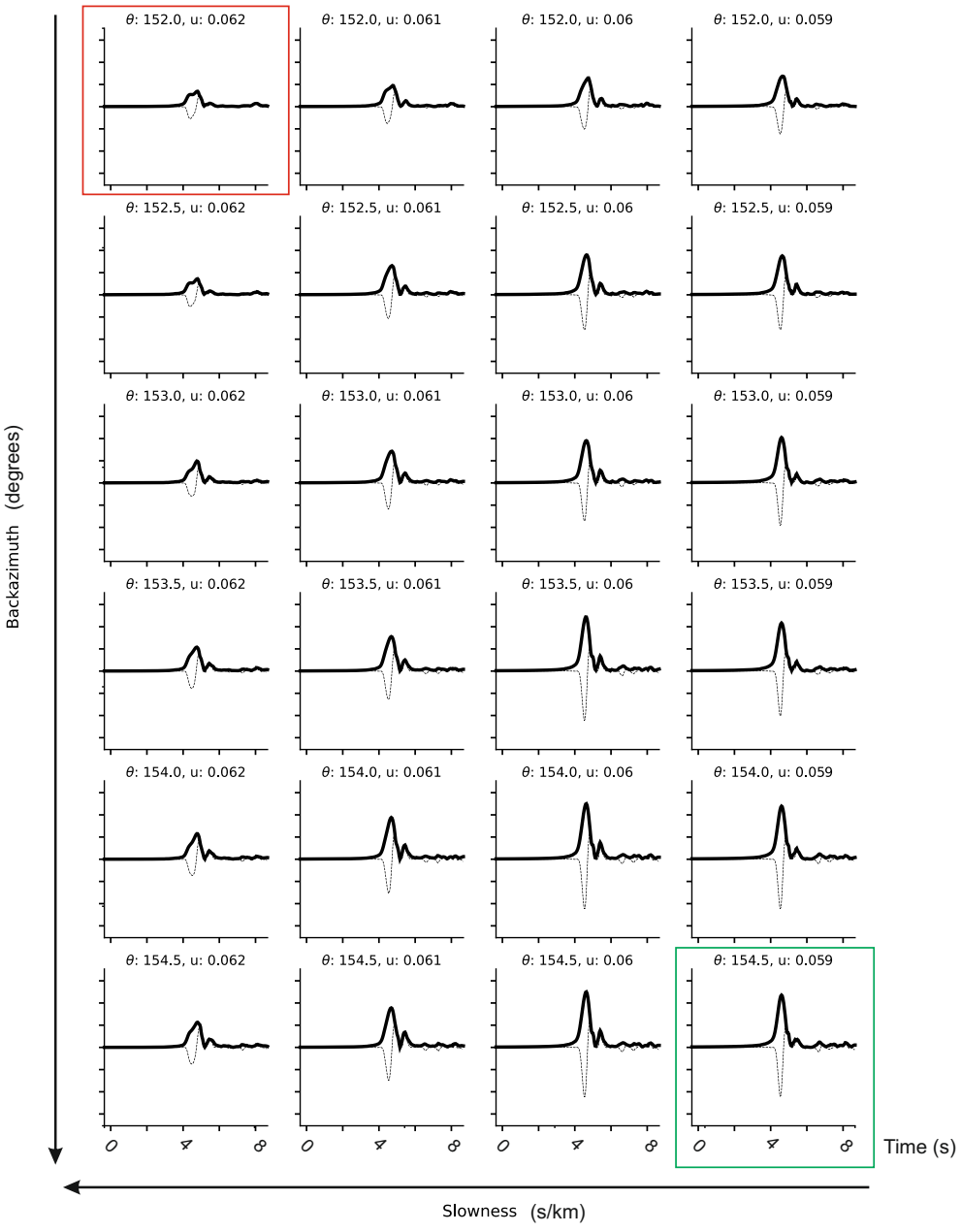

Figure A.4: Comparison grid of P arrival phase-weighted beams (power of 4) demonstrating the variation in the amplitude, and thus coherency, as the backazimuth and slowness values grade from those found by the geodetic calculations (red box) to those found by beampacking (green box). θ represents backazimuth and u represents slowness. Example is from an *ad-hoc* array located 57.9° from the 23rd May 2010, m_b 6.2 earthquake.

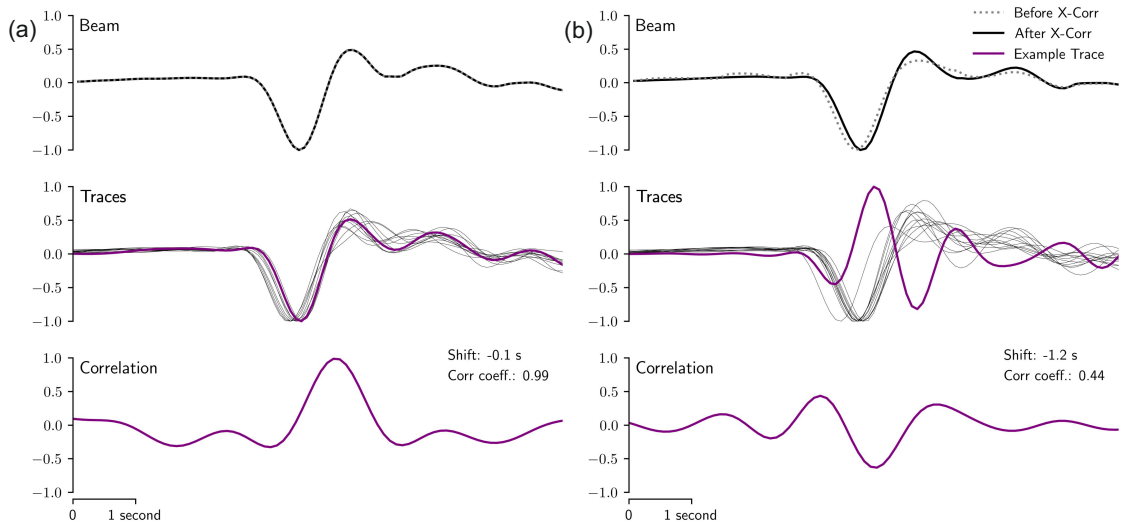

Figure A.5: Cross-correlation results for *ad-hoc* arrays located at (a) 83.2° and (b) 83.1° epicentral distances from the 23rd May 2010, m_b 6.2 earthquake. (a) demonstrates an array where no traces fail the cross-correlation quality control parameters, whilst (b) shows an *ad-hoc* array where the example trace fails to meet the specifications and is removed. The updated beam subsequently reflects an increased P arrival amplitude.

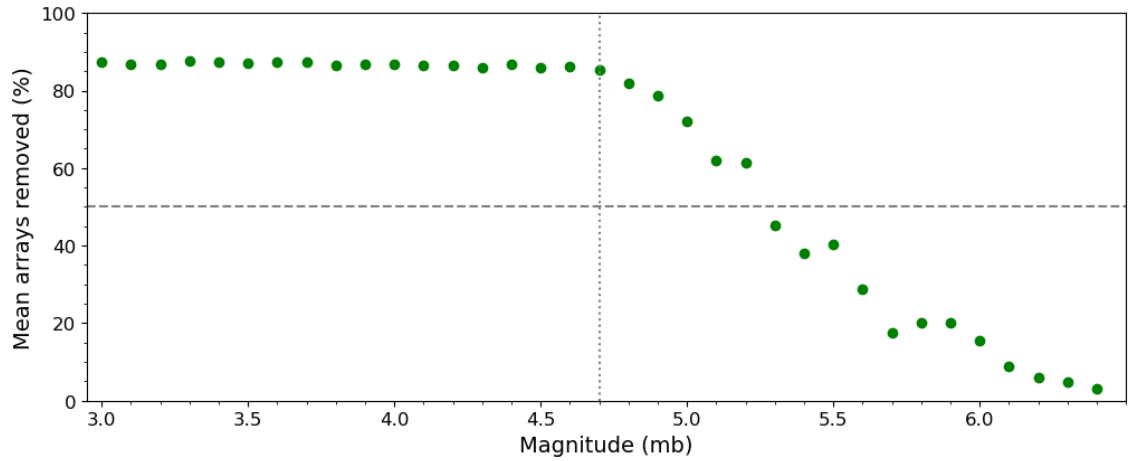

Figure A.6: Mean percentage of arrays removed by the two data quality assessments – cross-correlation and vespagram based – per magnitude (m_b) of earthquake in the Peruvian event catalogue defined in Section 2.2.1. The grey dashed line indicates where 50% of arrays are removed by the quality assessments, and the grey dotted line highlights the onset of the negative correlation between magnitude and percentage of arrays removed, occurring at approx. m_b 4.7.

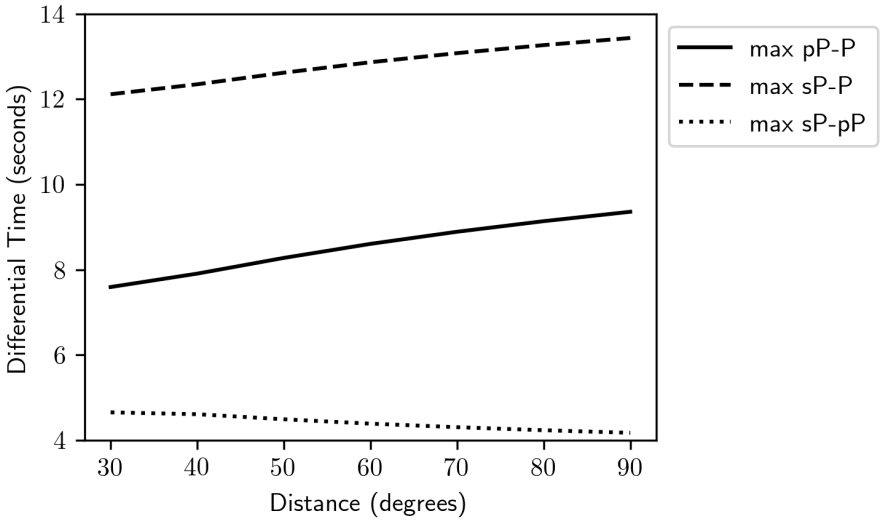

Figure A.7: Plot illustrating the maximum differential times between the given phases for a 40 km deep source, assuming a depth error of 40 km. This is to determine reasonable fixed time/error margins during the phase identification routine for shallow earthquakes. Deeper earthquakes use a 25% error margin during the phase identification routine.

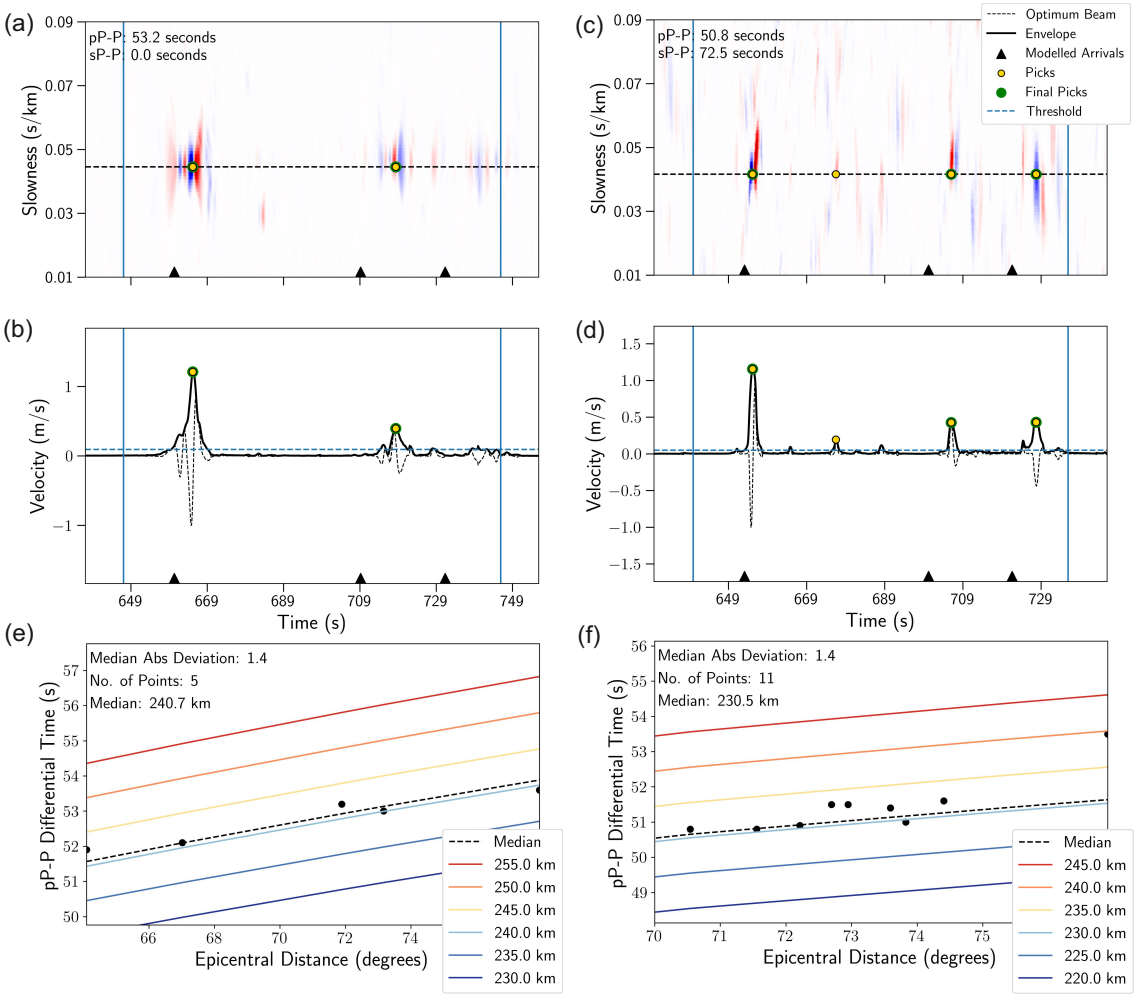

Figure A.8: Example *ad-hoc* arrays from northern Chile for 2 events with differing relocated depths to those found by Craig (2019). A Mw 6.4 event from 15th September 1999 with a hypocentre found to be 16.1 km deeper than Craig (2019) – vespagram (a) and optimum beam (b) for an *ad-hoc* array at an epicentral distance of 71.9°, and *pP-P* differential time plot (c). A Mw 5.3 event from 24th May 2001 with a 12.5 km deeper depth found by this study – vespagram (a) and optimum beam (b) for an *ad-hoc* array at an epicentral distance of 70.5°, and *pP-P* differential time plot (c).

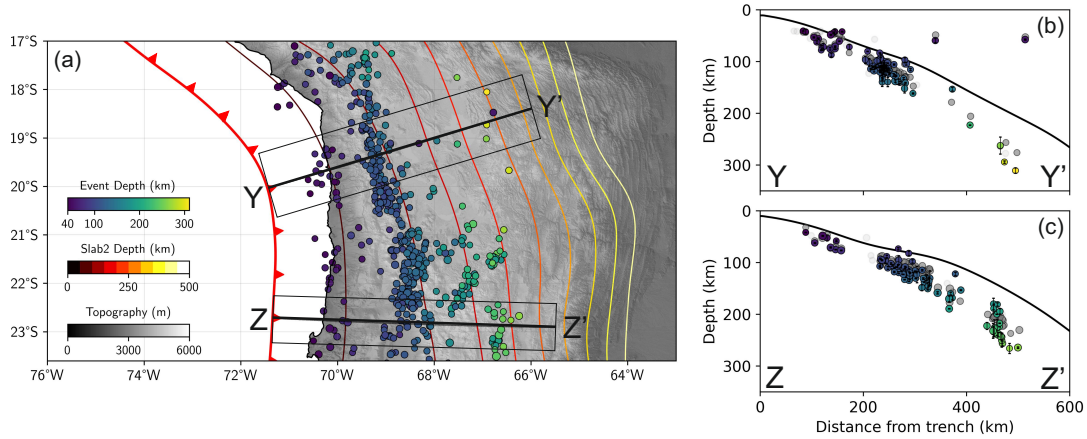

Figure A.9: Northern Chile catalogue with error bars determined though jack-knifing the *ad-hoc* arrays. The figure shows events with magnitudes between m_b 4.7-6.5, and have final relocated depths between 40-350 km with errors of less than 20 km. (a) Map of northern Chile, with the relocated hypocentres, example cross section locations and Slab2 contours plotted (Hayes et al., 2018). (b) and (c) Show example cross sections with our relocated hypocentral depths in colour with their error bars, the original ISC hypocentres which we relocated are in dark grey and ISC hypocentres which were not relocated by our approach in pale grey. All plotted hypocentres are scaled in size by magnitude

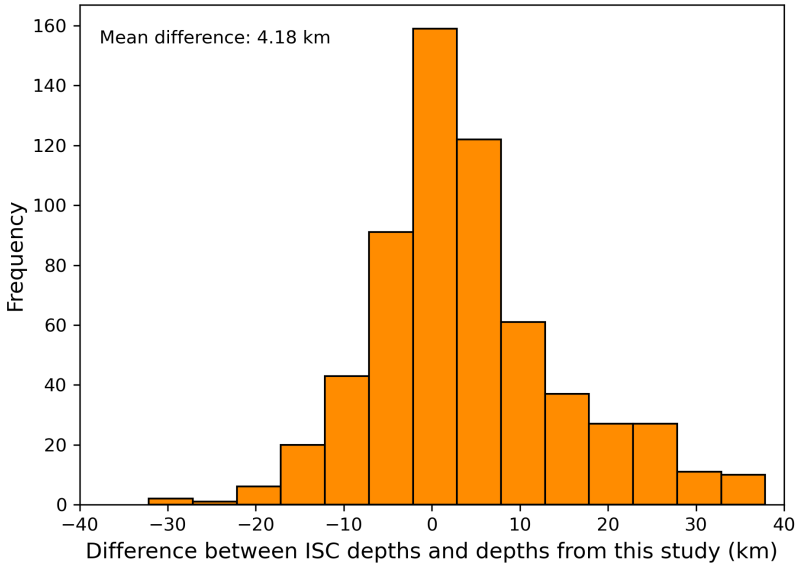

Figure A.10: Histogram showing the difference in depths between the initial ISC event catalogue and the final Peruvian catalogue determined during Chapter 2

A.2 Chapter 3: Automatically detecting *S* and *sS* on teleseismic data

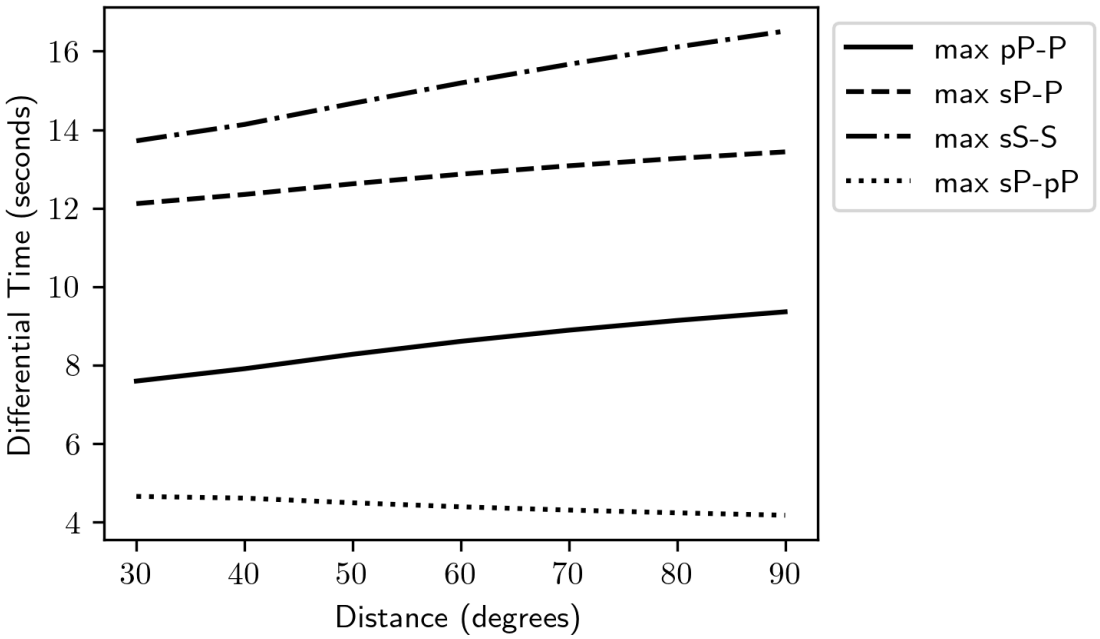

Figure A.11: Plot illustrating the maximum differential times between the given phases for a 40 km deep source, assuming a depth error of 40 km. This is to determine reasonable fixed time/error margins during the phase identification routine for shallow earthquakes. Deeper earthquakes use a 25% error margin during the phase identification routine.

A.3 Chapter 4: Assessing the impact of automatically-derived depth phases on global earthquake catalogues, and their relocation

A.4 Chapter 6: Crustal thickness determination using pmP phases identified from adaptive teleseismic array data

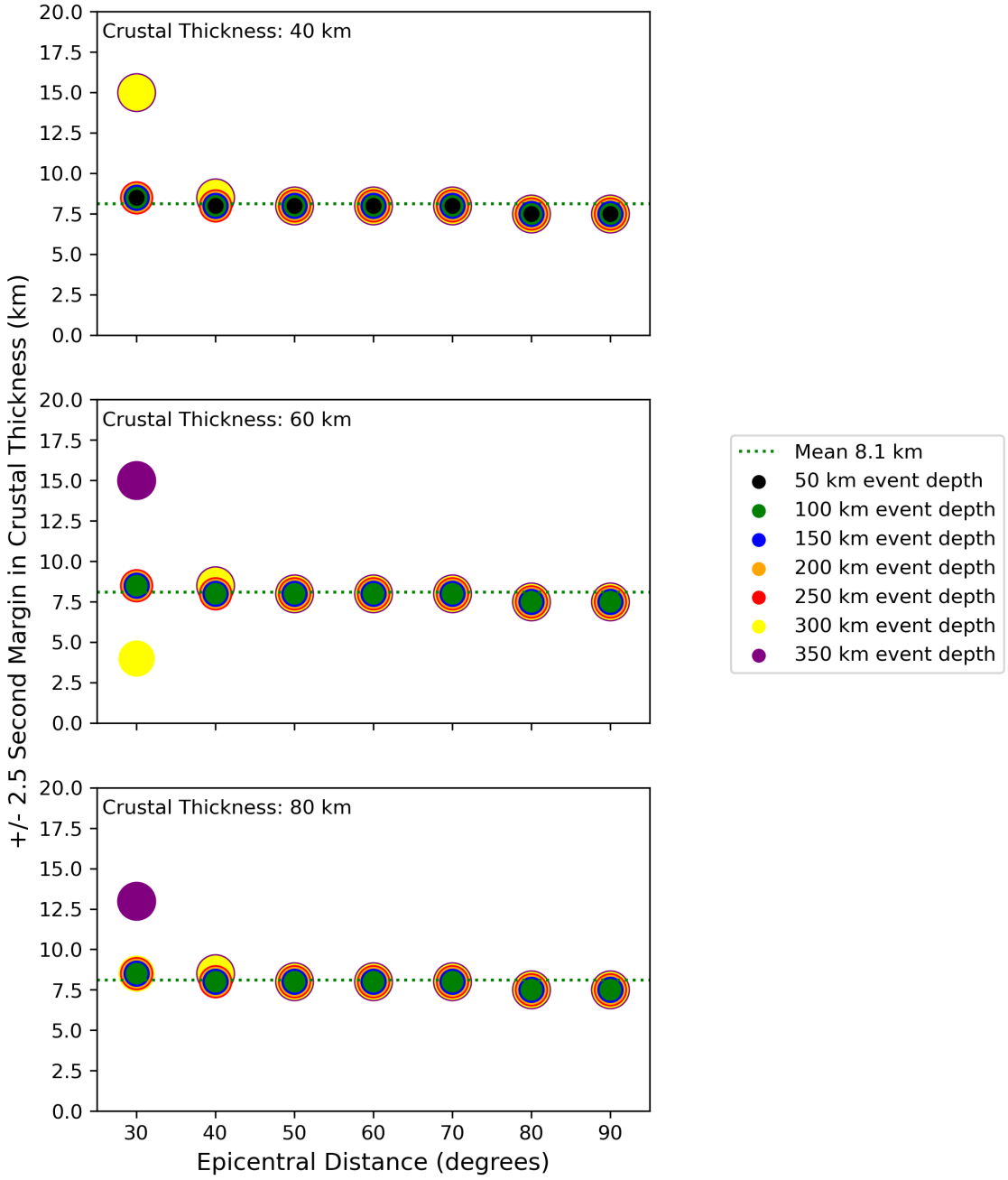

Figure A.12: Tests using the ak135 1D velocity model (Kennett et al., 1995) to determine the average crustal thickness a ±2.5 second search window allows, whilst varying event depth and initial crustal thickness. We find that a ±2.5 second window gives approximately ±8 km crustal thickness variation.

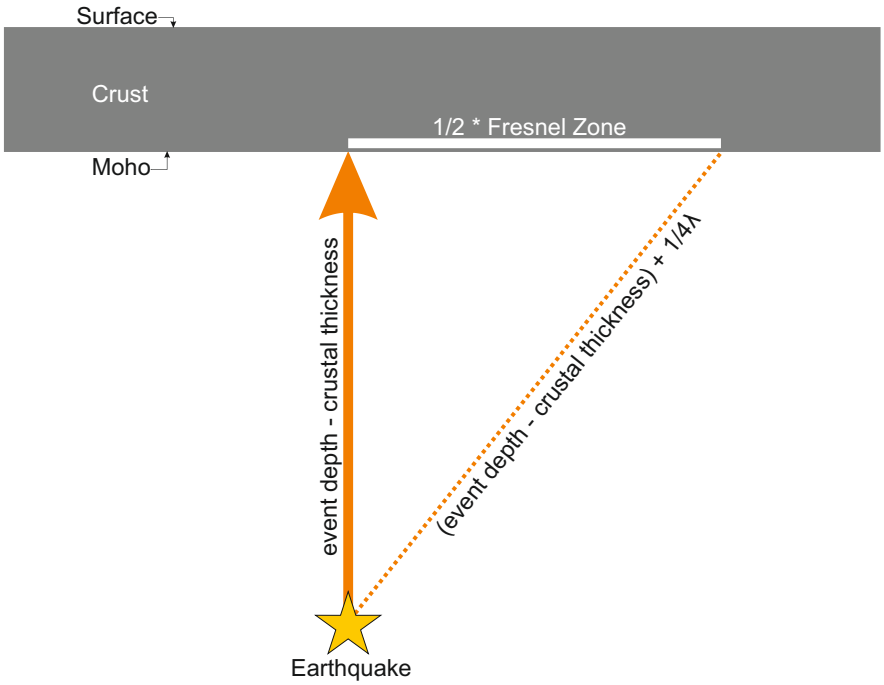

Figure A.13: Schematic demonstrating how to quickly calculate a Fresnel zone for a *pmP* bounce point at the Moho, assuming a ray path with a vertical take-off angle and a dominant wavelength (λ).

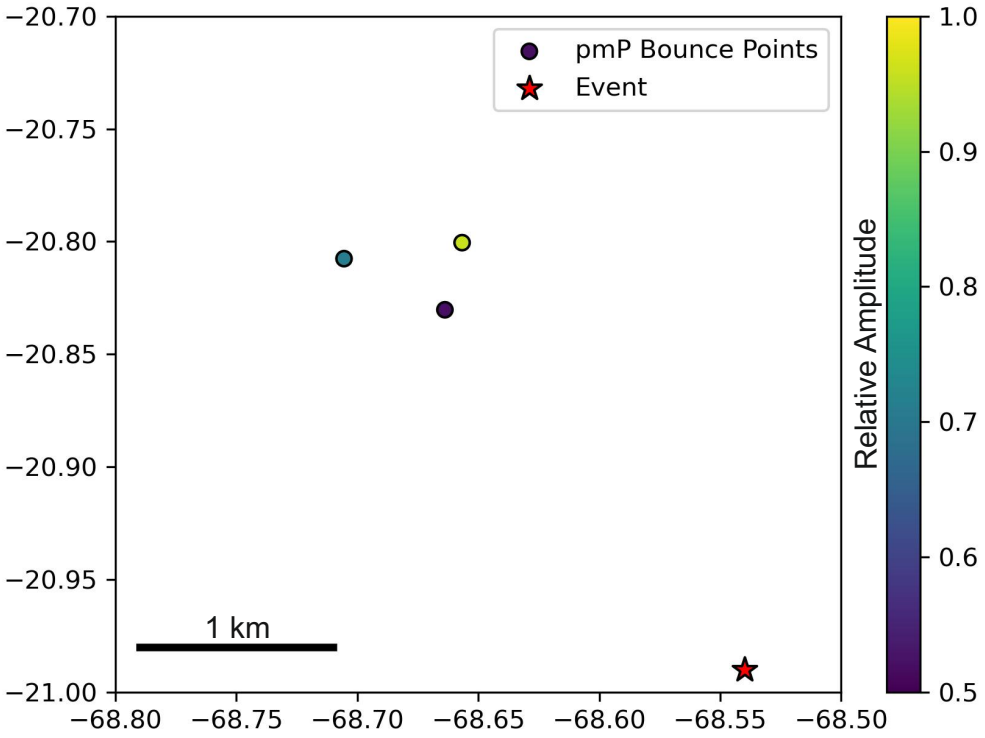

Figure A.14: Map of *pmP* bounce points for the *ad-hoc* array data shown in Figure 6.11, coloured by the linear optimum beam relative amplitude values for *pmP* and *P*. This demonstrates the spatial variability of the values within 1 km distance.

A.5 Chapter 7: South American Subduction Zone: a case study

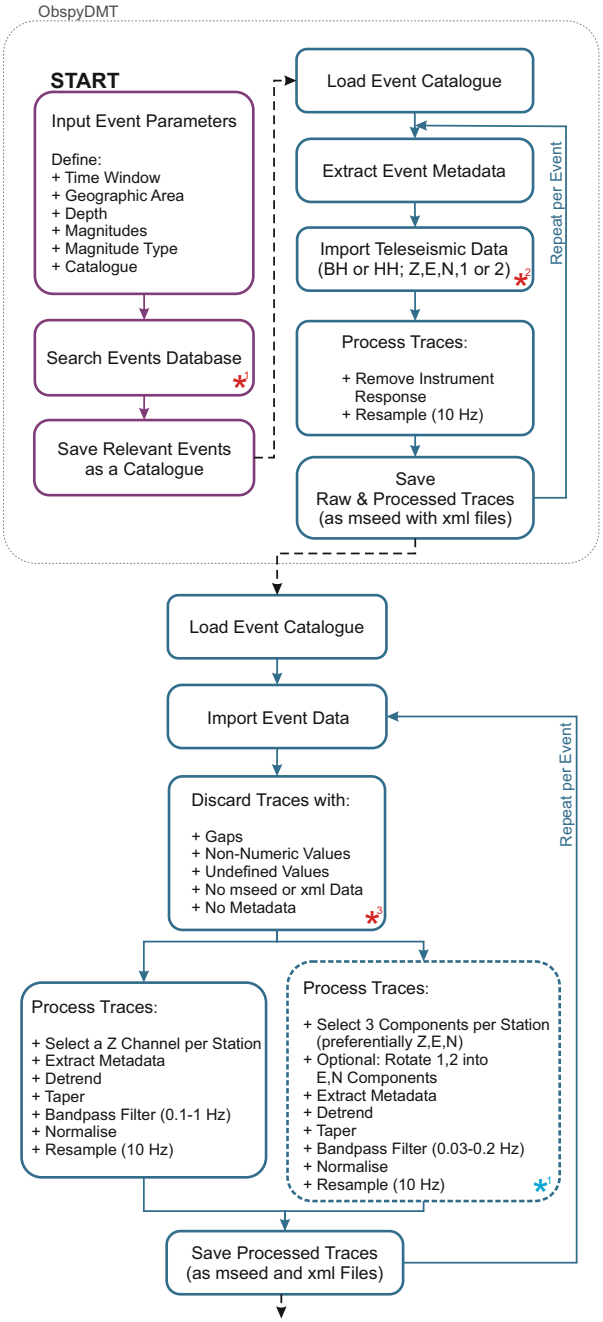

Figure A.15: Summary workflow.

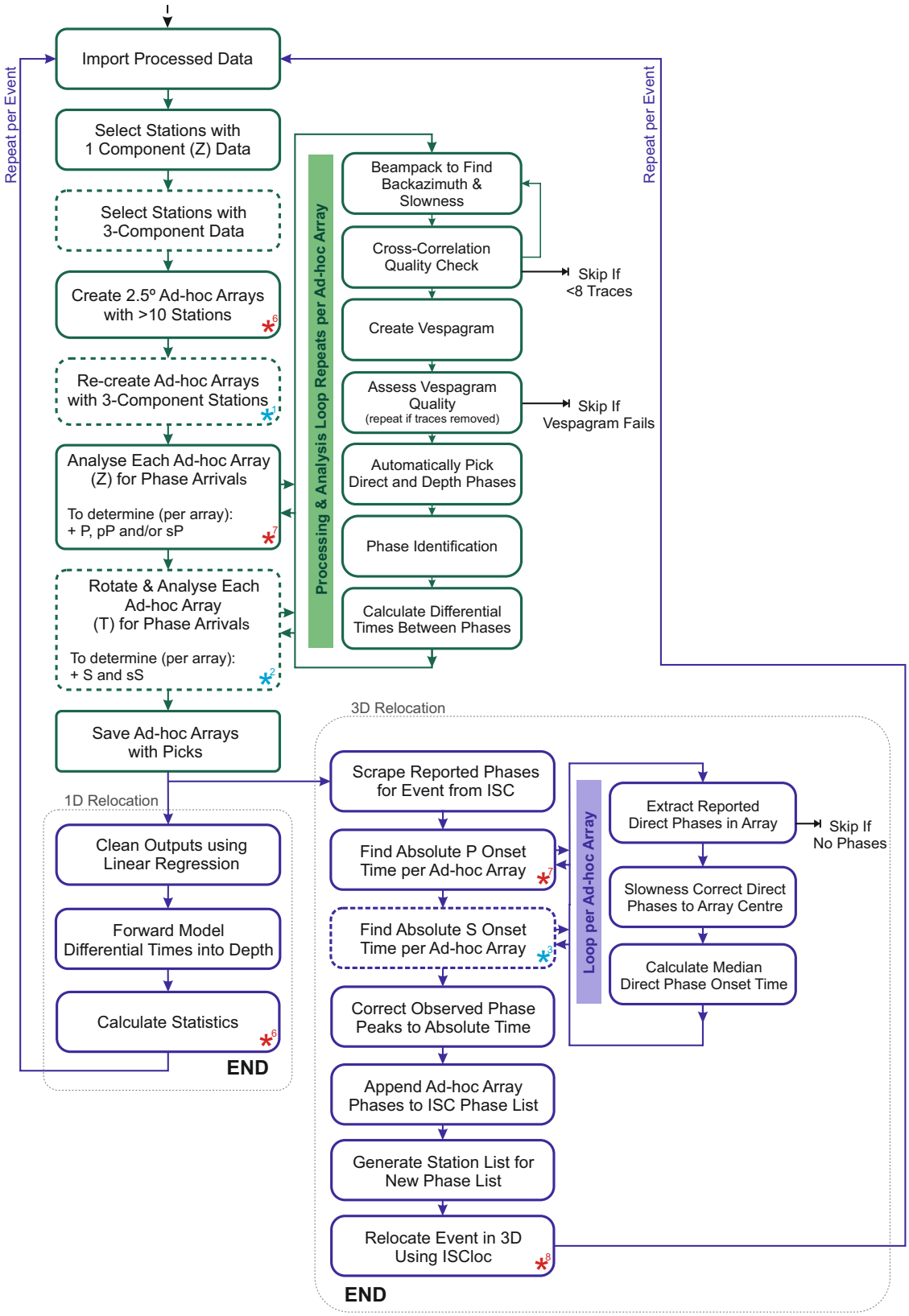

Figure A.16: Summary workflow (continued).

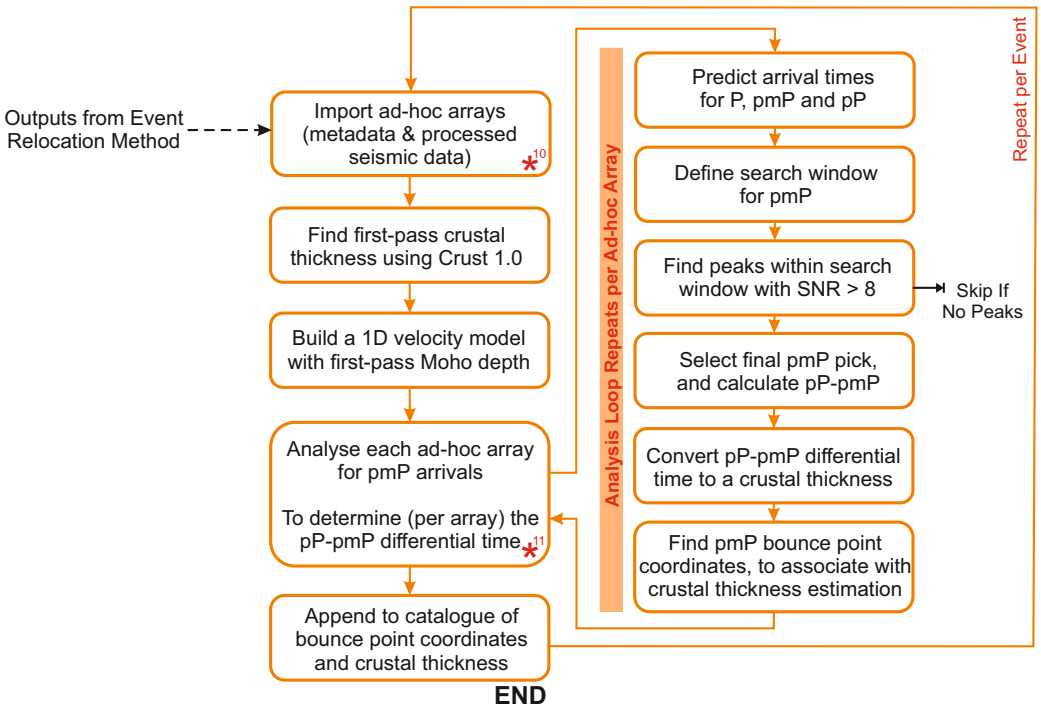

*Steps where the workflow may fail, and why:

1 - No events.
2 - No data available.
3 - No data without issues.
4 - Ad-hoc arrays can not be created with stations available.
5 - Ad-hoc arrays all fail quality control (QC) steps, have no picks, or failed for unique reason.
6 - Event will fail to be included in the catalogue if there are <2 defining data points.
7 - No ISC reported P arrivals within ad-hoc array aperture.
8 - ISCloc fails to relocate event.
9 - No outputs from P wave ad-hoc arrays.
10 - No pmP arrivals detected for any ad-hoc arrays for event.

*Steps where the workflow may fail for S wave data, and why:

1 - No stations with 3 component data available.
Relocate event using P wave data.
2 - S wave ad-hoc arrays all fail QC steps, have no picks, or failed for unique reason.
P wave results will continue.
3 - No ISC reported S arrivals within ad-hoc array aperture.
Event will be relocated using only P wave results.

Figure A.17: Summary workflow (continued).

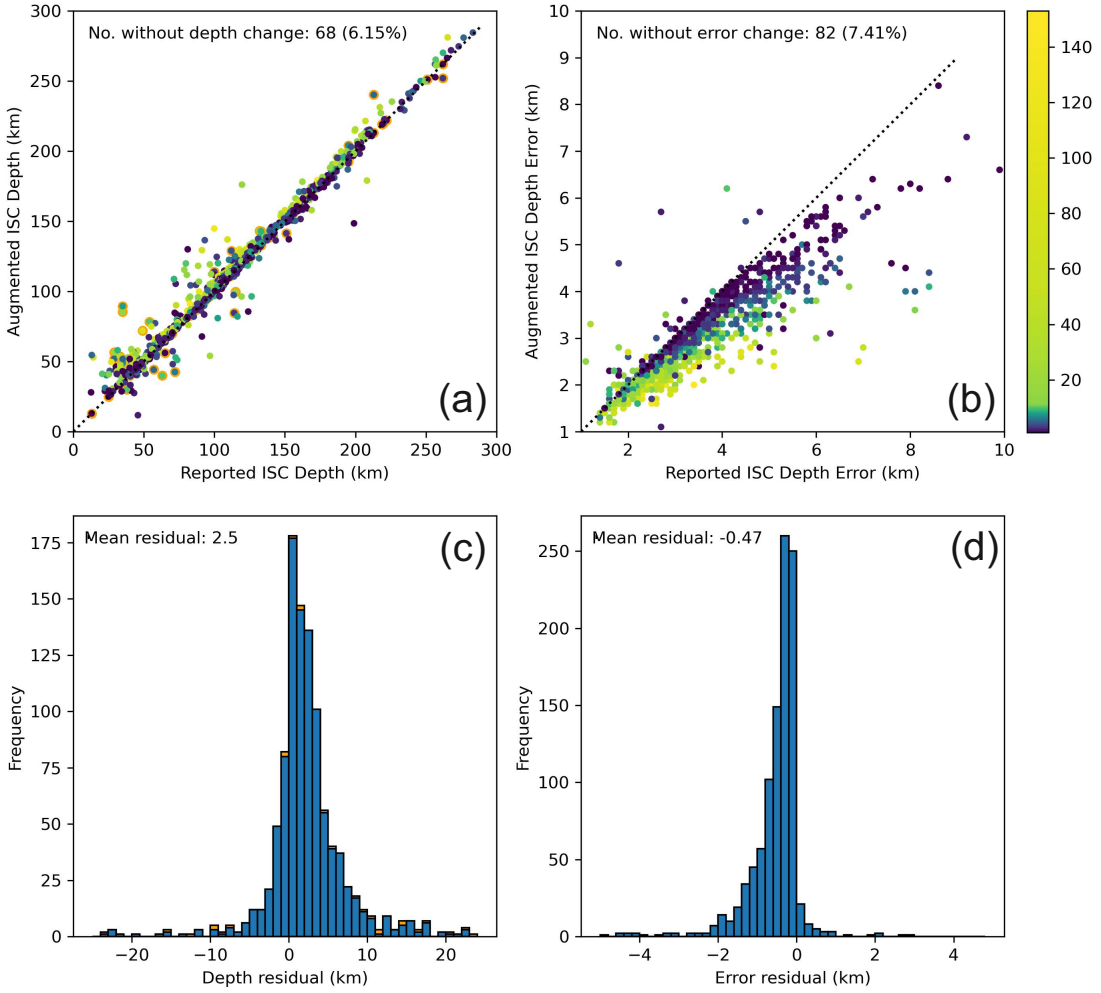

Figure A.18: Comparison of depth and depth error between the reported ISC and augmented ISC inputs (including *P*, *pP*, *sP*, *S* and *sS*) when applying ISCloc. (a) and (b) show the depth and depth error change when additional *ad-hoc* array phases are included. Both plots are coloured by number of additional time-defining phases, and (a) also has orange outlines for events which had fixed depths prior to the addition of phases. (c) and (d) are histograms showing the residual between the reported ISC and augmented ISC depths and depth errors respectively. (c) has orange bars indicating residual in depth when the fixed events are included. Events which did not have new time-defining phases from the augmented ISC input are not plotted.

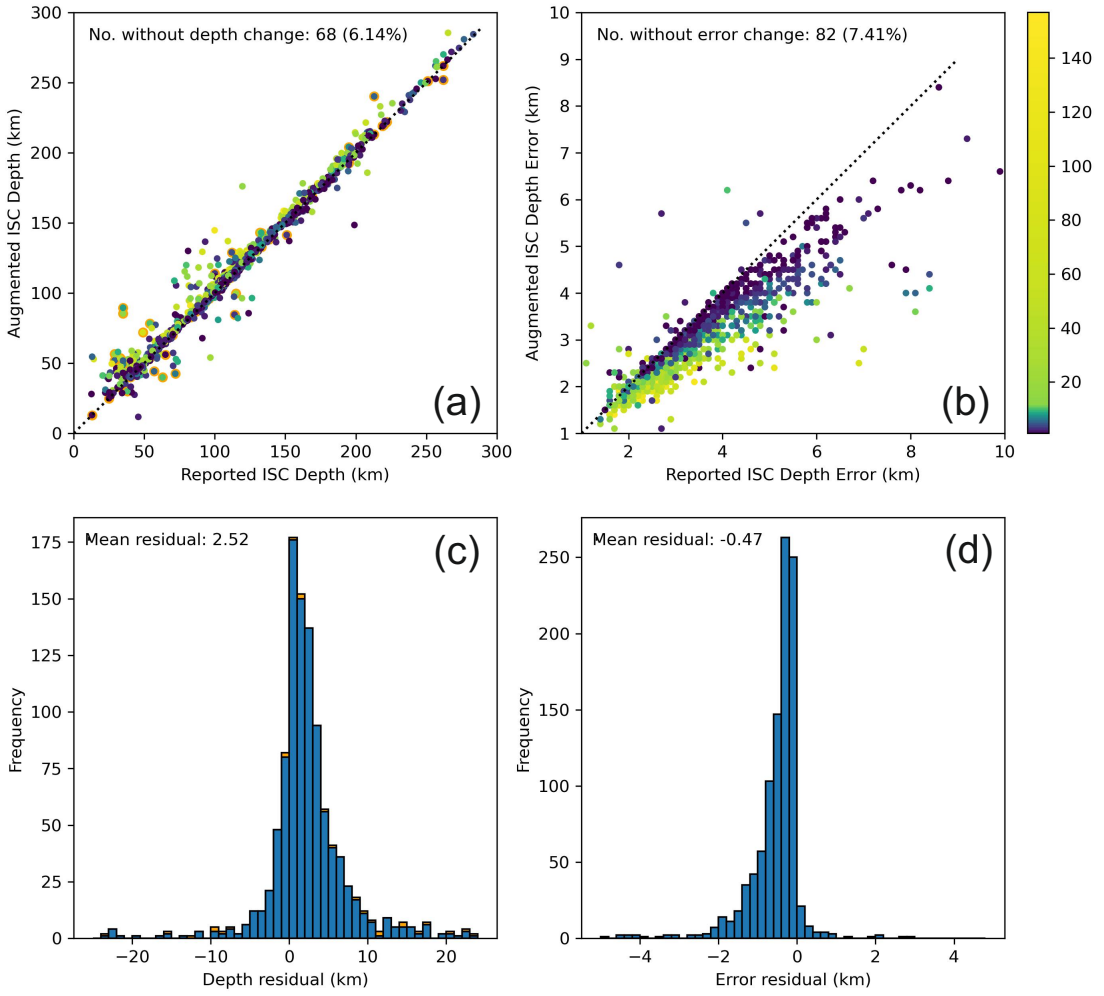

Figure A.19: Comparison of depth and depth error between the reported ISC and augmented ISC inputs (including *P*, *pP*, *sP*, and excluding *S* coda picks) when applying ISCloc. (a) and (b) show the depth and depth error change when additional *ad-hoc* array phases are included. Both plots are coloured by number of additional time-defining phases, and (a) also has orange outlines for events which had fixed depths prior to the addition of phases. (c) and (d) are histograms showing the residual between the reported ISC and augmented ISC depths and depth errors respectively. (c) has orange bars indicating residual in depth when the fixed events are included. Events which did not have new time-defining phases from the augmented ISC input are not plotted.

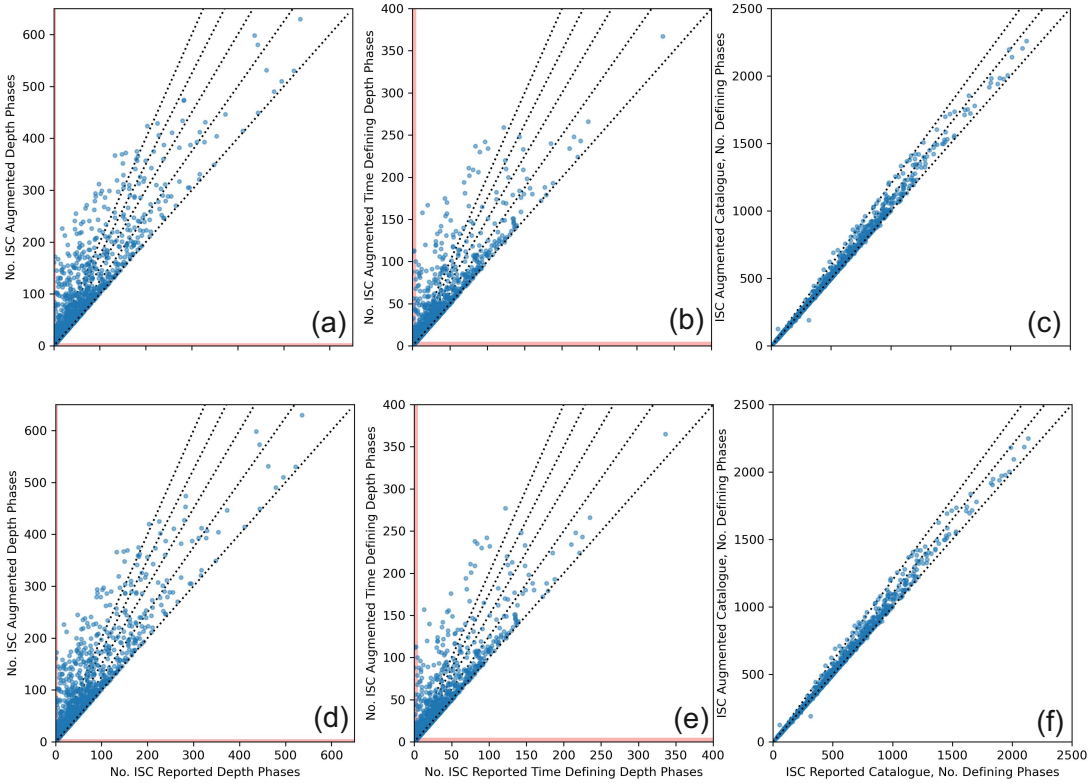

Figure A.20: Plots showing the number of input depth phases (a and d), time-defining depth phases (b and e) and all time-defining phases (c and f) for the ISC reported catalogue versus the augmented ISC catalogue. (a, b, c) show the results from the augmented catalogue including *P*, *pP*, *sP*, *S* and *sS*, whilst (d, e, f) show the augmented catalogue without *ad-hoc* array determined *S* coda picks. Red bands highlight events with less than 5 depth phases. It is apparent that the addition of *ad-hoc* array determined *S* coda picks is minimal during 3D relocation with ISCloc (Bondár & Storchak, 2011), due to their small numbers.